DOT/FAA/TC-17/57

Federal Aviation Administration
William J. Hughes Technical Center
Aviation Research Division
Atlantic City International Airport
New Jersey 08405

The Evaluation of Cold Dwell Fatigue in Ti-6242

February 2018

Final Report

U.S. Department of Transportation
Federal Aviation Administration

NOTICE

Technical Report Documentation Page

1. Report No.	2. Government Accession No.	3. Recipient's Catalog No.
DOT/FAA/TC-17/57		

4. Title and Subtitle	5. Report Date
THE EVALUATION OF COLD DWELL FATIGUE IN Ti-6242	February 2018
	6. Performing Organization Code

7. Author(s)	8. Performing Organization Report No.
Michael Mills[1], Somnath Ghosh[2], Stan Rokhlin[3], M.C. Brandes[1], A.L. Pilchak[1,4], and Jim Williams[1]	

9. Performing Organization Name and Address	10. Work Unit No. (TRAIS)
[1]Department of Materials Science and Engineering The Ohio State University Columbus, OH 43210 [2]Department of Civil Engineering Johns Hopkins University Baltimore, MD 21218 [3]Department of Industrial, Welding and System Engineering The Ohio State University Columbus, OH 43210 [4]Materials and Manufacturing Directorate, RXLMP Wright Patterson Air Force Base Dayton, OH 45433	
	11. Contract or Grant No. 2008-G-009

12. Sponsoring Agency Name and Address	13. Type of Report and Period Covered
U.S. Department of Transportation Federal Aviation Administration New England Regional Office 1200 District Ave Burlington, MA 01803	Final Report
	14. Sponsoring Agency Code AIR-6A1

15. Supplementary Notes

The FAA William J. Hughes Technical Center Aviation Research Division Technical Monitors were Joseph Wilson and Dave Galella.

16. Abstract

There is a failure mode in titanium alloys known as dwell fatigue. This mode is manifested by significant reductions in fatigue life, as measured by the number of cycles to failure, when the load is held at maximum value instead of continuously cycled. This failure mode is most prevalent in high-temperature alloys such as Ti-6Al-2Sn-4Zr-2Mo (+Si), IMI-829, IMI-834, and IMI-811, all of which contain a relatively low volume fraction of the body-centered-cubic b-phase. Dwell fatigue is most prevalent at temperatures below 300˚ C; therefore, it is sometimes also called “cold dwell fatigue.” The occurrence of this failure mode in aircraft engine rotors has been documented, but the methods for incorporating this possible failure mode into life calculations are less well developed. The consequences of a rotor failure can be severe, so conservative assumptions and field inspections are currently in use to prevent such an occurrence during service. Overly conservative assumptions are costly to the original equipment manufacturers and the operators, but the possible consequences of non-conservative assumptions are dangerously unacceptable. Therefore, there is a real need to better understand cold dwell fatigue to provide a more accurate indication of its effect on fatigue life. The objectives of this project have been to: 1) provide a fundamental understanding of the factors that promote the occurrence of dwell fatigue in Ti-6242 and other related titanium alloys and 2) to develop a quantitative model to predict crack initiation based on the alloy microstructure. This model development has been supported by state-of-the-art microstructure characterization involving electron optical and x-ray techniques. In addition, a new method for determining microstructures that are susceptible to dwell fatigue, by using nondestructive acoustic emission methods, has been demonstrated on test specimens. Validation on full-size engine rotor components remains to be conducted.

17. Key Words	18. Distribution Statement
Ti-6Al-2Sn-4Zr-2Mo alloy, Dwell fatigue, In-situ 3D High Energy X-Ray Diffraction, crack detection, Solid mechanics modeling, Nondestructive testing	This document is available to the U.S. public through the National Technical Information Service (NTIS), Springfield, Virginia 22161.

19. Security Classif. (of this report)	20. Security Classif. (of this page)	21. No. of Pages	22. Price
Unclassified	Unclassified	198	

ACKNOWLEDGEMENTS

The Ohio State University investigator team gratefully acknowledges the advice and guidance of our partners and collaborators from industry, university, and government.

In particular, the team thanks Andy Woodfield (GE Aircraft Engines), Jim Hall (Honeywell Engines), Daira Legzina (Honeywell Engines), Dietmar Helm (MTU), Andrew Haynes (Pratt & Whitney), Jack Schirra (Pratt & Whitney), Amit Chatterjee (Rolls-Royce®), Barry Kalb (GE Aircraft Engines), Olaf Roder (MTU), Claude Mons (Snecma), Dave Nissley (Pratt & Whitney), and Adrian Walker (Rolls-Royce). Thanks also to Mike Uchic and Dennis Dimiduk (Air Force Materials Laboratory), Jonathan Spowart (UES Incorporated), and Dave Furrer (Pratt & Whitney). The input provided by the Aerospace Industries Association (AIA)FAA Rotor Integrity Sub-Committee, chaired by Bill Knowles (Honeywell), is valued and appreciated. FAA sponsor representatives, Tim Mouzakis and Joe Wilson, provided invaluable advice and guidance.

The objective of this program was to assist the team's partners in understanding dwell fatigue. Without input from the aforementioned sources, this task would have been much more difficult.

TABLE OF CONTENTS

LIST OF FIGURES

LIST OF TABLES

LIST OF SYMBOLS, ABBREVIATIONS, AND ACRONYMS

σ	Flow stress
q	Non-dimensional material parameter
b	Burger's vector
B	Crack opening displacement
K	Stress intensity factor
n	strain hardening
Ti	Titanium
AC	Air-cooled
AN	Annealed
AR	As received
BA	Backscattering amplitude
BCC	Body centered cubic
BOR	Burgers orientation relationship
BS	Backscattered signal
CPFE	Crystal plasticity finite element
CPFEM	Crystal plasticity finite element model
CRSS	Critical resolved shear stress
DNF	Did not fail
EBSD	Electron backscattered diffraction
FC	Furnace-cooled
FE	Finite element
FEM	Finite element model
FFT	Fast Fourier transform
FIB	Focused ion beam
GND	Geometrically necessary dislocation
GSDF	Grain size distribution function
HCAP	Homogenization-based continuum-level anisotropic plasticity
HCP	Hexagonal close packed
HEDM	High-energy x-ray diffraction microscopy
IF	Initiation facets
LD	Loading direction
MoDF	Misorientation distribution function
MTR	Microtextured region
ND	Normal direction
ODF	Orientation distribution function
OIM	Orientation imaging microscopy
PF	Propagation facets
RMS	Root mean square
RSS	Resolved shear stress
RVE	Representative volume element
SEM	Scanning electron microscopy
SF	Schmid factor
SIS	Secondary initiation site(s)
SNR	Signal-to-noise ratio
SQ	Solution-quenched

SRO	Short range order
TD	Transverse direction
TDF	Texture distribution function
TEM	Transmission electron microscopy
TI	Texture index
TLD	Through lens detector

EXECUTIVE SUMMARY

Dwell fatigue is a failure mode in titanium alloys manifested by significant reductions in fatigue life, as measured by the number of cycles to failure, when the load is held at maximum value instead of continuously cycled. This failure mode is most prevalent in alloys designed for higher temperature service, such as Ti-6Al-2Sn-4Zr-2Mo (+Si), IMI-829, IMI-834, and IMI-811, all of which contain a relatively low-volume fraction of the body-centered-cubic β-phase. Dwell fatigue is most prevalent at temperatures below 300˚ C; therefore, it is sometimes also called cold dwell fatigue. The occurrence of this failure mode in aircraft engine rotors has been documented, but the methods for incorporating this possible failure mode into real-life calculations have not been developed. The consequences of a rotor failure can be severe, so conservative assumptions and field inspections are currently in use to prevent such an event during service. Overly conservative assumptions are costly to the original equipment manufacturers and the operators, and the possible consequences of nonconservative assumptions are dangerously unacceptable. Therefore, there is a real need to better understand cold dwell fatigue to provide a more accurate prediction of its effect on fatigue life.

This project had three principle objectives:

The first was to provide a fundamental understanding of the factors that promote the occurrence of dwell fatigue in the Ti alloy Ti-6242 and other related alloys. This has involved the use of state-of-the-art characterization techniques, including electron microscopy and synchrotron x-ray studies. Key findings from these studies include the following:

1. The dwell effect is observed in single-phase alloys having textures that lack hard grains.
2. Failure mechanisms are dependent on both slip character and loading conditions.
3. Crack propagation rates within the faceted region were considerably higher than those observed during continuous cycling. This finding implies that the small crack growth regime may be equally as important to explaining the dwell effect as the crack-initiation stage.

Second is to develop a robust nondestructive acoustic method for detecting microstructures potentially susceptible to dwell fatigue. Such a method has been developed and demonstrated in the laboratory on test specimens. Verification on full-size engine rotor components remains to be conducted. Key conclusions derived from these studies include the following:

1. It is possible to use ultrasonic attenuation to differentiate between different degrees of microtexture in alpha + beta processed titanium alloys.
2. The directional ratios of backscattering signals can be used to size the degree of microtexture. These ratios depend only on geometrical parameters of the elongated grains and on a newly introduced nondimensional material parameter, q.
3. The backscattering-to-attenuation ratio method allows one to obtain explicitly the effective size parameter of microtextured regions from combined measurement of the ultrasonic backscattering and attenuation from one side of the sample.
4. Good agreement was observed between microtexture region sizes in the direction of wave propagation directly measured by orientation imaging microscopy and the results of inversion by the theoretical models.

Third is to develop a model for predicting load-shedding and crack initiation in these titanium alloys. A completely novel, microstructure-sensitive finite element model (FEM) has been developed for this purpose. On the basis of this sophisticated FEM, homogenized models for time-dependent flow and crack initiation have also been developed. Key developments from this study include:

1. A homogenized continuum anisotropic plasticity model to make accurate predictions of evolving stresses and strains at any point of the microstructure.
2. A probabilistic macroscopic crack nucleation model for polycrystalline microstructures that can predict the probability of crack nucleation at any point in a component at any instant during the loading knowing the Schmid factor, misorientation, grain size, and macroscopic stress level.

The team of university researchers benefited tremendously from close and regular contact with representatives from the major aircraft engine manufacturers via monthly conference calls and periodic full-day reviews. These contacts were invaluable in keeping the project activities focused on the issues of greatest interest to the engine makers.

1. INTRODUCTION

The near-alpha titanium alloys are ubiquitous in applications for compressor rotor spools. In work conducted in several laboratories around the world, a significant debit in the fatigue capability (reduced lifetimes) of these alloys has been found when comparing results obtained from continuous cycling versus holding-at-maximum-load (dwell-fatigue) conditions. Because the magnitude of the life debit decreases with increasing temperature, the phenomenon has been called cold dwell fatigue. The least-understood aspects of this phenomenon are the variations in fatigue capability. These variations in behavior appear to be closely linked to variations in microstructure. In particular, there is an urgent need to develop an understanding of dwell-time fatigue-microstructure relations and dwell-time crack initiation. This is not a new phenomenon, but the details of the interaction between microstructure, loading history, hydrogen content, and fatigue strength (life) are not understood in a fundamental sense.

The consequence of dwell-life debit can be nonconservative life estimates for critical rotating parts in aircraft engines. It is, therefore, imperative that a better understanding of the factors that promote this failure mode be developed and communicated to the designers of aircraft engines. There have been several failures of compressor rotors due to dwell fatigue, and field inspections have found cracks in other rotors. There is no principle-based understanding of this failure mode; this makes it difficult to account for the possibility of dwell-fatigue failure in calculations of the life of rotors. Consequently, a conservative approach is currently taken to life calculations augmented by periodic field inspections. Although this approach is safe, it is impractical and disruptive to fleet operations.

It has been established that dwell fatigue is associated with internal cracking of microstructural regions for which the crystal orientation of the hexagonal close-packed (HCP) α-phase is close to the [0001] or "c" orientation. These regions have higher yield and flow strengths than the surrounding regions of softer orientation. Therefore, to model the crack-initiation process and be faithful to the microstructural characteristics of the alloy, it is crucial that the load-shedding from hard to soft regions be accurately modeled. The aim of much of this program—both experimental and modeling—is to comprehensively treat this load-shedding behavior through a detailed understanding of local deformation processes for different microstructures and loading conditions.

To model a given microstructure, the crystal plasticity modeling has required a sound understanding of the constitutive response of the individual components of the microstructure. This has been achieved by performing microtensile tests on oriented single crystals. In an effort to provide the broadest possible experimental basis for the parametric studies that are efficiently addressed by the crystal plasticity and derived homogenized models, the fundamental properties of several alloys (e.g., Ti-6242, Ti-811, and a single-phase Ti-7Al alloy) were systematically studied with respect to microstructure variations and loading conditions to access the effect on their dwell properties. The most detailed fractographic and substructure study yet performed was conducted on microtextured Ti-811. In this work, high-resolution scanning electron microscopy (SEM) was combined with orientation imaging microscopy (OIM) and in-depth defect (dislocation structure) analysis using scanning transmission electron microscopy, facilitated by site-specific focused ion beam (FIB) extraction of thin foils. The results of this work call into question the conventional wisdom concerning the local mechanisms associated with dwell-crack initiation in this class of titanium alloys. Advancements in the modeling capabilities that have been realized

during the course of this project require the development of more sophisticated experimental analyses for the validation of model predictions. Model validation requires site-specific measurements of the full 3D stress states that lead to cracking. In pioneering work, funded in part by this program, synchrotron x-ray analysis of in-situ loading of a polycrystalline Ti-7Al alloy has been performed, and the full stress tensor in a grain neighborhood has been determined. In addition, the critical resolved shear stresses (CRSS) have been determined for various slip systems and compared with the constitutive testing results. It is believed that this approach will open new strategies for the assessment of structural materials for safety-critical applications.

These experiments have helped provide quantitative, constitutive data and an understanding of deformation and crack initiation mechanisms used in the development of an image-based crystal plasticity finite element model (CPFEM) for Ti-6242. This model has been used to establish microstructure property relations regarding dwell-fatigue behavior for Ti-6242. A dwell-fatigue crack nucleation criterion was also developed at the length scale of individual grains. To incorporate the findings of the crystal plasticity model in macroscopic constitutive and fatigue models that can be incorporated in general purpose finite element model (FEM) codes, methods of homogenization have been conducted with the CPFEM results. This consists of a systematic sensitivity analysis to retain important variables in the functional dependence equations. Homogenization of the microscopic variables was conducted to develop macroscopic material and damage laws. A homogenization-based damage initiation model for macroscopic (structural scale) analysis of titanium-based alloys was formulated. The damage model is based on the crack initiation at the microcrystalline or polycrystalline scale, and incorporates functional dependencies between stresses and microstructural parameters like orientation (i.e., Schmid factor), misorientation, and grain sizes. The novelty of such damage surfaces is that they are completely based on the physics of the microstructure and are not phenomenological like other models.

A major thrust of the program has been a study of the ultrasonic backscattering and attenuation coefficients as a function of the scale of microtexture region sizes. Robust models have been developed for inversion of the mean microtextural region size and morphology from ultrasonic measurements. Estimation of the mean misorientation parameter of crystallites in the microtextured region (MTR) can also be made and validated by comparison with detailed OIM analysis. This resulted in the development of a model based on correlations between ultrasonically measured microtexture and dwell-fatigue life.

This research project was undertaken to provide a better understanding of the factors that cause dwell fatigue. The project involved metallurgy, solid mechanics, and nondestructive evaluation experts from The Ohio State University and Princeton University. A team of Ti experts from GE Aircraft Engines, Rolls-Royce®, Honeywell, and MTU was also formed, and the results of the research were communicated to them on a regular basis. The objective of this research project was to provide an improved level of understanding and modeling capabilities that will permit high-confidence rotor life calculations that include the possibility of occurrence of dwell fatigue.

2. EXPERIMENTAL SUPPORT FOR MODEL

2.1 CONSTITUTIVE DATA

To model a given microstructure, the crystal plasticity modeling required a sound understanding of the constitutive response of the individual components of the microstructure. The microstructure of most critical concern, Pancake 2, consists of globular alpha surrounded by regions of colony microstructure. The first step in the development of the crystal plasticity model for deformation in titanium alloys was the modeling of single-phase α HCP Ti-6wt%Al. The α phase is the principal constituent in near-α alloys, such as Ti-6242. As mechanical properties of the α phase are known to be anisotropic, it is necessary to characterize its properties. Because of a lack of relevant data in the literature, single crystal tests were conducted on a binary Ti-6.7 wt% aluminum (Al) alloy. The second step was to model the two-phase colony microstructure, consisting of α and β body centered cubic (BCC). In single colonies, the symmetry of slip systems is broken with the addition of the β phase, leading to an anisotropy in the mechanical behavior. Because this was not addressed in any significant detail in previous studies, single-colony mechanical tests were conducted to characterize the constitutive behavior of the colonies as a function of the operative slip system. The information derived from these tests was then incorporated into the crystal plasticity finite element (CPFE) modeling for creep and load shedding.

2.1.1 Yield Stress Anisotropy and Tension-Compression Asymmetry in the Room Temperature Deformation of Titanium Alloy Single Crystals

Table 1 summarizes the yield stress measurements for bulk compression, microtensile, and microcompression tests on single-phase α HCP Ti-6wt%Al and two-phase α+β (HCP + BCC) Ti-6242 single-colony crystals [1–6]. In all cases, the nominal imposed strain rate is $1x10^{-4}$ s^{-1}. There is significant anisotropy in the CRSS values. In the single-phase crystals, anisotropy depends primarily on active slip vector; the activation of <a> slip (i.e., <1123> slip) on basal, (0001), and prismatic planes, $\{10\bar{1}0\}$, requires significantly less stress than the activation of <c+a> slip (i.e., <1123> slip) on pyramidal planes. Only a slight anisotropy is observed between <a> slip systems; the yield stresses of crystals aligned for <a> $\{10\bar{1}0\}$ slip is lower than those aligned for <a>(0001) slip. In two-phase colony crystals, anisotropy depends both on the slip vector type (i.e., <a> or <c+a>) and the relationship of the slip vector to the β-phase. As shown in figure 1, there are three distinct <a> slip vectors: a_1, a_2, and a_3. For a_1 and a_2, the misalignment of a mating <111> slip vector in the β-phase is less than 15º; the a_3 slip vector is highly misaligned with $<111>_\beta$ but is close to an $<001>_\beta$ vector. In the case of <a> slip on first-order prismatic planes, yield stress increases with misalignment between the α- and β-phase slip vectors. The yield stress for a_1 slip is the lowest (approximately equal to the yield stress of the single-phase crystals), and the yield stress for a_3 slip is the highest. In the case of <a> slip on the basal plane, the a_2 basal system has a significantly larger CRSS value compared to the other a-type systems. Quite unexpectedly, the a_3 basal system has a relatively small CRSS value. Insight into this remarkable result was provided by the transmission electron microscopy (TEM) observations on the single colony compression samples (results are summarized in previous reports [7]). Yield stresses for <a>(0001) are sensitive to both misalignment between the α- and β-phase slip vectors and the line direction of <a> dislocations interacting with the α-β interface, where near-edge dislocation components impinge on the β-phase during a_1 and a_3 slip, and near-screw dislocation components impinge on the β-phase during a_2 slip [8, 9].

Table 1. Yield strengths of Ti alloy single crystals aligned for slip on <a> basal (B), <a> prism (P), and <c+a> systems: both tension (T) and compression (C) test results are shown

Author	Alloy	Strain Rate	Test	<a1> B	<a2> B	<a3> B	<a1> P	<a2> P	<a3> P	<c+a> (11$\underline{0}$1)	<c+a> (11$\underline{2}$2)
Savage (2000)	6.6Al	10^{-4}	C	620	620	620	595	595	595		1830
May (2010)	6.6Al	$1.7x10^{-4}$	T	595	595	595	561	561	561		1121
	6.6Al	$1.7x10^{-4}$	T	538	538	538					1152
	6.6Al	$5.3x10^{-4}$	T	662	662	662	687	687	687		1145
	6.6Al	$9.4x10^{-4}$	T	684	684	684					1128
Paton (1976)	5Al		T							759	
			C								1854
Suri (2000)	5Al-2.5Sn	10^{-4}	C		756	739	533	580			
Savage (2000)	6242	10^{-4}	T	540	680	500	500	510	540		
			C	670	824	765					
Norfleet (2007)	6242	10^{-4}	C								2200
May (2010)	6242	$1.7x10^{-4}$	T	540	555	558	607	642			
		$1.7x10^{-4}$	T		576			650			
		$5.3x10^{-4}$	T	640	593	538	562	681			
		$9.4x10^{-4}$	T	611	630	670	625	666			

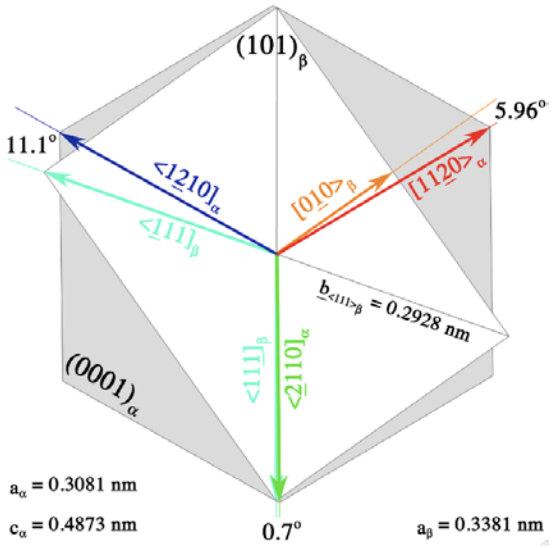

Figure 1. Orientation relationship between the α- and β-phases of Ti-6242. <1120> is the primary slip vector of the α-phase, and <111> is the primary slip vector of the β-phase

In addition to yield stress anisotropies, single crystals display yield and flow stress asymmetries. For both <a> and <c+a> slip, crystals deformed in compression show greater flow strengths than those deformed in tension. The modest asymmetry in <a> slip is the result of the glide behaviors of screw dislocations. As shown in figures 2 and 3 [10], the distribution of slip bands along the gage lengths of the single-phase samples deformed in tension is very different than those deformed in compression. Although similar <a> dislocation arrays are observed in TEM studies of the single-phase crystals when deformed in either tension or compression, frequent cross-slip and secondary slip are more readily observed as a result of tensile deformation. Yield strength asymmetry is particularly pronounced in the case of <c+a> slip. Postmortem TEM analyses of the single-phase crystals indicate that mechanisms of deformation due to <1123> slip are different under tensile loading than compressive loading. As seen in figure 4, <c+a> slip occurs on first-order pyramidal planes, $\{10\bar{1}1\}$, under tensile loading and on second-order pyramidal planes, $\{11\bar{2}2\}$, under compressive loading. Dislocations are well distributed along the gage length of tensile bars giving the crystal high ductility (>10% elongation at failure) but are arranged in a single, highly dense band in compression samples. Crystals deformed in compression were observed to undergo catastrophic failure at small strains because of adiabatic shear localization.

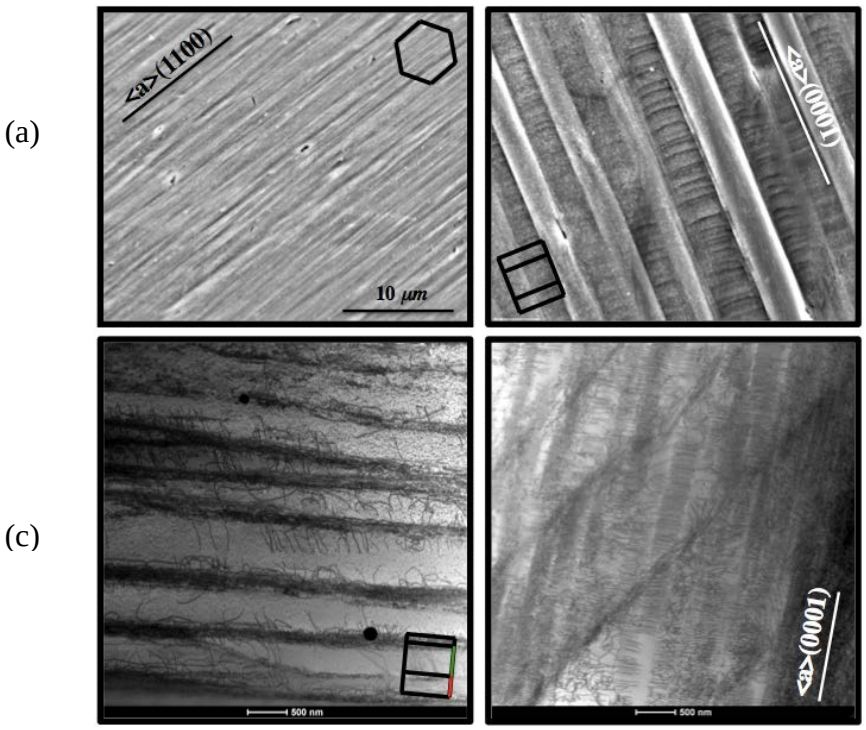

Figure 2. Surface slip traces (a, b) and dislocation arrangements (c, d) in single-phase crystals deformed in tension by <a> $\{10\bar{1}0\}$ (a, c) or <a>(0001) slip (b, d)

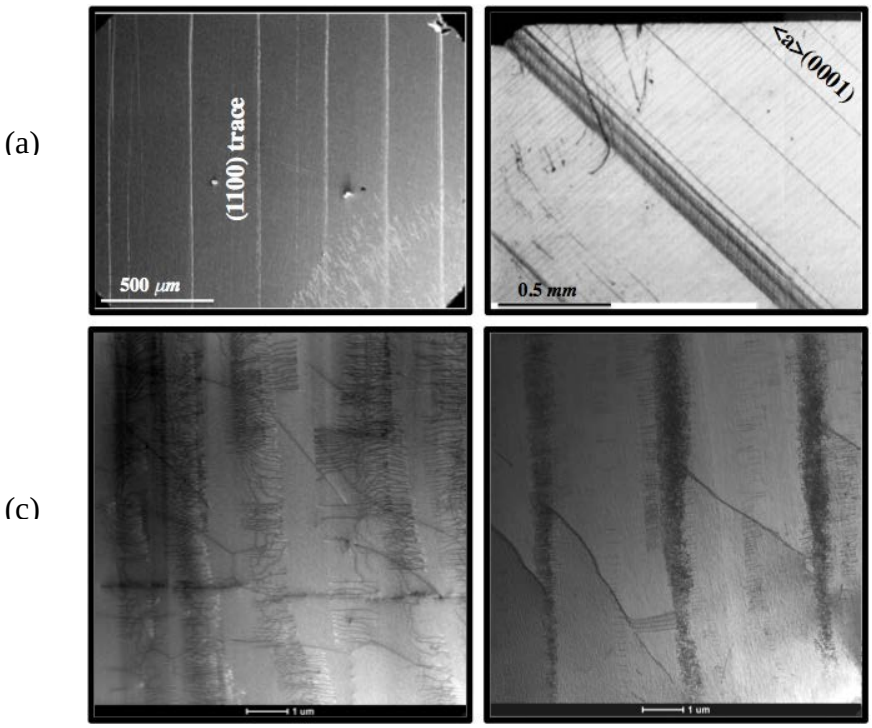

Figure 3. Surface slip traces (a, b) and dislocation arrangements (c, d) in single-phase crystals deformed in compression by <a> $\{10\bar{1}0\}$ (a, c) or <a>(0001) slip (b, d)

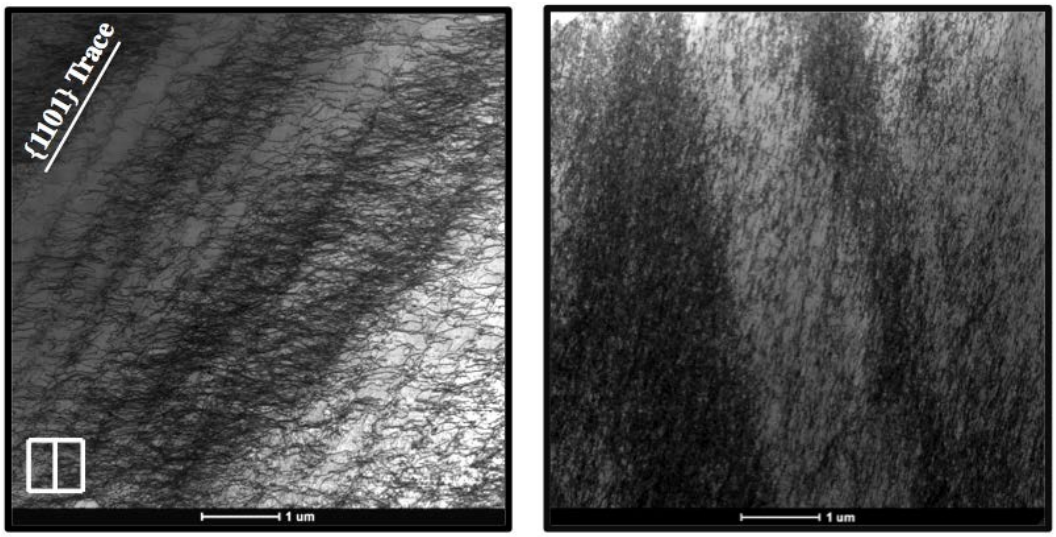

(a) (b)

Figure 4. Dislocation arrangements in single-phase crystals loaded along [0001] in (a) tension and (b) compression

2.1.2 Strain Rate Dependence of Single Slip in Titanium Alloy Single Crystals

It is well known that polycrystalline titanium alloys are sensitive to the deformation rate at room temperature [11, 12]. This strain rate dependence, in combination with strain-hardening behaviors, allows for the accumulation of plastic strain under static and dwell-fatigue loading. The relationships between strain hardening (n), strain-rate sensitivity (m), and flow stress (σ) are given by Hollomon form:

$$\sigma = K\varepsilon_{pl}^{\ n}\dot{\varepsilon}_{pl}^{\ m} \tag{1}$$

where K is a strength parameter and ε_{pl} is plastic strain. These parameters can be related to creep strain (ε_{creep}) by an Andrade form:

$$\varepsilon_{creep} = At^{a} \tag{2}$$

where A is a time constant, t is time, and

$$a = \frac{m}{m+n} \tag{3}$$

As time-dependent (creep) plasticity is a feature inherent to the dwell-fatigue phenomenon in near-α and α+β titanium alloys, a CPFM capable of capturing all aspects of dwell-fatigue responses must incorporate the rate effects of plastic flow for each slip system. As such, an effort to quantify these parameters for the single- and two-phase crystals was made. For these experiments, crystals orientated for single slip were loaded at nominal strain rates between 1×10^{-4} s^{-1} and 5×10^{-3} s^{-1}. As presented in table 2 [5, 10], strain-rate sensitivity, like yield stress, displays both anisotropies and asymmetries. Under compressive loading, the strain sensitivity of <a> slip is modestly affected by

the slip system, but ranges between 0.02 and 0.03. Under tensile loading, strain-rate sensitivity varies much more widely. Whereas *m* for <a> $\{10\bar{1}0\}$ slip is similar to that measured in compression, *m* for <a>(0001) is up to five times higher. Minimal rate sensitivity is observed for <c+a> slip; *m* is approximately one half that of <a> prism slip.

Table 2. Strain-rate sensitivities of Ti alloy single crystals aligned for slip on <a> and <c+a> systems

Alloy	Stress State	Slip System	*m*
Ti-6.6Al	Comp	<a> Prism	0.02
		<a> Basal	0.02
		<c+a>	---
	Ten	<a> Prism	0.086
		<a> Basal	0.155
		<c+a>	0.015
Ti-6242	Comp	a_1 Prism	---
		a_2 Prism	---
		a_3 Prism	---
		a_1 Basal	0.025
		a_2 Basal	0.0281
		a_3 Basal	0.024
		<c+a>	---
	Ten	a_1 Prism	0.01
		a_2 Prism	0.03
		a_3 Prism	---
		a_1 Basal	0.125
		a_2 Basal	0.115
		a_3 Basal	0.140
		<c+a>	> 0.07
Ti-52.5	Comp	a_1 Prism	0.0256
		a_2 Prism	0.0250
		a_2 Basal	0.0230
		a_3 Basal	0.0243

2.2 INFLUENCE OF MICROSTRUCTURE ON CREEP AND DWELL FATIGUE

The deformation, creep, continuous-cycling fatigue, dwell fatigue, and fracture responses of titanium alloys are highly sensitive to the nature of slip and slip length. In efforts to provide an experimental basis for the parametric studies that are efficiently addressed by CPFEM, the fundamental properties of several alloys were systematically modified to access the effect of various microstructural parameters on the dwell properties of titanium alloys.

Two-phase titanium alloys containing a majority volume fraction of the HCP α phase have long been known to undergo creep deformation at lower temperatures ($T < T_m$) and stress ($\sigma < \sigma_{ys}$). The time dependence of this plasticity, resulting from <a> slip in the α phase, has been found to be sensitive to the microstructural condition. It is now well understood that the dwell effect is a synergistic relationship between creep and fatigue deformation and damage mechanisms. In efforts to understand the contributions of fine-scale structure on the properties of two-phase colony microstructures, monotonic and creep experiments were carried out on Ladish Pancake 3. Previously reported work under this contract has indicated that the microstructure of this material is modestly sensitive to dwell fatigue, showing a dwell debit of 3–5. Taking creep strength as a proxy for dwell-fatigue resistance, the effect of lath and rib morphology on strength and creep were assessed without modifying primary α texture and colony size (maximum slip length or effective structural unit size). Modest variations in lath and rib structures were found to dramatically affect creep strength.

Current examinations of the dwell effect have been limited to commercial alloys with complex two-phase microstructures. Although this practice has practical industrial significance, it limits the extent to which the fundamental parameters controlling the dwell-fatigue phenomenon can be interrogated. Dwell-fatigue susceptibility is presumed to be maximized in alloys displaying highly planar slip (as is the case for most commercially processed materials), large grain or effective structural unit sizes, and a statistically significant population of rogue grains (i.e., grains with [0001] aligned to the tensile axis that are neighbored by grains with [0001] highly inclined to the tensile axis). However, no experiments to date clearly show the degree to which each of these factors contributes to dwell sensitivity. The effect of slip planarity on the creep, dwell fatigue, and continuous-cycling fatigue are examined in a single-phase α HCP phase alloy. Tests are run in both tension and compression to differentiate between the plastic and damage contributions to dwell fatigue. Under tensile loading, plastic response at the macroscale is a function of both plasticity and damage accumulation; in contrast, damage mechanisms are not expected to be active under compressive loading. Post-mortem fractographic studies were carried out to assess the mechanism of fracture under each condition.

Faceted crack growth features are widely associated with dwell-fatigue fracture. Based on experimental observations over the past several decades, there is a basic understanding of the sequence of fatigue crack formation during continuous cycling. Many researchers have observed the formation of planar slip bands, followed by crack initiation and propagation along these slip bands [13–15]. On the fracture surface, cracking along a slip band leads to the formation of planar features that are commonly referred to as facets [16]. Facets are present on failures resulting from continuous cycling and are also a characteristic of the fracture surfaces near the origin areas of specimens that have failed by dwell fatigue [17-19], static loading in air [5, 20], and stress corrosion cracking [21]. Among these, there has been considerable controversy surrounding the origins and characteristics of facets found on dwell-fatigue specimens.

Dwell-fatigue failures are generally characterized as having subsurface crack initiation sites with planar facets that can be either inclined or nearly perpendicular to the loading direction (LD), depending on the magnitude of applied stress [18, 20, 22]. Furthermore, dwell-fatigue facets have been generalized widely as being on or near the basal plane [18, 23–26]. Early work by Evans suggested that the facet planes were oriented within 5^o of the basal plane and were also nearly perpendicular to the LD. Therefore, it became necessary to rationalize how slip could occur on

basal planes that were oriented nearly perpendicular to the LD that had essentially zero resolved shear stress (RSS). Consequently, Evans and Bache proposed a conceptual model based on Stroh's formulation [27] of the stress field around a dislocation pileup in an isotropic material and subsequent crack nucleation from this pileup. Although qualitatively attractive, the assumptions of this model have yet to be demonstrated experimentally. In a study of a highly microtextured alloy, the fundamentals of the Stroh model are tested. Specimens brought to failure under creep, continuous cycling fatigue, and dwell-fatigue conditions are investigated by quantitative tilt fractography and TEM.

2.2.1 Influence of α-lath Morphologies on the Ambient Temperature Creep Responses of β-annealed Ti-6Al-2Sn-4Zr-2Mo

The microstructures of commercial titanium alloys belonging to the α, near α, and α+β classes are known to be varied and complex. Depending on alloy composition, processing route, and thermal treatment, they may display a range of α and β BCC-phase morphologies and size scales. A colony-type microstructure is developed by heating above the β transus temperature, T_{β}, and cooling at modest rates (β annealing). Frequently, β-annealed alloys will have what appears to be a lamellar microstructure consisting of primary α laths separated by ribs of the parent β phase. In addition, these ribs often contain α-phase precipitates, known as secondary α, of several size scales but always much finer than that of the primary α-laths.

As one might expect, the mechanical properties, particularly yield and ultimate tensile strengths and fatigue life, of these materials have been shown to be sensitive to variations in the morphologies and volume fractions of α-lath structures. However, few studies published in the literature to date have addressed these issues in a careful and methodical manner. The effects of primary α-lath and β-rib thicknesses and secondary α morphology have yet to be cleanly separated from the influences of other microstructural variables, such as prior-β grain size, colony size, grain boundary α thickness, short-range ordering, etc. The nature of low-temperature creep in heat-treatment modified β-annealed Ti-6Al-2Sn-4Zr-2Mo was examined as a function of primary and secondary α–lath and β-rib structures. Secondary α morphology and content were systematically modified and crept under tensile and compressive-loading conditions. Creep response is found to obey a power law form in which the time exponent varies with microstructural and loading conditions. Variations in plastic response are discussed in terms of strain hardening and strain-rate sensitivity parameters measured in single and polycrystalline titanium alloys.

Room-temperature creep experiments were performed on Ladish Ti-6242 Pancake 3; details of the forging and composition are presented in previous reports [7]. The as received (AR) microstructure and texture are observed in figures 5 and 6. To systematically vary the α-lath thicknesses, β-rib thicknesses, and secondary α morphologies without influencing the prior-β grain size, colony size, or primary α-lath texture, the AR material was sectioned, vacuum-encapsulated, and heat-treated according to four separate schedules: annealed (AN), furnace-cooled (FC), furnace-cooled then annealed (FC+AN), and solution-quenched (SQ):

AN: $T_{\beta - 95K}$ for 10 minutes + water quench

FC: $T_{\beta - 95K}$ for 1 hour + furnace cool

FC+AN: $T_{\beta - 95K}$ for 1 hour + furnace cool to room temperature + $T_{\beta - 65K}$ for 10 minutes + water quench

SQ: $T_{\beta - 10K}$ for 1 hour + quench to $T_{\beta - 120K}$ for 1 hour + water quench

Figure 5. Microstructure of Ti-6242 Pancake 3 in the AR condition

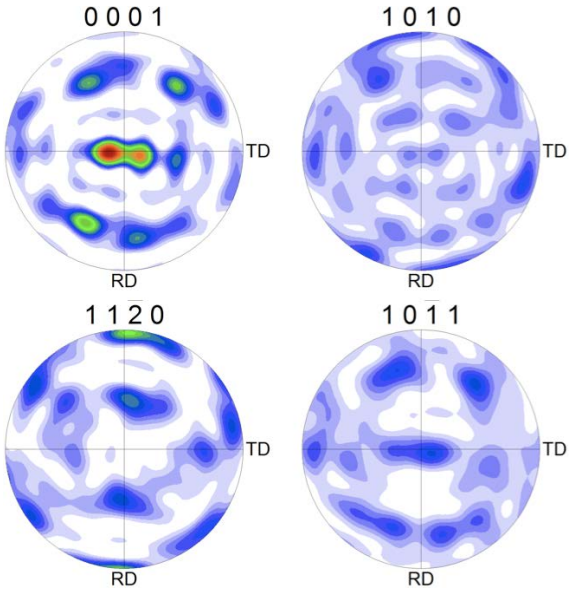

Figure 6. Texture of Ti-6242 Pancake 3 in the AR condition (highest texture index, 11x random, is red; lowest texture index, 0x random, is white)

Once machined and heat-treated, AN, FC, FC+AN, and SQ specimens were aged in evacuated quartz tubes for 2 hours at 873 K and oil quenched to minimize strong variations in short-range order (SRO) state. Figure 7 shows that three of the microstructures displayed similarly diffuse superlattice reflections, indicating that each heat treatment produced similar degrees of ordering within the primary α phase.

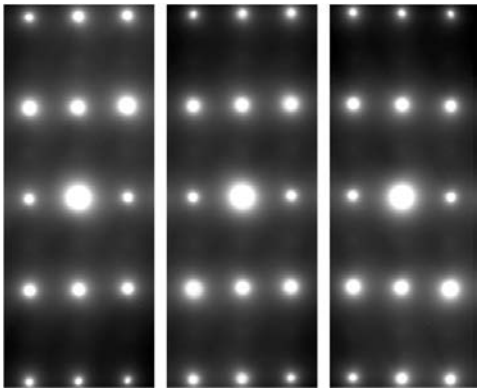

Figure 7. Electron beam diffraction patterns of the primary α-laths in the AR (a), FC+AN (b), and FC (c) Ti-6242material.; <1120> zone axis

Figure 8 shows the five Ti-6242 microstructures investigated in this study. The microstructure of the AR material (see figure 8, top) is a Widmanstätten colony structure with a disc- or pancake-shaped prior β grains, 300–400 μm wide and 300–400 μm long, and an average colony size of 75–150 μm. The primary α-laths and β-ribs have approximately equal thicknesses (1–4 microns). The β-ribs contain several size scales of secondary alpha: both fine laths (~20 nm thick x ~100 nm long) and extremely fine, short laths interspersed among long, thin laths (~100–200 nm in thickness) running parallel to thicker primary laths. TEM diffraction and orientation imaging studies show that the long, thin α-laths maintain the overall α orientation of the colony, whereas the finer structures generally have different orientations, as given by the Burgers orientation relationship (BOR).

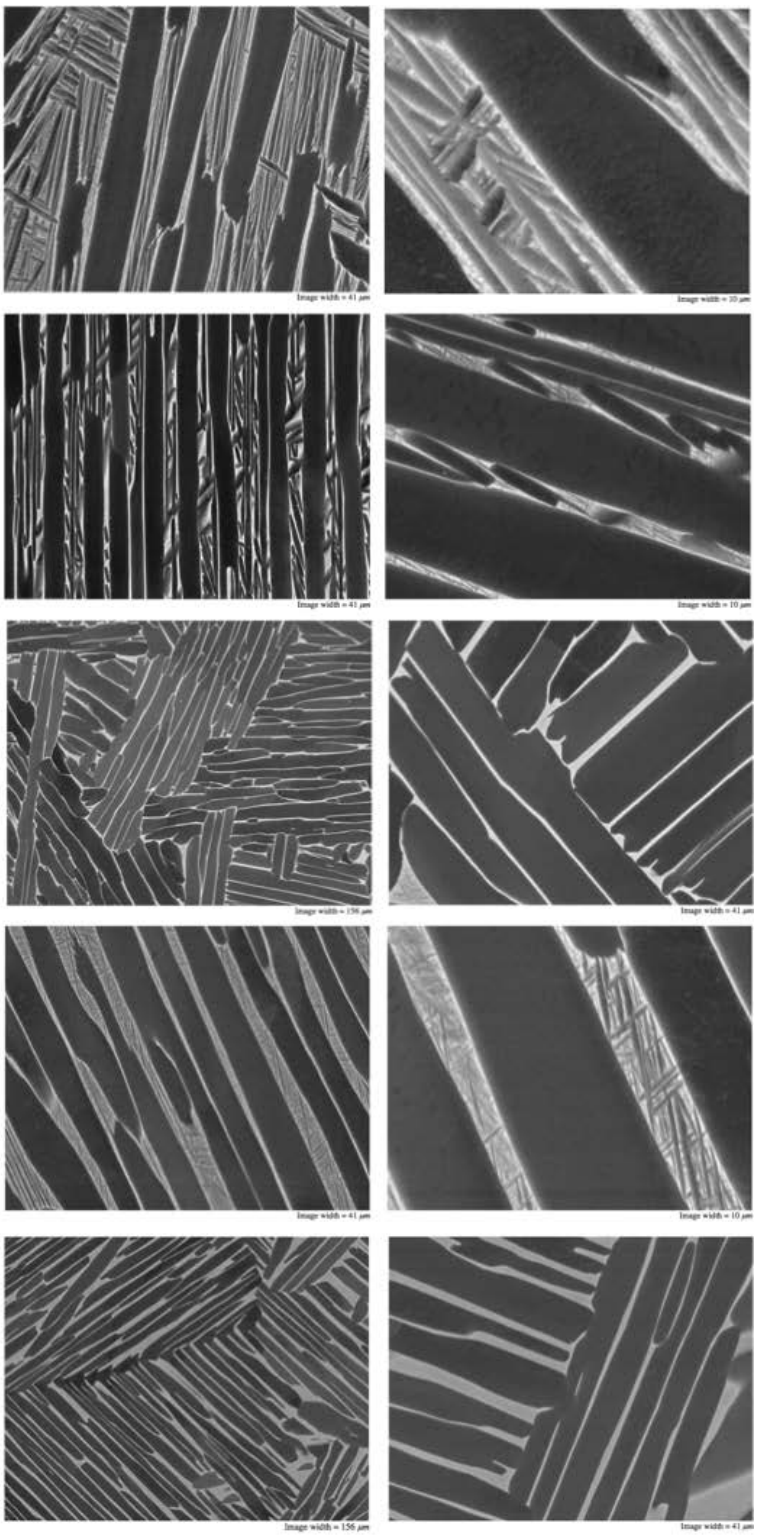

(column A) (column B)

Note: From top to bottom: AR, AR+AN, FC, FC+AN, SQ

Figure 8. Microstructures of the five microstructural conditions at low (column A) and high (column B) magnifications

The primary α-lath and β-rib thicknesses of the AN material are nearly identical to those of the AR material; however, the secondary α structures within the β-ribs are somewhat coarser. The FC microstructure contains thin β-ribs, largely devoid of secondary α structure, visible at the SEM level, and primary α-laths two to three times thicker than those observed in the AR alloy. The FC+AN material contains primary laths slightly coarser than those of the AR material and thick β-ribs packed with fine secondary α. The microstructure produced by solution quenching is similar to that of the furnace-cooled material, except that the primary α-lath thicknesses are nearly identical to that observed in the AR microstructure. The plastic flow properties of the various materials are presented in tables 1–3. Several important trends may be extracted from these data. First, yield stress generally increases with increasing α-lath refinement. This is observed in terms of reduced primary lath thickness and in terms of secondary α-lath morphology. As the average colony and prior-β grain sizes are similar within each microstructure of a given alloy (i.e., they are identical for the Ti-6242 microstructures), it is reasonable to apply a Hall-Petch form:

$$\sigma = \sigma_f + \frac{h}{\sqrt{d}} \tag{4}$$

to the data extracted from the microstructures of constant β-rib width lacking $\alpha_{secondary}$ (i.e., the FC and SQ structures). Taking *d* as average primary α-lath thickness, and neglecting BOR-related slip length factors, both data sets yield *h* values of ~7 $MPa \cdot mm^{-0.5}$. The Hall-Petch slope measured here is approximately twice the median value, ~3.5 $MPa \cdot mm^{-0.5}$, of those for lamellar microstructures extracted from the data reported in the literature [5]. Although the dimensions of several important microstructural features were kept constant, it is expected that effectiveness of slip barriers in strengthening should also be highly sensitive to material texture. For example, materials displaying a predominance of a_1 prism slip, with a mating β-phase easy slip vector, should not show the same behavior as those displaying a predominance of a_3 basal slip, having no mating $<111>_\beta$. The variations of strength with secondary α morphology within β-ribs can be observed in the Ti-6242 microstructures; the presence of both long, thin $\alpha_{secondary}$ laths combined with fine, multivariant $\alpha_{secondary}$ leads to the greatest increases in flow strength, indicating that the changes in orientation offered by the short, fine secondary α is secondary to other mechanisms.

Table 3. Plastic flow behaviors of Ti-6242 Pancake 3

Material	Microstructure	Stress State	σ_{ys} (*MPa*)	*m*	*n*	*a*
Ti-6242	AR	Comp	1037	0.011	0.131	0.155
		Ten	960	0.014	0.075	0.221
	AN	Comp	952	0.011	0.103	0.158
		Ten	890	0.015	0.068	0.248
	SQ	Comp	1012	0.011	0.100	0.182
		Ten	930	0.016	0.062	0.29
	FC	Comp	933	0.013	0.081	0.195
		Ten	837	0.020	0.046	0.37
	FC+AN	Comp	945	0.012	0.096	0.157
		Ten	880	0.014	0.067	0.242
σ_{ys} determined at $\dot{\varepsilon} = 10^{-4}\ s^{-1}$ *m* determined by rate jumps, $\dot{\varepsilon} = 10^{-4} \rightarrow 50^{-4}\ s^{1}$						

Second, it can be seen that strain-hardening behavior scales loosely with yield strength, in that weaker structures tend to display lower hardening rates. For instance, the weakest Ti-6242 structure (i.e., the FC material) displays an *n* value of 0.02 under tensile loading. By comparison, the strongest structure shows an *n* value of 0.033, a relative increase of ~65%. Under compressive loading, differences in hardening behavior are more muted. Variations in *n* between the various microstructural conditions may be taken as a measure of the ease of slip transmission from lath-to-lath and colony-to-colony in these materials. The occurrence of low hardening rates in the coarser structures indicates that a minimum number of additional slip systems need to be activated to transmit slip through barriers. This is expected, as slip transmission is greatly aided by the mechanical advantage offered by pileup structures. As the ability to form extended pileups is greatly hampered, and as lath spacing decreases, it is expected that accommodation of deformation would occur by the activation of higher energy dislocation sources.

Third, the data show that strain-rate sensitivity, determined on the basis of rate-change tests, increases with decreased flow strength. This is most obvious when comparing the tensile and compressive flow behaviors of Ti-6242, $m_{Ten} \approx 0.014 - 0.02$ and $m_{Comp} \approx 0.011 - 0.014$, but variation can also be observed between the various microstructural conditions. The *m* values of the FC and AR structures, for instance, are 0.02 and 0.014 under tensile loading, respectively. Subtle variations in the strain-rate exponent may be indicative of changes in deformation mechanism or changes in slip behavior. Although the differences in *m* relating to loading condition may be rationalized in terms of the tensile-compressive asymmetry phenomenon, differences in *m* relating to microstructure are not completely clear. The possibility exists that strain resulting from processes other than slip, namely sliding and cracking, may increase *a* under some conditions. Interfacial and grain-boundary sliding in titanium alloys has been reported under monotonic and creep-loading conditions by several authors.

The creep responses of the five Ti-6242 microstructures at a creep stress of 950 MPa are slightly below the tensile σ_{ys} of the AR material (see figure 9). Several features of these curves are worthy of note. First, transient behavior can reasonably be described by an Anrade form, in which the time

exponent ranges from 0.15–0.37, with weaker structures having increased *a* values. Moreover, materials lacking secondary alpha, FC and SQ, have noticeably higher *a* values; a likely result of decreased strain hardening. Second, variations in the measured strain-hardening and rate-sensitivity parameters are reflected in the creep responses of the materials, in that increased hardening and decreased rate sensitivity give increased creep strength. Third, slip length is a dominant factor governing creep resistance in these materials, as the gains in strength resulting from slip-length reductions are even more dramatic under creep loading. Even at similar fractions of yield stress, primary creep-strain accumulation is reduced significantly, and creep rates are reduced by orders of magnitude. As that microstructures for a given alloy had similar initial dislocation densities, and that the finer structures (having greater α/β interfacial area) provide a greater number of potential dislocation sources, these observations indicate that the dislocation-source argument for creep may be important only when significant (i.e., when several orders of magnitude difference in dislocation densities are present in the materials, or when the material is subject to reversed loading).

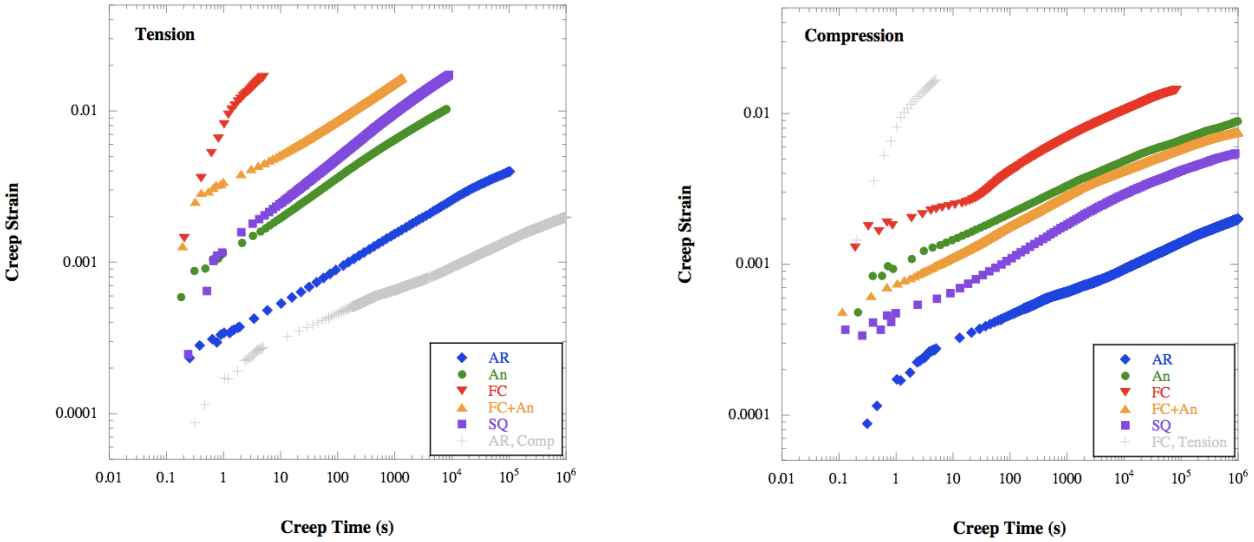

(a) (b)

Figure 9. Room temperature creep responses of the five microstructural conditions at 950 MPa under tensile (a) and compressive (b) loading

2.2.2 Influence of Slip Character and Stress Waveform on the Low-Temperature Creep-Fatigue Response of an α-Ti Alloy

To date, nearly all creep and fatigue studies on titanium alloys have focused on two-phase materials with relatively complex microstructures. Although it is known that the mechanical responses of these materials are sensitive to both slip character and applied load waveform, few studies have examined these factors in materials with simple, easily controlled microstructures. Subtle variations in SRO state have been shown to significantly affect slip planarity, hardening, and creep behaviors in binary Ti-Al alloys [12]; however, it is unknown whether SRO has any influence over the cyclic and dwell-fatigue behaviors in similar alloys. Additionally, it is known that cyclically loaded materials deform plastically. However, reports of fatigue behaviors, particularly low-cycle and dwell-fatigue behaviors, have focused on material life as a function of frequency, stress

amplitude/mean stress, and microstructural condition. Time-dependent damage accumulation responses and their relationships to static load creep behaviors are frequently ignored. To better understand the role of slip planarity on the cyclic-fatigue, creep, and dwell-fatigue responses of two-phase titanium alloys, these responses are examined in a single-phase α Ti-7 wt% aluminum (Al) alloy. The influences of slip character and waveform on both damage accumulation and fracture behaviors are observed and reported.

2.2.2.1 Experimental procedure

The Ti-7 wt% Al alloy examined in this study was obtained from Dr. S.L. Semiatin of the Air Force Research Laboratory in the Materials and Manufacturing Directorate at Wright Patterson Air Force Base, Dayton, Ohio. Materials were provided in the form of two extrusions of approximately 3 cm diameter and 75 cm in length. Alloys with the compositions listed in table 3 were furnished as 75 mm diameter, 125 mm thick billets by Flowserve Corporation Titanium and Reactive Metals Foundry of Dayton, Ohio. Billets were heated high in the α–phase and extruded. Once formed, the extrusions were cut into smaller pieces that were vacuum-encapsulated and AN at 1235K for 24 hours. This process produced an equiaxed structure, with average line-intercept grain size of 75 μm of low initial dislocation density. TEM investigations of the undeformed materials indicate that initial dislocation content is low. Few or no dislocations were observed within grain interiors; dislocation content was limited to those geometrically necessary dislocations (GNDs) at grain boundary interfaces. SEM-level electron backscattered diffraction (EBSD) texture measurements show that the AN materials displayed a weak texture, with most grains orientated with their c-axes ~45^{o} to the extrusion direction (see figure 10). SRO state (i.e., slip planarity) was manipulated by modifying cooling rate from the annealing temperature. All specimens were initially allowed to naturally cool from the annealing temperature, designated the air-cooled (AC) condition. Selected specimens were subsequently wrapped in Ti foil, solutionized at ~1200 K for 10 minutes in an environment of flowing argon gas, and dropped directly into iced water; this treatment, designated as ice water quenched (IWQ), had no influence on material structure other than to suppress the precipitation of SRO. Transmission electron diffraction studies indicate that air-cooling produced a relatively strong SRO state, similar to that observed in solution-treated and step-quenched Ti-6 wt % Al specimens studied in the neutron diffraction work of Neeraj [12]; no evidence of SRO was detected in IWQ specimens.

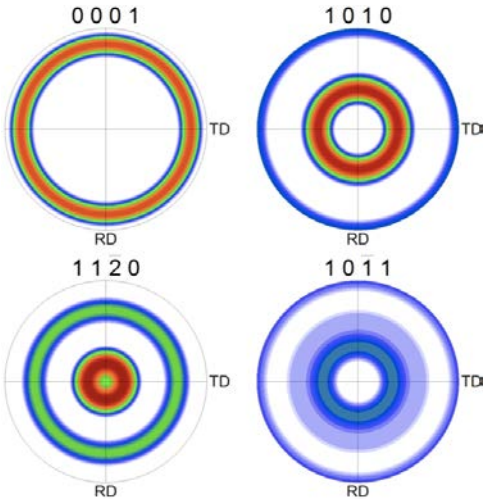

Note: Normal direction is coincident with the extrusion direction

Figure 10. Texture of the annealed Ti-7Al alloy (highest texture index, 3x random, is red; lowest texture index, 0x random, is white)

Mechanical testing of the materials was conducted on compression coupons and tensile rounds that were spark cut from each rod such that the deformation axis was parallel to the axial direction of the extrusion. Compression samples, 4 x 4 x 12 mm in dimension, were ground at low stress to a P2400 surface finish. Parallel gage tensile bars, 4.5 mm diameter x 18 mm gage length, were lathe-cut from cylinder blanks and low-stress ground to final dimensions before mechanically polishing the gage length. Specimens were quasistatically or cyclically loaded in an MTS servohydraulic test frame, or crept at room temperature in ATS dead load creep frames with 20:1 lever arm ratios. Creep and fatigue testing was performed at several stress levels corresponding to fractions of the quasi-static compressive yield stress of the AC material. Although the time necessary to load was approximately 1 second during creep testing, loads during cyclic and dwell testing were applied at rates of either 15 (slow) or 900 $MPas^{-1}$. Several waveforms and stress ratios (i.e., $R = \sigma_{min}:\sigma_{Peak}$) were used for testing: triangular cyclic, trapezoidal dwell with a 2-minute hold at peak stress, trapezoidal double dwell with 2-minute holds at both σ_{Peak} and $\sigma_{min,}$ and combined (see figure 11). The *R*-ratios applied during testing were -0.1, 0, 0.5, 0.7, or 0.95; for testing at $R = 0$, the minimum applied stress was 50 MPa.

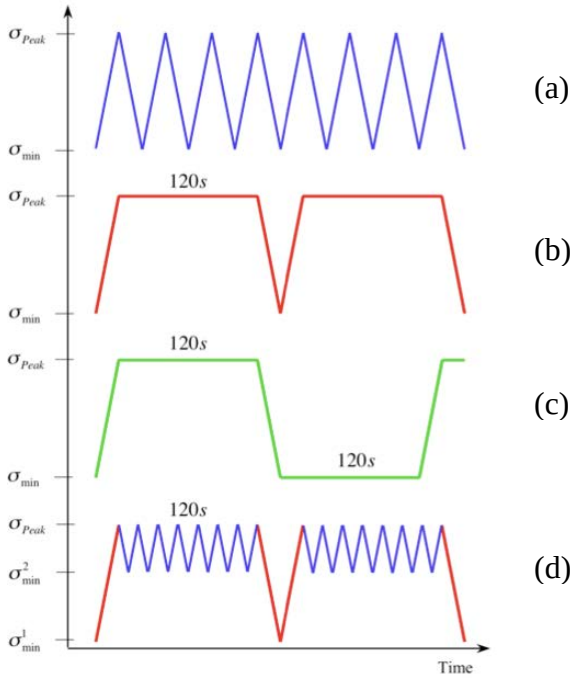

Note: Two-minute hold times were used for dwell and double dwell waveforms. The combined waveform is essentially a trapezoidal dwell wave with a cyclic ripple at peak stress. While $R = 0$ was utilized for the dwell wave component, a triangular wave with a stress ratio of 0.5, 0.7, or 0.95 was applied as the ripple

Figure 11. Waveforms used for (a) cyclic, (a, b) dwell, (a, c) double dwell, and (d) combined fatigue testing

2.2.2.2 Mechanical testing results

The AC material displayed higher yield strength than the IWQ material under both tension and compression, whereas the IWQ material displayed greater elongation at peak stress and at failure than the AC material (see table 4). No difference in yield or flow properties was noted between the two extrusions. These results are similar to those observed in precipitation-hardened systems in which slip planarity is induced by particle shearing, precipitating an increased yield stress at the expense of strain hardening.

Table 4. Compositions of Ti-7Al alloys

Alloy	Al	Sn	Zr	V	Mo	Fe	O	N	C	H
Ti-7Al #1	7.02	---	---	---	---	0.085	1240	150	50	43
Ti-7Al #2	7.10	---	---	---	---	0.015	1100	100	100	30
Heavy element content given as wt%; light element content given as weight parts per million										

The fatigue behaviors of tensile specimens are reported in table 5; selected results are also presented in figure 12. The alloys studied here clearly display a dwell effect; these data represent the first reported observations of such an effect in a single-phase α-Ti alloy with a simple, equiaxed microstructure. Until now, studies have focused on near-α and α/β alloys having relatively complex phase morphologies and textures. It can also be seen that the variations in fatigue life, N_f,

and damage accumulation follow several quickly recognized trends. First, specimen life and dwell debit vary strongly with peak stress. Whereas at high stresses $\sigma_{Peak} \geq \sigma_{y}$ a large dwell debit is measured, it decays rapidly as stress level is decreased. Although it appears that fatigue life may become independent of waveform at ~650 MPa, it should be noted that the cyclic life curve is expected to depend on specimen surface condition more greatly than the dwell-life curve because of differences in the crack-initiation processes observed under cyclic and dwell-fatigue loading. As specimens used in this study were not prepared for the maximization of cyclic life (surfaces were not shotpeened), it is more than likely that larger dwell debits would be observed at peak stresses in which creep deformation can occur readily.

Table 5. Mechanical properties of Ti-7Al

Material	Rate	σ_{ya}^{Comp}	σ_{ya}^{Ten}	ε_{pl}^{UTS}	ε_f
AC	10^{-4} s^{-1}	838	725	0.10	0.17
IWQ	10^{-4} s^{-1}	819	701	0.20	0.28

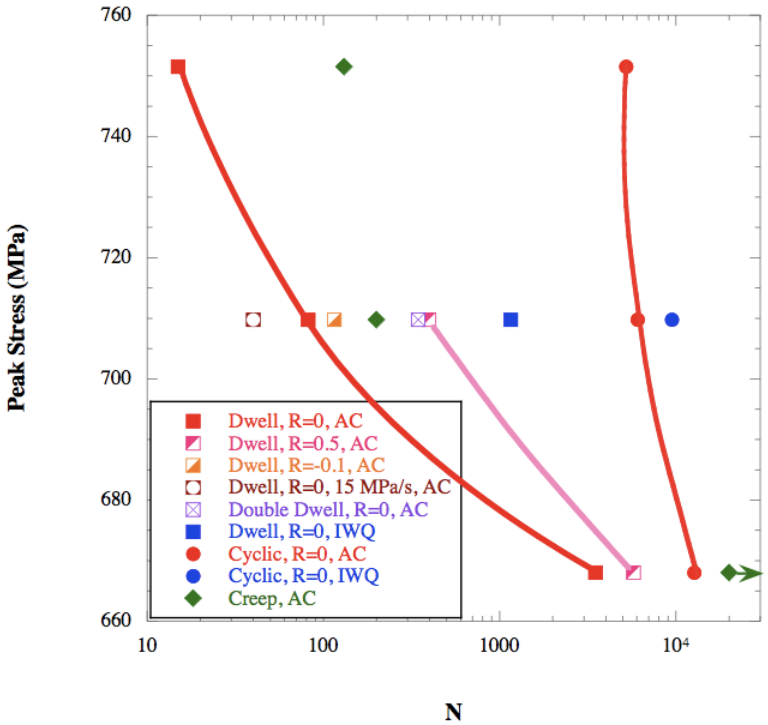

Note: Creep life is presented as equivalent dwell cycles (i.e., $N_f^{creep} = {}^{t_{failure}}/_{120s}$)

Figure 12. Lives of tensile specimens subjected to creep, continuous cyclic-fatigue, and dwell-fatigue waveforms (see table 5)

Second, fatigue life is affected by applied waveform. The influence of waveform on dwell life is readily observed in the lives of specimens cycled at lower loading rates, subjected to dwell periods at both peak and minimum stresses, or fatigued at non-zero stress ratios. Reducing loading rates by approximately one and a half orders of magnitude simultaneously decreases N_f and increases damage accumulation, e. It is more than likely that this factor would increase dwell debit as specimens subjected to dwell loading would experience stresses capable of inducing creep strains for a much longer period of time, effectively increasing the hold period. Inserting a dwell period at low stress appears to increase dwell-fatigue life at $R = 0$. Although the root of this behavior cannot be determined from these data, it is possible that a low-stress dwell allows for time-dependent redistribution of stress.

Changing R-ratio also influences dwell-fatigue behavior. For the single dwell waveform, N_f and e increase with the absolute value of stress ratio (see table 6). This observation is in direct opposition to that recorded in IMI-834 by Evans and Bache [28], who found that negative stress ratios increased N_f and positive stress ratios decreased N_f during dwell testing. At present, the origin of the discrepancy is unknown; however, it is possible that material microstructure may play a role. For the double-dwell waveform, non-zero R-ratios of -0.1 and 0.5 decrease specimen life when a hold time at minimum load is applied; the relative decrease is much enhanced at $R = 0.5$. It is unknown whether a double dwell waveform would increase life at higher absolute R-ratios. At more negative stress ratios (R<-0.3), a low-stress hold would likely promote slip and stress redistribution, and allow for crack closure, therefore increasing life. Evidence for slip/stress redistribution is observed in terms of damage accumulation; the strain accumulation measured at $R = -0.1$ is approximately two times greater than that measured at $R = 0$. At large positive R (R>0.5), two competing factors may determine specimen lifetime. The dwell period at lower stress would likely allow for time-dependent stress relaxation; however, crack growth rates would likely be much higher than those at lower R. These data suggest that crack growth rates may dominate when a low-stress dwell period is applied at a stress level below that at which creep deformation may occur.

Table 6. Tensile fatigue responses of Ti-7 wt% Al

σ_{Peak}	Waveform	SRO	*R*-ratio	$N_f^1(N_f^{Total})$	ε_{pl} |	ε_f
751	Creep	AC	1	131	3.4	3.9
	Dwell	AC	~ 0	21	4.6	7.5
	Dwell-slow	AC	~ 0	16	4.3	7.5
	Cyclic	AC	~ 0	2610	0.2	0.5
709	Creep	AC	1	150	1.2	1.7
	Dwell	AC	~ 0	81	2.9	5.8
			- 0.1	115	3.8	7.0
			0.5	397	10.7	13.5
		IWQ	~ 0	1155	11.1	14.0
	Dwell-slow	AC	~ 0	39	6.0	9.0
	Double. Dwell	AC	~ 0	345	4.3	6.0
			- 0.1	96	10.3	14.8
			0.5	110	5.0	8.0
	Cyclic. Dwell	AC	~ 0 (0.5)	317 (48406)	3.1	5.6
			~ 0 (0.95)	1446 ($2.2{\cdot}10^7$)	12.7	16.1
	Cyclic	AC	~ 0	6050	1.3	3.2
			0.5	21150	2.7	3.3
			0.7	50961	3.5	5.0
			0.95	139323	4.0	5.4
		IWQ	~ 0	9480	0.6	1.3
			0.5	49939	2.6	2.7
			0.95	$2.0{\cdot}10^7$	3.4*	DNF
668	Creep	AC	1	DNF	*	DNF
	Dwell	AC	~ 0	3490	4.3	5.5
	Cyclic	AC	~ 0	12700	1.7	3.6
			0.5	90125	1.3	3.2
			0.95	$2.6{\cdot}10^7$	1.9*	DNF
Stress given in MPa strain given in %						

* Strain at end of test
() = Minor *R*-ratio
DNF = Did Not Fail

Third, slip character has strong influence over both specimen life and damage accumulation. This is reflected in comparisons of material behavior, as a function of SRO state and as a function of waveform. In terms of SRO state, it can be seen that the highly planar slip observed in the AC material severely limits the ability of the material to deform homogeneously under dwell or creep-loading conditions, leading to failure at lesser macrostrains than measured in IWQ materials subjected to the same waveform. The influence of waveform on slip character is exhibited in several ways. In terms of cyclic loading, it can be seen that both cycles to failure and damage accumulation increase with increasing *R*-value. In the AC material, this likely indicates that the nature of slip is influenced by applied stress range or mean stress. For unreversed loading at a fixed peak stress, it is likely that slip at higher mean stresses is somewhat more diffuse than that observed at lower mean stresses. In the IWQ material, diffuse slip leads to much greater cyclic hardening than is observed in the AC material. Although this limits life at small, positive stress ratios, a lack of planarity greatly extends life at high positive stress ratios. In terms of dwell and combined loading, it is apparent that unloading halfway or less during dwell cycling, or applying small load ripples (R = 0.95) during the dwell period, significantly increases dwell-cycle life $\left(N_f^{Total}\right)$, total cyclic life $\left(N_f^{Total}\right)$, and damage accumulation compared to dwell, cyclic, and creep loading. As specimens loaded in this manner display strains similar to those observed in IWQ materials and evidence of necking prior to failure, it is likely that partial unloading allows for local stress/strain redistribution resulting in more homogenous slip distribution.

Fourth, dwell-loaded specimens accumulate more damage than do creep or cyclically loaded specimens. Cyclic loading at small, positive stress ratios induces very little plasticity before failure. Periodic unloading during dwell testing reduces part life compared with equivalent life under creep loading:

$$N_f^{creep} = \frac{t_{failure}^{creep}}{t_{\sigma_{peak}}^{dwell}} \tag{5}$$

where $t_{failure}^{creep}$ is time to failure under creep loading and $t_{\sigma_{peak}}^{dwell}$ is duration of the dwell period (120 s in these experiments). However, dwell loading induces greater strain accumulation before failure than measured in creep-deformed materials. These observations indicate a change in either slip distribution or crack-initiation/propagation behavior. Although not necessarily conclusive, previous TEM studies on dwell and creep-deformed materials do not demonstrate clear differences in dislocation-level behaviors. Additionally, in-situ x-ray and acoustic emission studies conducted under this project [7] indicate that behavior crack-initiation tendencies between the two loading conditions are similar. This being the case, it is likely that crack growth rates are affected by loading condition. As reported previously, creep crack growth rates have been found to be generally higher than cyclic growth rates. Therefore, it is reasonable to speculate that critical creep cracks initiate later and grow faster than dwell cracks.

As the failure mechanisms are known to affect macroscopic measurements of plasticity under tensile loading, compression tests were used to explore transient plastic strain accumulation as a function of the SRO state and loading conditions. A dwell effect has been recorded for the compressive deformation of a titanium alloy for the first time (see figure 13).

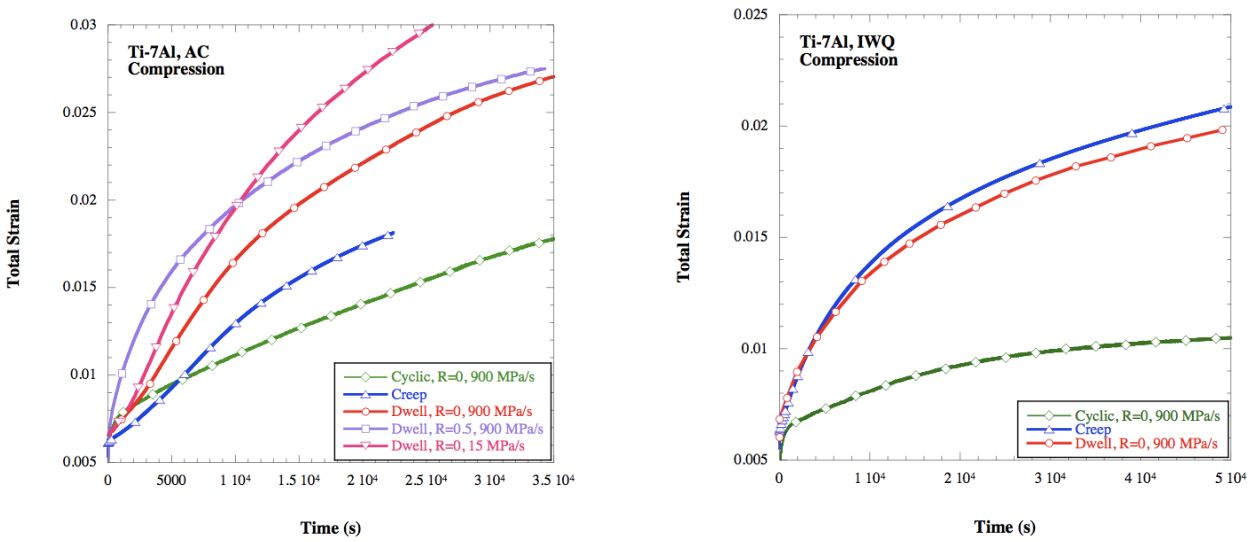

(a) (b)

Note: Dwell and creep strains are plotted as a function of time at peak load; cyclic strains are plotted as a function of total running time

Figure 13. Strain accumulation measured during cyclic, creep, and dwell loading of the AC (a) and IWQ (b) materials

It is apparent that waveform has significant influence over the plastic response of this material; strain accumulation under dwell loading is much greater than that under cyclic loading. Additionally, SRO state has a marked effect on both dwell and cyclic transients compared with creep transients. Whereas dwell loading yields more rapid straining in AC specimens, periodic unloads in IWQ specimens decrease strain accumulation, if only slightly. This observation strongly indicates that grain boundary stress concentrations resulting from highly planar slip are an important factor affecting plasticity under dwell-loading conditions. It is also apparent that the unloading-reloading process is responsible for greater strain accumulation under dwell conditions than creep conditions in the AC material (see figure 14). The creep response during each load cycle resembles the primary transient behavior observed during creep loading. Whereas inverse primary behavior is measured in the AC material, normal primary behavior is observed in commercial alloys. Therefore, it is possible that load cycling drives local processes (e.g., cross-slip) that provide fresh dislocation sources. These new sources activate and exhaust during the period of peak stress in a manner similar to that proposed to explain observations of low temperature recovery in similar materials [29–31]. It is also reasonable to speculate that the behavior of edge dislocations may contribute to these observations. It is known that dislocations of edge and near-edge line orientations in pileup structures do relax (i.e., are driven by grain boundary stress concentrations to run back toward their sources) when macroscopically applied loads are removed [12, 32]. As such, a local fatigue mechanism may induce additional plasticity under dwell loading compared with creep loading.

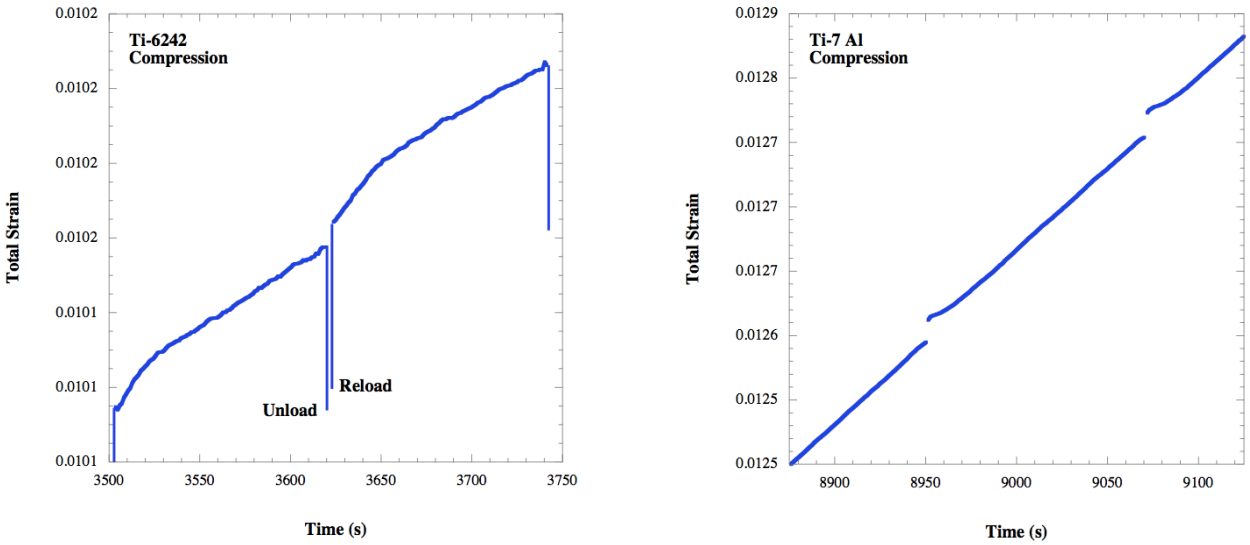

Note: Transient behavior during each load cycle resembles primary creep transients observed during constant load testing.

Figure 14. Strain accumulation at peak stress during dwell loading under compression

Under cyclic conditions, plasticity is greatly suppressed compared with creep or dwell loading—an observation that can be rationalized on the basis that the time spent at loads above which creep strain might accumulate is greatly reduced under cyclic loading compared with either dwell or creep loading. Slip planarity also affects cyclic response; after an initial period of rapid strain accumulation, IWQ specimens display much greater cyclic hardening than AC specimens with cyclic strain rate falling to near zero at long times. This observation underscores the role of stress concentrations in driving plasticity. The IWQ condition, being a weaker material, deforms rapidly until all low-energy sources are exhausted. Once this has occurred, the deformation rate falls off rapidly without productive mechanisms for new source activation, like the extended pileup structures that develop in the AC materials.

It can also be seen that waveform influences transient response in the AC material. Decreased loading rate allows more extensive creep to occur during loading and unloading periods, yielding increases in plastic strain accumulation per cycle. It is expected that this would trend strongly with $\sigma_{Peak,}$ with loading rate being less of a factor at lower peak stresses. Additionally, an increased *R*-ratio yields transient behavior, similar to that observed for the material of the IWQ condition, in that a strong inverse primary regime is not observed. Further, an elevated stress ratio induces greater hardening at longer times, indicating that partial unloads may serve to distribute slip much more homogeneously throughout the microstructure.

2.2.2.3 Fractography

Fractographic examinations were performed on tensile specimens pulled to failure under quasi-static-, cyclic-, dwell-, and creep-loading conditions. Fracture surfaces displayed features indicative of ductile failure under monotonic, quasi-static loading, both at constant strain rate, $\dot{\boldsymbol{\varepsilon}} = 10^{-5}$ to 10^{-3} s^{-1}, and constant stress rate, $\dot{\boldsymbol{\sigma}} = 15$ to 900 $MPa \cdot s^{-1}$ (see figure 15). As can be seen, both IWQ and AC materials exhibit similar features (i.e., shear lips, dimpling, and grain pullout), indicating that SRO state has minimal influence over fracture mechanism under such conditions. Although it is known that ordering does induce brittle fracture in these alloys [33–36], strain localization in short-range ordered materials is not as severe as in materials containing fully ordered precipitates. Specimens with SRO are able to accommodate deformation without fracture up to fairly large strains compared with peak- and over-aged specimens.

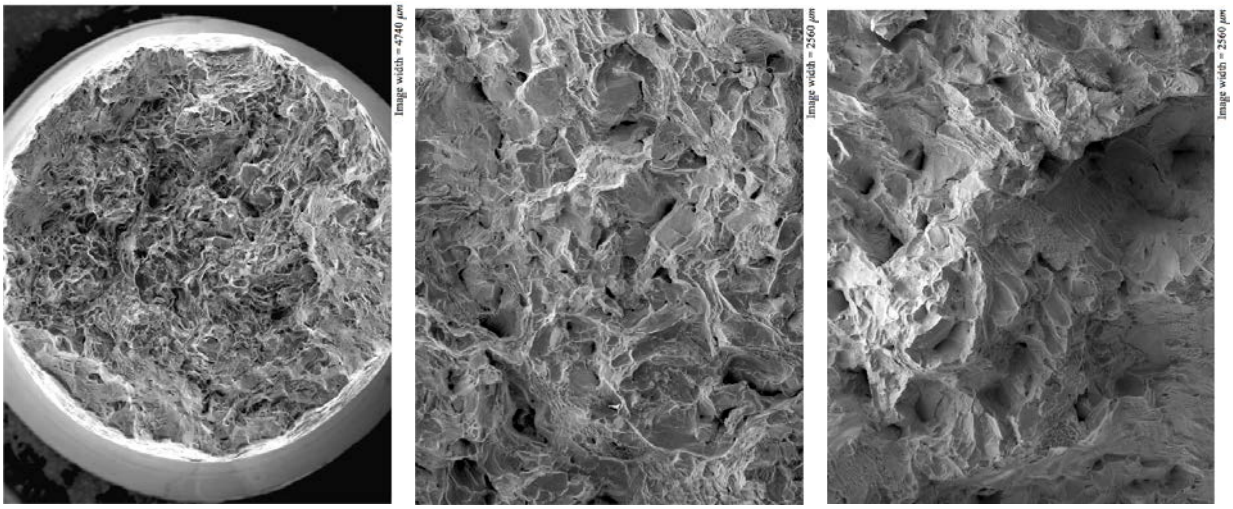

(a) (b) (c)

Figure 15. Typical fracture surfaces of the AC (a, b) and IWQ (c) materials pulled to failure under quasi-static loading conditions

Under cyclic loading at small stress-ratio, all specimens displayed surface crack initiation. Multiple faceted initiation sites were observed in both AC and IWQ specimens (see figure 16). Secondary surface cracks were observed both above and below the primary fracture surface. As specimen surfaces were not prepared in a manner to prevent the initiation of such cracks, this is not an unexpected result. SEM tilt studies indicate that these facets are highly inclined to the stress axis. This observation is consistent with the work of several researchers showing surface-initiated facets are prone to occur on planes of highest RSS [37–42]. Fracture surfaces in specimens of both SRO states show a mix of faceted and striated regions. Faceted regions tend to be located closer to the specimen surface and initiation sites. Qualitative comparisons indicate that striated regions tend to be larger and more common in the IWQ material. Counts of striation markings also show that cracks in the IWQ material remain stable for more cycles than those in the AC material. It is expected that a material displaying homogeneous slip character would more readily blunt advancing cracks, allowing for stable crack growth, than a planar slipping material.

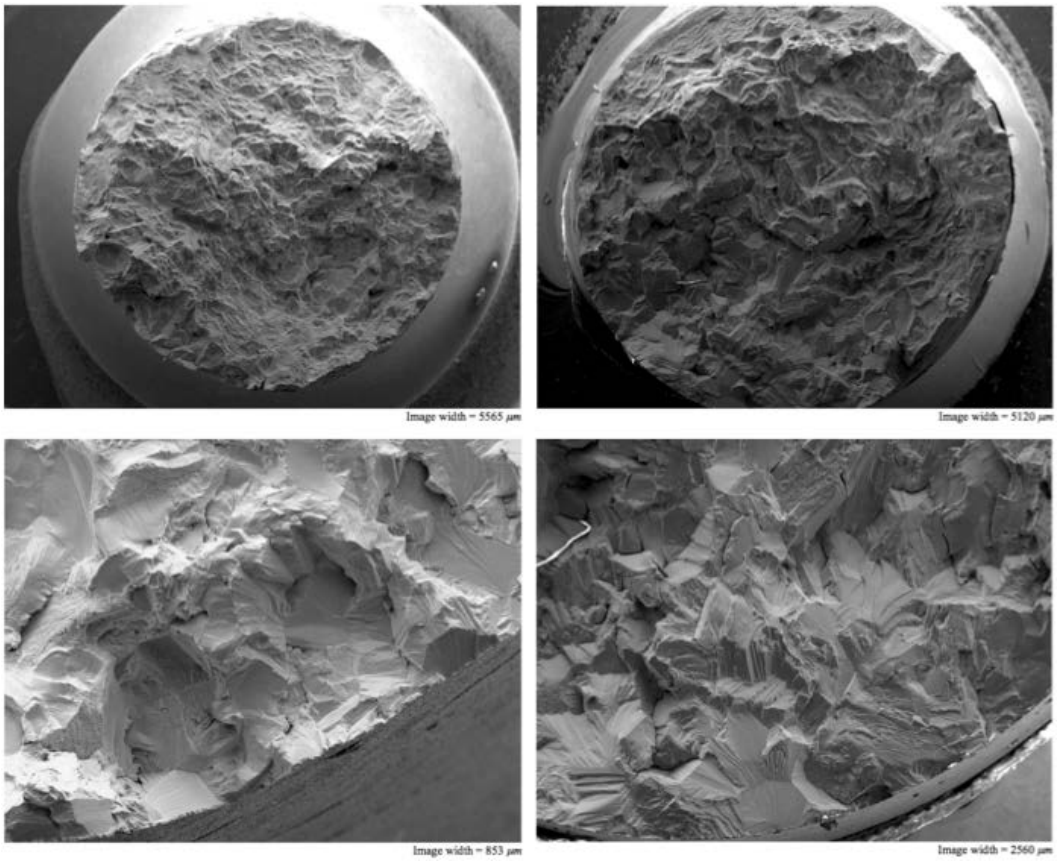

Note: On the AC fracture surface, multiple faceted surface initiation sites can be observed at the 3, 4, 6, 7, and 8 o'clock positions (a, b). Secondary surface cracking and striated regions of stable crack growth are observed in the lower right and upper left corners of (c, d), respectively. On the IWQ fracture surface, multiple faceted surface initiation sites can be observed between the 4 and 8 o'clock positions (a, b). A surface initiation site, as well as faceted and striated regions, are present (c, d).

Figure 16. Typical fracture surface of a cyclically loaded AC (a, c) and IWQ (b, d) specimens (σ_{Peak} = 709 *MPa*, *R* = 0)

The fracture surfaces of specimens that failed under creep and dwell conditions are presented in figures 17 and 18. Dwell or creep loading induces internal crack initiation; no specimens investigated in the course of this study showed evidence of a surface crack source. Specimens that failed under creep conditions show similar features to those failed under dwell-fatigue loading for a given SRO state. AC specimens display internal, faceted initiation sites. Whereas single initiation sites were generally observed in crept specimens, dwell specimens often showed two or more initiation sites. Additionally, internal facets are observed in dwell specimens subjected to non-zero *R*-ratios (*R* = -0.1 and 0.5), reduced loading rates, or double-dwell waveforms; both initiation facets (IFs) and striated regions are observed in specimens deformed at the lowest stress level, σ_{Peak} = 668 MPa. Facet angles vary widely from ~10 ^{o}–45^{o}; although every facet was not investigated, no IF was observed with a surface normal parallel to the LD. In agreement with measurements of material texture, preliminary EBSD studies indicate that facet planes are close to (0001).

(a) (b)

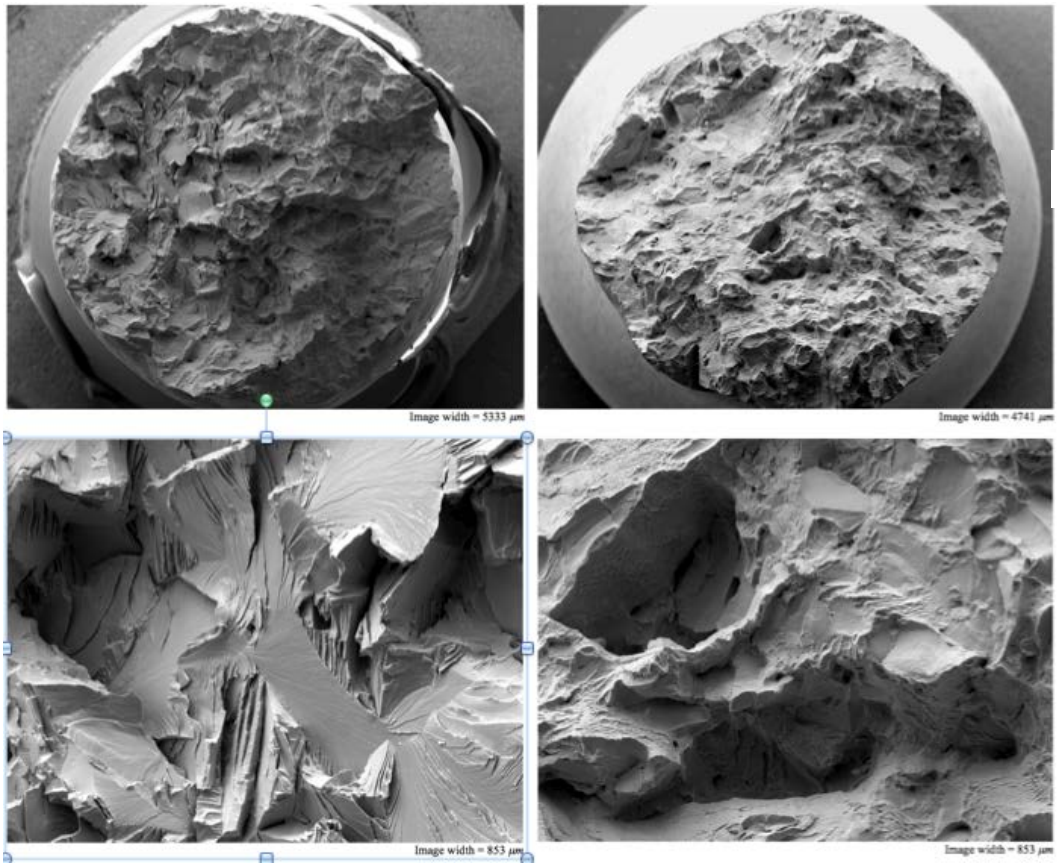

(c) (d)

Note: On the AC fracture surface, a large faceted region (a, b) is observed near the internal failure site (c, d). River markings on facet surfaces indicate the initiation site. On the IWQ fracture surface, evidence of ductile failure mechanisms (i.e., grain pullout, shallow dimples, and ductile tearing) is present**.**

Figure 17. Surface morphologies of AC (a, c) and IWQ (b, d) specimens crept to failure ($\sigma = 709$ *MPa*)

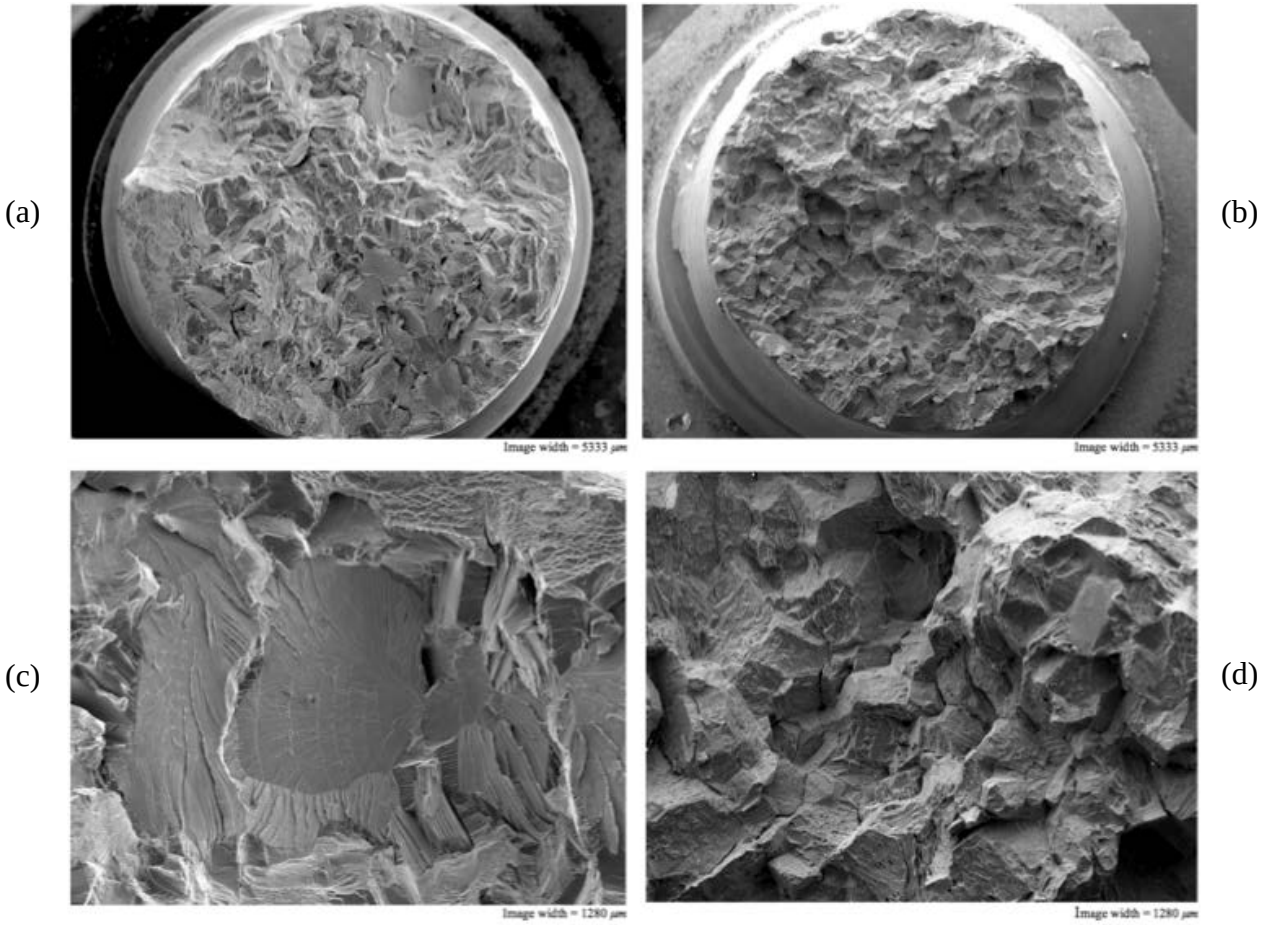

Note: On the AC fracture surface, multiple initiation sites are observed, i.e., near the center of the specimen and at ~ 1 o'clock (a, b). Fatigue crack growth markings are observed on many facets in dwell-fatigued specimens (c, d). On the IWQ fracture surface, no evidence of faceting or surface initiation is found (a, b). Fracture surfaces show evidence of ductile failure mechanisms similar to those observed in creep failure (c, d).

Figure 18. A fracture surface typical of AC specimens (a, c), subjected to dwell or double dwell loading and small stress ratios, and IWQ specimens (b, d) subjected to dwell loading (σ_{Peak} = 709 *MPa, R* = 0)

Subtle fatigue crack growth markings on facet surfaces are the only features that differentiate dwell facets from creep facets (see figures 17 and 18) in the AC material. Growth markings clearly demonstrate two important aspects to crack growth under dwell-loading conditions. First, faceting does not occur by a single-cycle cleavage mechanism. Instead it occurs progressively over a number of cycles. Recent work by Pilchak et al. [37, 43] examining fatigue crack growth rates in coarse-grained Ti-64 indicate that the quasi-cleavage mechanism is more appropriately described as crack growth at very low ΔK. Second, these observations support the argument that crack growth under dwell loading may be slower than that under creep loading. Under dwell conditions, it is likely that unloading allows for crack closure, leaving growth markings behind and slowing crack-tip advancement.

The fracture surfaces of the IWQ material that failed under creep and dwell conditions were drastically different from those observed in the AC material. IWQ specimens failed in a ductile

fashion, tearing apart at grain boundaries. Fracture surfaces lack evidence of either faceting or surface initiation (see figures 17 and 18); surfaces show extensive grain pullout and long cracks propagating along grain boundaries. Shallow dimples and ductile tears were found to cover surface features. These observations clearly demonstrate that stress concentrations resulting from highly planar slip are a primary factor that determines facet formation.

A material texture on which significant populations of grains are aligned, such that their $\vec{c}$ -axes are parallel to LD, was thought to be a requirement for faceting under dwell/creep-loading conditions. However, this was not the case because the material investigated here lacked such grains, with most oriented for $<\vec{a}>$ slip. These results call both the rogue grain and Stroh models into question [18, 24, 44, 45]. Faceting under dwell-time or creep loading does not require hard-soft grain combinations. Based on the observations presented in this study, the hard or rogue grain needs only to be resistant to $<\vec{a}>$ slip in relation to the slip vectors of a neighboring grain. A hard grain may readily deform by easy slip in response to the macroscopically applied stress but may not share compatible $<\vec{a}>$ slip systems with neighboring grains (see figure 19).

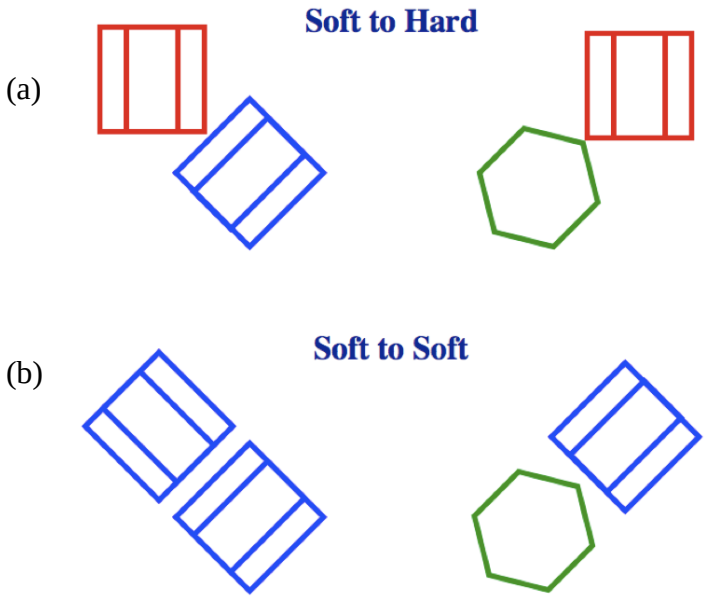

Note: Hard-soft grain combinations are (**a**) those thought to be most detrimental to part life; here, the *c*-axis the rogue grain is aligned with the stress axis. In the Ti alloys examined in this study, soft-soft grain pair combinations (**b**) produce facets. Both grains are able to deform by easy slip in response to a uniaxially applied stress (stress axis is vertical)**.**

Figure 19. Examples of neighbor grain configurations capable of producing basal plane facets in titanium alloys

In the case of two neighboring soft grains, the inability of an established $<\vec{a}>$ slip band within one of the grains to activate stress relieving $<\vec{a}>$ systems in the other grain would result in the formation of dense, extended pileup structures and intense, highly localized stress concentrations capable of initiating cracks. Under these conditions, failure occurs in the grain containing the problem slip band; the crack, once initiated, propagates along that slip band. Observations of dwell and creep faceting, in both this study and the published reports in the literature, indicate that faceting occurs on basal planes. Therefore, faceting is most likely to occur in materials of particular

textures and slip characters. The work of Woodfield et al. [46, 47] indicates that faceting may be the result of suppressed materials displaying primarily $<\vec{a}>\{1\bar{1}00\}$ (i.e., those materials having basal planes aligned with the deformation axis).

The observation that the highly planar slip in the AC material limits macroscopic strain accumulation and promotes faceting under static and dwell-loading conditions indicates that the local stresses developed at the intersection of slip bands, and grain boundaries govern mechanical performance. Recent microfocal 3D x-ray measurements of creep deformed Ti-6 wt% Al indicate the deviatoric stresses at grain boundaries approach and may exceed the yield stress of the material [48, 49]. Planar slip produces much larger and more concentrated crystal rotations at grain boundaries in the AC material than in the IWQ material. It is evident that the stress concentrations resulting from these rotations provide the driving forces for both damage accumulation and failure mechanisms in these materials.

2.2.3 Influence of Loading Mode on the Faceted Fracture in Ti-811

A 12.7 cm diameter, 127-cm-long Ti-8Al-1Mo-1V bar with ~10 ppm hydrogen was provided by Timet (Henderson, NV). This material was chosen because of the presence of extreme microtexturing and its low-volume fraction of β-phase. Furthermore, Ti-811 is historically known to fracture by faceted crack growth under static loading conditions [50]. Both of these features allowed for the examination of faceted crack initiation and growth in the α-phase over long crack lengths. The microstructure (see figures 20, 21, and 23) and texture (see figure 22) of the AR bar were characterized with SEM and EBSD. The microstructure was bimodal, consisting of a globular α grain approximately 10–15 μm in diameter, with approximately 30–35 volume % α+β colonies. The secondary α was not arranged into well-defined colonies as in classic bimodal microstructures. Instead, it was relatively coarse and, in many locations, seemed to have multiple variants of a phase. An EBSD analysis has shown that the secondary α has adopted similar basal plane orientation as the adjacent primary α grains in many locations, although this is certainly not a rule of the phase transformation. With respect to texture, there was a weak 1010 partial fiber aligned with the bar axis (see figure 22). EBSD scans made on large areas of longitudinal sections that contained the bar axis in the plane of polish revealed that there were elongated regions of similarly oriented grains, or MTRs, that had lengths of up to 4 mm and widths ranging between 100 and 500 μm (see figure 23). The size and shape of these MTRs are consistent with several of those Ti-6242 microstructures chosen for nondestructive sonic assessment (see section 4).

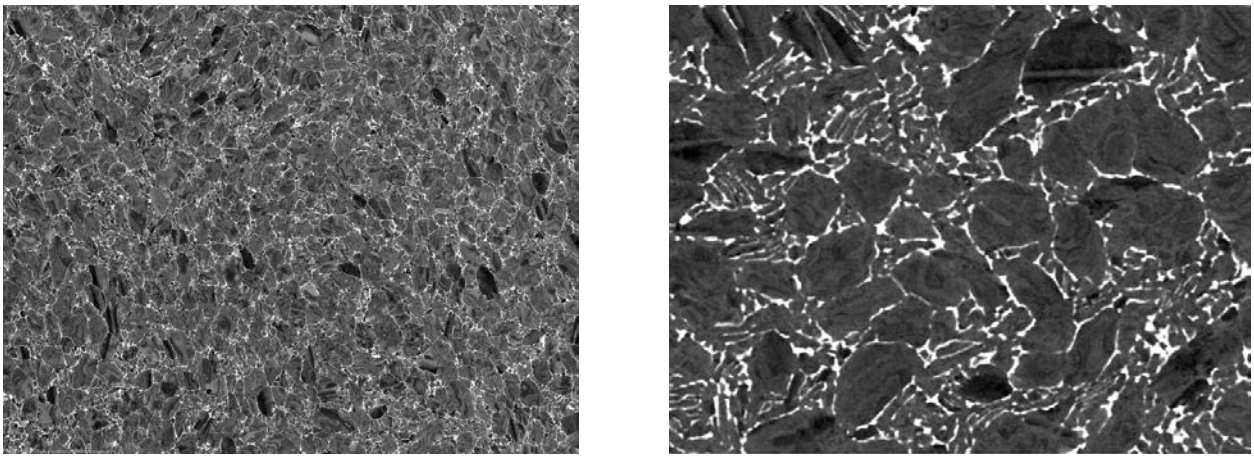

(a) (b)

Figure 20. Microstructure of the AR Ti-811 bar at (a) low and (b) high magnifications

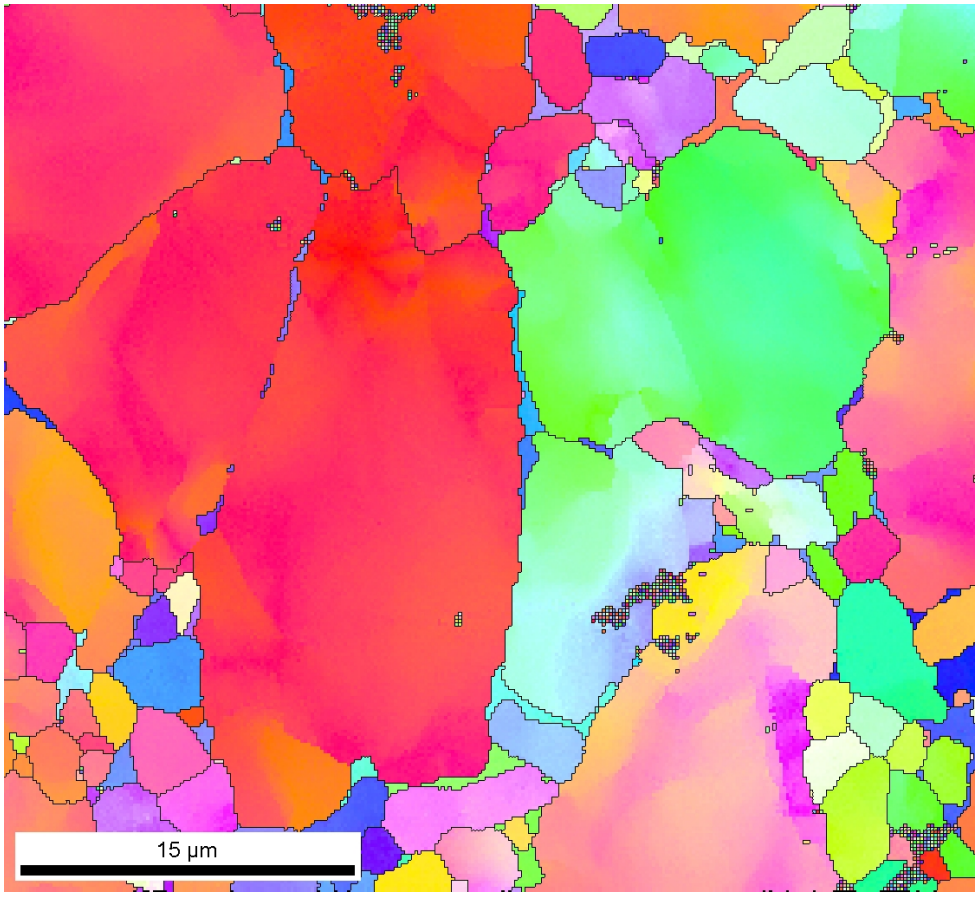

Figure 21. High point density EBSD scan of the AR Ti-811 bar

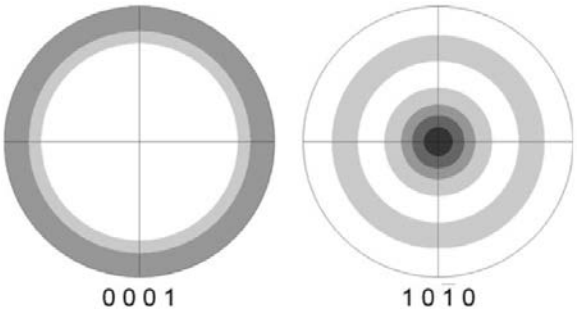

Figure 22. The texture of the AR bar indicating the presence of a weak 1010 partial fiber along the bar axis (which is perpendicular to plane of projection); the levels of intensity are in intervals of 0.5 multiples of the probability of a random distribution

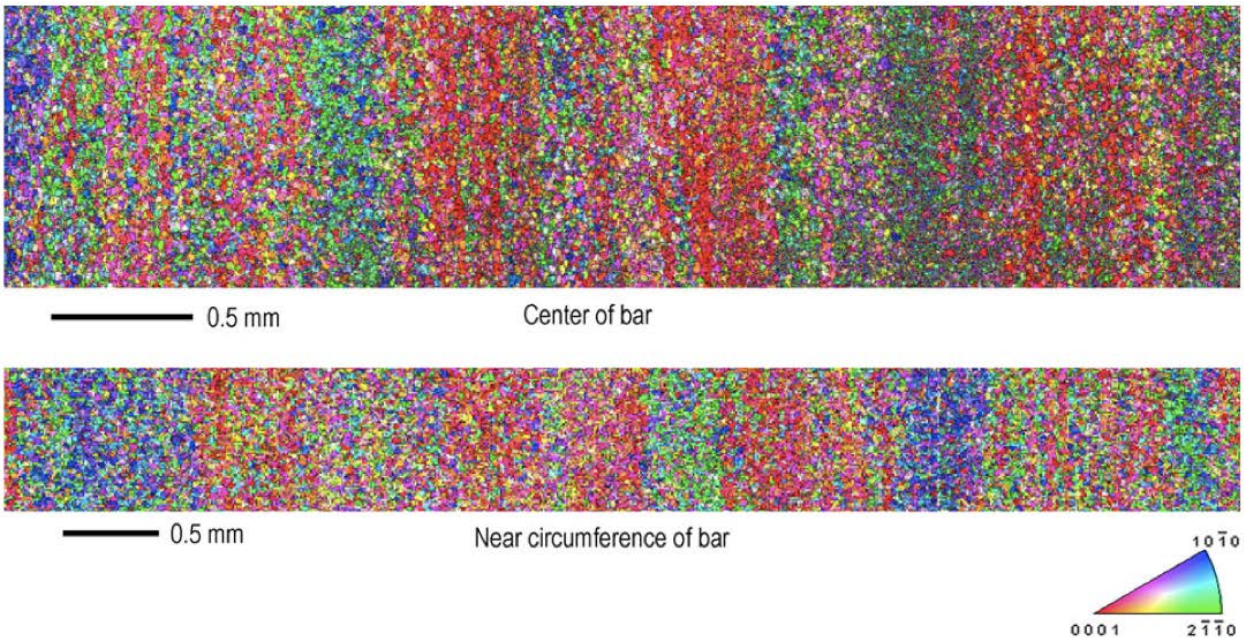

Figure 23. Normal direction inverse pole figure EBSD maps of longitudinal sections cut from near the center and edge of the bar showing elongated bands of microtexture; the LD is perpendicular to the plane of the page

Based on these data, specimens were cut transverse to the bar axis. As a consequence of the axial symmetry about the bar axis, there was an equal distribution of basal poles oriented between 0^o and 90^o to the LD. Therefore, the macroscopic texture of the bar would not influence the orientation of the grain in which crack initiation occurs as it might, for example, if there were limited grains in the gauge section or if in a highly textured plate.

Blanks for mechanical test specimens were extracted transverse to the bar axis by wire electrical discharge machining. All the tests were performed on material in the AR condition. The blanks were machined into round specimens with diameters of either 5.08 mm (cyclic and dwell loading) or 4.06 mm (static loading) and gauge lengths of 19.05 mm and 16.9 mm, respectively. The specimens were tested under four different loading conditions: continuous cycling at 30 Hz,

2-minute dwell periods with 1 second each of down- and up-ramp loading, and static loading at room temperature in lab air. All the tests were run in load control, and the peak stress attained during any one test was constant for all tests at 758 MPa, which was 95% of the yield strength measured from a tensile test conducted according to ASTM E8 standards. The load ratio was 0.1 for the continuous-cycling and dwell tests. The cyclic tests were performed on a servohydraulic test frame that was aligned precisely with a strain-gauged standard specimen prior to testing.

The specimen that was cycled continuously at 95% of the yield strength failed after 138,840 cycles, whereas the specimen subjected to 2-minute dwell periods at the same fraction of the yield stress failed after only 10,399 cycles, a debit of approximately 13 times. To the authors' knowledge, this is the first time dwell sensitivity has been reported in Ti-811. This alloy had not been investigated previously for dwell sensitivity because it is not an alloy used for jet engine rotors; however, this finding is potentially significant because there are Ti-811 fan blades in service. With regard to static loading, the specimen loaded at 758 MPa in air, in the absence of a crack-initiating notch and an aggressive environment, exhibited significantly longer life. This specimen was loaded for 426 hours at 758 MPa, at which point the load was increased to the macroscopic yield strength of 798 MPa. After the load increase, the specimen failed after an additional 26 hours and 42 minutes.

The fracture surfaces were all qualitatively similar in the sense that they contained facets and features, like dimples and shear lips, typically associated with overload failure. The regions between faceted growth and overload fracture were considerably different among the various specimens because of the different loading histories. However, the features from this region are not discussed in this manuscript because of the extent to which the facets are addressed. Although all the samples contained facets, the overall size and shape of the faceted regions were different. Secondary electron images of the as-fractured specimens are shown in figure 24.

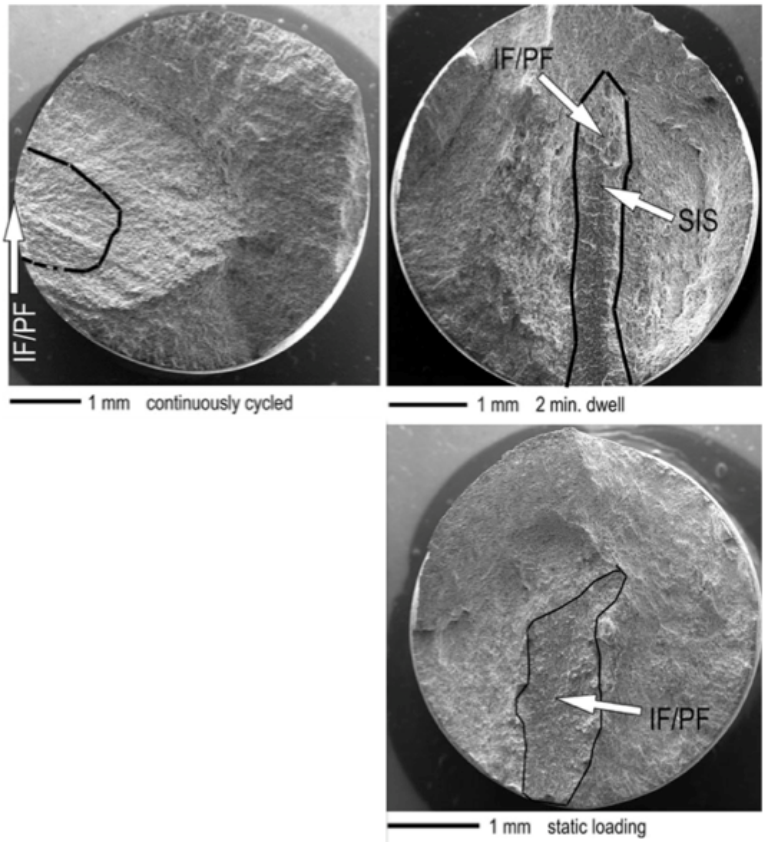

Note: The faceted regions on each specimen are enclosed by black lines. The locations of the IFs and propagation facets discussed in more detail in the text are identified on each fracture surface. The location of a secondary initiation site on the dwell-fatigue specimen is also shown.

Figure 24. Low-magnification SEM images of the fractured specimens

2.2.3.1 Continuous cycling fracture surface

The fracture surface of the cyclic specimen was typical of a fatigue failure, exhibiting surface crack initiation and a small, semi-elliptical faceted region near the surface of the specimen. The region of faceted growth transitioned to more conventional striation growth gradually, which is consistent with many observations of cyclic-fatigue crack growth [51–56]. Striations were first observed in isolated grains at crack lengths less than 200 μm and became the dominant propagation mechanism at crack lengths greater than 1 mm. Striation growth proceeded with the macroscopic fracture plane remaining approximately perpendicular to the LD until the critical crack length was reached and overload fracture occurred, resulting in the formation of a shear lip. There was a single clearly identifiable fatigue crack-initiation site in the specimen loaded by continuous cycling. This region is shown at two levels of magnification in figure 25. Although there was no large, contiguous-faceted region consistent with the MTRs in this specimen, several facets were observed at the crack-initiation site, as shown in figure 25.

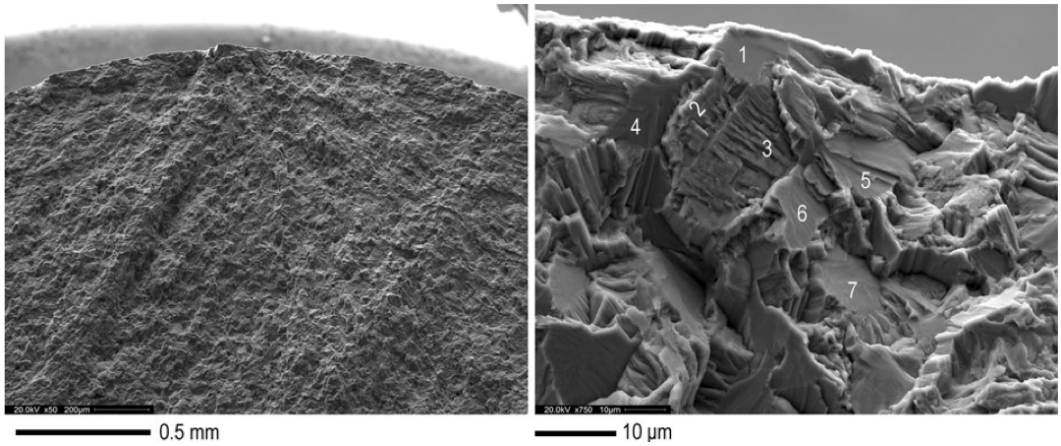

Figure 25. Surface initiation site in the continuously cycled specimen; several facets are identified by numbers 1 through 7 (CY-1 through CY-7)

Although some of the facets directly bordered one another, there were many locations separated by sharp, planar features, such as those identified as numbers 2 and 3. In the strictest sense, these could be called facets, but will be reserved for the more planar features, identified by the remaining numbers (1, 4–7). These more planar features are formed by a transgranular fracture through a primary α grain, with a fracture plane nearer the basal plane than any other low index plane, as will be shown in the subsequent sections. Except for the IF, several markings on the facet surfaces were indicative of the local crack propagation direction (see figure 26).

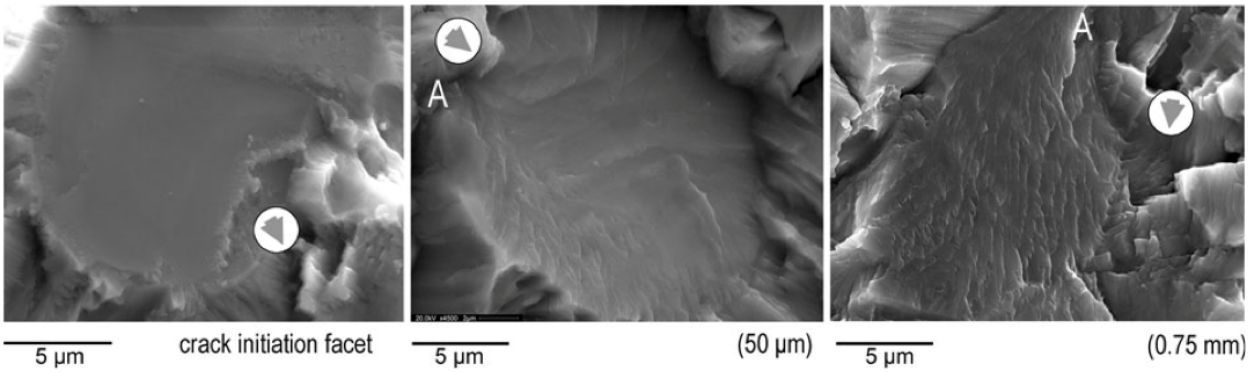

Note: The local crack propagation direction is indicated by the arrows, whereas the letter A designates the point at which the crack entered the grain

Figure 26. The effect of crack length on facet topography in the cyclically loaded specimen in the as-received condition

Subsequent facet surfaces were observed to be progressively and continuously more rough with increasing crack length. The number of steps on the facet surfaces also seemed to increase in density with each grain boundary encountered by the crack front. For the case of continuous cycling, this is related to the increase in the cyclic crack tip plastic zone size with increasing crack length [55], which results in a larger fracture process zone on each subsequent cycle. Striations were occasionally visible on some facets at high magnifications using the through lens detector (TLD) (see figure 27). On the left, the striations resemble slip steps on the facet surface, whereas, on the right, they resemble more conventional striations. At a crack length of approximately 100 μm, the spacing of these striations was on the order of 150 nm per cycle.

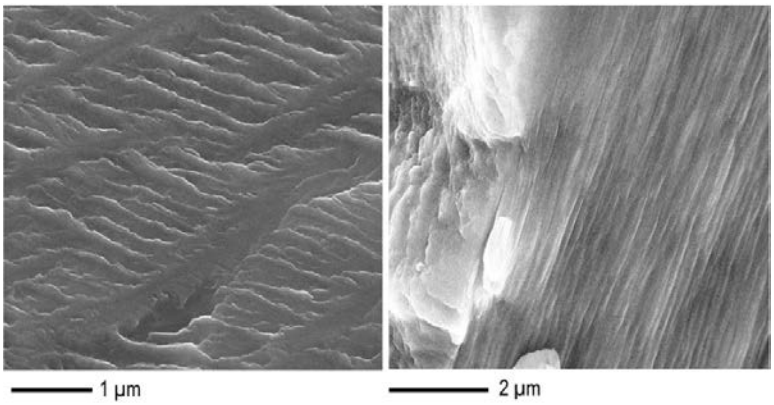

Note: Facet surface markings suggest the crack growth rate is on the order of 150 nm/cycle

Figure 27. Two different facet surfaces in the continuously cycled specimen at crack lengths ~100 μm

The spatial and crystallographic orientations of all the facets identified in figure 25 (except for CY-7) were determined using the combined EBSD/quantitative tilt fractography technique. The results are shown in figure 28, which shows the orientations of each fractured grain with respect to the LD and to the facet normal direction (ND). A total of seven individual EBSD patterns were collected and indexed from the first grain to fracture (CY-1), whereas two patterns were collected from the remaining grains. Initiation occurred within a primary α grain that had its *c*-axis oriented

24° from the LD. The angle between the facet normal and the LD was 27°, and the fracture plane was determined as being parallel to the basal plane for all seven indexed patterns within the resolution of the technique. The spatial and crystallographic orientations of this primary α grain initiation site are consistent with observations made on fatigue crack IFs in α grains in continuously cycled Ti-6Al-4V [57, 58] and Ti-6246 [59] specimens with bimodal microstructures. In addition, despite being near the surface of the specimen, the orientation of this grain is such that it could not have formed a slip band extrusion on the surface of the specimen because the only available <a> slip system that could intersect the specimen surface had the lowest RSS. Therefore, in this case, crack initiation seems to be the result of grain-to-grain interactions and not classic surface intrusion/extrusion. Two grains (CY-2 and CY-3) directly adjacent to the crack-initiating grain have their *c*-axes nearly perpendicular to the applied LD. In this orientation, the maximum RSS is on the prismatic <a> slip systems, and there is nearly zero RSS on the basal plane. Whereas there are also suitably oriented <c+a> slip systems, the higher CRSS of these systems implies that the grains would tend to deform by prismatic <a> slip. As these two grains did not fracture on a flat and continuous faceted plane, the average fracture plane was determined over several areas spanning ~8 μm each on the fracture surface. After correcting for this average fracture plane normal, the plane of fracture was determined to be near $\{10\bar{1}0\}$ for CY-2 and $\{\bar{7}520\}$ (parallel to the α/β interface) for CY-3. The average fracture plane normal for these regions was determined to be 41° (CY-2) and 25° (CY-3). The size, appearance, and spatial orientation of these regions are consistent with the underlying microstructure being transformed β, based on previous work conducted on bimodal Ti-6Al-4V, in which there was direct observation of the fracture surface and the underlying microstructure [58].

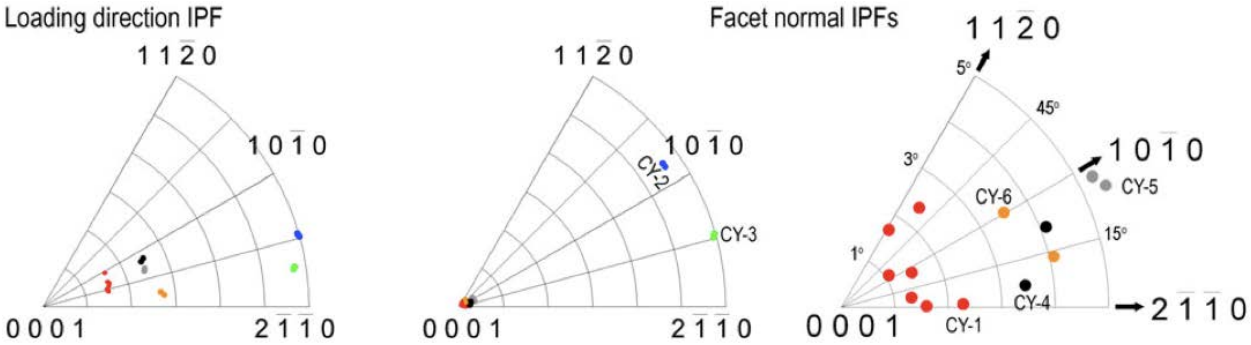

Note: The IPF on the right is a magnified view of the region around 0001 in the center facet normal IPF (also note the change in scale for this IPF)

Figure 28. Results from the facet crystallography analysis on the continuously cycled fatigue specimen

The remaining facets, CY-4 through CY-6, can be characterized as transgranular propagation facets (PFs) through primary α grains. These facet NDs made angles (in order) of 36°, 40°, and 44° with the LD. The crystallographic plane of fracture was near the basal plane for all facets; however, there was a slight deviation from the basal plane observed for all specimens with facet CY-5 being the furthest, at an angle of ~5°. It is believed that these discrepancies can be attributed to errors introduced to the spatial orientation calculation by the increased facet surface roughness and the formation of steps, as discussed in depth by Pilchak et al. [27]. Therefore, these grains are all present in orientations that could have easily formed a slip band on the basal plane followed by cracking along that slip band.

The transformed β regions adjacent to the primary crack-IF were in elastically and plastically soft orientations. The crack initiating grain was in neither a hard nor a soft orientation, as it was capable of slip on the basal plane. However, the spatial orientation of the facet also resulted in a considerable resolved normal stress on the facet plane, which has been suggested as being necessary for crack nucleation during continuous cycling fatigue of Ti-8Al-1Mo-1V [15]. It is likely that crack initiation occurs in the primary α constituents because of the elemental partitioning effect, which results in higher Al content in this constituent during elevated temperature thermomechanical processing. Therefore, it is more prone to planar slip than the transformed β regions, which also have many α/β interfaces that can form pileups under certain circumstances [9, 60] and can presumably result in delayed crack initiation [16]. However, the definition of a detailed, mechanism-based understanding of the crack nucleation process for the continuously cycled specimen tested here is still unclear.

It is clear, however, that the initiation mechanism is not the result of a classic cleavage mechanism. The crack-IF is inclined to the LD and has formed on a plane in which slip has occurred previously. Furthermore, spectrum loading experiments [43, 51] have shown conclusively that facets do not form during a single-load cycle during continuous cycling, but rather that the crack tip advances incrementally, cycle by cycle through each individual grain. Then, depending on the details of the local grain boundary structure, there might be an incubation period [61] before the crack begins to propagate into the next grain. The incubation period would be governed by microstructural factors, such as crystallographic misorientation, grain boundary orientation, and the degree of coplanarity between the current crack plane and the preferred crack propagation plane in the adjacent grain. As this is a plasticity-controlled growth mechanism, the local stress intensity range would be the dominant factor driving crack extension, as opposed to exceeding a critical normal stress as in classic cleavage.

Subsequent faceted propagation occurred through nearby primary α grains that were also inclined to the LD. As shown in the inverse pole figures (see figure 28), seven EBSD patterns were collected from the crack-initiation facet (CY-1) along a horizontal line spanning the diameter of the facet. Although the data seem to be noisy, when plotted on 0001 and 1120 equal angle projections (see figure 29(a)), it is evident that these patterns reveal a continuous lattice rotation about [0001] of approximately 10^o collectively. Although it is tempting to relate this to the facet formation process, high-resolution EBSD analysis of the AR material indicated that similar lattice rotations were present within the primary α grains (see figures 29(b) and (c)). As can be seen, the basal pole remains in the same position; however, there is a rotation of 10^o about [0001] over a distance of approximately 7 μm on the facet. High-resolution (0.35 μm step size) inverse pole figure map (+ image quality overlay) of the as-received material (b), and cumulative misorientation distributions along profiles (1) and (2) in (b) and (c). It should be noted that a similar analysis of facets formed during cyclic loading of well-AN material (with no residual dislocation content) produced similar facet surface features on both initiation and PFs. Therefore, the presence of residual stored work does not seem to influence fracture topography.

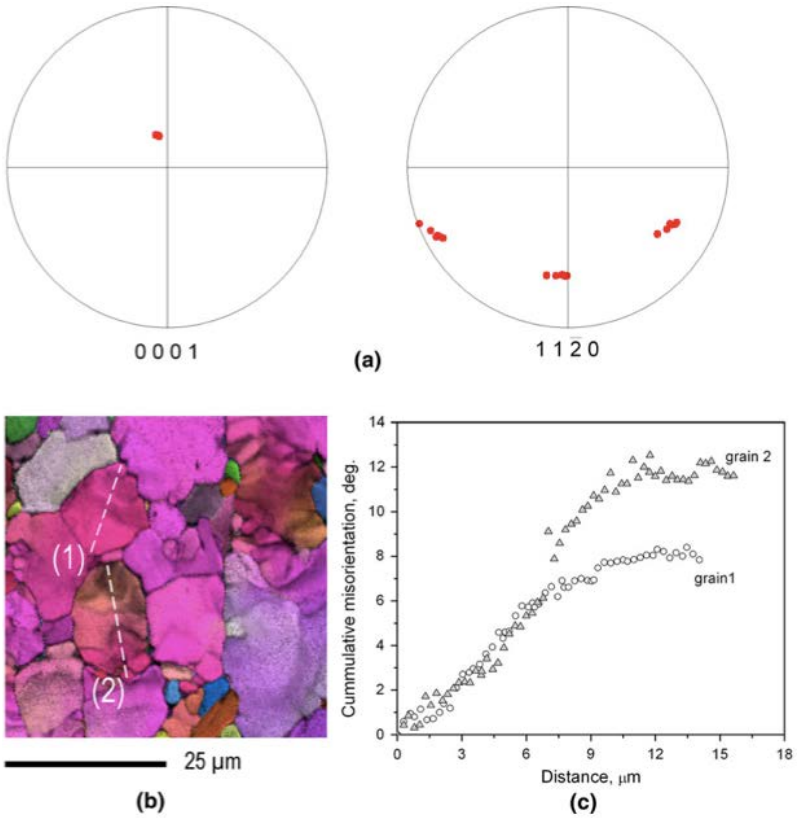

Figure 29. 0001 and 1120 equal-area-projection pole figures showing all of the orientations indexed from the crack-initiation facet (CY-1) in the continuously cycled specimen (a)

2.2.3.2 Creep fracture surface

The specimen crept in air was most similar to the dwell-fatigue specimen in the sense that there was subsurface initiation and subsequent formation of an elongated faceted region, and the fracture surface was relatively flat, aside from the shear lip (see figure 24). It was more difficult to locate the crack initiation site in the specimen statically loaded in air compared with all of the others investigated in the current study. This was because the facet surface topography (roughness), which was the primary indicator of crack length in the continuously cycled specimen, was relatively consistent throughout the entire faceted region. Several representative PFs are shown in figure 30. These facets had markings on their surfaces that corresponded well with the overall sense of crack propagation. After examining several millimeters of the faceted region at magnifications greater than 800 times, a single facet was identified at a subsurface location that had the planar, featureless surface topography characteristic that is typically associated with crack-IFs. This facet is identified as ST-1 in figure 31. The surrounding facets were characterized as PFs, and those in the immediate vicinity of the initiation site were both inclined, and nearly perpendicular to, the LD. Although the test was conducted in laboratory air, it is important to note that the facets formed at subsurface crack-initiation sites were not surface connected and were therefore propagating in a high vacuum.

Regardless of spatial orientation, all PF surfaces had a similar appearance, which is shown in the lower portion of figure 31. This surface topography is considerably different than that observed on

the continuously cycled specimen and appears more ductile. The markings on the facet surfaces had a distinct directionality, which was consistent with the macroscopic crack propagation direction; however, the orientation of these markings often changed substantially at grain boundaries, suggesting that the crack propagation path was strongly dependent on crystallographic orientation—more so than those facets on the continuously cycled specimen. In general, the size, shape, and density of the markings on the facet surfaces remained relatively constant throughout the entire faceted region. On each facet, there were typically several large ridges extending along the crack propagation direction. These ridges had several smaller ridges, or tributaries, branching off from them at an angle to the overall crack propagation direction. These tributaries became gradually smaller until they eventually were indistinguishable from the flat part of the facet surface between the ridges.

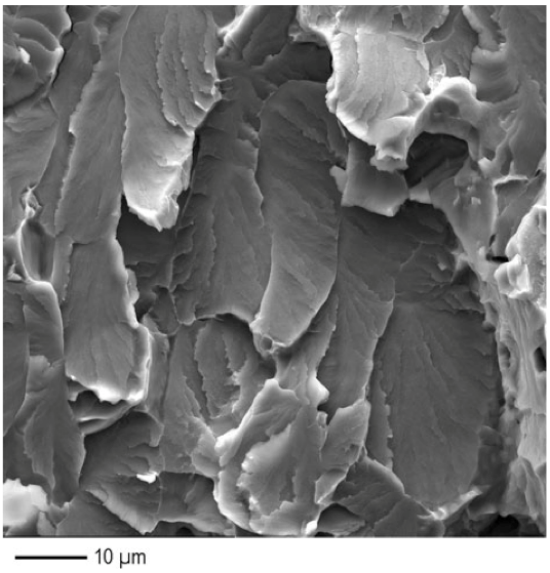

Figure 30. Typical facet appearance throughout the entire faceted region on the creep specimen

The top of the primary ridge was peak shaped and often came to a point, suggesting that these features were formed by plastic flow of the α phase. Between the larger primary ridges, there was another set of more shallow ridges that had similar shape, termed secondary ridges. There were occasionally acicular features on the facets, located near the ridges, that were typically less than 100 nm long and 25 nm wide. In some locations, the features appeared as if they were particles on the facet surface, whereas in others they seemed to be partially embedded in a ridge (see arrows in figure 31). They became most apparent on the facets only when imaged with the TLD. The particles appeared bright when imaged with secondary electrons and were indistinguishable from the rest of the facet when imaged with backscattered electrons, other than contrast changes caused by variations in surface height. Although these features are often associated with ridges, their significance in the formation of the ridge markings is not entirely clear because the frequency of ridges far exceeded the density of particle-like features.

(a)

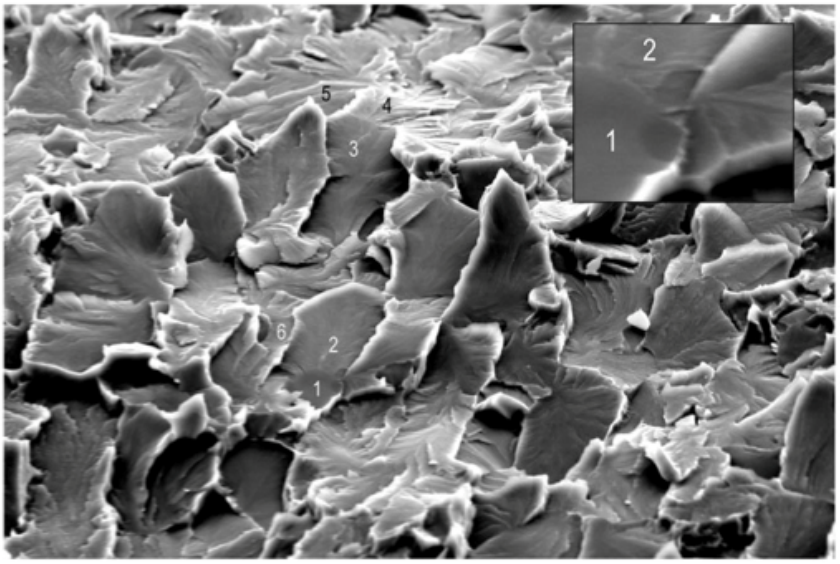

(b)

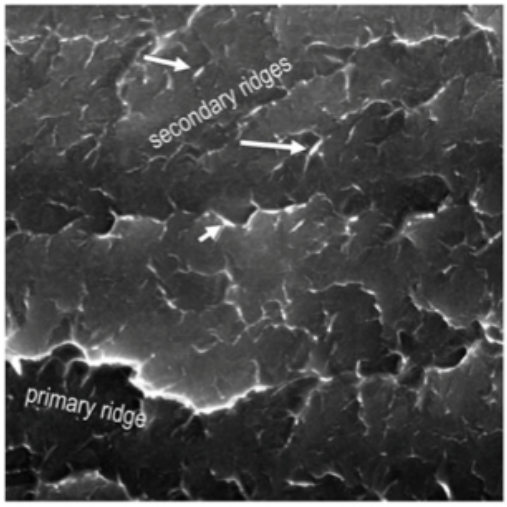

(c)

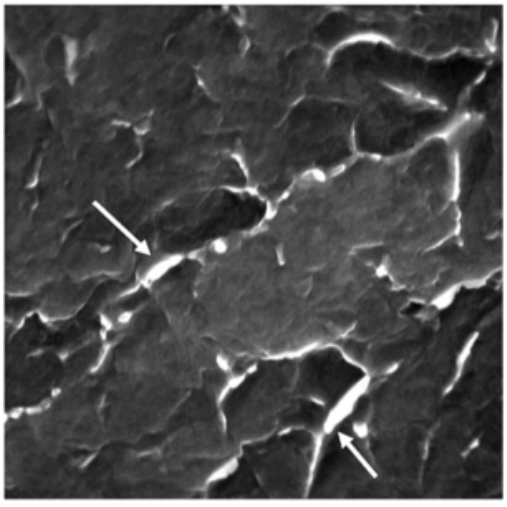

Figure 31. (a) Crack-initiation site in the statically loaded specimen. Six facets are identified, which were analyzed in detail. The initiation site is shown at higher magnification in the inset. High-resolution images showing the facet topography of typical crack PFs. The macroscopic crack propagation direction is from left to right (b, c)

The crystallographic orientations of the IF and five PFs (see figure 31) were studied in detail, and the results have been plotted on the inverse pole figures in figure 32. The initiation site, facet ST-1, had a normal orientation that was 23º from the LD, whereas the PFs at the smallest crack length, ST-2 and ST-6, had angles of 18º and 11º, respectively. The plane of fracture, ST-1, was approximately 5º from the basal plane, whereas ST-2 and ST-6 have fractured on planes approximately 15º from (0001). Similar to the case of continuous cycling, the crack initiated within a grain whose [0001] direction was inclined to the LD (~25º). Therefore, the grain in which the crack started was oriented so that there was sufficient RSS for slip on the basal plane at the applied stress, but also a significant resolved normal stress. The nearby PFs were less inclined, however, than those surrounding the continuous-cycling IF. It is also noted that the first PFs, ST-2 and

ST-6, were also in an orientation where they could deform easily by basal slip, both having their *c*-axes more inclined to the LD than the crack initiating grain. However, despite the almost certain presence of basal slip bands, the crack clearly propagated along a crystallographic plane that was inclined to the basal plane and close to $\{10\bar{1}7\}$.

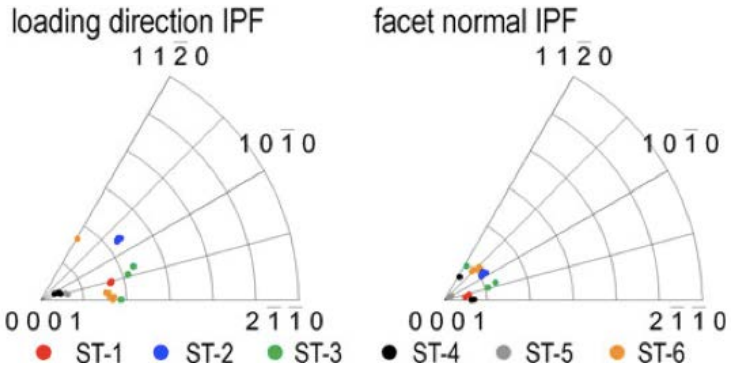

Figure 32. Results from the facet crystallography analysis on the initiation (ST-1) and propagation (all others) facets from the statically loaded specimen

Of the facets analyzed at a slightly longer crack length (see facets ST-3, ST-4, and ST-5 in figure 31), facet ST-3 was oriented crystallographically for easy basal slip like those grains near the initiation site; however, it fractured ~15° from (0001) with a facet normal angle of 14°. Facet ST-3 also had two different underlying grain orientations as evidenced by the LD pole figure; however, when the difference was accounted for in fracture plane normal among the various regions on the facet where EBSD patterns were collected, the crystallographic fracture plane was similar for all data points measured. The *c*-axes of facets ST-4 and ST-5 were oriented only 4° and 8°, respectively, from the LD. However, despite the high resolved normal stress on the basal plane of grain 4, it fractured on an irrational plane that was ~6° from the LD; whereas grain 5 had the highest normal stress on the irrational plane near $\{10\bar{1}7\}$, but it fractured precisely on the basal plane.

In this specimen, the initiation grain and the first few neighboring grains were in neither hard nor soft orientations. In contrast to the continuously cycled specimen, the PFs were less inclined to the LD. Under sustained loading, this might be expected because, according to fracture mechanics [62], cracks propagating in mode I have the highest strain energy release rate per unit crack advance. Therefore, this would be the preferred crack propagation mode under sustained tension loading, assuming there is a crack extension mechanism available to support this. This may help explain why the crystallographic plane of fracture can be either (0001) or inclined to it. The fact that $\{10\bar{1}7\}$ occurs more frequently might be related to the fact that there are six $\{10\bar{1}7\}$ planes and only one basal plane, so it is more likely that a $\{10\bar{1}7\}$ plane will have higher resolved normal stress. The fact that the experimental data do not rigorously support this speculation (e.g., facet ST-4) is likely related to crack front incompatibility and local neighborhood effects resulting in grain-level stress states that are considerably more complicated than when it is assumed that each grain experiences a simple uniaxial load, as has been shown in localized plastic deformation. Similar features were observed on the stress corrosion and dwell-fatigue crack PFs. Therefore, discussion of the mechanism of facet formation is reserved until all data have been presented.

2.2.3.3 Dwell fracture surface

In contrast to the continuously cycled sample, the dwell-fatigued specimen exhibited subsurface crack initiation. It had a considerably larger faceted region that was on the order of 250 μm wide and extended approximately 3 mm from the circumference of the specimen into the gauge section. Similar elongated faceted regions were observed on all the statically loaded specimens, suggesting that the formation of such regions is unique to sustained loading. It is noteworthy that the length scale, aspect ratio, and physical orientation of these elongated faceted regions is consistent with those of the MTRs observed in the AR bar material (see figure 23). This correlation has possibly been overlooked in the past because the MTRs in the α+β forged Ladish Pancake 2 material analyzed in previous reports were approximately equiaxed in shape. These analyses also did not explicitly identify where in the faceted region the crack started; therefore, a preferential growth could not be identified. Uta et al. [63] have also studied the fracture surface specimen that failed during dwell-fatigue loading, which had elongated bands of microtexture similar to the material studied here. However, the authors used a 30-second dwell period and did not observe such a strong preference for the faceted region to correlate with the underlying MTRs.

In addition to the primary and secondary initiation sites (SIS) identified in the low-magnification image of the fracture surface in figure 24, another five subsurface SIS were identified near the primary initiation site (see figure 33). At least six other subsurface initiation sites were identified throughout the rest of the faceted region that extended toward the other side of the specimen, although the search of the faceted region was by no means exhaustive. As mentioned previously, the crack would have been propagating in a high vacuum throughout the faceted region in this specimen because of the subsurface initiation.

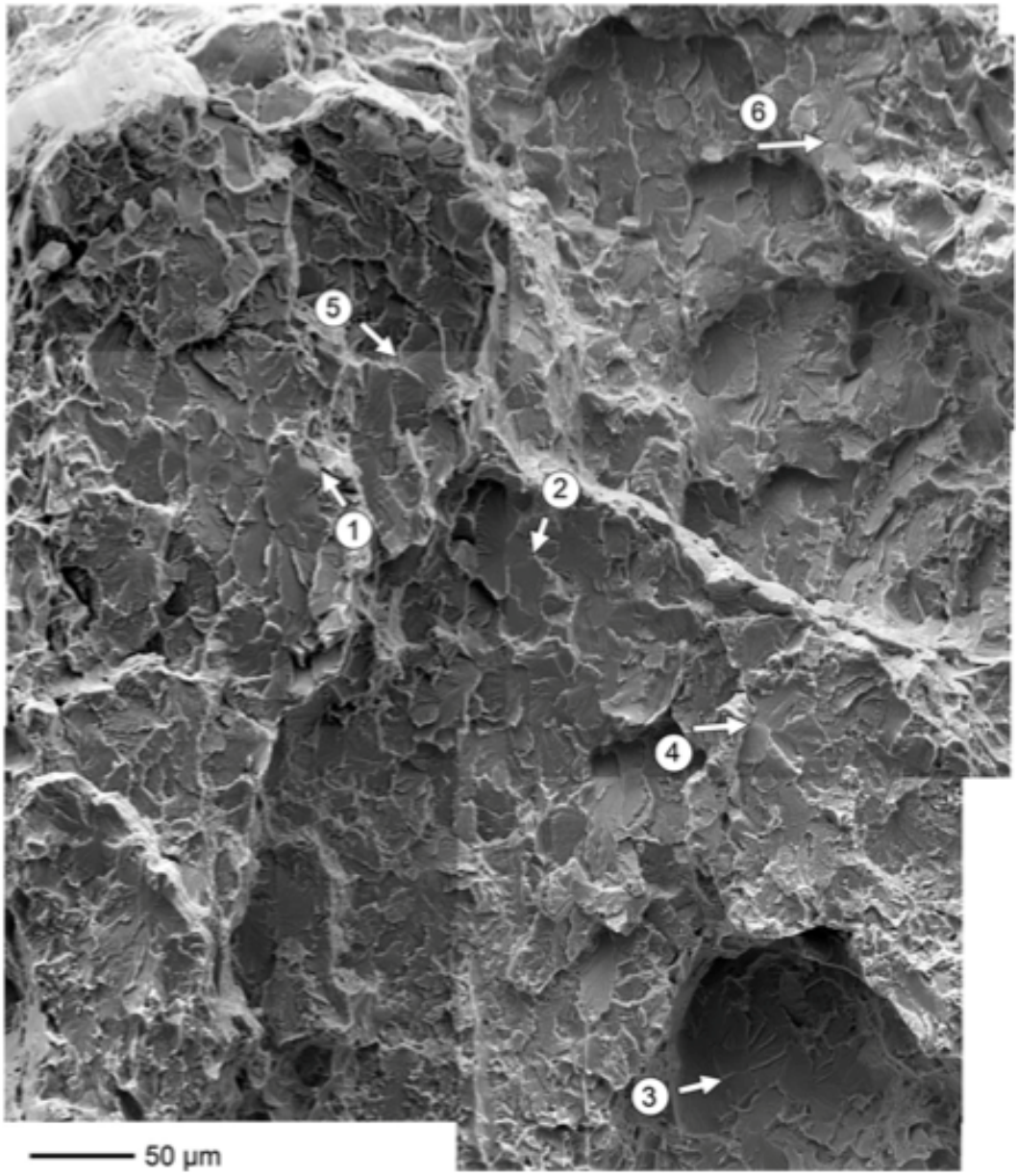

Figure 33. Montage of the region around the primary initiation site (1), which reveals several SIS (2–6)

The primary initiation site (see figure 33) serves as a good example to demonstrate the necessary characteristics to be classified as the primary initiation site. The term “primary” implies that the location was where the first crack formed during testing, whereas the term “secondary” implies only that the initiation event occurred after the primary one. The fractographic analysis could not discern the order of subsequent initiation events. This terminology is consistent with that of Uta et al. [63] and also supports the authors’ observation of multiple initiation events within a single MTR during a dwell-fatigue test of IMI834. The facet topography in this region is consistent with that on the specimen statically loaded in air, with ridges extending along the direction of crack propagation. These markings lead back to the intersection of two facets on the fracture surface,

DW-1 and DW-2, which are shown at a higher magnification in figure 34. There were steps on the surface of facet DW-1 and ridges on the surface of facet W-2, both leading away from the grain boundary (see segment A-A' in figure 35). This implies that the crack initiated at the grain boundary where these two particular planes met. It is noted that there was extremely good mating between the facet planes over the length of the boundary, which suggests that this is a primary α/primary α boundary as opposed to a primary α/retained β/primary α or a primary α/retained β /transformed β boundary. After the crack initiated at the boundary, it propagated by faceted growth through the surrounding grains, labeled DW-3 through DW-7, and beyond.

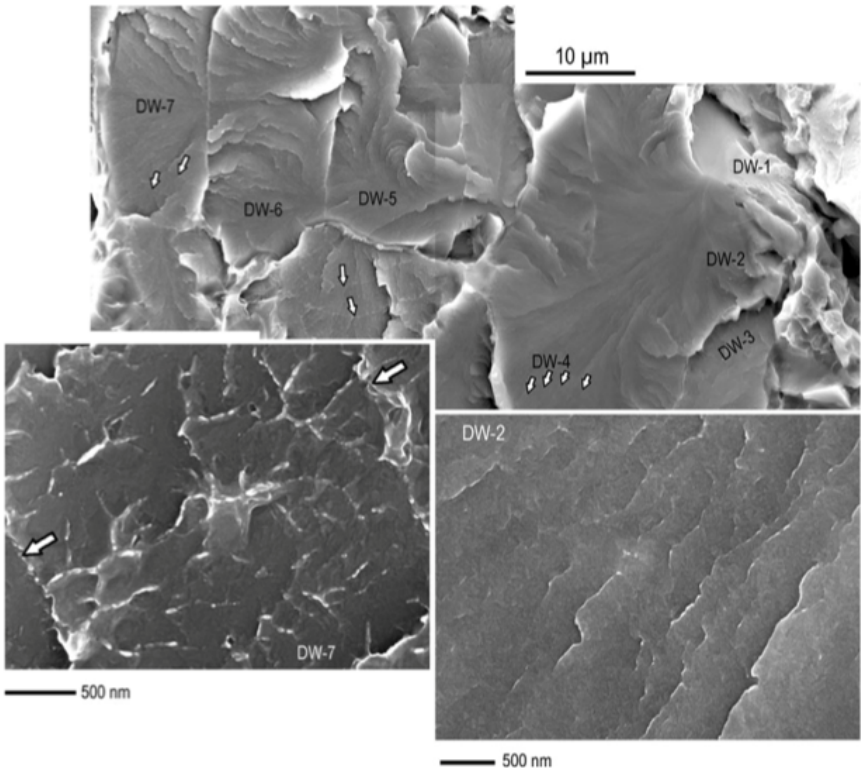

Figure 34. Fracture surface of the dwell-fatigue specimen (all at 0º stage tilt). The top image shows the initiation facet (DW-1), which is inclined substantially to the loading axis and subsequent PFs (DW-2 through DW-7). The arrows in the top image identify crack-front arrest marks

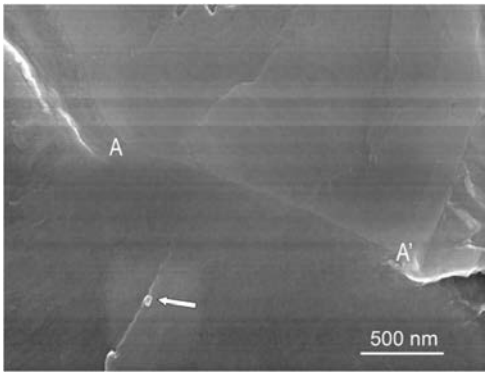

Figure 35. The intersection of facets DW-1 (A) and DW-2 (A') at the primary dwell-fatigue crack-initiation site

Facet DW-1 was more planar than any of the adjacent facets and had the smooth surface topography consistent with the IF on the continuously cycled specimen. This facet normal was 41° from the LD, whereas the adjacent facet normal, DW-2, was less than 3° from the LD. These facet planes were, therefore, near the maximum RSS and resolved normal stress orientation, respectively. The subsequent PFs, DW-3 through DW-6, were also in near-maximum resolved normal stress orientations with facet normal angles of 8°, 7°, 8°, and 6°, respectively. With regard to facet topography, facet DW-2 had a series of parallel, shallow ridges extending away from the grain boundary initiation site. With increasing crack length from the initiation site, these ridges became larger and began to exhibit branching, which is evident on facet DW-7. Crack-front arrest marks with spacing of 1.5–2.0 μm were also evident on the facet surfaces at crack lengths greater than ~20 μm and became more apparent at magnifications of 500–1000 times at crack lengths of ~100 μm (see figure 34). The primary ridges parallel to the local crack-propagation direction were generally orthogonal to the crack-front arrest marks. If not for these arrest marks, the dwell facets would be indistinguishable from those formed during static loading in air (but propagating in vacuum). It has been noted that several arrest marks can be observed within a single facet, indicating that these are neither cleavage nor quasi-cleavage facets, as the observed characteristics do not conform to the definition of either term as they were used originally [55, 64]. It is worth mentioning that Meyn [65] has observed crack-front arrest markings on facet surfaces of Ti-811 subjected to static loading in hydrogen gas. Considering that similar markings were not observed on either of the statically loaded specimens, it is believed that the crack-front arrest markings observed on dwell-fatigue facets were formed during the unload/reload cycle. The markings were also observed to change direction drastically at some grain boundaries, similar to the other loading conditions involving a static component, which suggests that this mechanism of faceted crack growth is highly crystallographic.

Surprisingly, neither the facet topography nor the crack-front arrest mark spacing changed significantly with increasing crack length throughout the faceted region, which was several millimeters in length (see figure 36). At crack lengths greater than ~1 mm from the primary initiation site, the crack-front arrest mark spacing was only on the order of 2.0–3.0 μm, which is just slightly larger than that measured at crack lengths between 20–100 μm. The facets consistently had ridges extending in the direction of local crack propagation, and there were often adjacent

facets with varying areal densities of ridges. Presumably, this is an orientation dependency, although no attempt was made here to quantify it. The effect of the unload/reload cycle on the primary ridges and facet topography is evident in figure 36. The crack-front arrest markings were similar to striations—they denote the occurrence of one unload/reload cycle, but because of their curved shape marking the local crack front, they could not have been formed by intersection of slip bands with the fracture surface and, therefore, could not have been formed by Laird's classic "sliding off" mechanism involving duplex slip ahead of the crack tip [66].

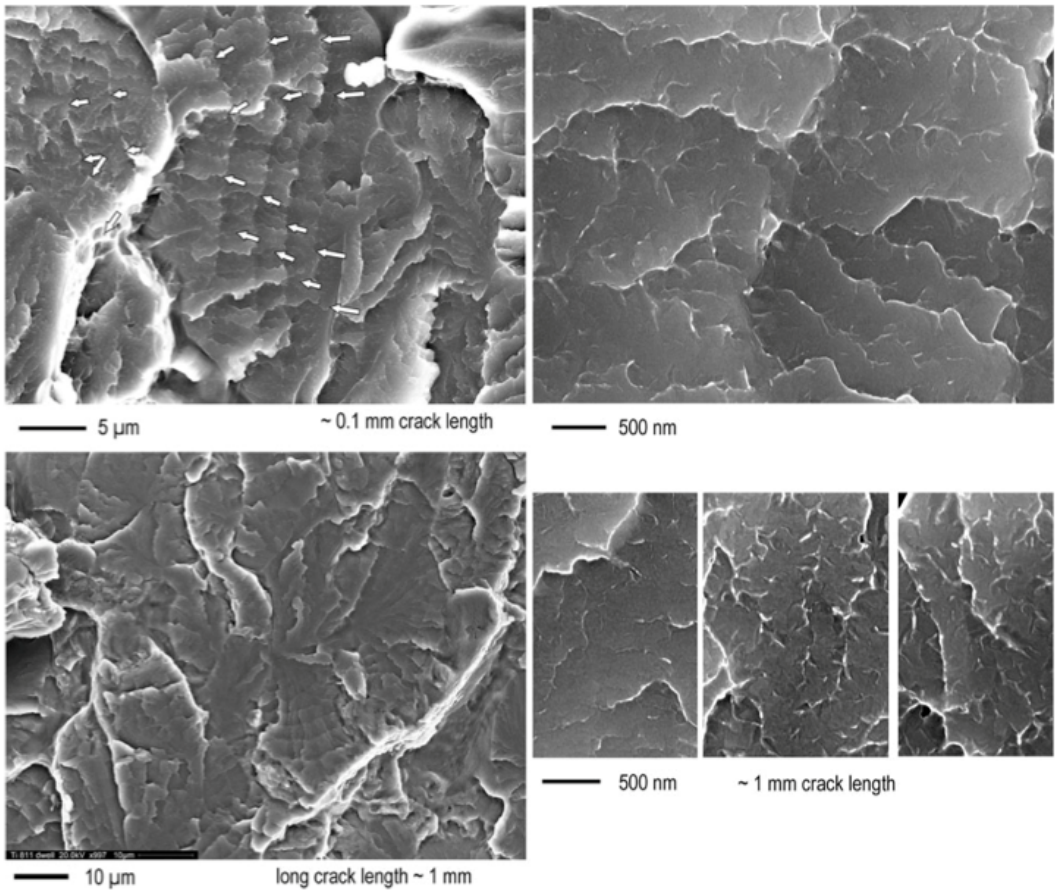

Figure 36. Facet surface topography as a function of crack length in the dwell-fatigued specimen; a secondary initiation site is also evident in the center of the lower left image

The crystallographic plane of fracture, for the two grains involved in the crack-initiation process and several of the subsequent PFs, was investigated using the tilt fractography/EBSD technique (see figure 37). With respect to the LD, the *c*-axis of grain DW-1 is inclined approximately 43°, whereas the remaining PFs all have *c*-axis inclinations between 8° and 26°. After accounting for the spatial orientation of each facet, the crystallographic plane of fracture was identified as being less than 1° away from the basal plane for the initiation facet (DW-1) and inclined between 16° and 22° to the basal plane for the remaining PFs. The crystallographic misorientation angle between grains DW-1 and DW-2 was 48.6°, indicating that this was a high-angle grain boundary. Furthermore, the potential for slip transfer was investigated by the method described [16], and it was found that no slip systems were suitably aligned for transfer through the grain boundary.

Therefore, it is reasonable to conclude that this grain boundary was amenable to the formation of a dislocation pileup of significant strength.

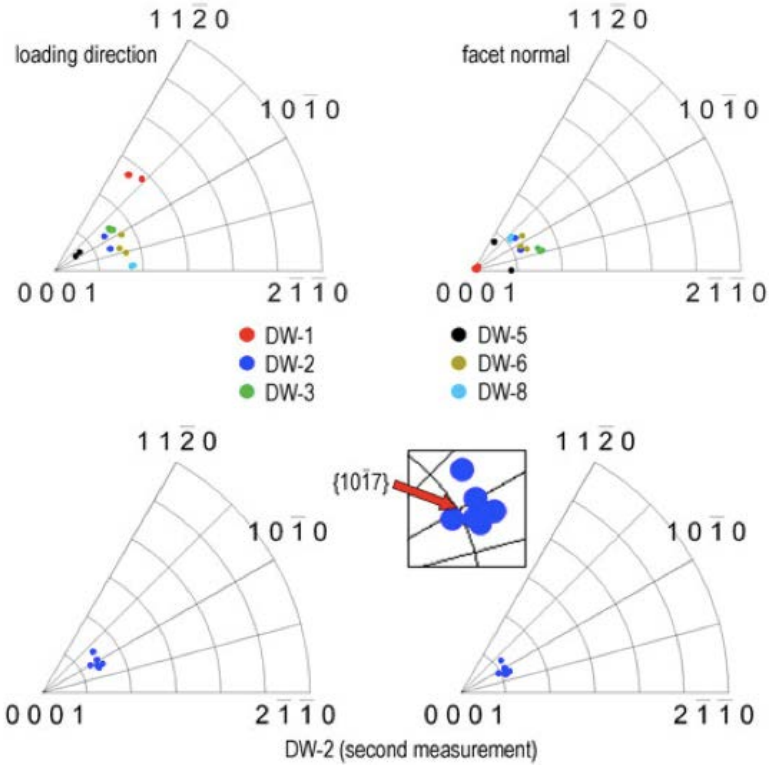

Note: Equal-angle inverse pole figures showing the orientations of the faceted grains identified in figure 35 with respect to the LD and facet normal.

Figure 37. Dwell-fatigue facet crystallography

The spatial and crystallographic orientation of facet DW-2 was measured in a different SEM to confirm the results. During this second analysis, seven EBSD patterns were collected along a line extending perpendicular to the facet boundary toward grain DW-4. These orientations are shown on the inverse pole figures at the bottom of figure 37, which clearly reveals that the fracture plane is inclined 15° to the basal plane, making it close to $\{10\bar{1}7\}$. The facets on all the grains surrounding the initiation site, except DW-5, were oriented such that the *c*-axes were inclined 20°–25° to the LD, indicating that they were capable of basal slip. However, all the facet NDs were nearly parallel to the LD, with the largest deviation being ~7°, indicating that the fracture plane was not the basal plane but rather inclined to it (see figure 37). Other facets surrounding the primary initiation site, from which EBSD data were not collected, exhibited angles as large as 16° between the facet normal and the LD. Although these grains should have been capable of basal slip and likely developed basal slip bands during loading, they did not fracture on this plane. The fracture planes instead deviated between 12° and 23° from (0001). The similarity in spatial and crystallographic orientation and facet-surface topography among the facets formed by these three types of loading suggests that all the cracks are propagating by similar mechanisms.

The secondary initiation site (SIS) identified on the dwell specimen in figure 15 was also examined with tilt fractography and EBSD (see figure 38). The initiation facet (DW-B1) was identified by its smooth, planar surface topography, which became more apparent at large stage tilts. This facet had a normal that was 25° from the LD, whereas the two neighboring PFs (i.e., DW-B2 and DW-B3) made angles of 14° and 20°, respectively. After accounting for the spatial orientation, the fracture planes were determined to be between 2° and 5° from (0001) for grain DW-B1, ~15° for grain DW-B2, and ~16° for DW-B3. These observations provide additional confirmation for the initiation mechanism observed at the primary initiation site. It is argued that the primary site was more favorable for early crack initiation because of the better matching of the fracture planes in the grain boundary, along with the higher RSS for slip on the basal plane of grain DW-1, allowing for easier accumulation of the necessary shear strain.

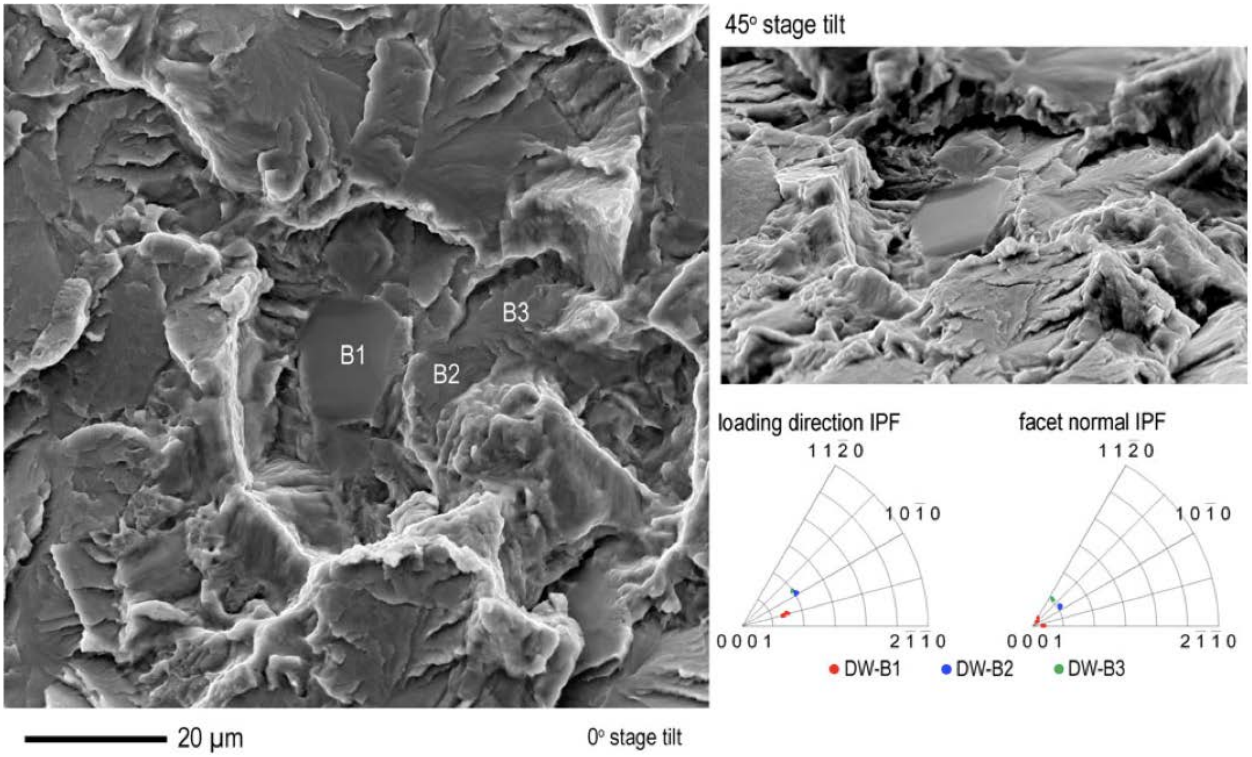

Figure 38. Facet crystallography analysis of an SIS in the dwell-fatigued specimen; this location was approximately 380 μm away from the primary initiation site

The fractographic and crystallographic observations presented above provide further support for the reports of Sinha et al. [19, 20] and Uta et al. [63] regarding the crystallography of dwell-fatigue crack PFs. The authors of both investigations have reported that dwell-fatigue crack PFs were inclined between 10° and 20° to the basal plane in the near-α alloys Ti-6242 and IMI834, respectively. Using the same technique to locate the initiation sites as reported here—namely, tracing the fine markings on the facet surfaces to a convergence point—Uta et al. [63] identified a primary initiation site and several SIS. The authors characterized each initiation site as containing a "pure cleavage facet with no local marks" that was surrounded by quasi-cleavage PFs. Ignoring the inconsistencies regarding the use of the words "cleavage" and "quasi-cleavage" to describe both types of facets, it is noted that crystallographically, the primary initiation site observed by

Uta et al. [63] is consistent with these observations. Specifically, there was one grain with its *c*-axis inclined to the LD such that it can deform by basal slip that faceted near the basal plane, resulting in a microscopically smooth, planar fracture surface. Adjacent to this was another grain, the *c*-axis of which was less inclined to the LD that formed a facet on an irrational plane inclined between 10° and 20° to the basal plane, which has markings indicative of crack propagation. Uta et al. [63] reported neither the spatial orientation of the facet NDs nor the facet normal inverse pole figures, so no further comparison to their results can be made here. The spatial and crystallographic characteristics of the PFs analyzed here are, however, consistent with the measurements made on dwell-fatigue PFs by Sinha et al. [19, 20].

Near the initiation site and within the first several hundred microns, the arrest mark spacing was on the order of 1–1.5 μm per cycle, whereas at longer crack lengths of more than 1.5 mm and throughout the entire faceted region, the crack-front arrest marks saturated to a value between 2.0 μm and 3.0 μm per cycle. As a comparison, the crack was advancing at a rate of approximately 150 nm per cycle (see figure 18) at a crack length of ~100 μm in the continuously cycled specimen. From this value, the crack-front indicators on the continuously cycled specimen gradually increased with crack length, eventually evolving into classic fatigue striations. If the internal lattice resistance were the only force responsible for retarding crack growth during dwell fatigue, then the crack growth rate should increase monotonically with increasing crack length because the cyclic crack tip plastic zone has a square dependence on ΔK similar to the continuously cycled specimen. This observation is potentially important, especially when considered in the context of two other relevant facts. First, the size and shape of the faceted region reflects the underlying microtextured bands that were observed in the AR material, and, second, the apparent facet surface roughness of the dwell PFs does not increase systematically with increasing crack length.

Both observations suggest that the fracture process is not controlled solely by the size of the crack tip plastic zone, but rather it is a time-dependent growth mechanism. The fact that the size and shape of the faceted regions is similar to those of the MTRs in all of the specimens subjected to a sustained mode I loading condition implies that the crack grew preferentially through this region before extending into the surrounding microstructure. This assertion is supported by results from nondestructive evaluation measurements performed on an additional sample from this study, which did not fail after 26,263 dwell cycles. A subsurface crack was identified in the gauge section of the specimen after reconstructing the entire volume with x-ray computed tomography (see figure 39). These data, which are shown from two orthogonal directions, reveal an internal flaw approximately 2.4-mm long, 0.25-mm wide, and perpendicular to the LD. The size and shape of this flaw are entirely consistent with the size and shape of the MTRs observed in the AR material and within the faceted regions on the other specimens. This observation has important implications on the variability of dwell-fatigue life in laboratory specimens. For example, the faceted region on the dwell specimen studied in detail here intersected the surface of the specimen, resulting in a larger stress concentration and exposure of the laboratory environment to the crack tip, both of which can accelerate crack growth rates through the nonfaceted regions. In contrast, the specimen shown in figure 39 had already experienced more than double the number of cycles and revealed no significant crack growth into the adjacent microstructure. This sample failed after an additional 2604 dwell cycles after the image in figure 39 was taken.

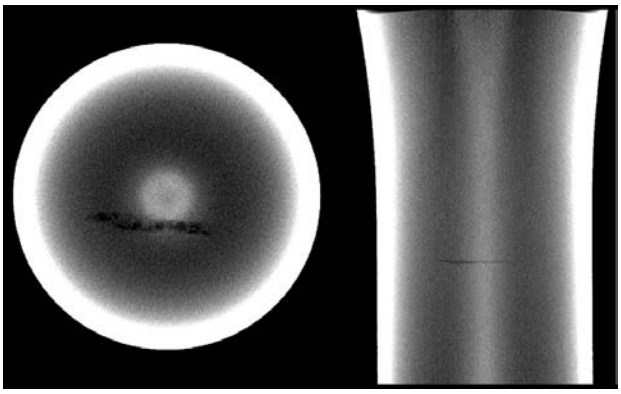

Figure 39. Two orthogonal views of a subsurface crack imaged with x-ray computed tomography in a dwell specimen that had not failed after 26,263 cycles

The markings on the dwell and continuously cycled specimens, which indicate the position of the crack front on successive cycles, have shown that crack growth rates are several orders of magnitude faster in the faceted region for the dwell-fatigue specimen compared with the continuously cycled one for the same crack length. Having established that the size and shape of the faceted region is dictated by the underlying microtextured regions, and that the crack forms within and propagates preferentially through these regions, it becomes clear that the crack growth rates outside the faceted region during dwell fatigue are even less important to the total life. The fact that crack growth rates measured on compact tension specimens are often insensitive and occasionally slower during dwell loading further suggests that the crack-initiation and small crack growth stage are more critical to explaining the observed life debit. The reduction in the number of cycles to crack initiation resulting from dwell loading is obvious; however, the considerably higher growth rates measured directly from the facet surfaces in the current study suggest that the faceted crack growth stage is equally or even more important. This concept is consistent with the recent work of Toubal et al. [67], who suggested that specimens with better resistance to crack propagation exhibit longer dwell-fatigue lives, although the authors have not identified the particular importance of resistance to faceted growth.

Now that the preferred orientation of crack-initiating and crack-propagation grains has been identified, it is possible to discuss the effect of microtexture region size on dwell-fatigue life. Consider the EBSD map of the entire transverse cross section of the dwell-fatigue specimen gauge section, collected approximately 1.3 mm below the fracture surface but within the reduced section of the specimen (see figure 40). These data illustrate that a range of sizes and aspect ratios of MTRs with *c*-axes are near—or are slightly inclined to—the LD (red hues), so it becomes useful to understand why crack initiation might be favorable in one location compared with another. Once a crack has initiated, it is useful to know which neighborhoods will facilitate faceted crack growth and ultimately lead to fracture of the component in comparison with those that result in crack arrest.

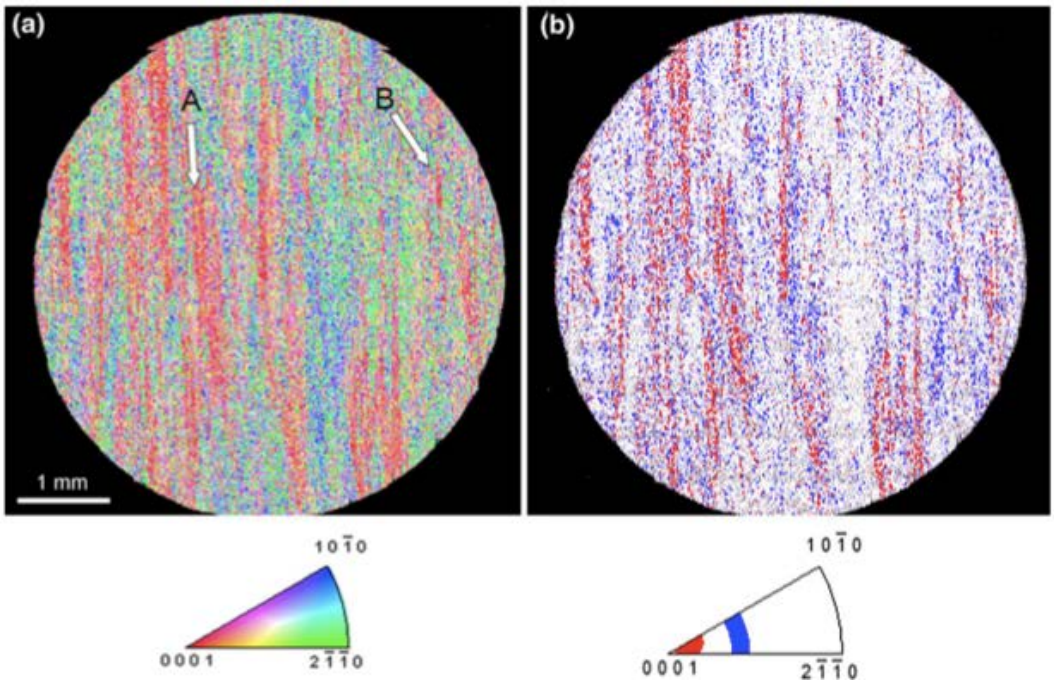

Figure 40. (a) LD inverse pole figure map of a transverse cross section of the dwell-fatigue specimen approximately 1.3 mm beneath the fracture surface. In (b), those grains with basal poles inclined 40°–50° from the LD have been colored blue, whereas the red grains are those with a $\{10\bar{1}7\}$ plane that is no more than 10° away from being orthogonal to the LD, as indicated by the inverse pole figures beneath each diagram. See text for details regarding locations A and B in (a)

For discussion purposes, consider the following simple example: Two cracks initiate on the same dwell cycle at locations A and B in figure 40(a). They initiate at grains like those previously described, which happen to be near the interface between "hard" and "soft" MTRs because of the locally higher stresses developed here as a result of load shedding [68]. After crack initiation, continued growth of the crack depends on its surrounding microstructure. Based on the tilt fractography/EBSD studies, it was identified that grains with $\{10\bar{1}7\}$ planes nearly perpendicular to the LD provide easy propagation paths. Therefore, in figure 40(b), the color-coding in blue corresponds to the grains with high RSS on the basal plane (i.e., the initiation grains), whereas the easy propagation paths are colored in red. Both cracks advance on each subsequent dwell cycle through their respective MTRs. After reaching the edge of the MTR, crack B is arrested because the soft-oriented grains on the other side can accommodate its plastic zone, similar to what has been observed during continuous cycling [58, 69]. The crack does not grow readily because there are no more basal planes suitably oriented for faceted growth. Crack A, on the other hand, continues to propagate through the larger MTR until it reaches a soft-oriented grain. Outside the faceted region, dwell-fatigue cracks have been observed to propagate by more conventional striation growth [56], which is controlled by crack tip plasticity. Therefore, it is reasonable that the driving force for subsequent crack propagation is proportional to ΔK, which would be considerably larger for crack A, suggesting that it would most likely propagate to catastrophic failure, as has been suggested by Sinha et al. [70]. Therefore, the size and shape of the MTR is the most important attribute affecting dwell-fatigue life because, in materials with

large MTRs, a large internal crack can develop while the crack is still growing at high rates under relatively microstructure-insensitive conditions, until faceted growth is exhausted. This internal flaw then serves as the initial condition for the second stage of crack growth, which seems to occur by more conventional striation growth mechanisms. For modeling purposes, it is likely that the size and morphology of the MTR could be used to select an appropriate K solution to model subsequent plasticity controlled long crack growth. The direct observation of several dwell-fatigue crack-initiation sites (both primary and secondary initiation in the current study and by Uta et al.[63] in a different alloy) that contain pairs of adjacent primary α grains similar to those described previously is potentially significant; it seems to both confirm and contradict several things considered to be characteristic of dwell-fatigue failures. First, these results confirm that a pair of grains is involved in the crack-initiation process as first proposed by Evans and Bache [23]. Here, despite the relatively high-volume fraction of transformed β, both of the grains involved in the initiation event were primary α grains. The adaptation of the Stroh model proposed by Evans and Bache contends that slip in the soft grain and the formation of a dislocation pileup are necessary to induce slip on the basal plane of the hard grain. This is necessary to obtain the critical combination of shear stress (or strain) and tensile stress normal to the slip plane required for facet formation.

This requirement for facet formation is discussed throughout the dwell-fatigue literature; however, the original citation for this requirement is from the work of Wojcik et al. [15], who studied the facets formed on large, single colonies of Ti-811 subjected to continuous cycling. All but one of the single colonies studied by Wojcik et al. had the basal plane oriented such that there was sufficient RSS for slip. Consequently, it would be expected that this would be the plane that accumulates damage most quickly, leading to crack initiation and propagation during cyclic loading.

The applicability of the results of Wojcik et al. to subsurface dwell-fatigue crack initiation in a polycrystalline material is not immediately obvious. The tilt fractography/EBSD analysis presented previously in this section, showed that the crack initiated in the grain with the substantially inclined basal plane as opposed to in the hard grain. Moreover, the first PF was actually parallel to an irrational plane near $\{10\bar{1}7\}$ that was incapable of slip. In addition, the difference in surface topography between the facets formed during continuous cycling and dwell-fatigue loading are unmistakable. There is no reason to expect that the mechanism that forms a smooth facet directly on a basal plane that is inclined to the LD, and the mechanism that forms a facet with ridges and rough topography that is perpendicular to the LD and parallel to an irrational $\{hkil\}$ plane inclined 10^o–15^o to the basal plane, should be the same. Therefore, the requirement for slip on the basal plane of the hard grain prior to fracture is unfounded and does not seem to be necessary, based on the observations.

The second point that the experimental results presented here draw into question does not relate to the adaptation of the Stroh model itself but rather to how a specific orientation has been attached to the phrase “soft grain.” With the use of EBSD analysis [71] and careful serial sectioning [70], it was observed that dwell-fatigue cracks generally initiated in regions of the sample that had both hard and soft MTRs. The soft regions were those with an elastically and plastically more compliant orientation—their *c*-axes were nearly perpendicular to the LD, and they could deform by prismatic <a> slip. Based on these experimental studies, the understanding of the source slip band in the

originally proposed Stroh-like model evolved into meaning a soft grain oriented for prismatic <a> slip. Several authors [44, 68, 72, 73] have addressed the phenomenon of room-temperature creep in the soft grain and the resulting stress redistribution onto the hard grain using CPFE simulations. Although there are differences among the results of the models, they generally agree on the fact that stress redistribution within the microstructure results in the formation of large stresses at, or near, the interfaces between hard and soft MTRs, and the spatial orientation of the interface can either increase or decrease these stresses. This latter point is useful in understanding why a crack forms at one location within the component as opposed to others with nominally the same crystallographic misorientation. However, even though the experimental observations [70] suggest this phenomenon is occurring on a length-scale consistent with the MTRs, some models have attempted to employ it on the grain level [44, 74]. In addition, the tilt fractography/EBSD analysis suggests that the softer of the two grains is one that can deform easily by basal <a> slip as opposed to prismatic <a> slip. The harder grain has its *c*-axis inclined ~20^{o} to the LD, implying that it is not truly a hard grain in the sense that <c + a> pyramidal slip is not necessarily enforced, and it subsequently cracked on an irrational $\{hkil\}$ plane.

Finally, it has been reported [18, 22] that when the applied load is below the macroscopic yield strength of the material, facets are formed nearly perpendicular to the LD regardless of whether a cyclic or dwell waveform is imposed. The results from the facet normal calculations as a function of loading type have been summarized in figure 41. In this plot, the IFs are represented by filled symbols. It should be noted that IFs were observed on all samples with an angle of approximately 25^{o} (SIS in dwell specimen). This is most likely related to the fact that the underlying grain orientation influences fracture topography as much as crack tip plasticity does, or more so. This is evidenced by the fact that fracture topography was observed to change from ductile to faceted growth with increasing crack length. Furthermore, all these facets were formed below the macroscopic yield strength of the material, including those on the continuously cycled specimen; therefore, the concept that facets should be normal to the LD [22] does not hold rigorously.

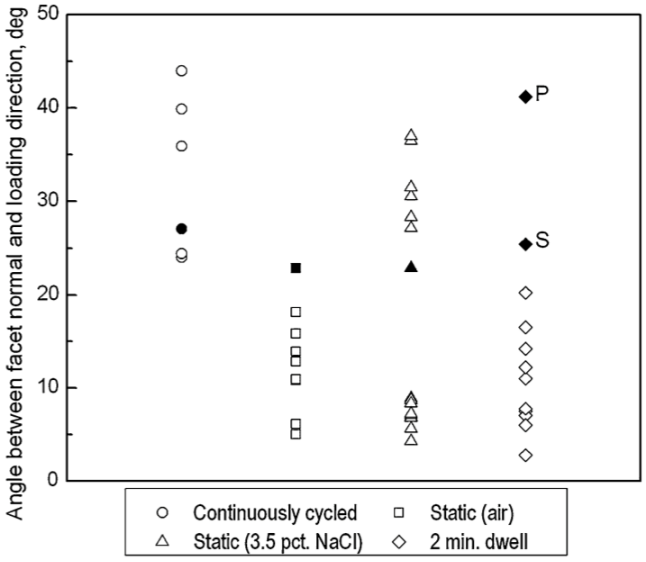

Note: Filled symbols indicate IFs, whereas open symbols designate PFs. Letters P and S designate the primary and SIS studied on the dwell specimen, respectively.

Figure 41. Angle between facet normal and LD

2.2.4 Dislocation Substructure Under Dwell-Fatigue-Induced Facets

In efforts to gain insight into the deformation processes that lead to facet formation under dwell-fatigue loading, the EBSD and quantitative tilt fractography efforts were augmented by site-specific TEM studies. The FIB in situ lift-out technique was used to extract thin foils from locations in the AR material, in the uncracked grain boundaries in the deformed volume ~2 mm below the primary fracture surface, in the faceted regions on the dwell-fatigue fracture surface. Thin foils were analyzed by STEM imaging under a variety of imaging conditions, allowing for both the imaging of wide areas and the analyses of specific features (i.e., diffraction contrast imaging).

The Ti-811 alloy in the AR condition exhibited a complicated dislocation substructure as a result of processing (see figures 42 and 43). In the EBSD maps and stereographic pole figures presented in figure 42, evidence of intragranular rotations on the order of tens of degrees and subgrains can be observed. The dislocation substructures in these highlighted grains were investigated by TEM (see figure 43). It can be seen that the initial dislocation density in the undeformed grains is quite high. These dislocations are arranged into dislocation networks and subgrain boundaries. Tilt diffraction imaging experiments indicate that networks are composed primarily of <a> dislocations, whereas the boundaries of subgrains contain dislocations containing *c*-components (i.e., <1123> and [0001] dislocations and <a> dislocations).

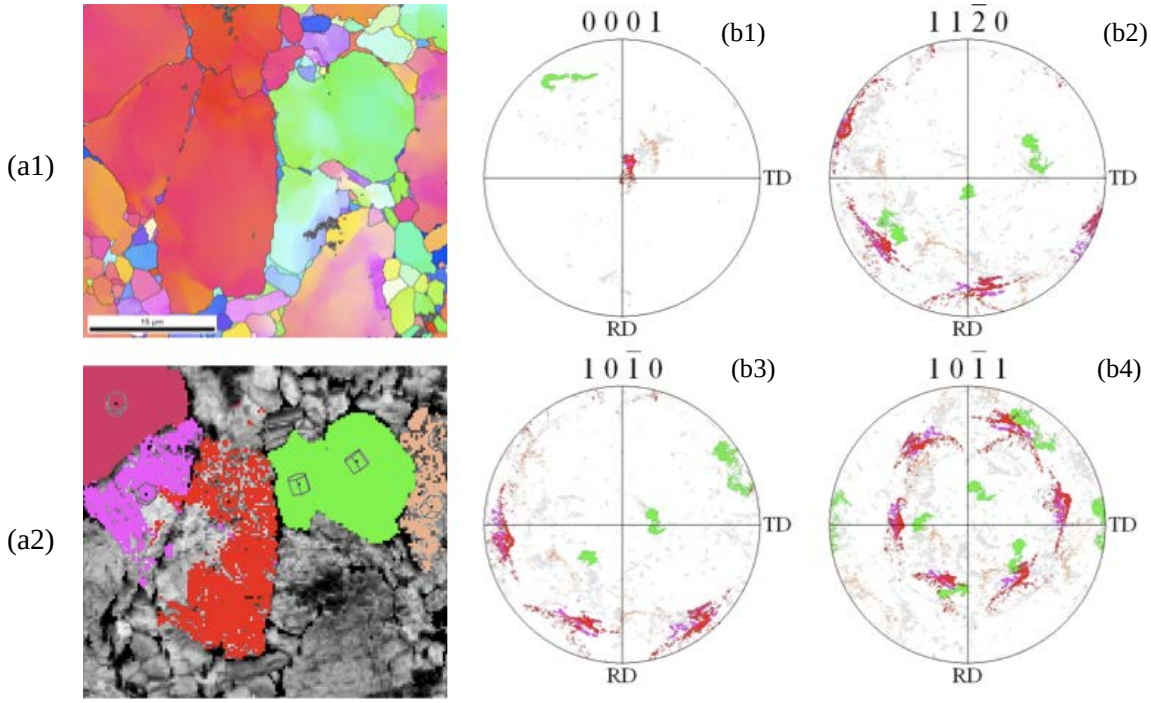

Figure 42. EBSD maps (a1, a2) of hard (red) and soft (green) grain orientations in the undeformed AR Ti-811; evidence of subgrains can be observed in the inverse pole figure map (b1), and grains highlighted in image quality map (b3) are plotted on stereographic pole figures (b1-b4)

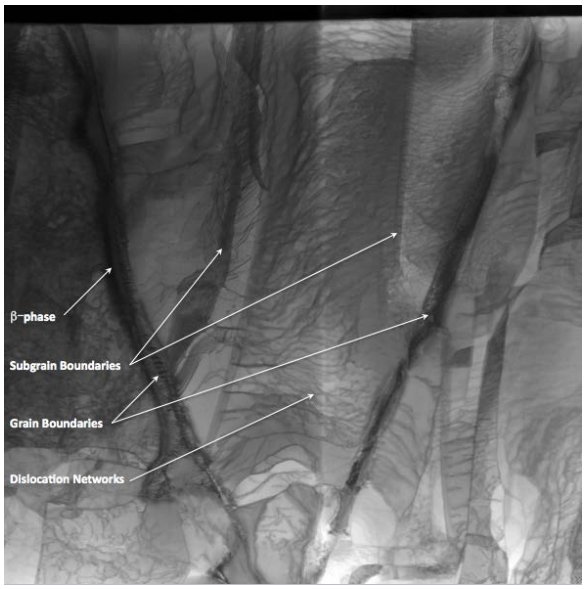

Figure 43. Thin foil extracted across the area in figure 42

With the expectation that the analyses of dislocation substructures created in grains undergoing a cracking process are likely to be complicated by the large-strain gradients and triaxial stress states that develop around cracks, foils were taken from uncracked grain boundaries in the deformed volume ~2 mm below the primary fracture surface. As this location is close to the primary crack, the dislocation structures developing as a result of dwell cycling are representative of those associated with the plastic processes preceding crack initiation. With this in mind, foils were extracted from several types of grain boundaries that have been identified as sites capable of initiating cracks. The first type of boundary (type I) was that where one grain was oriented with [0001] within 5^{o} of the tensile axis. Two grain boundaries of this type were investigated (see figure 44):

- Grain boundary with a grain orientated for <a>(0001) slip. The highest probability for <a>(0001) slip occurs when the *c*-axis inclined ~45^{o} to the tensile axis.
- Grain boundary with a grain orientated for <a> $\{10\bar{1}0\}$ slip. The highest probability for <a> $\{10\bar{1}0\}$ slip without the occurrence of <a> on other systems occurs when the *c*-axis inclined ~90^{o} to the tensile axis.

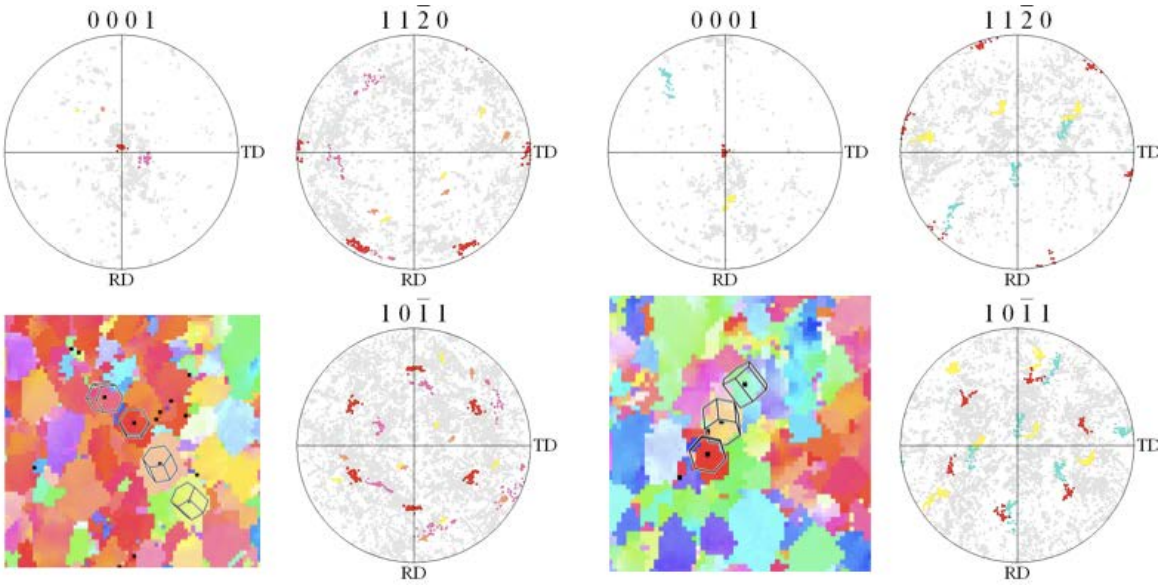

Note: These boundaries are characterized by a hard grain with a *c*-axis aligned to the tensile direction (out of the plane of the page) and a soft grain with an orientation conducive for either basal (a) or prismatic (b) slip.

Figure 44. Type I grain boundaries investigated by TEM

The second type of boundary (type II) that was investigated was a boundary between a grain with a *c*-axis inclined ~15°–20° to the tensile axis and a soft grain with a *c*-axis inclined ~45° to the tensile axis. Two grain boundaries of this type were investigated (see figure 45):

- A grain boundary with a grain orientated for <a>(0001) slip, where the <a> slip vector with the highest RSS due to the macroscopic load is aligned to a <1120> in the hard grain.
- A grain boundary with a grain orientated for <a> $\{10\bar{1}0\}$ slip, where the <a> slip vectors with the highest RSS caused by the macroscopic load is misaligned with the <1120>s of the hard grain.

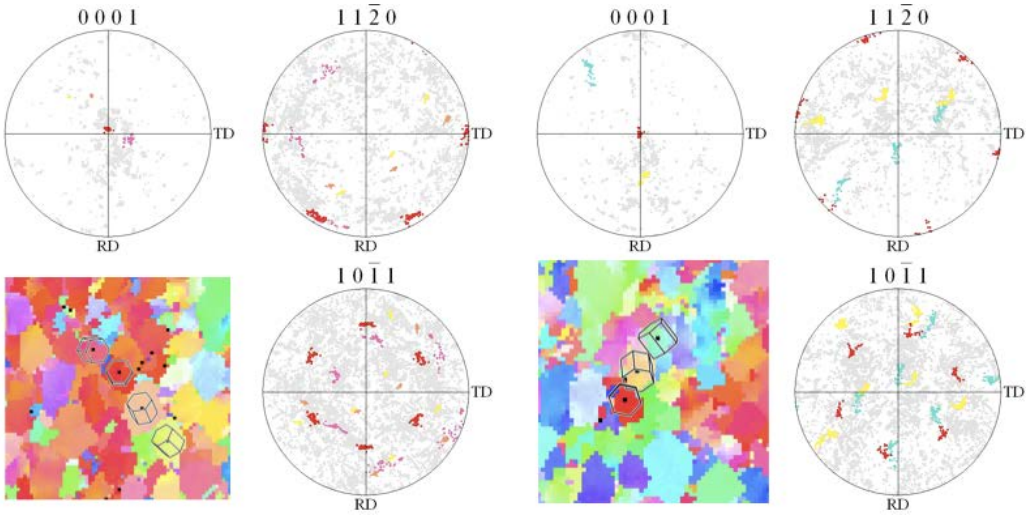

Note: These boundaries are characterized by a hard grain with a *c*-axis inclined ~15–20 to the tensile axis, and a soft grain with a *c*-axis inclined ~45o to the tensile axis (out of the plane of the page)**.**

Figure 45. Type II grain boundaries investigated by TEM

The dislocation structures observed at the type I boundaries are well represented by the TEM image presented in figure 46. The <a> slip bands (e.g., basal slip bands) traverse the entire soft grain and impinge on the grain boundary. The pileups that develop at the intersection of the slip band and the boundary contain hundreds of tightly spaced dislocations. Given that the stresses at the tip of the pileup scale with the number and spacing of dislocations in the pileup (stress increases as the number of dislocations increases and their spacing decreases), it might be expected that slip in the hard grain would be initiated at the intersection points. In fact, the initiation of basal slip in the hard grain is predicted by the Bache-Evans version of the Stroh model. However, this does not appear to be the case at this boundary or the other boundaries of this type. Although significant <a> dislocation density is observed in the hard grain (see figure 46(a)), the morphology of these dislocations is consistent with those in the AR material (see figure 43) and are not a result of deformation during dwell loading or the grain boundary pileups. The hard grain deforms by <c+a> slip, not <a> slip; this can be seen when the grain is imaged with the (0002) reflection (see figure 46(b)). Despite the accumulation of ~2% plastic strain in the sample (measured macroscopically), it is apparent that the deformation-induced dislocation densities of grains having [0001] aligned to the tensile axis is quite low, especially in comparison with those observed in soft grains. Interestingly, the sources of <c+a> dislocations do not appear to be associated with the slip bands in the soft grain. The reason for this is currently unknown, but it is possible that the stress concentrations at the tips of pileups are mitigated by the β-phase grains lining the boundary, or longer-range stress fields drive that deformation, even close to the boundary, in hard grains.

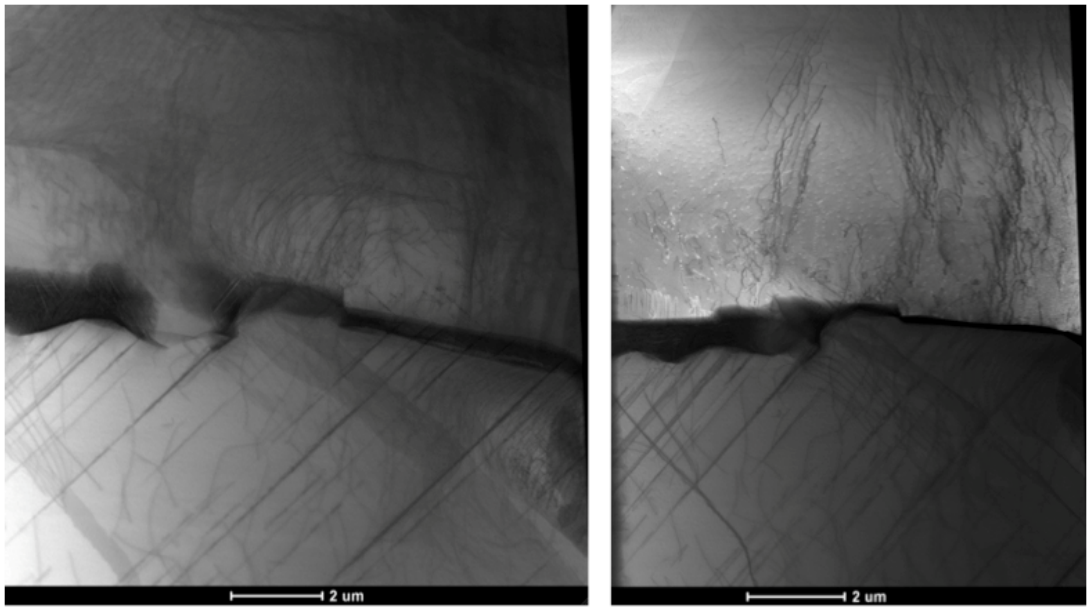

(a) (b)

Figure 46. Dislocation configurations observed at a type I grain boundary; the hard grain is at the top of the images, and <a> slip bands are observed in the soft grain

In contrast to the type I grain boundaries, the hard grains at type II boundaries show evidence of <a> slip. Although the resolved stresses on <a> slip/systems are likely low, the anisotropy between <a> and <c+a> slip is large enough to allow for <a>, when the applied and local stresses are relatively large. This observation is consistent with the observations of Williams et al. [36], showing the activation of basal slip in single crystals compressed along a direction more than ~10^{o} from [0001].

With an understanding of the dislocation structures present in the AR material and in the dwell-fatigued material as a result of plastic deformation, it is possible to understand the features observed under facets on the primary fracture surface. The foils extracted directly from the fracture surface were taken from three locations: 1) the primary initiation site, (i.e., the grain boundary between facets DW-1 and DW-2); 2) an SIS ~400 μm away from the primary site, (i.e., the grain boundary between facets B1 and B2); and 3) a PF ~2 mm away from the primary initiation site. The orientations of the facets at each of these sites are shown in figure 47. The orientations of the hard grains at the primary and SIS are such that their basal planes are inclined to the tensile axis (out of the plane of the page in figure 47); [0001] is inclined by more than 15^{o} for each facet. To maintain consistency, a PF with a *c*-axis inclination similar to that of DW-2 was chosen to assess the effect of crack length on dislocation substructures.

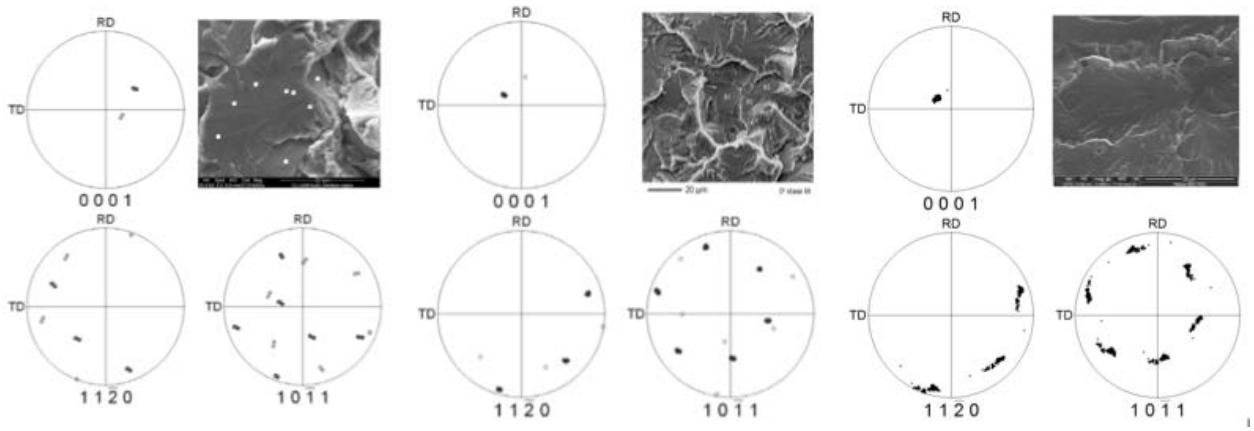

Figure 47. Facets investigated by TEM; primary initiation site (DW-1/DW-2) (a), SIS (B1/B2) (b), and PF (c)

Figure 48 shows the dislocation substructure under the primary initiation site. As can be observed in low magnification images, the faceted grains at the primary initiation site are divided into several subgrains (labeled A–F) misoriented by ~1˚, and all grains are highly deformed, showing slip activity on multiple systems. Many of the grains investigated in the foil showed some evidence of basal slip, although some more than others; basal slip traces are outlined in figure 48(a). Many of the grains in the foil, even those not traversed by the crack, showed evidence of <c+a> slip. Figure 48 (b–d) shows the slip behavior within each facet grain. Extensive <c+a> slip is observed in the hard grain (see figure 48(c)). The <c+a> dislocations are well distributed throughout the grain, but dislocation densities are elevated close to the initiation site "I". A similar trend is observed for <a> slip. The number of basal slip traces increases close to "I," although the traces of some basal slip bands are observed to traverse the entire width of the grain and its neighbor along the fracture surface (DW-4). The presence of basal slip bands in hard grains, even those removed from the fracture surface or initiation site, is in agreement with the observations in the type I and II foils above. Grains with [0001] inclined by more than ~10^{o} to the tensile axis may be prone to <a>(0001) slip before the formation of a crack. As in the hard grain, both <c+a> and <a> dislocations can be observed in the soft grain (DW-1); however, <c+a> dislocations are confined to regions near "I" and near the fracture surface (see figure 48(d)), and their densities are much lower than observed in the hard grain.

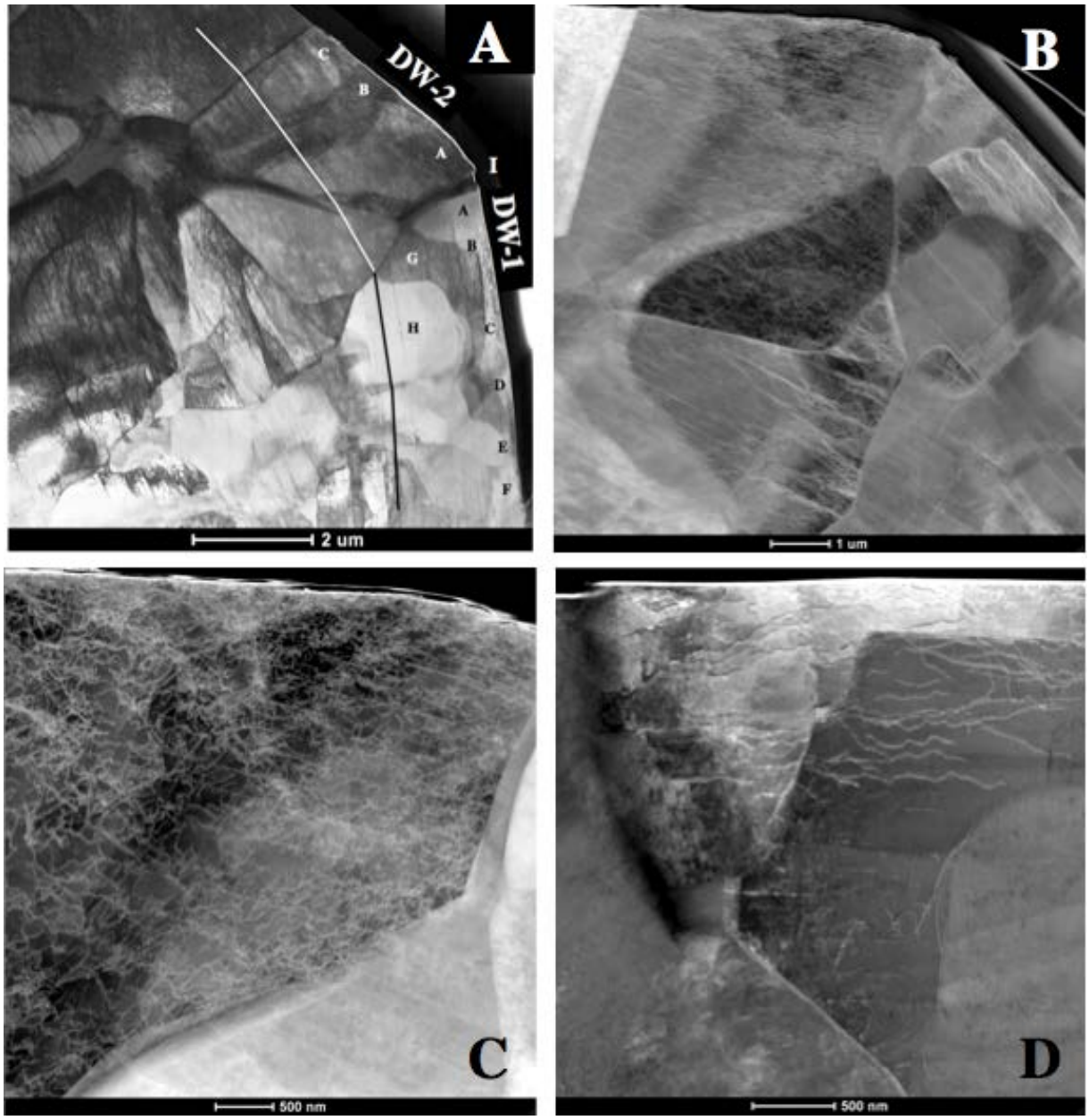

Figure 48. Dislocation substructures under the primary initiation site (DW-1/DW-2) on the fracture surface

Figure 49 shows the dislocation substructure under the SIS. Unlike the grains at the primary initiation site, the faceted grains at the SIS are generally free of subgrains. The three grains shown in figure 49(a) show evidence of slip on multiple systems. It is clear the slip in B1 occurs by the <1123> $\{10\bar{1}1\}$ slip on one primarily pyramidal plane (see figure 49(b), top) and by <a> slip on pyramidal planes. A single <a>(0001) slip band is observed near the boundary of the third grain. As only about a micron of the grain is captured in the foil, it is possible that basal slip bands appear at other locations in the part of the grain on the other side of the crack. As is the case for DW-1, <c+a> densities are increased near the fracture surface and the initiation boundary "I" (see figure 49(b), bottom). Slip in B2 occurs by slip on at least three systems (see figure 49(c)): <1123>slip

on one primary $\{10\bar{1}1\}$ plane (bands running from top to lower right), <a> slip on the basal plane (horizontal bands), and <a> slip on one prismatic plane (bands running from top center to lower left). With decreasing distance from "I", the densities of <c+a> dislocations, $\{10\bar{1}1\}$ slip bands, and (0001) slip bands increase. As is the case for the other facets investigated, <c+a> dislocation density is highest near the fracture surface (see figure 49(d)). The third grain shows evidence of double-prism slip (i.e., <a> slip on two prism planes) and <c+a> slip.

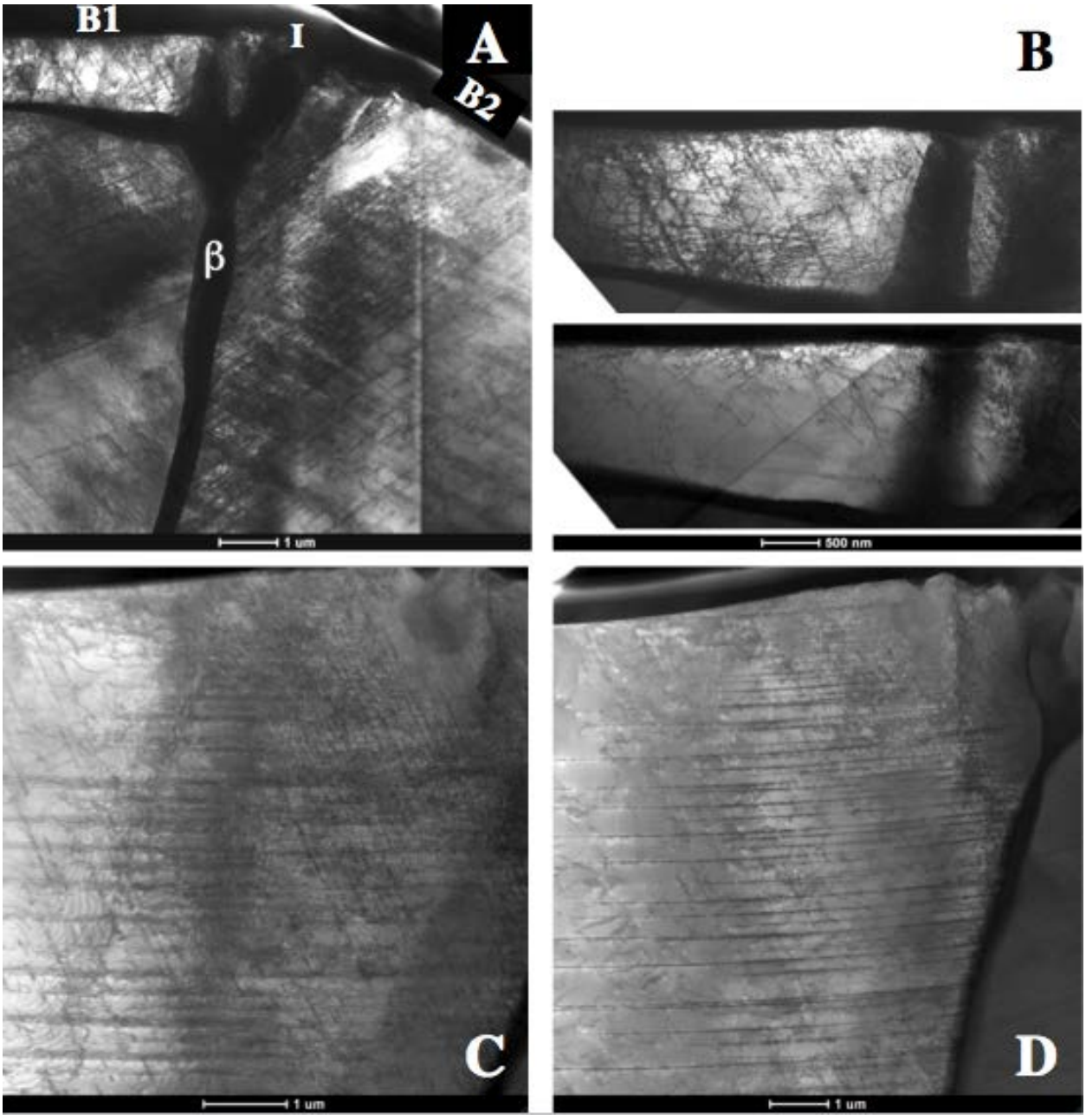

Figure 49. Dislocation substructures under the SIS (B1/B2) on the fracture surface

In general, crack plane traces did not lie parallel to basal plane traces—this was obvious when imaging parallel to (0002). With the exception of a section near subgrain "E" in DW-1 (see figure 48(a)) on the side of the grain opposite "I", the crack plane was found to deviate from (0001) by several degrees or more. Much higher deviations were noted for the orthogonal facets compared with the smooth, glassy facets (B1). The crack plane was observed to deflect at subgrain boundaries in both the inclined and orthogonal facets. Larger subgrain misorientations were qualitatively correlated to larger crack deflection. Crack arrest and crack deflection ridges seen on the surfaces of rough facets DW-2 and B2 (see section 2.2.3 for high-resolution SEM images of these markings) were associated with subsurface strain contours made visible by changes in local deviation parameter under two-beam conditions (marked by arrows in figure 50). Dislocation density at arrest/deflection markings is increased, demonstrating that local plastic flow allows for their formation. Taking the depth of local distortions as a measure of plastic zone size, it can be estimated that crack tip plasticity in DW-2 extends <200 nm below the surface close to "I", implying that this fracture process is highly localized even at crack lengths less than a grain diameter. Interestingly, plastic zone size decays with crack length; strain zones of <100 nm were measured below DW-4. In B2, crack tip plasticity extends ~1 μm below the fracture surface near "I" and also appears to decay with crack length (see figure 50). The difference in plastic zone size between DW-2 and B2 in regions close to "I" can be attributed to differences in crack mode; it is expected that the crack growing into B2 (and into DW-1) is driven in large part by mode II loading, whereas the crack in DW-2 (and B1) is driven mostly by mode I with a smaller mode II component. Such small plastic zone sizes are not surprising given the small crack length at this stage of growth; however, it is somewhat unexpected that they decrease with increasing crack length.

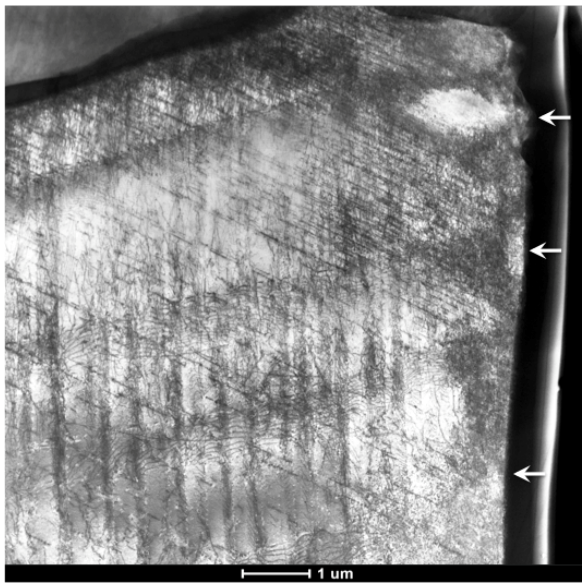

Figure 50. Strain contours under facet B2 corresponding to points of crack arrest on the fracture surface (denoted by arrows)

To further investigate this phenomenon, a foil was extracted at a crack length of ~2mm. The dislocation structures under the PF are similar to those under the other facets (see figure 51). Multiple slip on <1123> $\{10\bar{1}1\}$ and <a>(0001) systems is observed, and, similar to DW-2, the grain shows a high density of <c+a> dislocations. Given the similarity in the crystal orientation of

the grain containing the PF to the grain containing DW-2, this result is not unexpected. Basal slip traces indicate that the crack plane is inclined significantly to the basal plane (i.e., >10^{o}) like the other facets. Close examination of the strain contours associated with surface ridges indicates that the strain contours at long crack lengths are <50 nm deep (see figure 52). This observation confirms the trends observed and indicates that dwell cracks do not blunt with increasing crack length as long as crack extension occurs by faceted growth. Furthermore, these observations suggest that dwell cracks sharpen with increasing crack length. The mechanisms of sharpening are, at this point, not well understood.

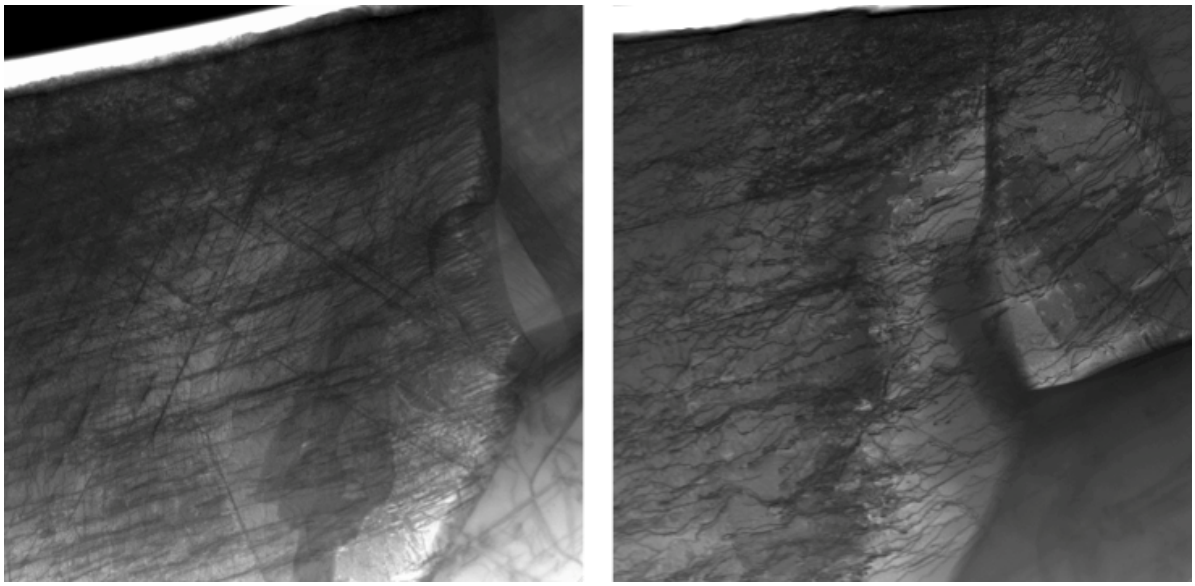

Figure 51. Dislocation substructure under the PF (grain on left side of images)

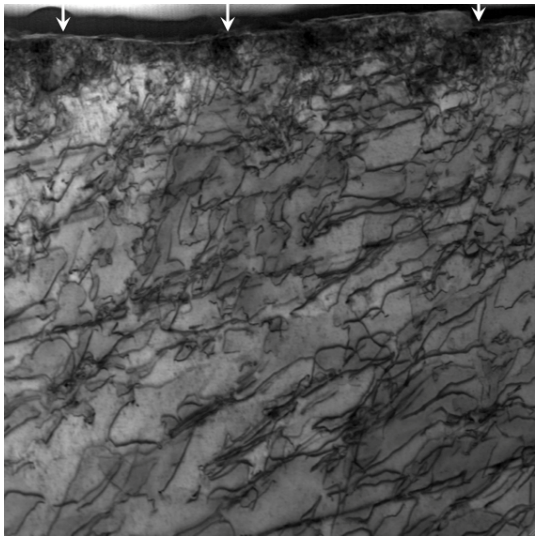

Figure 52. Strain contours under the PF corresponding to points of crack arrest on the fracture surface (denoted by arrows)

2.3 IN-SITU MEASUREMENT OF CRYSTAL STRESS STATES IN DEFORMING POLYCRYSTALS BY HIGH-ENERGY X-RAY DIFFRACTION

The nature of the dwell-fatigue phenomenon in titanium alloys makes it challenging to understand by macroscale testing and postmortem fracture analyses. It is known that dwell-fatigue cracking is driven by local, internal processes at boundaries between grains that are unable to communicate slip, and these testing methods do not allow for the direct interrogation of the internal stress states that drive crack initiation and propagation. The advancements in modeling capabilities that have been realized during the course of this project require the development of more sophisticated experimental analyses for the validation of model predictions. Model validation requires site-specific measurements of the full 3D stress states that lead to cracking; this is best accomplished by the in-situ loading of polycrystalline alloys.

2.3.1 High-Energy X-Ray Diffraction Capabilities and Techniques

High-energy x-rays (E>30 KeV) provide an effective means for the interrogation of polycrystalline engineering materials because they are capable of penetrating several millimeters of material. High-energy x-ray diffraction microscopy (HEDM) techniques have the following clear advantages over current technologies that have been applied to the study of deformation, including neutron diffraction, surface strain mapping, and EBSD:

- Spatially resolved orientation mapping within bulk materials—Unlike EBSD/OIM, orientation mapping by HEDM is nondestructive. Large volumes (tens of cubic millimeters) can be mapped in short times (<100 hrs) with ~1 μm spatial resolution, without the application of tedious serial sectioning techniques.
- In-situ (4D) spatially resolved orientation and strain mapping within bulk materials—The nondestructive aspect of HEDM is ideal for in-situ studies. High-spatial resolution maps of large volumes of material can be generated as a function of time (i.e., studies focused on creep straining, crack growth, grain growth, and structural evolution) or plastic strain (i.e., studies focused on strain partitioning on the subgrain scale). As x-ray diffraction techniques allow for the extraction of the full-strain tensor (unlike EBSD, which allows for the extraction of 6–9 strain tensor components at best), the stresses associated with local (i.e., subgrain scale) processes within internally situated grains may be measured.
- High-resolution, spatially resolved orientation and lattice strain mapping—Unlike neutron diffraction (a technique in which lattice strain measurements are averaged over the entire volume of a polycrystalline aggregate), HEDM techniques allow for the quantification of lattice strains averaged over the volumes of single grains. Furthermore, HEDM, unlike EBSD, provides subdegree measurements of absolute grain orientation even in highly strained materials. Current analysis techniques allow for absolute lattice strain measurements with a resolution of ~10^{-4}. This resolution is in excess of that accessible by EBSD and is sufficient for high-fidelity measurements of the elastic modulus in many engineering alloys.
- Dynamic, in-situ orientation and lattice strain mapping—HEDM techniques allow for the rapid acquisition of data in large volumes of material compared with 3D EBSD or neutron diffraction. Full-strain tensor measurements for each grain in an aggregate of ~1,000 grains can be obtained in approximately 1 minute. The speed of data acquisition allows for the in-situ quantification of dynamic processes in 5D (x,y,z,t, σ/ε).

- In-situ high-resolution orientation mapping within single grains—HEDM techniques are easily extended to the interrogation of single grains with exceptionally high angular resolution (< 0.01^{o} in all directions). The 3D reciprocal space mapping allows for the detailed characterization of strain and orientation gradients at resolutions inaccessible by other techniques.

HEDM techniques provide detailed information on microstructural scales that are readily useable by finite element (FE) and CPFE models. The data derived from HEDM studies have the potential to be extended seamlessly to the study of deformation, crack initiation, and fracture in engineering materials.

2.3.2 Application to In-Situ Loading of α-Ti-7Al

Two HEDM methods were applied to the examination of deformation of the Ti-7Al alloy discussed in section 2.2.2. This alloy was chosen because of the simplicity of its microstructure (i.e., single phase α) and its high sensitivity to dwell loading (dwell debit greater than 50). Furthermore, dwell sensitivity of the alloy can be tuned by controlling the degree of slip planarity. Therefore, two microstructural conditions (AC and IWQ) were investigated to observe potential differences in strain partitioning in the microstructure. The first round of experiments was performed in-situ but not under dynamic-loading conditions; load was increased incrementally, and diffraction data were acquired at a limited number of points. Several important points from this study are outlined here: First, the grain averaged stress states on individual grains are not uniaxial. Although grains undergo small physical rotations (~1^{o} per 1% strain), grain-average stress states deviate more significantly. An example of stress state rotation for four grains at four different loads is shown in figure 53, in which the orientation and values of the principle stresses are plotted on jacks. The tilt and rotation of a jack gives an indication of orientation of the stress state relative to the macroscopic sample directions: LD, transverse direction (TD), and ND. The six arms of the jacks represent the principle stresses and are color-coded to indicate the magnitude and sense of the stress. For reference, a jack displaying a uniaxial stress state would show no tilt or rotation and a single set of arms (i.e., those along LD would be colored according to the macroscopically applied load). Measurements at the first load (395 MPa) were taken prior to plastic deformation. It can clearly be seen that stress state non-uniaxiality develops under nominally elastic loads; the jack of each grain shows some tilt and/or rotation, and the arms closest to the ND-TD plane develop non-zero stresses (i.e., are colored). As deformation proceeds, 595 MPa and 630 MPa, stress states rotate significantly and become much more triaxial in nature. These changes are due to both elastic and plastic deformation; however, it can be seen by comparing the jacks after unloading to 400 MPa that the contribution of plastic deformation is dominant.

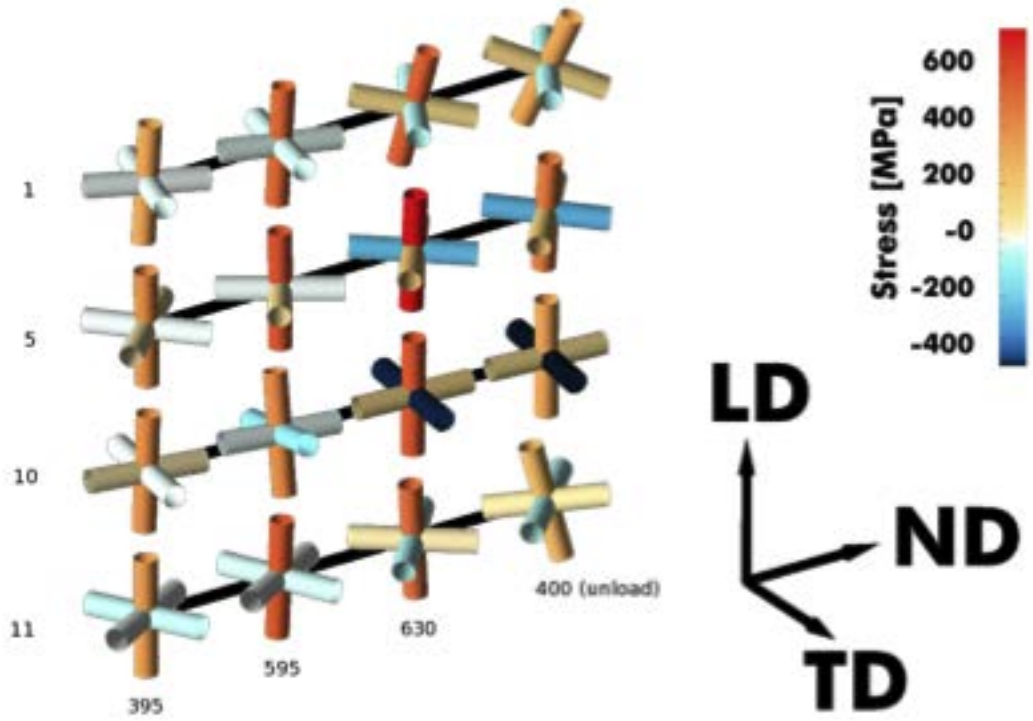

Figure 53. Principal axis jacks depicting the orientation of the principal stress state at four indicated macroscopic stress levels (in MPa) for four grains in the polycrystalline aggregate

The second notable result is that Schmid factor (SF) assumptions based on the macroscopically applied load are poor assumptions. It is necessary to resolve the full stress tensor, not the macroscopic stress tensor, onto individual slip systems to measure the shear stress applied on a given system. This is observed in figure 54 where the resolved stresses for <a>(0001) slip are plotted for a single grain. Errors in the estimations of resolved stress are particularly large if the grain has undergone slip on the slip system onto which the stresses are resolved. This can be seen by comparisons of the RSSs on [$\underline{1}2\underline{1}0$](0001) and [$2\underline{11}0$](0001) (i.e., the green and blue lines, respectively). As indicated by the drop in the dotted RSS line between 595 MPa and 630 MPa, the crystal has deformed by [$\underline{1}2\underline{1}0$](0001) slip. After the point of yield, the RSS derived from the grain-averaged stress state (i.e., ~130 MPa at the applied load of 630 MPa) is ~60% less than that derived from the uniaxial stress state (i.e., ~220 MPa). In contrast, errors are much smaller if the slip system has not yielded, as is the case for the [$2\underline{11}0$](0001) system.

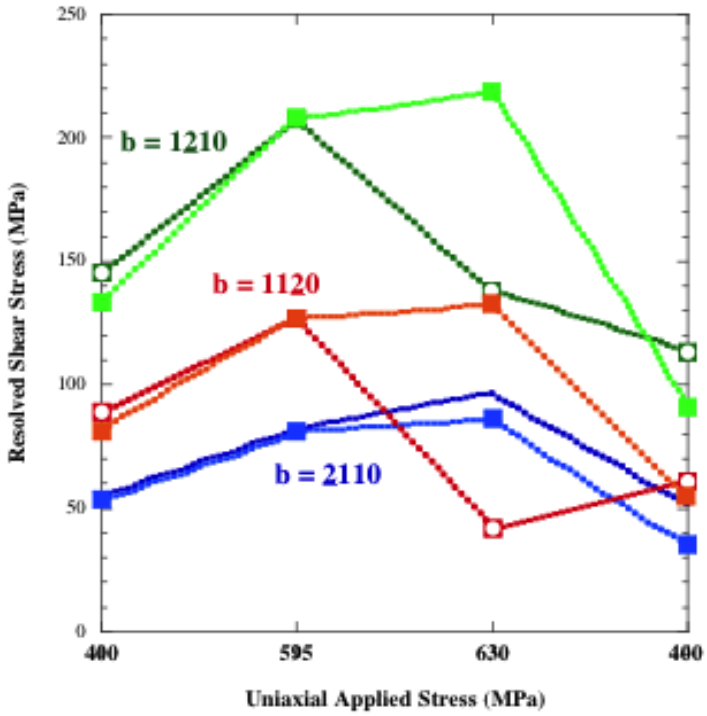

Figure 54. RSSs for basal slip of the AC grain as a function of the applied load. The values were calculated assuming a uniaxial stress state (filled squares and solid lines) and using the full stress tensor (empty squares and dashed lines)

Given that much greater amounts of accumulated plastic strain are observed under dwell fatigue than under continuous cycling, simple SF rules cannot be applied to the analyses of fracture surface features.

The third notable result is that grains, as a result of plastic deformation, split into subgrain-like domains. This can be seen in a single-grain orientation distribution function (ODF) and directional projections presented in figure 55. The origin of these subgrain-like domains is not yet completely clear; however, extensive TEM analyses have shown that they are not the result of the formation of classic subgrains as might be observed in FCC metals. In the case of the single-grain ODF in figure 55, <c+a> $\{10\bar{1}1\}$ slip is the only mechanism active in the grain, and dislocation densities are relatively uniform throughout the grain volume. The non-uniformity of reciprocal space distributions gives rise to anisotropic strain broadening, which is governed by the specific nature of dislocation populations present and their distribution throughout the grain. In principle, dislocation densities can be derived from the integration of diffraction peak intensities; however, the results at hand clearly demonstrate that such an exercise is non-trivial. One-shot estimates of dislocation densities can only be measured at diffraction spots close to the axis of rotation of the grain.

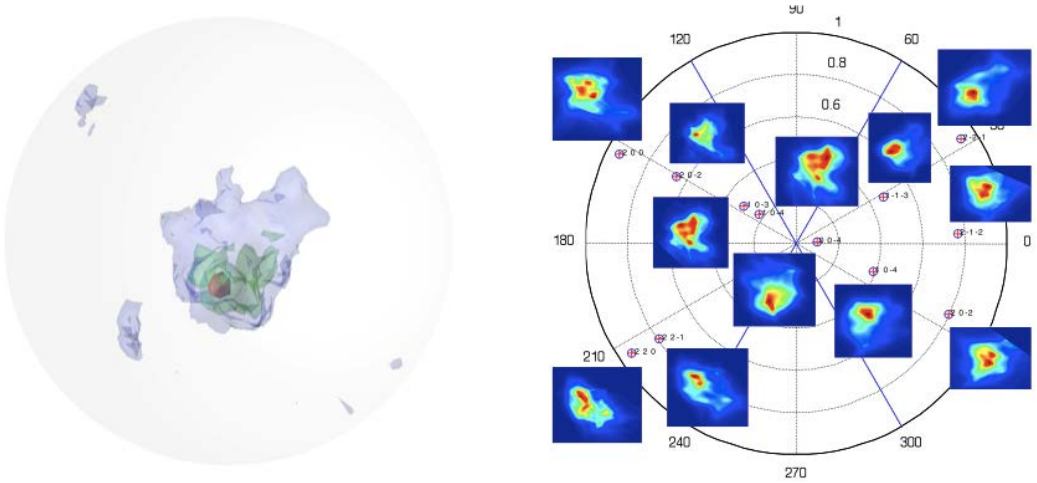

(a) (b)

Figure 55. 3D ODF (2º diameter) for a single grain after deformation to ~1.5% plastic strain (a) and 2D projections of the ODF along specific crystallographic directions (b)

A second round of in-situ experiments was conducted on the Ti-7Al alloy (IWQ and AC conditions) under dynamic-loading conditions. In these experiments, the stress state development of ~700 grains in each sample were tracked continuously during monotonic loading at 10^{-5} s^{-1}. The number of grains tracked in these experiments provides the ability to measure single-crystal like properties (elastic tensor, yield/flow stresses, orientationally dependent hardening, strain-rate sensitivity) in a polycrystalline aggregate. For instance, the grain-averaged stress tensors can be resolved onto each slip system at each point on the stress-strain curve. Therefore, a plot similar to that schematically illustrated in figure 56 can be extracted for each slip system in each grain; as drawn, the trends in an RSS-stress plot due to the loading of a slip system can take several forms. If the slip system has a reasonably high SF but does not yield, RSS should increase nearly linearly with uniaxial stress (red line) if the grain does not undergo large stress state rotations. Alternatively, a slip system with a small SF may display the behavior sketched by the green line, where RSS saturates at a level well below yield. In cases where yield is observed (blue and orange lines), RSS initially varies linearly with uniaxially applied stress but saturates or drops after yield.

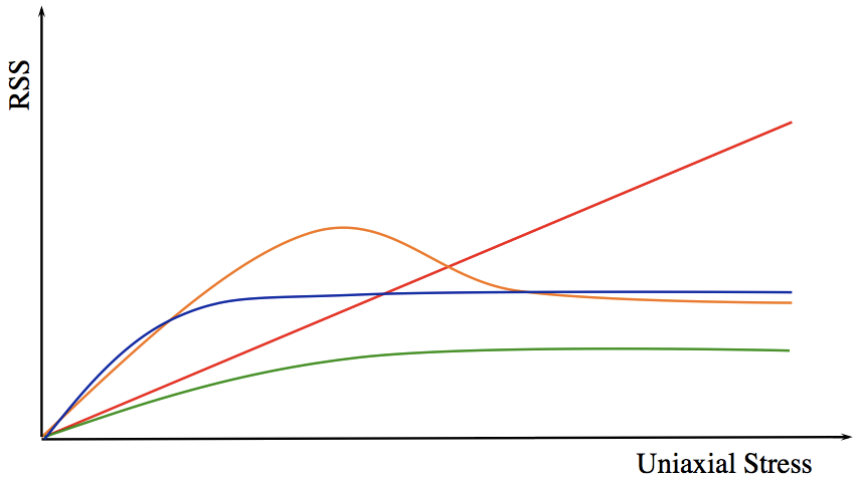

Figure 56. Schematic illustration of the evolution of RSS for a single-slip system in a single grain as a function of macroscopically applied uniaxial stress

As these data are collected for every slip system at every load step, the RSSs for all grains and for each slip system can be quantified and statistically analyzed. Such an analysis is presented in figure 57 for a single-load step at a uniaxial stress close to macroscopic yield, ~650 MPa. Here, the RSSs for each basal, prism, and <1123> $\{10\bar{1}1\}$ slip system for each grain, in a volume containing ~700 grains, are plotted according to their frequency. The interpretation of these plots is relatively straightforward. After a slip system yields, the RSS on that system cannot increase; therefore, a sharp edge develops in the histogram at the stress equal to the single-crystal, single-slip flow strength. Sharp edges develop in the case of the prismatic and basal slip systems but not the <1123> $\{10\bar{1}1\}$ systems because of the texture of the alloy. In the test orientation, ~1 in 200 grains (less than 10 total grains) had their [0001] aligned within 15° of the tensile axis; therefore, very few grains had the opportunity to deform by <c+a> slip at a uniaxial stress close to the macroscopic yield stress. As plastic strain in the material (and uniaxial stress) increased and stress states rotated, deformation by <c+a> slip became necessary, and a sharp edge could be observed in the histogram. A full picture of the slip systems active in the aggregate can be generated at each load step along the stress-strain curve. As the number of grains deforming on a given slip system increases, a peak forms around the CRSS of that system; such a peak has begun to form in the case of the <a> $\{10\bar{1}0\}$ systems.

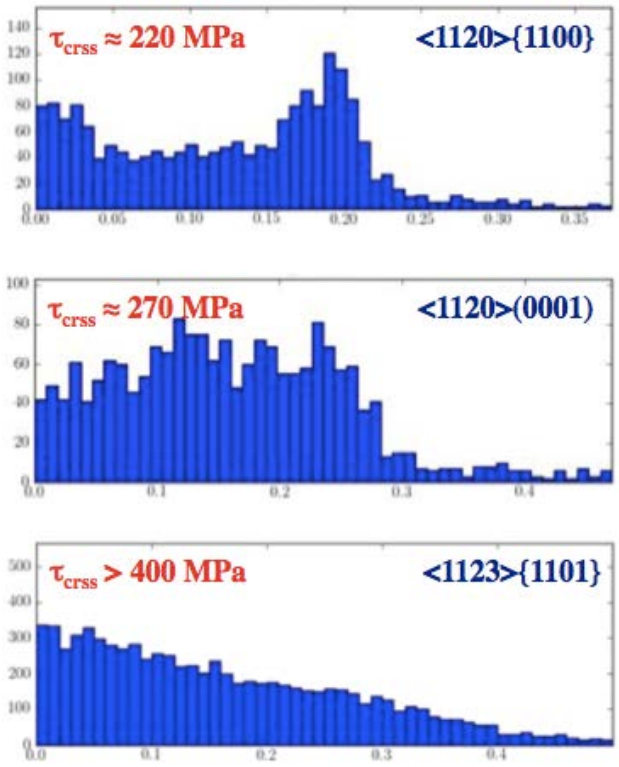

Figure 57. Histograms illustrating the distribution of RSS on each of the slip systems in each grain in a volume containing ~700 grains

More extensive data can also be extracted from the diffraction data. For instance, streak analyses can be applied to diffraction spots of each grain as more than ~40 spots are recorded for each grain at each load step. Diffraction spots removed from the rotation axis of the grain tend to streak in rational directions (see figure 58). The direction of streaking is indicative of the type and frequency of slip events occurring within the grain; therefore, these data can be subsequently compared with the RSS-stress trends to determine the relative activity of specific slip systems as a function of uniaxial load. These data can be analyzed on a statistical basis to gain insight into the behaviors of the aggregate. Moreover, diffraction spot analyses will be invaluable for the detection of cracks. The application of the diffraction data is not limited to statistical treatments because they may also be used to interrogate specific grain environments because they contain spatial information. For example, the effects of grain neighborhood on the stress state development and yield of a given grain can be quantified in great detail.

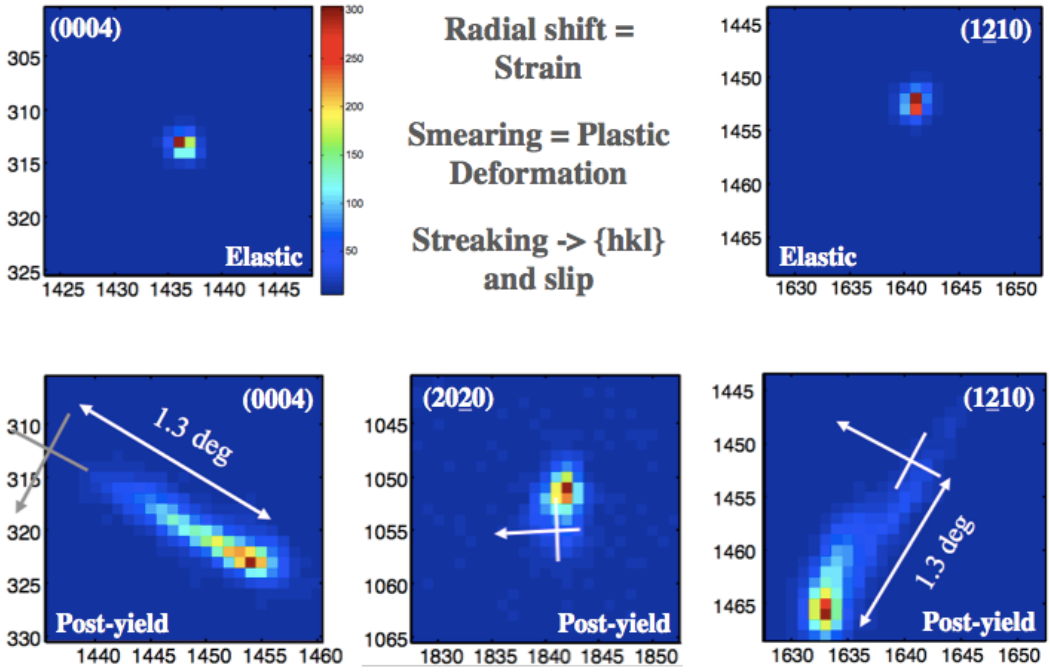

Figure 58. Example of diffraction spot streaking due to plastic deformation; the direction and degree of streaking/smearing is directly related to slip activity within the grain

3. CRYSTAL PLASTICITY FEM BASED MODELING AND SIMULATION OF TI-6242

In this task, the four following major accomplishments have been achieved:

1. CPFEM for Ti-6242—A system of integrated, experimentally validated, computational models for establishing microstructure-property relations with respect to dwell-fatigue behavior for Ti-6242 was developed. This system has coupled advanced techniques in material characterization and image analysis as well as image-based micromechanical modeling of polycrystalline aggregates for analyzing mechanical response and fatigue failure.
2. Dwell-fatigue crack nucleation criterion for Ti-6242—A material microstructure-based detailed mechanistic model for fatigue crack nucleation was developed in this module. This model is at the length scale of individual grains and is set for each hard grain-soft grain combination in the polycrystalline aggregate.
3. Homogenization-based macroscopic anisotropic plasticity model for titanium alloys—To incorporate the findings of the crystal-plasticity model in macroscopic constitutive and fatigue models that can be incorporated in general purpose FEM codes, methods of homogenization were conducted with the CPFEM results. This consisted of a systematic sensitivity analysis to retain important variables in the functional dependence equations. Finally, homogenization of the microscopic variables was conducted to develop macroscopic material and damage laws.
4. Macroscopic crack nucleation model for Ti-6242—This module has developed a homogenization-based damage-initiation model for macroscopic (structural scale) analysis of titanium-based alloys. The damage model is based on the crack initiation at the micro or polycrystalline scale and incorporates functional dependencies between stresses and

microstructural parameters, such as orientation (SF), misorientation, and grain sizes. The novelty of such damage surfaces is that they are completely based on the physics of the microstructure and are not phenomenological like other models.

The developments pertaining to these topics are detailed in sections 3.1–3.4.

3.1 CPFEM FOR TI-6242

The plastic part of the crystal plasticity equations involves a combined effect of slip on multiple slip systems. The plastic slip rate $\dot{\gamma}^{\alpha}$ on the α^{th} slip system has a power law dependence on the resolved shear stress (τ^{α}) and the slip system deformation resistance (g^{α}), which is given as:

$$\dot{\gamma}^{\alpha} = \dot{\gamma}_0 \left| \frac{\tau^{\alpha} - \chi^{\alpha}}{g^{\alpha}} \right|^{1/m} sign(\tau^{\alpha} - \chi^{\alpha}) \tag{6}$$

Here, *m* is the material rate sensitivity parameter, $\dot{\gamma}_0$ is the reference plastic shearing rate, and χ^{α} is the back-stress that accounts for kinematic hardening in cyclic deformation [68]. The evolution of the slip system deformation resistance is assumed to be controlled by both statistically stored dislocations corresponding to homogenous plastic deformation and GND that accommodate the incompatibility of the plastic strain field. This is expressed as:

$$\dot{g}^{\alpha} = \sum_{\beta} q^{\alpha\beta} h^{\beta} |\dot{\gamma}^{\beta}| + \frac{k_0 \alpha^2 G^2 b}{2(g^{\alpha} - g_0^{\alpha})} \sum_{\beta} \lambda^{\beta} |\dot{\gamma}^{\beta}| \tag{7}$$

where h^{β} in the first term of equation 7 is self-hardening rate, and $q^{\alpha\beta}$ is a matrix describing the latent hardening. The second term accounts for the effect of GNDs on the work hardening [75], in which k_0 is a dimensionless material constant, *G* is the elastic shear modulus, *b* is the Burgers vector, g_0^{α} is the initial deformation resistance, and α is a nondimensional constant taken to be $\frac{1}{3}$ in this work. λ^{β} is a slip plane lattice incompatibility measure that can be expressed for each slip system as a function of slip plane normal ($\boldsymbol{n}^{\beta}$) and another incompatibility tensor ($\boldsymbol{\Lambda}$) as:

$$\lambda^{\beta} = (\boldsymbol{\Lambda}\boldsymbol{n}^{\beta} : \boldsymbol{\Lambda}\boldsymbol{n}^{\beta})^{\frac{1}{2}} \tag{8}$$

The dislocation density tensor $\boldsymbol{\Lambda}$, introduced by Nye [76], is a direct measure of GND density. Nye's tensor can be expressed using the curl of plastic part of the deformation gradient tensor

$\mathbf{F}^P$. As this crystal plasticity formulation does not explicitly incorporate a dislocation density tensor, it is indirectly extracted from the CPFE output data as:

$$\mathbf{\Lambda} = \nabla^T \times \mathbf{F}^p \tag{9}$$

3.1.1 Homogenized Equivalent Model of the Transformed β Colony

The explicit modeling of the transformed β region is computationally prohibitive; therefore, a simpler model capable of representing the essential features of Ti-6242 behavior was developed for use in polycrystalline simulations. The β phase region is homogenized, and an equivalent region containing both HCP and BCC slip systems at the same point is considered. The two phases (at the same point) are subject to the macroscopic strain that is present at that point. As a result, the morphology of the β region can be represented using a single element. The stress response of the two phases is computed separately using a crystal plasticity model. The final macroscopic stress response at the point is computed as a weighted average of HCP and the BCC responses based on their volume fractions.

In this model, the volume fractions are taken to be 0.88 and 0.12 for the α and β phases, respectively. The model accommodates for the tension-compression asymmetry observed, with the crystal plasticity properties associated with a slip system chosen based on the sign of the hydrostatic stress. A combination of microtesting, OIM, computational simulations, and minimization processing is implemented in this study for careful characterization and calibration of material parameters [77].

3.1.2 Grain Size Effects in the CPFEM

The effect of microstructure size on the mechanical response of two-phase polycrystalline Ti-6242 alloy was studied as part of this research [78, 79]. The model developed quantifies the dependence of grain and lath sizes and slip-system deformation resistance of individual slip systems in a rate-dependent anisotropic elastic-crystal plasticity constitutive model. The initial slip system deformation resistances in the crystal plasticity relations are expressed as Hall–Petch type relations. Three different characteristic lengths (i.e., colony size, α lath thickness, and β lath thickness) are used to incorporate the size effect in the transformed β-phase, whereas the size effect in the primary α region is characterized by its grain size alone. Different slips are grouped as soft and hard slip modes depending on the nature of slip transmission, and the characteristic length for each slip system is defined accordingly. The slip-system deformation resistance of individual slip systems is obtained from the values calibrated from corresponding single-crystal and single-colony experiments. The accuracy of the size-dependent model for polycrystalline Ti-6242 is established by comparing the simulation results for constant strain rate and creep tests in tension and compression with experiments.

The validated model is then used to understand the effects of grain size on the load shedding between grains, which result in high-stress gradients at the interface. To understand this phenomenon, the load-shedding response is simulated in creep for various combinations of hard and soft grain sizes. It can be observed that a change in the size of hard grains does not significantly change the load-shedding response because the size-effect contribution to the slip-system

resistance is small compared to its initially high value. However, a change in the size of the soft grains considerably changes the peak stress due to load shedding.

The size-dependent crystal-plasticity model established in this research has the capability to quantify the effects of various microstructural parameters and can be used for further study of critical combinations of these parameters that would result in localized fracture in Ti-6242 microstructures under dwell-fatigue loading.

3.2 DWELL-FATIGUE CRACK-NUCLEATION CRITERION FOR TI-6242

3.2.1 Model Description

Traditionally, fatigue-life prediction models have used macroscopic parameters, such as applied stresses, cyclic frequency, loading waveform, hold time, and statistical distributions of fatigue life and fatigue strength. However, predictions of these widely used models can suffer from significant scatter. This is primarily because of the absence of robust underlying physical mechanisms and information on the material microstructure in their representation. Morphological and crystallographic characteristics of the microstructure (e.g., crystal orientations, misorientations, and grain size distribution) play significant roles in the mechanical behavior and fatigue failure response.

In this research, a material microstructure-based detailed mechanistic model for fatigue crack nucleation was developed. This model is at the length scale of individual grains and is set for each hard grain-soft grain combination in the polycrystalline aggregate. It is non-local; whereas crack nucleates in the hard grain because of load-shedding, it is affected by plasticity in the neighboring soft grains due to dislocation pileups at grain boundary barriers. The intergranular crack nucleation model is built on the premise that a wedge crack nucleates in the neighboring grain as a dislocation approaches the grain boundary. An edge dislocation, which is an extra half plane of atoms wedged between two complete planes, is equivalent to a microcrack with opening displacement of one atomic spacing b. As more dislocations are piled up, the opening displacement increases in size (see figure 59(a)). The crack opening displacement corresponds to the closure failure along a circuit, surrounding the piled-up dislocations. If n edge dislocations of Burger's vector, b, contribute to the formation of a microcrack, a wedge with opening displacement $B = nb$ is produced. It should be noted that, as the dislocations are piled up at the grain boundary of a soft grain, the wedge crack initiates in the adjacent hard grain (see figure 59(b)).

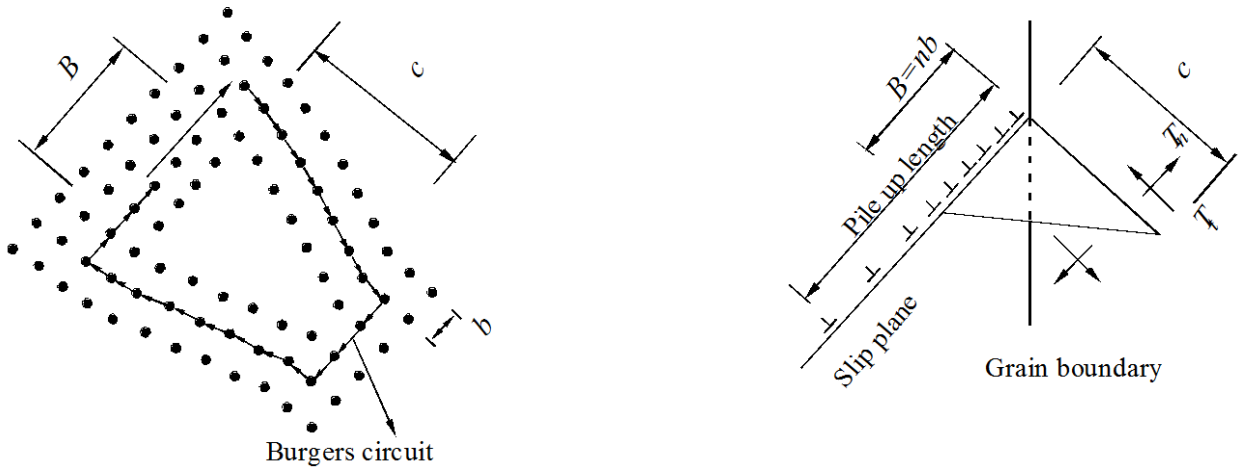

(a) (b)

Figure 59. A wedge crack with opening displacement of 4b, produced by coalescence of four dislocations (a); and nucleation of a wedge crack in the hard grain resulting from a dislocation pileup in the soft grain (b)

The microcrack length, *c*, can be considered to be the length after which the disturbance in the lattice structure of the hard grain subsides. This disturbance is caused by extra half planes of atoms in the soft grain. The equilibrium length of a wedge crack with an opening displacement, *B*, is related to the elastic properties and surface energy, γ_s, in [27] as:

$$c = \frac{G}{8\pi(1-\upsilon)\gamma_s} B^2 \tag{10}$$

where υ is the Poisson's ratio, and *G* is the shear modulus.

The wedge crack is initially stable. As more dislocations enter the crack, the crack opening size increases and, therefore, the crack length also increases. However, the applied stress across the microcrack, which is associated with the hard grain, will also help open up the crack. The acting stress on the microcrack surface is a combination of normal and shear stresses (see figure 59(b)). The microcrack becomes unstable when the mixed-mode stress intensity factor, K_{mix}, exceeds a critical value, K_c. K_{mix} is expressed in terms of normal stress intensity factor, K_n, and shear stress intensity factor, K_t, as:

$$K_{mix} = K_n^2 + \beta K_t^2 \tag{11}$$

β is a shear stress factor, which is used to assign different weights to the normal and shear traction components for mixed mode. It is defined as the ratio of the shear to normal fracture toughness of the material, (i.e., $\beta \approx K_{nc} / K_{tc}$) [80].

Using the definitions for stress intensity factors, $K_n = \langle T_n \rangle \sqrt{\pi c}$ and $K_t = T_t \sqrt{\pi c}$, and noting that the microcrack grows when $K_{mix} \geq K_c$, the hard grain crack nucleation criterion, ahead of dislocation pileups in adjacent soft grain is stated as:

$$T_{eff} = \sqrt{\langle T_n \rangle^2 + \beta T_t^2} \geq \frac{K_c}{\sqrt{\pi c}} \tag{12}$$

or equivalently:

$$R = T_{eff} \sqrt{c} \geq R_c, \text{ where } R_c = \frac{K_c}{\sqrt{\pi}} \tag{13}$$

T_{eff} is an effective stress for mixed-mode crack nucleation. The stress component normal to the crack surface is given as $T_n = n_i^b (\sigma_{ij} n_j^b)$, in terms of the Cauchy stress tensor σ_{ij} and the components of unit outward normal to the slip plane n_i^b. Only the tensile normal stress $\langle T_n \rangle$, represented by the McCauley bracket $\langle\ \rangle$, contributes to the effective stress because compressive stresses do not contribute to crack opening. The shear stress component T_t is obtained by the vector subtraction of T_n from the stress vector on the plane (i.e., $T_t t^b = T - T_n n^b$ where t^b is the unit vector tangent to the plane). It should be noted that the stress components in equation 12 are remote applied stresses. The typical values of *c*, which give rise to an unstable cracking, are of the order of nanometers, whereas the typical grain size is of the order of microns. Therefore, it is reasonable to consider the maximum stress at the grain boundary of the hard grain as the remote stress.

R_c is a parameter that depends on the material elastic properties and on the critical strain energy release rate, $\mathcal{G}_c$. It has the units of stress intensity factor ($\mathrm{MPa}\sqrt{\mathrm{im}}$). A value of $\beta = 0.7071$ suggested for Ti-64 alloys in [81] is used in this study. Sensitivity analysis with different values of β indicate that T_{eff} is not very sensitive to β for <*c*+*a*> oriented hard grains, since $T_n >> T_t$. As more dislocations are added to the pileup with time, the wedge-crack opening displacement and length increase. This implies that a smaller T_{eff} is needed to initiate a crack with increasing plastic deformation and pileup. This contributes to the non-locality aspect of the crack nucleation criterion.

3.2.2 Numerical of the Crack Nucleation Criterion

This section describes a method for calculating microcrack opening displacement *B*, required in equation 10 to estimate the microcrack length. Crack nucleation is examined on different planes in the hard grain of the polycrystalline microstructure. For estimating *B*, it is necessary to know the distribution of dislocations inside the soft grain. The crystal-plasticity model discussed in section 4 does not explicitly have dislocation density as a state variable. Therefore, the plastic strains and their gradients that are available from the results of the CPFEM simulations are used to estimate the microcrack opening displacement *B*. The wedge opening displacement in figure 59(a) is equal to the closure failure along a circuit surrounding the piled-up edge dislocations on

one slip plane. This can be extended to a generalized 3D representation of dislocations for multiple slip systems. The corresponding closure failure, which is manifested as the crack opening displacement, is a vector quantity. In the dislocation glide model, the lattice incompatibility can be measured by the closure failure of a line integral along a Burgers circuit $\bar{\Gamma}$ in the intermediate configuration. Closure failure is equivalent to the net Burgers vector **B** of all dislocations passing through the region $\bar{\Omega}$, bounded by the circuit. The Burgers vector can be mapped to a line integral along a referential circuit, Γ, using the plastic deformation gradient $\mathbf{F}^p$. Using Stoke's theorem, the closure failure is related to the surface integral of the curl of $\mathbf{F}^p$ over a referential surface Ω as:

$$\mathbf{B} = \oint_{\bar{\Gamma}} d\bar{\mathbf{x}} = \oint_{\Gamma} \mathbf{F}^p d\mathbf{X} = \int_{\Omega} \Lambda . \mathbf{n} d\Omega \tag{14}$$

where **n** is the unit normal to the surface and Λ is the Nye's dislocation tensor given in equation 4. Components of Λ are evaluated at each quadrature point using shape-function-based interpolation of nodal values of $\mathbf{F}^p$ [82].Consider a point *A* on the hard-soft grain boundary, shown in figure 60(a), which impedes dislocations generated from a source in the soft grain. There are different planes with different normal vectors that contain point *A*. The closure failure caused by dislocations piercing each of these planes depends on the normal, **n** based on equation 14. The stresses on each of the resulting microcracks are also different. Consequently, there are different possible competing microcracks with dissimilar stress intensity factors at point *A*. The crack with the highest mixed-mode stress intensity factor is considered the critical one. If the unit normal to the unit area surrounded by a Burgers circuit containing point *A* in figure 60(a) is denoted by **n**, the size of crack opening displacement *B* is calculated using equation 14 as:

$$B = \left\| \Lambda . \mathbf{n} \right\| \tag{15}$$

This is used in equation 10 to estimate the crack length *c*. Neglecting the effect of screw dislocations on the wedge crack opening, the unit normal to the wedge crack surface is obtained as:

$$\mathbf{n}^b = \frac{\Lambda . \mathbf{n}}{B} \tag{16}$$

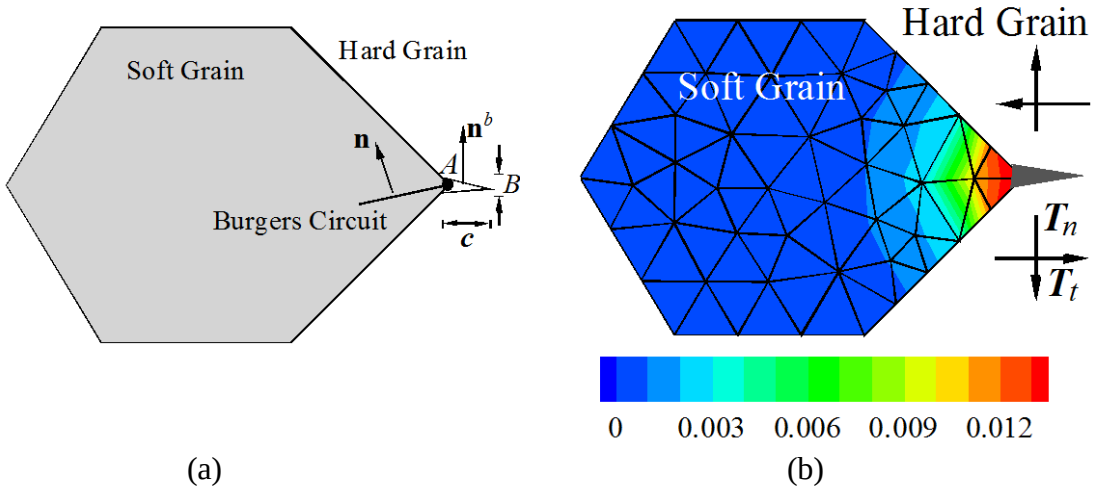

Figure 60. (a) Wedge-crack in the hard grain as a result of dislocation pileup in adjacent soft grain; (b) distribution of the norm of Nye's dislocation tensor inside a representative soft grain

The effective stress T_{eff} on the wedge crack surface is measured using the procedure described in section 2. The mixed-mode stress intensity factor that corresponds to the wedge crack produced by dislocations passing through the unit area surface with unit normal of **n** is obtained as:

$$K_{mix} = T_{eff}\sqrt{\pi c} \tag{17}$$

This procedure is executed for all possible **n** vectors in the 3D space. The vector $\mathbf{n}_{cr}$, which yields the highest stress intensity factor, is considered as the critical normal vector. The critical crack opening displacement at the hard-soft grain boundary is then obtained as $\mathbf{B}_{cr} = \boldsymbol{\Lambda}.\mathbf{n}_{cr}$. This relation is true when all dislocations are concentrated in a very small portion of the soft grain, surrounding the point *A*. However, dislocations are distributed in the entire soft grain. Figure 60(b) shows the contour of the norm of Nye's dislocation tensor inside a representative soft grain. The maximum value occurs at the hard-soft grain boundary (point *A*), and the values decrease with increasing distances from the grain boundary. $\boldsymbol{\Lambda}$ is available at the Gauss point of all the tetrahedron elements within the soft grain from the CPFE simulations. Each element *I* contains its own dislocations quantified by Nye's dislocation tensor $\boldsymbol{\Lambda}_I$ at that element. Dislocations associated with element *I* produce a crack opening displacement as:

$$\mathbf{B}_I = W_I A_I \boldsymbol{\Lambda}_I.\mathbf{n}_{cr} \tag{18}$$

Here, A_I is the surface area associated with element *I*, into which the dislocations penetrate. It is estimated through the assumption of an equivalent spherical domain that has the same volume as the element. The center of this sphere is assumed to coincide with the element integration point. Assuming that the plane containing the Burgers circuit in the element *I* passes through the integration point, A_I is equal to the circular cross-sectional area passing through the center of sphere expressed as:

$$A_I = \pi R_I^2 = 1.77(V_I)^{\frac{2}{3}} \text{ where } R_I = \sqrt[3]{\frac{3}{4\pi} V_I} \tag{19}$$

V_I is the element volume and R_I is sphere's radius. A weighting parameter W_I is introduced to B_I to account for the diminishing effect of a dislocation on the crack opening displacement with distance. Therefore, the crack opening displacement, *B*, accounting for the contribution of all elements in the soft grain on the hard grain crack, is stated as:

$$B = \|\mathbf{B}\| = \left\| \sum_I \mathbf{B}_I \right\| = \left\| \sum_I W_I A_I \boldsymbol{\Lambda}_I . \mathbf{n}_{cr} \right\| \tag{20}$$

Defining an effective dislocation tensor as:

$$\mathbf{D}_{eff} = \sum_I W_I A_I \boldsymbol{\Lambda}_I \tag{21}$$

equation 20 can be rewritten as:

$$B = \left\| \mathbf{D}_{eff} . \mathbf{n}_{cr} \right\| \tag{22}$$

Using equation 10 to relate the microcrack length to the crack opening displacement, *c* is estimated as:

$$c = \frac{G}{8\pi(1-\upsilon)\gamma_s} \left\| \mathbf{D}_{eff} . \mathbf{n}_{cr} \right\|^2 \tag{23}$$

The unit normal to the wedge crack surface in the hard grain is:

$$\mathbf{n}^b = \frac{\mathbf{D}_{eff} . \mathbf{n}_{cr}}{\left\| \mathbf{D}_{eff} . \mathbf{n}_{cr} \right\|} \tag{24}$$

The effective traction T_{eff} is updated using the procedure described in section 2 and $\mathbf{n}^b$ from equation 24. Finally, T_{eff} and *c* are used in equation 13 to calculate the effective nucleation variable *R*. *R* is checked for every grain pair in the CPFEM at the post-processing stage.

3.2.3 Parameter Calibration and Validation of the Crack Nucleation Criterion

Experimental data [7, 83] are used for calibrating and validating the proposed crack nucleation model. Experiments in [83] use three dog-bone specimens that are extracted from a Ti-6242 pancake forging provided by Ladish. The microstructure of these specimens has significant differences in crystallographic orientation, misorientation, and microtexture distribution. The dwell tests subject these specimens to cyclic loads with trapezoidal waveforms. Each load cycle has a maximum applied traction of 869 MPa (~ 95% of the macroscopic yield stress for the overall

material) at a hold time of 2 minutes and a loading/unloading time of 1 second. The *R*-ratio, measured as the ratio of the minimum to maximum loading amplitudes, is zero.

The specimens 1, 2, and 3 fail after 352, 663, and 447 cycles, respectively. Crack growth in specimens 2 and 3 is monitored through microradiographic images taken by interrupting the experiment every 15 cycles [7]. The primary crack initiates at 83% life (550 cycles) for specimen 2, whereas it nucleates at 85% life (380 cycles) for specimen 3. The results generally suggest that primary crack nucleation in dwell fatigue occurs in the range 80%–90% of the total number of cycles to failure.

Computer microstructures are reconstructed using methods developed in [84–86] from OIM images at a critical region of a dwell-fatigue crack tip in the material specimens. Statistical distribution functions of various microstructural parameters in the two-dimensional (2D) OIM scan are generated and stereologically projected in the third dimension for creating the three-dimensional (3D) statistics [84, 85]. The reconstructed 3D models have distributions of orientation, misorientation, microtexture, grain size, and number of neighbors that are statistically equivalent to those observed experimentally in the OIM scans. Subsequently, CPFEM of the statistically equivalent microstructures are developed for analyzing the behavior of the critical regions.

3.2.4 Calibration of R_c for α/β forged Ti-6242

The crack nucleation parameter R_c in equation 13 is calibrated from results of 2-minute dwell-fatigue CPFEM simulations of a critical microstructure of specimen 1. Experimental crack nucleation data are not available for this specimen. Therefore, crack nucleation is assumed at 282 and 300 cycles, corresponding to 80% and 85% of the total life of ~ 352 cycles, respectively. The variable *R* in the LHS of equation 13 is determined for all grain pairs at the end of 282 and 300 cycles, respectively. The hard grain with the maximum value of *R* is identified, and the evolution of this maximum *R* with number of cycles is plotted in figure 61(a). There are two limiting values of R_c determined from the values of *R* at 282 and 300 cycles, respectively:

$$\begin{aligned} R_{c(80\%)} &= 178.73 MPa^{1/2} \\ R_{c(85\%)} &= 180.55 MPa^{1/2} \end{aligned} \tag{25}$$

The calibrated values of R_c are subsequently used for predicting crack nucleation in other specimens.

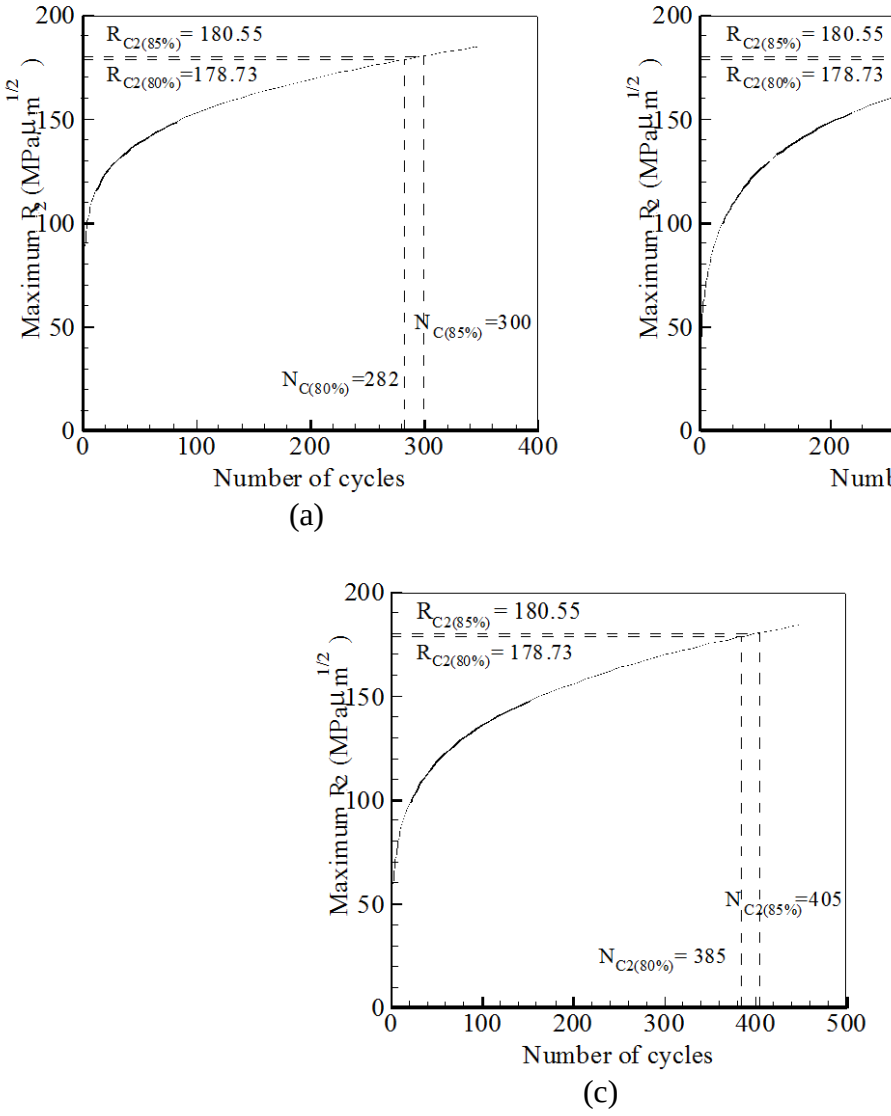

Figure 61. Evolution of the maximum *R* over number of cycles for the FE model of critical microstructure of (a) specimen 1; (b) specimen 2; and (c) specimen 3

3.2.5 Predicting Crack Nucleation in Specimens 2 and 3

Statistically equivalent CPFEM of the critical microstructure of specimens 2 and 3 are generated from OIM scans surrounding dwell-fatigue cracks in the failed specimens. For specimen 2, crack nucleation is experimentally determined to occur at 530 cycles. The 2-minute CPFEM simulation is performed for 663 cycles using loading conditions described in [7, 83]. Figure 61(b) shows the evolution of the maximum *R* with cycles. In this figure, the number of cycles to nucleation are predicted as $N_{c(80\%)} = 534$ and $N_{c(85\%)} = 567$. These correspond to the locations where the *R* curve in figure 61(b) intersects the critical values of $R_{c(80\%)}$ and $R_{c(85\%)}$, respectively. The difference with the experimentally determined value of 530 cycles is 0.72% for 80% of life and 6.93% for 85% of life. This agreement is considered to be excellent. Finally, the 2-minute dwell-fatigue problem is

simulated for 447 cycles for the critical microstructure of specimen 3. Evolution of the maximum *R* is plotted in figure 61(c). The number of cycles to nucleation are predicted to be $N_{c(80\%)} = 385$ and $N_{c(85\%)} = 405$. From the experimental observations this crack initiates at 380 cycles.

The differences in the simulated and experimental results are 1.35% for 80% of life and 6.49% for 85% of life. From these results, it is evident that using the proposed crack nucleation model results in excellent agreement of the predicted number of cycles to crack nucleation and experimental observations.

3.3 HOMOGENIZATION-BASED MACROSCOPIC ANISOTROPIC PLASTICITY MODEL FOR TITANIUM ALLOYS

In this section, an anisotropic continuum plasticity model is developed for titanium alloys undergoing deformation due to cyclic loading. This is a major task in the overall effort that can be incorporated in a commercial FE code or engineering-based fatigue tool. Spatial multiscaling requires development of a robust anisotropic continuum plasticity model that has its roots in the microstructural stress-strain and accounts for morphological and crystallographic features as well. This model explicitly accounts for deformation mechanisms and microstructural characteristics, and will be computationally efficient. Homogenization of crystal plasticity FE results of polycrystalline representative volume elements (RVE) will yield a macroscopic constitutive model that can be incorporated into general purpose FEM codes like ABAQUS® and MARC. Parametric studies will be performed with microstructural variations (e.g., orientation, misorientation, microtexture distribution, and grain sizes). This sensitivity analysis will identify important variables that need to be incorporated into the macroscopic material law.

3.3.1 Selection of an Appropriate Continuum Yield Criterion

An appropriate continuum yield criterion needs to capture different characteristics observed in mechanical behavior of titanium alloys, encompassing:

1. Pressure insensitivity
2. Anisotropy due to crystallographic texture
3. Tension-compression asymmetry
4. Kinematic hardening

Table 7 summarizes the most common anisotropic yield functions and their characteristics.

Table 7. The most common anisotropic yield functions

Model	Pressure Insensitive	Anisotropy	Tension-Compression Asymmetry	Kinematic Hardening	# of Parameters in Principal Axis
Hill (1948)	♣	♣			3
Hosford (1966)	♣	♣	♣	♣	5
Cazacu-Barlat (2004)	♣	♣	♣	♣	8

3.3.1.1 Hill's model

The functional form of this criterion in principal coordinate system is as follows:

$$F(\sigma_1-\sigma_2)^2+G(\sigma_1-\sigma_3)^2+H(\sigma_2-\sigma_3)^2-Y_f^2=0 \tag{26}$$

In this model *F*, *G*, and *H* are anisotropic parameters and Y_f is the flow stress. This model has been used mostly to model cubic metals with no tension-compression asymmetry, so it is not suitable criterion for modeling titanium alloys with predominantly HCP crystalline structure.

3.3.1.2 Hosford model

Hosford [87] modified Hill's model to take into account the tension-compression asymmetry by adding terms linear in stresses:

$$A\sigma_1+B\sigma_2+(-B-A)\sigma_3+F(\sigma_1-\sigma_2)^2+G(\sigma_1-\sigma_3)^2+H(\sigma_2-\sigma_3)^2-Y_f^2=0 \tag{27}$$

This function corresponds to an elliptical yield locus with low eccentricity. It can also model the kinematic hardening. However, this criterion is not suitable to model the highly anisotropic behavior of titanium alloys. Because of this high anisotropy, a yield function including higher order stress terms is required.

3.3.1.3 Cazacu-Barlat model

This model was proposed by Cazacu and Barlat [88, 89], which is of the form:

$$(J_2^0)^{\frac{3}{2}}-J_3^0-Y_f^3=0 \tag{28}$$

J_2^0 is the generalization of second stress invariant J_2 to orthotropy, and is expressed as:

$$J_2^0=\frac{a_1}{6}(\sigma_{xx}-\sigma_{yy})^2+\frac{a_2}{6}(\sigma_{xx}-\sigma_{zz})^2+\frac{a_3}{6}(\sigma_{yy}-\sigma_{zz})^2+a_4\sigma_{xy}^2+a_5\sigma_{xz}^2+a_6\sigma_{yz}^2 \tag{29}$$

J_3^0 is the generalization of third stress invariant J_3 to orthotropy as:

$$\begin{aligned} J_3^0 = {} & \frac{1}{27}(b_1+b_2)\sigma_{xx}^3 + \frac{1}{27}(b_3+b_4)\sigma_{yy}^3 + \frac{1}{27}[2(b_1+b_4)-(b_2+b_3)]\sigma_{zz}^3 + \frac{2}{9}(b_1+b_4)\sigma_{xx}\sigma_{yy}\sigma_{zz} \oplus \\ & -\frac{1}{9}(b_1\sigma_{yy}+b_2\sigma_{zz})\sigma_{xx}^2 - \frac{1}{9}(b_3\sigma_{zz}+b_4\sigma_{xx})\sigma_{yy}^2 - \frac{1}{9}[(b_1-b_2+b_4)\sigma_{xx}+(b_1-b_3+b_4)\sigma_{yy}]\sigma_{zz}^2 + 2b_{11}\sigma_{xy}\sigma_{xz}\sigma_{yz} \\ & -\frac{\sigma_{yz}^2}{3}[(b_6+b_7)\sigma_{xx}-b_6\sigma_{yy}-b_7\sigma_{zz}] - \frac{\sigma_{xz}^2}{3}[2b_9\sigma_{yy}-b_8\sigma_{zz}-(2b_9-b_8)\sigma_{xx}] \\ & -\frac{\sigma_{xy}^2}{3}[2b_{10}\sigma_{zz}-b_5\sigma_{yy}-(2b_{10}-b_5)\sigma_{xx}] \end{aligned} \tag{30}$$

The number of anisotropic parameters in this criterion is 17, which includes a_i $(i=1,....,6)$ and b_i $(i=1,....,11)$. If all coefficients b_i $(i=1,....,11)$ set to zero, the Cazacu-Barlat criterion reduces to the Hill's model. In fact, J_3^0 with stress terms with odd exponents has been added to account for the tension-compression asymmetry. For isotropic conditions $a_i=a_j$ $(i,j=1,....,6)$ and $b_i=b_j$ $(i,j=1,....,11)$. Both J_2^0 and J_3^0 are insensitive to pressure:

$$\sigma_{ij} = \begin{cases} \sigma & \text{if } i=j \\ 0 & \text{if } i\neq j \end{cases} \qquad \Rightarrow \qquad J_2^0 = J_3^0 = 0 \tag{31}$$

Therefore, the Cazacu-Barlat model is pressure insensitive. This model with higher order stress compared with Hill's criterion is expected to successfully represent the highly anisotropic behavior of titanium alloys. Y_f in this criterion is the yield stress in shear.

3.3.2 Selection of Important Microstructural Parameters

To develop a macroscopic constitutive model for titanium alloys taking into account the underlying microstructure, the anisotropic parameters in equations 29 and 30 are related to the important microstructural features. This is done by homogenization of micro-level CPFEM results of polycrystalline RVE. It is essential to find out the critical parameters, which adequately characterize a microstructure. As an initial try, the following four microstructural parameters are considered:

1. ODF
2. Texture distribution function (TDF)
3. Grain-size distribution function (GSDF)
4. Misorientation distribution function (MoDF)

In this section, definitions of these four parameters are first presented, and sufficiency of these parameters to characterize a microstructure is investigated.

3.3.2.1 Orientation distribution function

Plastic deformation in HCP crystalline titanium alloys has considerable dependence on the crystal orientation because of their low symmetries. Based on crystal plasticity formulations, the plasticity begins when $\tau^{\alpha} = g^{\alpha}$ for a slip system. Here τ^{α} is the resolved shear stress, and g^{α} is the slip system deformation resistance for slip system α. In addition, the plastic slip rate on slip system α has a power dependence of ~ 50 on $\frac{\tau^{\alpha}}{g^{\alpha}}$. Because of this large exponent, the plastic deformation depends only on the slip activity on the slip system with the highest value of $\frac{\tau^{\alpha}}{g^{\alpha}}$. The deformation resistance for the < c + a > slip on pyramidal planes is up to three to four times larger than that for < a >-type slip on prism or basal planes. Therefore, plastic deformation in soft grains is a result of slip activity on basal and prism slip systems with very similar values of g^{α}. This implies that the plastic deformation in polycrystalline titanium alloys is mainly controlled by slip activity on the basal or prism slip system with the highest value of τ^{α}.

The SF for slip system α is defined as $SF = \cos\varphi\cos\lambda$, where φ is the angle between loading axis and the slip plane normal $\mathbf{n}^{\alpha}$, and λ is the angle between loading axis and the slip direction $\mathbf{m}^{\alpha}$ in the reference configuration. The SF transforms the applied stress to the RSS on a given slip system. Therefore, SF of each grain has a direct effect on the plastic behavior of that grain and consequently on the overall plastic response of the microstructure. In this study, SF for each grain means the highest SF among basal and prism slip systems of the grain. Softer grains in a microstructure have higher SF compared with other grains. SF for each slip system depends on the loading axis. Therefore, in the most general case, the orientation of each grain is represented by three SFs labeled SF_x, SF_y, and SF_z, which denote the SF of the grain in case of *x*-, *y*- and *z*-directed loadings, respectively.

Distribution function of these three SFs is expected to be a good representation of orientation. Therefore, the average value of these distribution functions is considered as the scalar measure of orientation.

Figure 62 shows the distribution functions of SF_x, SF_y and SF_z for a sample microstructure including 600 grains. The average values of these parameters are $\overline{SF}_x = 0.405$, $\overline{SF}_y = 0.425$ and $\overline{SF}_z = 0.441$. For this microstructure, *z*-direction has the least yield strength (YS) compared with another direction. This confirms that microstructures with lower average value of SF have higher yield strengths.

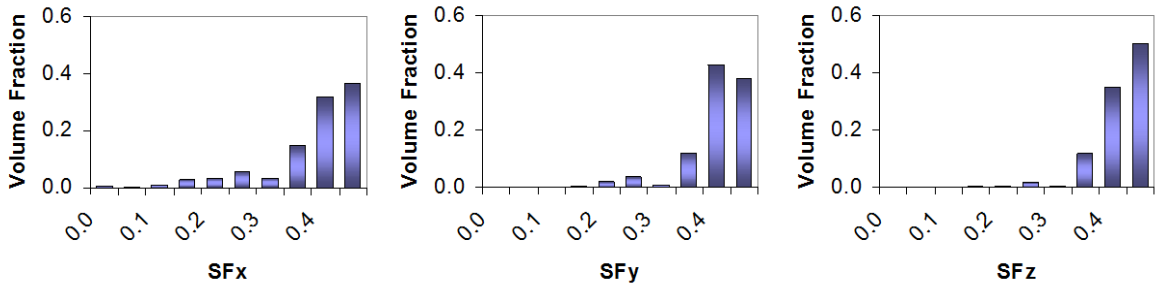

Figure 62. Sample distribution functions of SF_x, SF_y and SF_z

3.3.2.2 Texture

A texture index (TI) is defined for each grain in the microstructure as the volume fraction of its neighbors with similar orientation. A neighbor is considered to have similar orientation as the main grain if the misorientation angle between the two grains is less than 15°. The TI is always between 0 and 1. In the case of a completely textured microstructure, the TI is one for all grains. The TI tends to be zero for all grains in the case of a completely random microstructure. It should be noted that the orientation of a textured region also affects the material macroscopic response. A microstructure with hard texturing shows a higher YS compared with a microstructure with soft texturing. Therefore, the TI for each grain is refined by multiplying the old TI by the SF of that grain. The definition of SF is the same as the section in 3.3.2.1. The new TI varies between 0 and 0.5. The distribution function of the refined TI is considered as a representative of texturing and is denoted by a TDF. In general, TDF can be of any arbitrary shape, and it does not follow any standard distribution function. Three scalar representatives are considered for TDF:

1. Average
2. Standard deviation
3. Percentage of grains with a TI greater than a tolerance (e.g., 0.25)

3.3.2.3 Grain Size

The mechanical behavior of polycrystalline titanium alloys has a strong dependence on grain size. The size of each grain is defined to be the diameter of an equivalent sphere with the same volume as the grain. Grain-size distribution in titanium alloys follows a log-normal distribution function if the number fraction of grains in each bin is considered to generate the GSDF. This distribution function is specified by the mean and standard deviation of the grain size's natural logarithm. These two parameters are initially considered as scalar measures for grain-size distribution.

3.3.2.4 Misorientation

The misorientation between two neighboring grains 1 and 2 is measured in terms of a rotation axis vector **n** and a misorientation angle, θ_{mis} [77]. The axis **n** represents a common crystallographic lattice or slip direction for both crystal lattices. The misorientation angle θ_{mis} between two neighboring grains is the rotation about **n** required to bring the two crystal lattices into coincidence and is expressed as:

$$\theta_{mis} = \min\left|\cos^{-1}\left\{\frac{\mathrm{tr}(\boldsymbol{g}_1\boldsymbol{g}_2^{-1}\mathbf{O} - \mathbf{I})}{2}\right\}\right| \quad (32)$$

where $\boldsymbol{g}_1$ and $\boldsymbol{g}_2$ are the orientation matrices of grain 1 and 2, respectively, and **O** is the crystal symmetry operator.

MoDF for a microstructure can be of any arbitrary shape. Therefore, it cannot be fit to any standard distribution function. Three scalar representatives are considered for MoDF:

1. Average
2. Standard deviation
3. Percentage of grain pairs with misorientation less than a tolerance (e.g. 20^o)

3.3.2.5 Sufficiency of the selected microstructural parameters

To examine the sufficiency of the considered parameters for characterizing a microstructure, two different microstructures (MS1 and MS2) with the same statistics are simulated, and the corresponding yield strengths are compared. If the yield stresses match, then the considered parameters are enough to characterize a microstructure. The yield strength of the microstructures in each direction is obtained by applying a tensile constant strain rate of $10^{-4}\frac{1}{s}$ in that direction, and applying the 0.2% offset rule on the resulting stress-strain curve. Figure 63 shows the stress-strain curve for both microstructures corresponding to *x*- and *y*-directed strain loading. Table 8 summarizes the corresponding yield strengths.

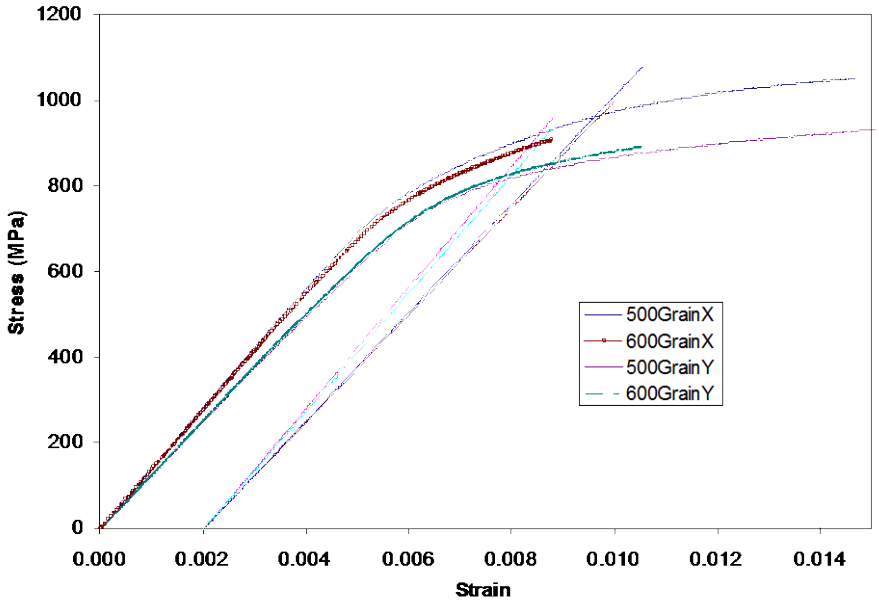

Figure 63. Stress-strain curve corresponding to microstructures MS1 and MS2

Table 8. Yield stress comparison between microstructures MS1 and MS2

Microstructure	# of grains	# of TET4 elements	# of nodes	Yield Stress (MPa)		
				X-direction	Y-direction	Z-direction
MS1	500	102697	18040	922.35	840.02	811.74
MS2	600	124820	21884	897.48	851.67	826.00

The maximum observed error is 2.7%, which is negligible. Therefore, the considered parameters are sufficient to characterize a microstructure.

3.3.3 Sensitivity Studies

In this section, the sensitivity of the macroscopic response (stress-strain curve) to the microstructural parameters introduced in section 3.3.2 is studied. The stress-strain curves are characterized by three quantities: the Young's modulus, yield strength, and hardness (the slope of stress-strain curve in the plasticity region). The difference between the macroscopic responses of two microstructures is negligible if all of the following three criteria are met:

1. The difference between the Young's modulus (E) of two stress-strain curves is less than 4%.
2. The difference between the yield strengths (σ_y) is less than 4%.
3. The difference between the hardness values (H) is less than 20%.

Because of the smaller values of hardness compared to the Young's modulus, more tolerance is allowed for hardness. Figure 64 depicts different stress-strain curves with the same values of YS ($\sigma_y = 936MPa$) and Young's modulus ($E = 1.17\times10^5 MPa$) but different values of hardness. As can be observed, a 20% difference in hardness does not make a significant difference in the stress-strain curve.

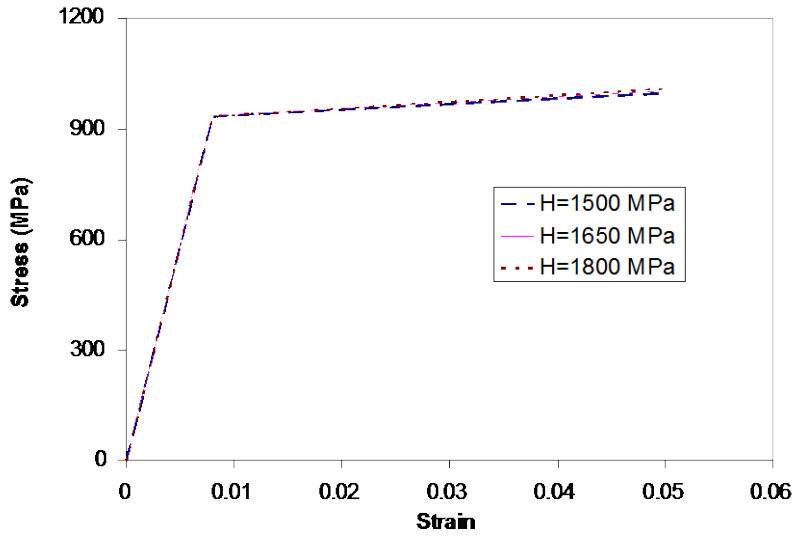

Figure 64. Macroscopic stress-strain curves with the same values of YS and Young's modulus but different values of hardness

3.3.3.1 Sensitivity of macroscopic response to TDF and MoDF

Two sets of microstructures are generated to determine the sensitivity of macroscopic response to TDF and MoDF. All microstructures include $7\times7\times7$ cubic grains. All grains have the same size ($7.5\mu m$). For set 1, two microstructures are considered, namely MS3 and MS4. Both microstructures have the same average SFs, ($\overline{SF}_x = 0.417$, $\overline{SF}_y = 0.434$ and $\overline{SF}_z = 0.452$) and were subject to a tensile constant strain rate of $10^{-4}\frac{1}{s}$ in the *y*-direction. Figure 65 shows the TDF and MoDF for MS3 and MS4. The distributions of misorientation and texture for the two microstructures are completely different. The scalar representatives of MoDF (e.g., average, standard deviation, and percentage of grain pairs with misorientation less than 20° (R20)) and the scalar representatives of TDF (e.g., average, standard deviation, and percentage of grains with a TI greater than 0.25 (R25)) for MS3 and MS4 are summarized in table 8. To investigate the sensitivity of macroscopic response to MoDF and TDF, the stress-strain curves corresponding to the two microstructures are obtained, and the values of σ_y, *H*, and *E* are compared. Table 9 shows that the percentages of difference between the values of σ_y, *H*, and *E* are 3.49, 5.8, and 0.53, respectively, which is less than the considered threshold values.

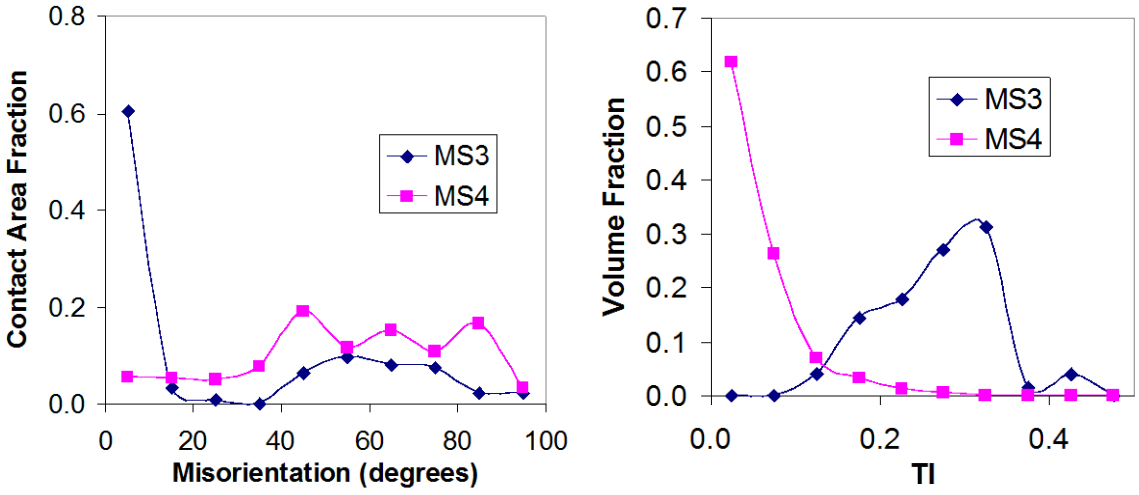

(a) (b)

Figure 65. (a) MoDF and (b) TDF for MS3 and MS4

Table 9. Scalar representatives of MoDF and TDF along with the values of σ_y, *H*, and *E* for MS3 and MS4

	σ_y (MPa)	*H* (MPa)	*E* (MPa)	MoDF			TDF		
				Average	Standard Deviation	R20	Average	Standard Deviation	R25
MS3	824.1	979.17	1.17E+05	25.05	30.52	0.63	0.27	0.064	0.64
MS4	853.9	1038.1	1.18E+05	54.92	24.17	0.11	0.04	0.056	0.006
Diff. (%)	3.49	5.8	0.53						

For set 2, three microstructures are considered, namely MS5, MS6, and MS7. All three microstructures have the same average SF ($\overline{SF}_x = 0.434$, $\overline{SF}_y = 0.418$, and $\overline{SF}_z = 0.428$). Figure 66 shows the corresponding TDF and MoDF plots. The scalar representatives of MoDF and TDF, along with the values of σ_y, *H*, and *E* for these microstructures, are summarized in table 10.

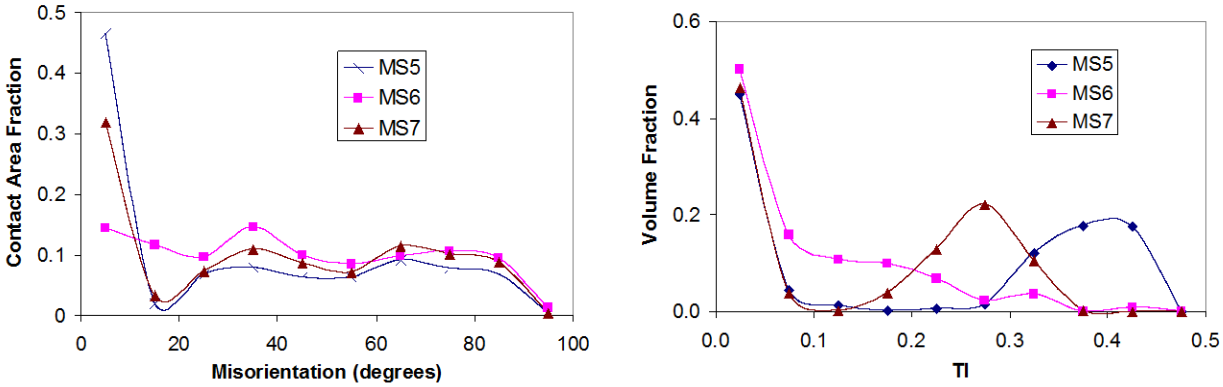

Figure 66. (a) MoDF and (b) TDF for MS5, MS6, and MS7

Table 10. Scalar representatives of MoDF and TDF along with the values of σ_y, H, and E for MS3 and MS4

	σ_y (MPa)	H (MPa)	E (MPa)	MoDF			TDF		
				Average	Standard Deviation	R20	Average	Standard Deviation	R25
MS5	855.3	1065	1.15E+05	30.45	29.99	0.49	0.19	0.184	0.49
MS6	860.5	1121.3	1.15E+05	42.74	26.77	0.26	0.08	0.098	0.07
MS7	857.5	996.4	1.15E+05	37.20	30.51	0.35	0.14	0.135	0.33
Diff. (%)	0.61	11.8	0.17						

Again, the difference between the values of σ_y, H, and E is less than the considered threshold values. Therefore, TDF and MoDF are considered to have no effect on the macroscopic response of a microstructure. In fact, these parameters are responsible for stress and strain redistribution between different grains in the microstructure. Therefore, they are important for local phenomena like crack nucleation, and their effect can be neglected on the macroscopic response.

3.3.3.2 Sensitivity of macroscopic response to GSDF

As discussed in section 3.3.2., GSDF can be characterized by the mean (μ_{GSDF}) and standard deviation (σ_{GSDF}) of the grain size's natural logarithm, if the number fraction of grains in each bin is considered to generate the distribution function.

3.3.3.2.1 Sensitivity to the standard deviation (σ_{GSDF})

To study the sensitivity of the macroscopic response to σ_{GSDF}, two microstructures (e.g., MS8 and MS9) were generated, which have the same average SFs in all directions. The microstructures have the same average grain size ($\mu_{GSDF} = 1$) but different standard deviation (0.486 for MS8 and 0.2 for MS9). Figure 67(a) shows the GSDF for MS8 and MS9. CPFE simulations are done on the two microstructures by applying a tensile constant strain rate of $10^{-4}\frac{1}{s}$ in the y-direction. The macroscopic stress-strain curves are represented in figure 67(b), and the corresponding yield strengths are $\sigma_y = 838.5MPa$ for MS8 and $\sigma_y = 892.9MPa$ for MS9. The difference between these two yield strengths is 6.1%, which is bigger than the allowable difference of 4%. Therefore, the effect of standard deviation of grain size on the macroscopic response cannot be ignored. Although both microstructures have the same average grain size, MS9—with higher σ_{GSDF}—has a small number of very large grains. The number fraction of these grains is negligible. However, the volume fraction of these grains is appreciable. Because volume averaging is done to get the macroscopic response, the effect of these grains is important. The volume average of grain size for MS8 and MS9 is $5.16\mu m$ and $2.55\mu m$, respectively. Therefore, the scalar measure for grain size

distribution is changed to the average of GSDF, based on volume fraction of grains, and is denoted by *D*.

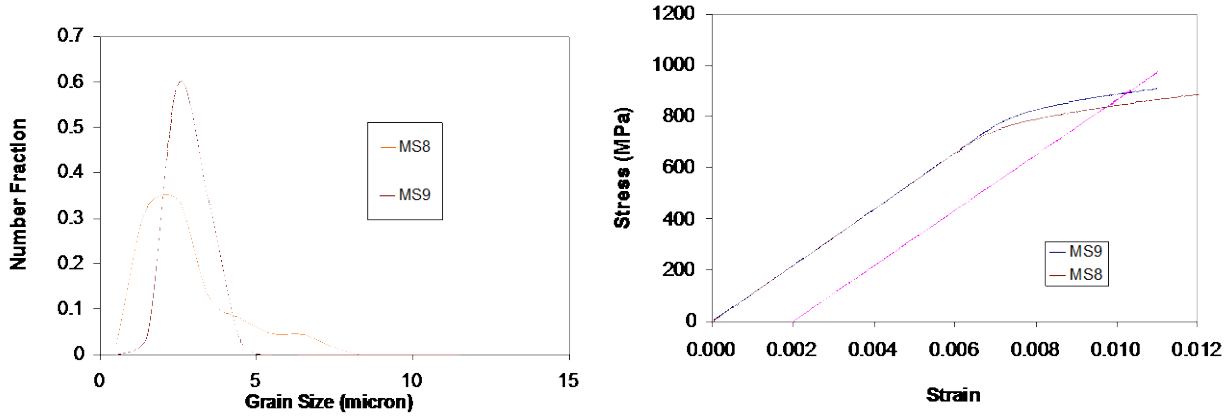

(a) (b)

Figure 67. (a) GSDF and (b) macroscopic stress-strain curve for MS8 and MS9

3.3.3.3 Sensitivity of macroscopic response to ODF

In this section, the sensitivity of the macroscopic response to the average SF is studied by performing CPFE simulations on a microstructure (i.e., MS10). This microstructure is soft in the *y*-direction ($\overline{SF}_y = 0.47$) and hard in the *z*-direction ($\overline{SF}_z = 0.15$). Two CPFE simulations were done on this microstructure. In the first simulation, a tensile constant strain rate of $10^{-4}\frac{1}{s}$ was applied in *y*-direction, and the same strain rate is applied in the *z*-direction in the second one. Figure 68 shows the macroscopic stress-strain curves corresponding to the *y*- and *z*-directed loadings. Table 11 shows the values of σ_y, *H*, and *E* corresponding to these two curves. The values of σ_y, *H*, and *E* in the *y*-direction are significantly different from those in the *z*-direction. This emphasizes the major effect of average SFs on the macroscopic response.

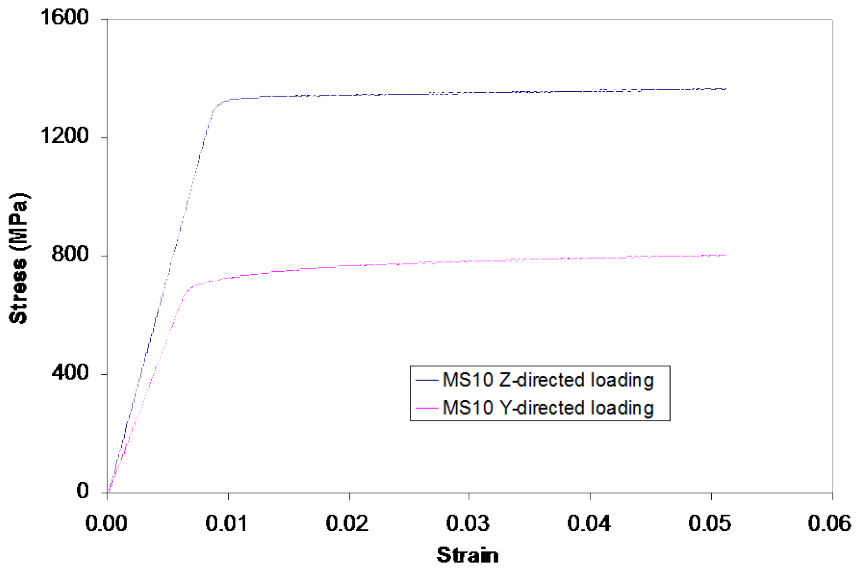

Figure 68. Macroscopic stress-strain curves for MS10 in *y* and *z* directions

Table 11. Microstructure properties along with the values of σ_y, *H*, and *E* for MS10

	SF	σ_y (MPa)	*H* (MPa)	*E* (MPa)
Y-directed Loading	0.47	717.58	918.12	1.06E+05
Z-directed Loading	0.15	1331.7	701.74	1.48E+05
Difference (%)		59.9	26.7	33.1

3.3.4 Development of Homogenization-Based Continuum-Level Anisotropic Plasticity Model

Based on the sensitivity studies in section 3.3.2, four parameters are considered as microstructure descriptors to develop the homogenization-based continuum-level anisotropic plasticity (HCAP) model. These include three orientation-related parameters (SF_x, SF_y, and SF_z) and the volume average of grain size *D*. The HCAP model is for 3D analysis, as it is created from 3D micromechanical analysis by the CPFE model. The Cazacu-Barlat yield function is used to represent the highly anisotropic behavior of titanium alloys described in section 4.1. The 17 anisotropic parameters in this yield criterion (see equations 28–30) are calibrated by homogenization of CPFE micromechanical analyses conducted on RVEs of the microstructure with different microstructural features. Therefore, these parameters would be functions of the microstructure descriptors. These parameters are not necessarily constant for a particular microstructure but evolve with increasing plastic flow. The homogenized flow stress in shear, Y_f in equation 28 is a function of the microstructural descriptors and the macroscopic plastic work.

3.3.4.1 Cazacu-Barlat yield function for titanium alloys

In this section, the suitability of the Cazacu-Barlat yield criterion to capture the anisotropic behavior of titanium alloys is examined. For this purpose, numerical tests are conducted for an RVE with a strong microtexture (i.e., M10) under 19 loading conditions including:

1. Three uniaxial tension tests along the *x*, *y*, and *z* directions
2. Three pure shear tests on *xy*, *xz*, and *yz*
3. Three uniaxial compression tests along x, y, and z directions
4. Three biaxial tension tests ($\varepsilon_{xx}:\varepsilon_{yy}:\sigma_{zz}=1:1:0, \varepsilon_{zz}:\varepsilon_{xx}:\sigma_{yy}=1:1:0$ and $\varepsilon_{yy}:\varepsilon_{zz}:\sigma_{xx}=1:1:0$)
5. Three biaxial compression tests ($\varepsilon_{xx}:\varepsilon_{yy}:\sigma_{zz}=-1:-1:0, \varepsilon_{zz}:\varepsilon_{xx}:\sigma_{yy}=-1:-1:0$ and $\varepsilon_{yy}:\varepsilon_{zz}:\sigma_{xx}=-1:-1:0$)
6. Four tension tests with constrained transverse strain ($\varepsilon_{xx}:\sigma_{yy}:\varepsilon_{zz}=1:0:0$, $\varepsilon_{xx}:\varepsilon_{yy}:\sigma_{zz}=1:0:0$, $\sigma_{xx}:\varepsilon_{yy}:\varepsilon_{zz}=0:1:0$ and $\varepsilon_{xx}:\sigma_{yy}:\varepsilon_{zz}=0:0:1$)

The values of the microstructure descriptors for M10 are:

$SF_x : SF_y : SF_z : D = 0.471 : 0.470 : 0.146 : 7.5$, in which D is in microns.

Because Y_f is the homogenized flow stress in shear, the CPFE simulation of the simple shear test on the *xy* plane is considered to calculate Y_f. Micromechanical analysis is followed by homogenization, in which the macroscopic plastic work (W_p) and stresses (σ_{ij}) are evaluated from the microstructural variables using these equations:

$$W_p = \frac{1}{V}\sum_{I=1}^{N^e} W_p^I V^I \text{ and } \sigma_{ij} = \frac{1}{V}\sum_{I=1}^{N^e} \sigma_{ij}^I V^I \tag{33}$$

where W_p^I and σ_{ij}^I are the plastic work and stress components at tetrahedron element number I. V^I is the volume of I^{th} element, and V is the total volume of the microstructure. For pure shear loading on *xy*, the only nonzero macroscopic stress component is σ_{xy}. Therefore, equations 28–30 reduce to $(a_4)^{\frac{3}{2}}\sigma_{xy}^3 - Y_f^3 = 0$. Parameter a_4 is set to 1 to make $Y_f(W_p) = \sigma_{xy}$. The flow stress Y_f is plotted as a function of W_p in figure 69(a).

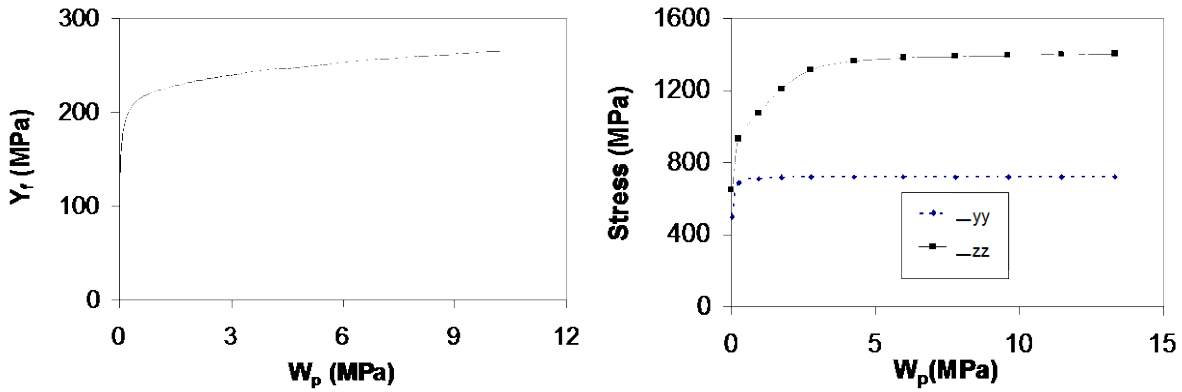

(a) (b)

Figure 69. (a) Yield stress for shear loading and (b) homogenized stresses for the biaxial tension loading $\varepsilon_{yy} : \varepsilon_{zz} : \sigma_{xx} = 1 : 1 : 0$, plotted as functions of macroscopic plastic work

To calibrate the anisotropic parameters a_i $(i = 1,2,3,5,6)$ and b_i $(i = 1,....,11)$, CPFE analyses are performed for M10 under the 19 loading conditions mentioned earlier, followed by homogenization. All loading conditions are prescribed with a constant strain rate of $10^{-4}\frac{1}{s}$. At the end of each strain increment in the CPFE analyses, macroscopic stresses and plastic work are obtained from equation 28. The stress components are plotted as functions of W_P in figure 69(b) for one of the biaxial tension loadings ($\varepsilon_{yy} : \varepsilon_{zz} : \sigma_{xx} = 1 : 1 : 0$). As it is observed, the macroscopic normal stress in the *y*-direction is much less than that in the *z*-direction because of the high anisotropy associated with this microstructure.

For a given value of W_P, the stress components are obtained from plots such as those in figure 69(b). This is done for all the loading conditions. The anisotropic parameters are then evaluated by the least square minimization of equation 28 as:

$$\min_{a_i\,(i=1,6),\,b_i\,(i=1,11)} \sum_{I=1}^{19} [(J_2^0)_I^{3/2} - (J_3^0)_I - Y_f^3]^2 \tag{34}$$

where:

$$(J_2^0)_I = \frac{a_1}{6}(\sigma_{xx}^I - \sigma_{yy}^I)^2 + \frac{a_2}{6}(\sigma_{xx}^I - \sigma_{zz}^I)^2 + \frac{a_3}{6}(\sigma_{yy}^I - \sigma_{zz}^I)^2 + a_4(\sigma_{xy}^I)^2 + a_5(\sigma_{xz}^I)^2 + a_6(\sigma_{yz}^I)^2 \tag{35}$$

and:

$$\begin{aligned}(J_3^0)_I = {} & \frac{1}{27}(b_1+b_2)(\sigma_{xx}^I)^3 + \frac{1}{27}(b_3+b_4)(\sigma_{yy}^I)^3 + \frac{1}{27}[2(b_1+b_4)-(b_2+b_3)](\sigma_{zz}^I)^3 + \frac{2}{9}(b_1+b_4)\sigma_{xx}^I\sigma_{yy}^I\sigma_{zz}^I \\ & -\frac{1}{9}(b_1\sigma_{yy}^I + b_2\sigma_{zz}^I)(\sigma_{xx}^I)^2 - \frac{1}{9}(b_3\sigma_{zz}^I + b_4\sigma_{xx}^I)(\sigma_{yy}^I)^2 - \frac{1}{9}[(b_1-b_2+b_4)\sigma_{xx}^I + (b_1-b_3+b_4)\sigma_{yy}^I](\sigma_{zz}^I)^2 + 2b_{11}\sigma_{xy}^I\sigma_{xz}^I\sigma_{yz}^I \\ & -\frac{(\sigma_{yz}^I)^2}{3}[(b_6+b_7)\sigma_{xx}^I - b_6\sigma_{yy}^I - b_7\sigma_{zz}^I] - \frac{(\sigma_{xz}^I)^2}{3}[2b_9\sigma_{yy}^I - b_8\sigma_{zz}^I - (2b_9-b_8)\sigma_{xx}^I] \\ & -\frac{(\sigma_{xy}^I)^2}{3}[2b_{10}\sigma_{zz}^I - b_5\sigma_{yy}^I - (2b_{10}-b_5)\sigma_{xx}^I]\end{aligned} \tag{36}$$

In 35 and 36, σ_{ij}^I are the macroscopic stress components in loading number I at the given value of W_P. After evaluating the anisotropic parameters for the given value of W_P, the 3D yield locus in the principal coordinate system can be obtained from equations 28–30 by setting the shear stress components to zero, resulting in:

$$\begin{aligned}&\left[\frac{a_1}{6}(\sigma_x-\sigma_y)^2 + \frac{a_2}{6}(\sigma_x-\sigma_z)^2 + \frac{a_3}{6}(\sigma_y-\sigma_z)^2\right]^{\frac{3}{2}} - \left[\frac{1}{27}(b_1+b_2)\sigma_x^3 + \frac{1}{27}(b_3+b_4)\sigma_y^3 + \frac{1}{27}[2(b_1+b_4)-(b_2+b_3)]\sigma_z^3 + \right. \\ &\left. \frac{2}{9}(b_1+b_4)\sigma_x\sigma_y\sigma_z - \frac{1}{9}(b_1\sigma_y+b_2\sigma_z)\sigma_x^2 - \frac{1}{9}(b_3\sigma_z+b_4\sigma_x)\sigma_y^2 - \frac{1}{9}[(b_1-b_2+b_4)\sigma_x + (b_1-b_3+b_4)\sigma_y]\sigma_z^2\right] - Y_f^3 = 0\end{aligned} \tag{37}$$

where σ_x, σ_y and σ_z are the principal stresses. The 3D yield locus for microstructure M10 at

W_P =0.1 MPa is shown in figure 70(a). The projection of this yield surface on the $\sigma_x - \sigma_z$ plane is shown in figure 70(b), compared with the numerical data obtained from CPFE simulations. Good agreement can be observed between the Cazacu-Barlat yield locus and the stress data points obtained from CPFE simulations. Figure 70(c) shows the evolution of the yield locus with plastic work increase. The yield loci in this figure correspond to $W_P = 0.1, 1.0, 4.0$ and $10.0\ MPa$.

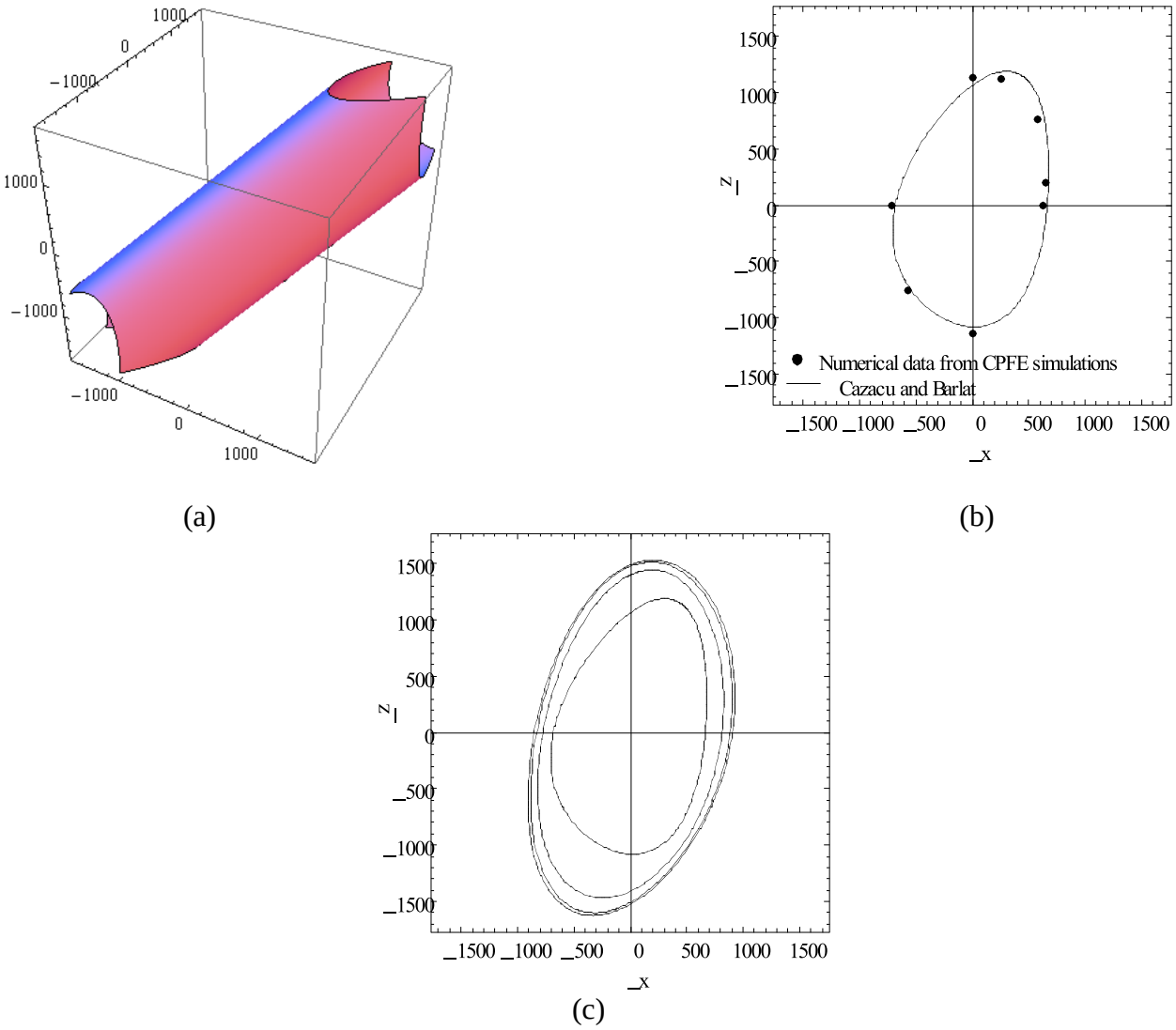

Figure 70. (a) 3D yield locus for microstructure M10 at W_P =0.1 MPa; (b) projection of the 3D yield surface on the $\sigma_x - \sigma_z$ plane; and (c) evolution of the yield locus with plastic work increase

Table 12 shows the values of the anisotropic parameters in equation 37, corresponding to W_P =0.1 MPa. The values of b_i are smaller than those of a_i. This is also observed in other microstructures. Therefore, some of the b_i parameters in the Cazacu-Barlat yield criterion are set to zero to reduce the number of coefficients, which require calibration. As the first attempt, all b_i parameters are set to zero. This reduces the Cazacu-Barlat criterion to the Hill's model with only six anisotropic parameters. The process of calibrating the anisotropic parameters is repeated by least square minimization of this function:

$$\min_{a_i\,(i=1,6)} \sum_{I=1}^{19} [(J_2^0)_I^{3/2} - Y_f^3]^2 \qquad (38)$$

where $(J_2^0)_I$ is obtained from equation 35. Table 13 summarizes the calibrated parameters in the Hill's model, corresponding to W_P =0.1 MPa. The resulting Hill's yield surface at W_P =0.1 MPa is projected on the $\sigma_x - \sigma_z$ plane (see figure 71(a)). This yield locus is compared with the Cazacu-Barlat yield locus. The difference between the two yield loci is not negligible.

Table 12. Cazacu-Barlat anisotropic parameters for M10 corresponding to W_P =0.1 MPa

a_1	a_2	a_3	a_4	a_5	a_6	b_1	b_2	b_3	b_4
0.364	0.060	0.108	1	0.542	0.547	-0.048	0.026	-0.072	0.023

(a) (b)

Table 13. Calibrated Hill's anisotropic parameters for M10 corresponding to W_P =0.1 MPa

a_1	a_2	a_3	a_4	a_5	a_6
0.359	0.055	0.105	1	0.542	0.547

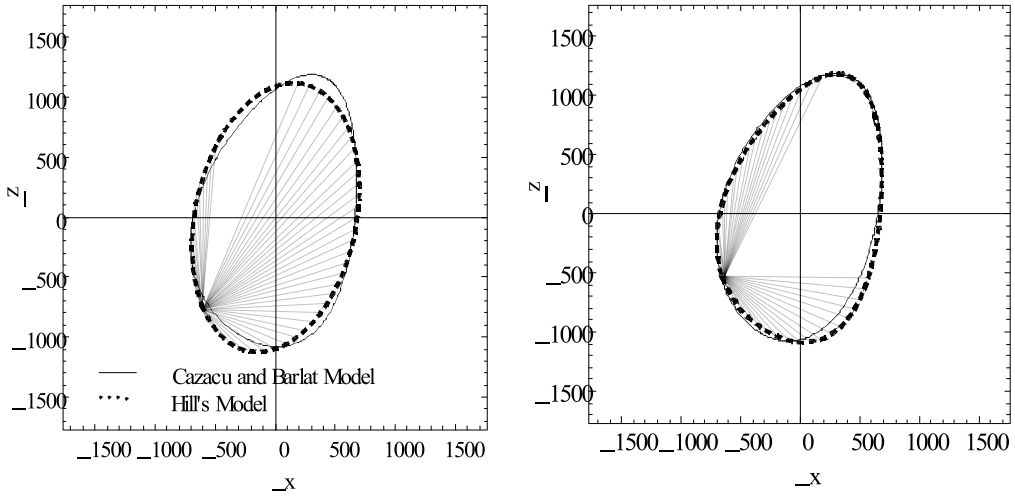

Figure 71. Comparison of Cazacu-Barlat yield locus with (a) Hill's locus, and (b) reduced Cazacu-Barlat locus, obtained for microstructure M10 at W_P =0.1 MPa

As the second attempt, the parameters b_i $(i = 5,6,....,11)$ are set to zero. This removes the shear terms from J_3^0, and the number of parameters, which require calibration, reduces to 10. In this case, only the following 15 loading conditions are considered for homogenization and calibration purposes:

1. Three uniaxial tension tests along the *x*, *y*, and *z* directions
2. Three pure shear tests on *xy*, *xz*, and *yz*
3. Three uniaxial compression tests along the *x*, *y*, and *z* directions

4. Three biaxial tension tests ($\varepsilon_{xx}:\varepsilon_{yy}:\sigma_{zz}=1:1:0, \varepsilon_{zz}:\varepsilon_{xx}:\sigma_{yy}=1:1:0$ and $\varepsilon_{yy}:\varepsilon_{zz}:\sigma_{xx}=1:1:0$)
5. Three biaxial compression tests ($\varepsilon_{xx}:\varepsilon_{yy}:\sigma_{zz}=-1:-1:0, \varepsilon_{zz}:\varepsilon_{xx}:\sigma_{yy}=-1:-1:0$ and $\varepsilon_{yy}:\varepsilon_{zz}:\sigma_{xx}=-1:-1:0$)

The parameters $a_i\ (i=1,....,6)$ and $b_i\ (i=1,....,4)$ are calibrated by least square minimization of this function:

$$\min_{a_i(i=1,6),b_i(i=1,4)} \sum_{I=1}^{15}[(J_2^0)_I^{3/2}-(J_3^*)_I-Y_f^3]^2 \tag{39}$$

where $(J_3^*)_I$ is the reduced form of $(J_3^0)_I$ as:

$$\begin{aligned}(J_3^*)_I=&\frac{1}{27}(b_1+b_2)(\sigma_{xx}^I)^3+\frac{1}{27}(b_3+b_4)(\sigma_{yy}^I)^3+\frac{1}{27}[2(b_1+b_4)-(b_2+b_3)](\sigma_{zz}^I)^3+\frac{2}{9}(b_1+b_4)\sigma_{xx}^I\sigma_{yy}^I\sigma_{zz}^I\\&-\frac{1}{9}(b_1\sigma_{yy}^I+b_2\sigma_{zz}^I)(\sigma_{xx}^I)^2-\frac{1}{9}(b_3\sigma_{zz}^I+b_4\sigma_{xx}^I)(\sigma_{yy}^I)^2-\frac{1}{9}[(b_1-b_2+b_4)\sigma_{xx}^I+(b_1-b_3+b_4)\sigma_{yy}^I](\sigma_{zz}^I)^2\end{aligned} \tag{40}$$

It should be noted that the reduced Cazacu-Barlat criterion ($(J_2^0)^{\frac{3}{2}}-J_3^*-Y_f^3=0$) still stratifies the required characteristics for an acceptable yield criterion, which are pressure-insensitivity, anisotropy, and tension-compression asymmetry. Table 14 summarizes the calibrated parameters corresponding to W_P =0.1 MPa. The resulting yield surface at W_P =0.1 MPa is projected on the $\sigma_x-\sigma_z$ plane, as shown in figure 71(b). This yield locus is compared with the one obtained from the Cazacu-Barlat model with all 17 parameters. There is no significant difference between these two yield loci. Therefore, the Cazacu-Barlat yield model with a reduced number of parameters will be used to develop the macroscopic constitutive model for titanium alloys, which is discussed in section 3.3.4.2.

Table 14. Calibrated anisotropic parameters of the reduced Cazacu-Barlat model for M10 corresponding to W_P =0.1 MPa

a_1	a_2	a_3	a_4	a_5	a_6	b_1	b_2	b_3	b_4
0.359	0.074	0.093	1	0.542	0.547	-0.032	-0.004	-0.057	0.003

3.3.4.2 Evaluation of anisotropic constitutive parameters in the HCAP model

Following the discussions in the previous sections, the anisotropic parameters ($a_i\ (i=1,....,6)$, $b_i\ (i=1,....,4)$) and the flow stress (Y_f) in the reduced Cazacu-Barlat model are microstructure-dependent. Therefore, 70 different polycrystalline RVEs with different microstructure descriptors

are considered to relate the HCAP model to the microstructural parameters. The properties of these microstructures are summarized in table 15. Each RVE consists of 7x7x7 cubic grains. The volume averages of SFs (SF_x, SF_y, and SF_z) are between 0.146 and 0.498 in each microstructure. For the average grain size *D*, three values are considered: 7.5, 15, and 40 microns.

Table 15. Properties of different RVEs used for development of the HCAP model

Microstructure	SF_x	SF_y	SF_z	*D*
M10	0.471	0.470	0.146	7.5
M11	0.471	0.470	0.146	15
M12	0.471	0.470	0.146	40
M20	0.445	0.446	0.360	7.5
M21	0.445	0.446	0.360	15
M22	0.445	0.446	0.360	40
M30	0.445	0.446	0.496	7.5
M31	0.445	0.446	0.496	15
M32	0.445	0.446	0.496	40
M40	0.430	0.435	0.401	7.5
M41	0.430	0.435	0.401	15
M42	0.430	0.435	0.401	40
M50	0.470	0.437	0.268	7.5
M51	0.470	0.437	0.268	15
M52	0.470	0.437	0.268	40
M60	0.428	0.470	0.473	7.5
M61	0.428	0.470	0.473	15
M62	0.428	0.470	0.473	40
M70	0.382	0.323	0.448	7.5
M71	0.382	0.323	0.448	15
M72	0.382	0.323	0.448	40
M80	0.483	0.482	0.498	7.5
M81	0.483	0.482	0.498	15
M82	0.483	0.482	0.498	40
M91	0.470	0.146	0.471	15
M92	0.470	0.146	0.471	40
M100	0.446	0.360	0.445	7.5
M101	0.446	0.360	0.445	15
M102	0.446	0.360	0.445	40
M110	0.446	0.496	0.445	7.5
M111	0.446	0.496	0.445	15
M112	0.446	0.496	0.445	40
M120	0.435	0.401	0.430	7.5
M121	0.435	0.401	0.430	15
M122	0.435	0.401	0.430	40
M130	0.437	0.268	0.470	7.5
M131	0.437	0.268	0.470	15
M132	0.437	0.268	0.470	40

Table 15. Properties of different RVEs used for development of the HCAP model (continued)

Microstructure	SF_x	SF_y	SF_z	*D*
M140	0.470	0.473	0.428	7.5
M141	0.470	0.473	0.428	15
M142	0.470	0.473	0.428	40
M150	0.323	0.448	0.382	7.5
M151	0.323	0.448	0.382	15
M152	0.323	0.448	0.382	40
M160	0.482	0.498	0.483	7.5
M161	0.482	0.498	0.483	15
M162	0.482	0.498	0.483	40
M171	0.146	0.471	0.470	15
M172	0.146	0.471	0.470	40
M180	0.360	0.445	0.446	7.5
M181	0.360	0.445	0.446	15
M182	0.360	0.445	0.446	40
M190	0.496	0.445	0.446	7.5
M191	0.496	0.445	0.446	15
M192	0.496	0.445	0.446	40
M200	0.401	0.430	0.435	7.5
M201	0.401	0.430	0.435	15
M202	0.401	0.430	0.435	40
M210	0.268	0.470	0.437	7.5
M211	0.268	0.470	0.437	15
M212	0.268	0.470	0.437	40
M220	0.473	0.428	0.470	7.5
M221	0.473	0.428	0.470	15
M222	0.473	0.428	0.470	40
M230	0.448	0.382	0.323	7.5
M231	0.448	0.382	0.323	15
M232	0.448	0.382	0.323	40
M240	0.498	0.483	0.482	7.5
M241	0.498	0.483	0.482	15
M242	0.498	0.483	0.482	40

CPFE simulations were conducted only for M10 to about M82. For each of these RVEs, CPFE simulations were conducted under 12 loading conditions including:

1. Three uniaxial tension tests along the *x*, *y*, and *z* directions
2. Three pure shear tests on *xy*, *xz*, and *yz*
3. Three uniaxial compression tests along the *x*-, *y*- and *z*-directions
4. Three biaxial tension tests ($\varepsilon_{xx}:\varepsilon_{yy}:\sigma_{zz}=1:1:0, \varepsilon_{zz}:\varepsilon_{xx}:\sigma_{yy}=1:1:0$ and $\varepsilon_{yy}:\varepsilon_{zz}:\sigma_{xx}=1:1:0$)

For each microstructure, the flow stress Y_f is obtained at different values of W_P using the same procedure explained in section 3.3.4.1. The anisotropic parameters for each microstructure are evaluated at different values of W_P by least square minimization of this function:

$$\min_{a_i\,(i=1,6),b_i\,(i=1,4)} \sum_{I=1}^{12}[(J_2^0)_I^{3/2} - (J_3^*)_I - Y_f^3]^2 \tag{41}$$

The definitions for $(J_2^0)_I$ and $(J_3^*)_I$ were given in the previous section. The procedure explained in section 3.3.4.1 is used to calibrate $a_i\ (i=1,....,6)$ and $b_i\ (i=1,....,4)$.

RVEs M91 ~ M162 are obtained from M11 ~ M82 by rotating the coordinate system so that $X_{new} = Y_{old}$, $Y_{new} = Z_{old}$, and $Z_{new} = X_{old}$, where $X_{new}, Y_{new}, Z_{new}$ are the new axes, and $X_{old}, Y_{old}, Z_{old}$ are the old axes. The microstructure descriptors for the rotated microstructure are:

$$(SF_x)_{new} = (SF_y)_{old},\ (SF_y)_{new} = (SF_z)_{old},\ (SF_z)_{new} = (SF_x)_{old},\ D_{new} = D_{old} \tag{42}$$

RVEs M171 ~ M242 are obtained from M11 ~ M82 by rotating the coordinate system such that $X_{new} = Z_{old}$, $Y_{new} = X_{old}$ and $Z_{new} = Y_{old}$. The microstructure descriptors for the rotated microstructure are:

$$(SF_x)_{new} = (SF_z)_{old},\ (SF_y)_{new} = (SF_x)_{old},\ (SF_z)_{new} = (SF_y)_{old},\ D_{new} = D_{old} \tag{43}$$

No CPFE simulation is required for M91 ~ M242. The macroscopic stresses and plastic work at each time increment can be obtained from those of M11 ~ M82 by applying an appropriate rotation of the coordinate system. Then, the flow stress and the anisotropic parameters are evaluated for these microstructures using the same procedure described for M11 ~ M82.

Here are some observations from the homogenization efforts made on the 70 microstructures:

- The anisotropic parameters for each microstructure can change with the amount of plastic work.
- The flow stress for each microstructure evolves with an increase in the amount of plastic work.
- The flow stress for a given value of W_p decreases with an increase in the average grain size, *D*.
- If $SF_i > SF_j > SF_k$, then $a_l > a_m > a_n$, where a_l, a_m, a_n are the anisotropic parameters corresponding to the normal stress components in the J_2^0 part of the yield criterion so that $J_2^0 = \frac{a_l}{6}(\sigma_i - \sigma_j)^2 + \frac{a_m}{6}(\sigma_i - \sigma_k)^2 + \frac{a_n}{6}(\sigma_j - \sigma_k)^2 + a_4\sigma_{xy}^2 + a_5\sigma_{xz}^2 + a_6\sigma_{yz}^2$.
- Higher SFs in the *x* and *y* directions result in lower flow stress, Y_f.

3.3.4.3 Functional form of the HCAP model in terms of the microstructure descriptors and amount of plasticity

The calibrated values of the anisotropic parameters ($a_i \ (i=1,....,6)$ and $b_i \ (i=1,....,4)$) and the flow stress (Y_f) for different RVEs (see table 15) are used to come up with a functional form of the HCAP model in terms of microstructural descriptors (SF_x, SF_y, SF_z, and D) and plastic work (W_P). A power law functional form is assumed for this purpose as:

$$a_i = (A_1^i + A_2^i\, SF_x^{\alpha_i})(A_3^i + A_4^i\, SF_y^{\beta_i})(A_5^i + A_6^i\, SF_z^{\gamma_i})(A_7^i + A_8^i\, D^{\eta_i})(A_9^i + A_{10}^i\, W_P^{\kappa_i}) \qquad i=1,...,6$$

$$b_i = (B_1^i + B_2^i\, SF_x^{\chi_i})(B_3^i + B_4^i\, SF_y^{\delta_i})(B_5^i + B_6^i\, SF_z^{\varepsilon_i})(B_7^i + B_8^i\, D^{\phi_i})(B_9^i + B_{10}^i\, W_P^{\varphi_i}) \qquad i=1,...,4 \quad (44)$$

$$Y_f = (C_1 + C_2\, SF_x^{\lambda})(C_3 + C_4\, SF_y^{\mu})(C_5 + C_6\, SF_z^{\nu})(C_7 + C_8\, D^{\theta})(C_9 + C_{10}\, W_P^{\psi})$$

Parameters $A_j^i(i=1,...,6\,;\, j=1,...,10)$, $B_j^i(i=1,...,4\,;\, j=1,...,10)$, $C_i(i=1,...,10)$, $\alpha_i(i=1,...,6)$, $\beta_i(i=1,...,6)$, $\gamma_i(i=1,...,6)$, $\eta_i(i=1,...,6)$, $\kappa_i(i=1,...,6)$, $\chi_i(i=1,...,6)$, $\delta_i(i=1,...,6)$, $\varepsilon_i(i=1,...,6)$, $\phi_i(i=1,...,6)$, $\varphi_i(i=1,...,6)$, λ, μ, ν, $\theta$and $\psi$are obtained from a least square fit of the data in table 15 along with the corresponding values of $a_i \ (i=1,....,6)$, $b_i \ (i=1,....,4)$, and Y_f. The resulting functional forms are:

$$a_1 = (0.89 + 15.61 SF_x^{1.89})(-0.33 - 5.93\, SF_y^{1.82})(0.01 - 6.57 SF_z^{10.66})(-66.56 - 0.36\, D^{0.48})(-2.19 + 2.25\, W_P^{0.002}) \quad (45a)$$

$$a_2 = (1.55 + 14.21 SF_x^{2.08})(0.41 - 1.12\, SF_y^{2.22})(0.04 + 2.35 SF_z^{2.46})(-39.95 - 0.12\, D^{0.44})(0.80 - 0.82\, W_P^{0.003}) \quad (45b)$$

$$a_3 = (1.59 - 3.20 SF_x^{1.82})(0.44 + 4.68\, SF_y^{2.59})(0.08 + 4.80 SF_z^{1.96})(33.81 + 0.03\, D^{0.84})(-1.21 + 1.22\, W_P^{0.001}) \quad (45c)$$

$$a_4 = 1.0 \quad (45d)$$

$$a_5 = (0.23 + 3.43 SF_x^{-0.01})(0.05 - 0.07\, SF_y^{1.37})(-0.05 - 0.23 SF_z^{1.95})(36.43 - 1.31\, D^{0.09})(-3.04 + 6\times10^{-7}\, W_P^{4.54}) \quad (45e)$$

$$a_6 = (-3.93 + 4.15 SF_x^{-0.07})(-0.12 + 0.76\, SF_y^{7.78})(0.22 + 0.93 SF_z^{1.05})(-5.19 + 0.002\, D^{0.97})(6.06 - 0.006\, W_P^{0.72}) \quad (45f)$$

$$b_1 = (-0.007 - 0.6 SF_x^{3.4})(0.5 + 0.07\, SF_y^{2.8})(2\times10^{-4} + 5.43 SF_z^{3.65})(22.11 + 0.12\, D^{0.77})(0.15 + 0.29\, W_P^{0.27}) \quad (45g)$$

$$b_2 = (1.57 - 1.8 SF_x^{0.05})(1.5 - 2.1\, SF_y^{0.68})(1.56 - 2.55 SF_z^{1.11})(42.62 + 0.34\, D^{0.75})(-1.97 + 2.02\, W_P^{0.005}) \quad (45h)$$

$$b_3 = (0.79 + 2.43 SF_x^{2.74})(-0.81 + 5.71\, SF_y^{1.74})(-0.002 - 0.03 SF_z^{3.80})(24.72 + 0.05\, D^{0.97})(0.23 + 0.95\, W_P^{0.2}) \quad (45i)$$

$$b_4 = (1.83 - 1.96 SF_x^{0.18})(1.76 - 1.95\, SF_y^{0.58})(1.87 - 3.64 SF_z^{1.91})(34.49 + 0.09\, D^{0.96})(1.42 - 1.44\, W_P^{0.003}) \quad (45j)$$

$$Y_f = (3.70 - 39.06 SF_x^{7.6})(0.67 - 40.42\, SF_y^{9.8})(16.15 + 17.65 SF_z^{1.04})(40.5 - 12.92\, D^{0.07})(-3.26 + 3.45\, W_P^{0.005}) \quad (45k)$$

3.3.4.4 Extension of the HCAP model to account for rate dependency

In the macroscopic constitutive model, the total strain rate is assumed to admit an additive decomposition into an elastic and viscoplastic part as:

$$\dot{\mathbf{I}} = \dot{\mathbf{a}}^{e} + \dot{\mathbf{a}}^{p} \tag{46}$$

For small elastic strains, the rate of Cauchy stress, $\dot{\sigma}$, is related to the elastic part of the strain rate tensor as: $\dot{\mathbf{\&}} = \mathbf{C}^{e} : \dot{\mathbf{\&}}$, where $\mathbf{C}^{e}$ is a fourth-order anisotropic elasticity tensor. Rate dependency is introduced through an over-stress viscoplastic model, developed by Perzyna [89]. In this model, the viscoplastic strain rate is expressed in terms of a function $\phi(F)$ of the overstress F as [17]:

$$\dot{\mathbf{I}}^{p} = \lambda_0 \phi(F) \frac{\partial F / \partial \mathbf{\acute{o}}}{\left\| \partial F / \partial \mathbf{\acute{o}} \right\|} \tag{47}$$

where λ_0 is a temperature-dependent viscosity coefficient. The viscoplastic strain rate in equation 47 follows the associated flow rule, therefore satisfying normality and incompressibility conditions. A power law expression (i.e., $\phi(F) = \langle F \rangle^{n}$) was discussed to adequately represent the behavior of most metals [90, 91]. $\langle\ \rangle$ is the Mac-Cauley operator corresponding to the positive sign of the argument. The over-stress F corresponds to a measure of the excess stress over the rate-independent flow stress Y_f:

$$F = \sigma_{eq} - Y_f \tag{48}$$

The functional form of the flow stress is determined from the homogenization process as described in sections 3.3.4.2 and 3.3.4.3 and presented in equation 40(k). The equivalent stress σ_{eq} in equation 48 is expressed using the anisotropic reduced Cazacu-Barlat model as:

$$\begin{aligned}
\sigma_{eq}^{3} = (J_2^0)^{3/2} - J_3^{*} = &\left(\frac{a_1}{6}(\sigma_{xx} - \sigma_{yy})^2 + \frac{a_2}{6}(\sigma_{xx} - \sigma_{zz})^2 + \frac{a_3}{6}(\sigma_{yy} - \sigma_{zz})^2 + a_4\sigma_{xy}^2 + a_5\sigma_{xz}^2 + a_6\sigma_{yz}^2 \right)^{3/2} \\
&- \left(\frac{1}{27}(b_1 + b_2)\sigma_{xx}^3 + \frac{1}{27}(b_3 + b_4)\sigma_{yy}^3 + \frac{1}{27}[2(b_1 + b_4) - (b_2 + b_3)]\sigma_{zz}^3 + \frac{2}{9}(b_1 + b_4)\sigma_{xx}\sigma_{yy}\sigma_{zz} \right. \\
&\left. - \frac{1}{9}(b_1\sigma_{yy} + b_2\sigma_{zz})\sigma_{xx}^2 - \frac{1}{9}(b_3\sigma_{zz} + b_4\sigma_{xx})\sigma_{yy}^2 - \frac{1}{9}[(b_1 - b_2 + b_4)\sigma_{xx} + (b_1 - b_3 + b_4)\sigma_{yy}]\sigma_{zz}^2 \right)
\end{aligned} \tag{49}$$

Anisotropy parameters $a_i\ (i = 1,....,6)$ and $b_i\ (i = 1,....,4)$ in this equation are determined from the homogenization process, as described in sections 3.3.4.2 and 3.3.4.3, and presented in equations 45(a) ~ (j). These parameters evolve with plastic work.

The homogenized viscoplastic parameters in the HCAP model (λ_0 and n) are calibrated from a set of loading conditions combining N different imposed strain ratios and M applied strain rates for each loading. At each increment, the stress tensor $\mathbf{\acute{o}}$, the plastic strain rate tensor $\dot{\mathbf{I}}^{p}$, and the

plastic work W_p are computed from CPFE simulation results on microstructure M11. The corresponding yield stress $Y_f(W_p)$ and anisotropy coefficients a_i $(i = 1,....,6)$ and b_i $(i = 1,...., 4)$ are evaluated using the previous calibration results (see equation 45). The overstress *F* is then obtained at each time increment using equations 48 and 49. $\partial F / \partial \sigma_{ij}$ $(i, j = x, y, z)$ is evaluated by taking the derivative of equation 48 with respect to σ_{ij} as:

$$\frac{\partial F}{\partial \sigma_{ij}} = \frac{\partial \sigma_{eq}}{\partial \sigma_{ij}} = \frac{1}{3}\left((J_2^0)^{3/2} - J_3^*\right)^{2/3}\left(\frac{3}{2}(J_2^0)^{1/2}\frac{\partial J_2^0}{\partial \sigma_{ij}} - \frac{\partial J_3^*}{\partial \sigma_{ij}}\right) \tag{50}$$

Taking the logarithm of both sides of (47) and considering $\phi(F) = \langle F \rangle^n$, this equation can be rewritten as:

$$\ln(\dot{\varepsilon}_{ij}^p) = \ln(\lambda_0) + n \ln\langle F \rangle + \ln\left(\frac{\partial F / \partial \sigma_{ij}}{\|\partial F / \partial \boldsymbol{\sigma}\|}\right) \tag{51}$$

Rearranging the terms in equation 51 results in:

$$\ln\left(\frac{\dot{\varepsilon}_{ij}^p \|\partial F / \partial \boldsymbol{\sigma}\|}{\partial F / \partial \sigma_{ij}}\right) = \ln(\lambda_0) + n \ln\langle F \rangle \tag{52}$$

This is a linear equation in *U* and *V*, where $U = \ln\langle F \rangle$ and $V = \ln\left(\frac{\dot{\varepsilon}_{ij}^p \|\partial F / \partial \boldsymbol{\sigma}\|}{\partial F / \partial \sigma_{ij}}\right)$. A plot of *V* versus *U* would give a straight line with slope equal to *n* and the intercept equal to $\ln(\lambda_0)$. Therefore, the macroscopic viscoplastic parameters (λ_0 and *n*) are obtained by finding the best linear fit to the measured data (*U*, *V*) corresponding to different stress components for different loading conditions at different time increments. For the calibration of viscoplastic parameters, four different strain rates in uniaxial tension are applied (i.e., *N* = 1 and *M* = 4). The applied strain rates are $\dot{\varepsilon}_{xx}^{(1)} = 0.0001 s^{-1}$, $\dot{\varepsilon}_{xx}^{(2)} = 0.0005 s^{-1}$, $\dot{\varepsilon}_{xx}^{(3)} = 0.001 s^{-1}$, and $\dot{\varepsilon}_{xx}^{(4)} = 0.002 s^{-1}$. Figure 72 shows the best linear fit to the measured data at different time increments considering only $\dot{\varepsilon}_{xx}^p$ and $\dot{\varepsilon}_{yy}$. The viscoplastic parameters are evaluated as:

$$n = 1.44 \;\; \lambda_0 = e^{-10.16} = 3.9 \times 10^{-5} \tag{53}$$

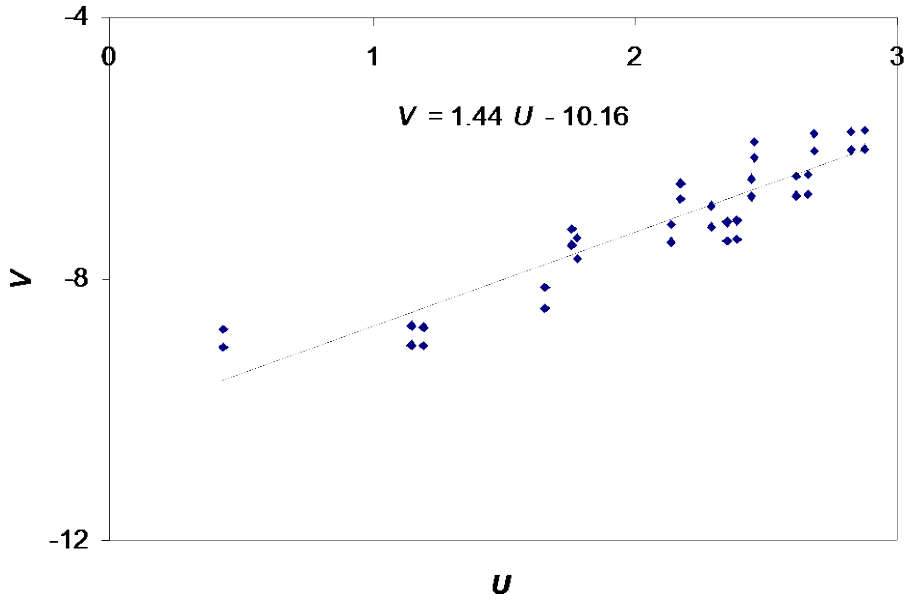

Figure 72. Linear fit to the measured data at different time increments to calibrate the viscoplastic parameters

3.4 MACROSCOPIC CRACK NUCLEATION MODEL FOR TI-6242

The aim of this section is to develop a homogenization-based damage initiation model for macroscopic (structural scale) analysis of titanium-based alloys. The damage model will be based on the crack initiation at the microcrystalline or polycrystalline scale and will incorporate functional dependencies between stresses and microstructural parameters like orientation (SF), misorientation, and grain sizes. The novelty of such damage surfaces is that they are completely based on the physics of the microstructure and are not phenomenological like other models. This task is done in two steps:

1. Crystal plasticity simulations are done on an RVE of a two-grain system. Using the crack nucleation model proposed in section 3.2.2, the time to crack initiation (t_f) is related to the stress level and microstructural parameters to arrive at a functional form, as described in section 3.4.1.
2. The functional form so obtained is further used in the study to develop a probabilistic model for damage in real microstructures consisting of a few hundred grains. The inputs to this model are the functional form of t_f along with the distribution functions of orientation, misorientation, and grain sizes in the microstructure.

3.4.1 Sensitivity Studies on RVE

The load-shedding phenomenon, which is responsible for crack initiation in titanium alloys, is due to strength mismatch between hard and soft regions. Time-to-crack initiation t_f for a hard-soft grain pair is assumed to depend on:

- Misorientation between hard and soft grains, θ_{mis}
- SF of the soft grain, *SF*
- Soft grain size, *D*

The time-to-crack initiation (t_f) also depends on the macroscopic stress level, *P*. The dependence of t_f on these four parameters is studied in detail through creep simulation of an RVE of a two-grain system using crystal plasticity. The FEM consists of an inner cube representing a primary α hard grain contained in an outer cube representing the softer primary α grain (see figure 73). A load of magnitude *P* is applied along the global *y*-axis. The loading axis is assumed to coincide with the *c*-axis of the hard grain, for which all basal and prismatic SFs are 0. The orientation of the soft grain is chosen in such a way that a specified SF for the soft grain and a specified misorientation between hard and soft grains is achieved. The inner cube (hard grain) is discretized into a mesh of 1,296 four-noded linear tetrahedron elements, whereas the outer cube (soft grain) has a mesh of 15,168 elements. A mesh convergence study is first undertaken with respect to both macroscopic and microscopic response to arrive at this optimal mesh size for the FEM. The two regions in the model can differ in their orientation and size.

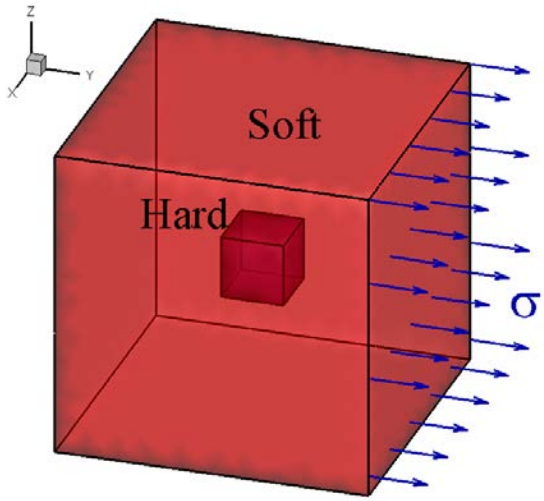

Figure 73. RVE of a two-grain system used for crack nucleation studies

The initial slip system deformation resistance g_0^α of individual slip systems for the crystal plasticity simulation is obtained from a Hall-Petch relation [78]. All other crystal plasticity parameters are based on calibrated values [77]. Several CPFE simulations with different stress levels are done on the two-grain model with different combinations of microstructural parameters. For each simulation, the variable t_f is obtained for the two-grain model. Each creep simulation is continued until a value of $R_{c(80\%)} = 178.73\ MPa\mu m^{1/2}$ is achieved for effective nucleation variable *R*, which is a parameter proposed in equation 13 for prediction of crack nucleation. This parameter evolves with time in every study until the time of crack initiation (t_f), when it reaches a critical value R_c, equal to 178.73 MPa $\mu m^{1/2}$ for the titanium alloy under consideration. Figure 74 shows the plot for *R* versus time for an RVE with *D = 7.5 μm, SF = 0.425,* $\theta_{mis} = 46^\circ$ *and P=750 MPa.*

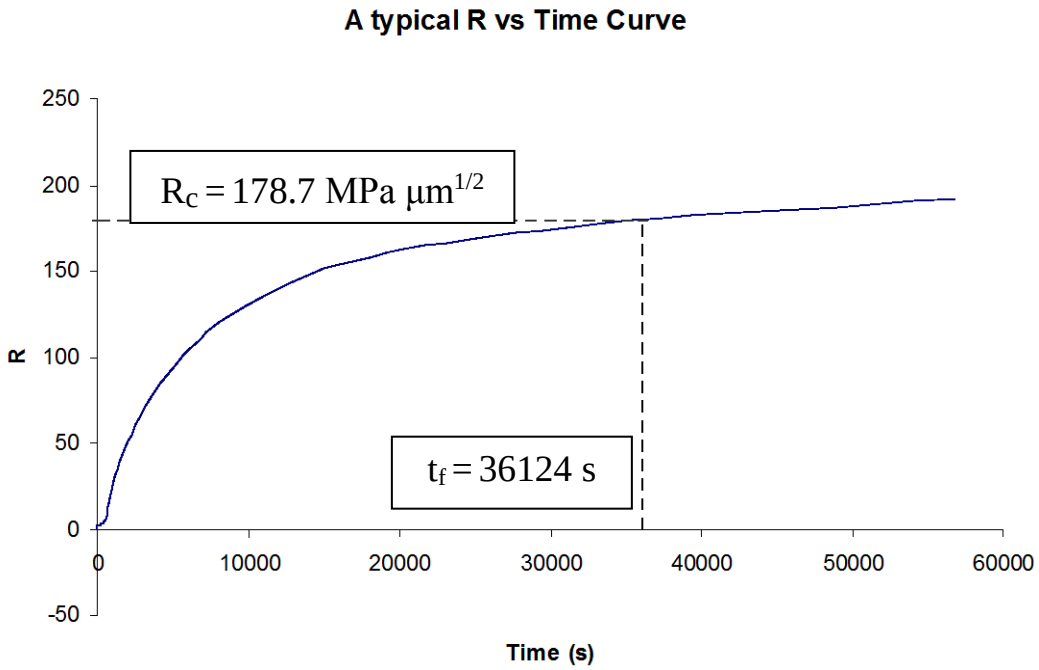

Figure 74. The evolution of the parameter *R* with time; this corresponds to the simulation with *D=7.5 μm, SF=0.425,* $\theta_{mis} = 46^{\circ}$ and *P=750 MPa*

A functional form of t_f can be established in terms of stress level and microstructural parameters through a full parametric study:

$$t_f = t_f\ (\theta_{mis}, SF, D, P) \tag{54}$$

The function t_f represents the effect of misorientation, SF, grain size, and stress level on t_f. This function can be identified by studying the sensitivity of t_f to each one of the microscopic parameters and the stress level.

The SF and misorientation (θ_{mis}) follow the definitions in sections 3.3.4.3 and 3.3.4.4, respectively. To study the effect of *SF* and θ_{mis} on t_f, the model is adjusted so that the SF of the soft outer grain assumes the values 0.425, 0.45, 0.475, 0.49, and 0.5. The possible range of θ_{mis} depends on the *SF* value. For lower values of *SF*, θ_{mis} can vary in a broader range, while for the highest possible SF of 0.5, θ_{mis} can just take the value of 45º. Table 16 shows 17 different combinations of *SF* and θ_{mis} values considered in this parametric study.

Table 16. The 17 combinations of *SF* and θ_{mis} considered for this parametric study

SF	0.425	0.45	0.475	0.49	0.5
θ_{mis}	30.94	32	36.5	40	45
	46	45	40	45	
	60.5	55	52	50.8	
	67	60	60.5	56	

The hard grain size does not have any appreciable effect on load shedding and, therefore, crack nucleation. The study of the effect of soft grain size is conducted on the RVEs with different combinations of SF, misorientation (θ_{mis}), and macroscopic stress level (*P*) for each grain size. For *SF* = 0.5 and *P* = 650 MPa, different sizes from 7.5–100μm are considered for the soft grain. For other values of *SF*, three values of 7.5, 15, and 30 μm are considered for the soft-grain size.

The applied creep stress is expected to have a significant effect on crack nucleation in polycrystalline materials. For high-stress creep tests, the microcracks due to the load-shedding phenomenon happen earlier in comparison to low-stress tests. To study the influence of *P* on t_f, the RVE is subject to various stress levels from 450–950 MPa, depending on other parameters. A CPFE creep simulation followed by a post-process step is done for each combination of *SF*, θ_{mis}, *D*, and *P*, and the natural log of the time-to-crack initiation is summarized in table 17. The total number of 183 simulations has been conducted.

Table 17. Time-to-failure for 183 different RVEs

RVE Number	*SF*	θ_{mis}	*P (MPa)*	*D (μm)*	*Ln (t_f)*
1	0.425	30.94	550	7.5	28.34
2	0.425	30.94	550	15	25.89
3	0.425	30.94	650	7.5	19.27
4	0.425	30.94	650	15	16.57
5	0.425	30.94	750	7.5	11.11
6	0.425	30.94	750	15	8.36
7	0.425	30.94	850	7.5	4.02
8	0.425	30.94	850	15	1.56
9	0.425	30.94	950	7.5	0.12
10	0.425	30.94	950	15	-0.02
11	0.425	46	500	7.5	32.34
12	0.425	46	500	15	31.00
13	0.425	46	650	7.5	18.99
14	0.425	46	650	15	16.38
15	0.425	46	750	7.5	10.49
16	0.425	46	750	15	7.72
17	0.425	46	900	7.5	0.75
18	0.425	46	900	15	0.07
19	0.425	60.5	500	7.5	31.56
20	0.425	60.5	500	15	29.66
21	0.425	60.5	650	7.5	17.23
22	0.425	60.5	650	15	14.44
23	0.425	60.5	750	7.5	8.84
24	0.425	60.5	750	15	6.03
25	0.425	60.5	900	7.5	0.21
26	0.425	60.5	900	15	-0.01
27	0.425	67	500	7.5	29.08
28	0.425	67	650	7.5	14.37
29	0.425	67	750	7.5	6.65
30	0.425	67	850	7.5	0.72
31	0.45	32	500	7.5	31.93
32	0.45	32	650	7.5	18.03
33	0.45	32	750	7.5	9.67
34	0.45	32	950	7.5	0.00
35	0.45	45	500	7.5	31.34
36	0.45	45	650	7.5	18.27
37	0.45	45	750	7.5	8.35
38	0.45	45	900	7.5	0.12
39	0.45	55	500	7.5	29.02
40	0.45	55	650	7.5	14.61
41	0.45	55	750	7.5	6.56
42	0.45	55	850	7.5	0.61
43	0.45	60	500	7.5	28.31

Table 17. Time-to-failure for 183 different RVEs (continued)

RVE Number	*SF*	θ_{mis}	*P (MPa)*	*D (μm)*	*Ln* (t_f)
44	0.45	60	650	7.5	12.97
45	0.45	60	750	7.5	5.17
46	0.45	60	800	7.5	1.94
47	0.45	32	500	15	30.00
48	0.45	32	650	15	15.31
49	0.45	32	750	15	6.88
50	0.45	32	950	15	-0.05
51	0.45	45	500	15	30.44
52	0.45	45	650	15	15.04
53	0.45	45	750	15	5.54
54	0.45	45	900	15	-0.01
55	0.45	55	500	15	26.65
56	0.45	55	650	15	11.75
57	0.45	55	750	15	3.89
58	0.45	55	850	15	0.04
59	0.45	60	500	15	25.69
60	0.45	60	650	15	10.23
61	0.45	60	750	15	2.62
62	0.45	60	800	15	0.33
63	0.45	32	500	30	28.11
64	0.45	32	650	30	13.27
65	0.45	32	750	30	4.81
66	0.45	32	950	30	-0.08
67	0.45	45	500	30	28.69
68	0.45	45	650	30	12.77
69	0.45	45	750	30	3.57
70	0.45	45	900	30	-0.05
71	0.45	55	500	30	24.67
72	0.45	55	650	30	9.70
73	0.45	55	750	30	2.01
74	0.45	55	850	30	-0.02
75	0.45	60	500	30	23.56
76	0.45	60	650	30	8.27
77	0.45	60	750	30	1.06
78	0.45	60	800	30	0.04
79	0.475	36.5	500	7.5	29.62
80	0.475	36.5	650	7.5	13.47
81	0.475	36.5	750	7.5	4.75
82	0.475	36.5	800	7.5	1.24
83	0.475	40	500	7.5	28.88
84	0.475	40	650	7.5	14.28
85	0.475	40	750	7.5	6.01
86	0.475	40	850	7.5	0.28
87	0.475	52	500	7.5	25.68
88	0.475	52	650	7.5	10.92
89	0.475	52	750	7.5	3.26
90	0.475	52	800	7.5	0.61

Table 17. Time-to-failure for 183 different RVEs (continued)

RVE Number	*SF*	θ_{mis}	*P (MPa)*	*D (μm)*	*Ln* (t_f)
91	0.475	60.5	500	7.5	25.06
92	0.475	60.5	600	7.5	13.89
93	0.475	60.5	650	7.5	9.40
94	0.475	60.5	750	7.5	1.88
95	0.475	36.5	500	15	27.44
96	0.475	36.5	650	15	10.64
97	0.475	36.5	750	15	2.11
98	0.475	36.5	800	15	0.19
99	0.475	40	500	15	26.53
100	0.475	40	650	15	11.38
101	0.475	40	750	15	3.28
102	0.475	40	850	15	0.00
103	0.475	52	500	15	22.91
104	0.475	52	650	15	8.26
105	0.475	52	750	15	1.06
106	0.475	52	800	15	0.05
107	0.475	60.5	500	15	22.36
108	0.475	60.5	600	15	11.12
109	0.475	60.5	650	15	6.72
110	0.475	60.5	750	15	0.19
111	0.475	36.5	500	30	25.54
112	0.475	36.5	650	30	8.55
113	0.475	36.5	750	30	0.70
114	0.475	36.5	800	30	0.01
115	0.475	40	500	30	24.60
116	0.475	40	650	30	9.30
117	0.475	40	750	30	1.53
118	0.475	40	850	30	-0.03
119	0.475	52	500	30	20.87
120	0.475	52	650	30	6.31
121	0.475	52	750	30	0.24
122	0.475	52	800	30	-0.02
123	0.475	60.5	500	30	20.30
124	0.475	60.5	600	30	9.12
125	0.475	60.5	650	30	3.99
126	0.475	60.5	750	30	0.01
127	0.49	40	500	7.5	28.49
128	0.49	40	650	7.5	12.09
129	0.49	40	750	7.5	3.38
130	0.49	40	800	7.5	0.50
131	0.49	45	500	7.5	23.62
132	0.49	45	600	7.5	13.64
133	0.49	45	650	7.5	9.37
134	0.49	45	750	7.5	0.53
135	0.49	50.8	500	7.5	23.75
136	0.49	50.8	650	7.5	8.80
137	0.49	50.8	750	7.5	1.37

Table 17. Time-to-failure for 183 different RVEs (continued)

RVE Number	*SF*	θ_{mis}	*P (MPa)*	*D (μm)*	*Ln* (t_f)
138	0.49	56	500	7.5	22.82
139	0.49	56	600	7.5	12.58
140	0.49	56	650	7.5	8.04
141	0.49	56	750	7.5	0.90
142	0.49	40	500	15	26.07
143	0.49	40	650	15	9.23
144	0.49	40	750	15	1.04
145	0.49	40	800	15	0.03
146	0.49	45	500	15	22.35
147	0.49	45	600	15	11.36
148	0.49	45	650	15	6.08
149	0.49	45	750	15	0.03
150	0.49	50.8	500	15	21.10
151	0.49	50.8	650	15	6.17
152	0.49	50.8	750	15	0.19
153	0.49	56	500	15	20.11
154	0.49	56	600	15	9.81
155	0.49	56	650	15	5.41
156	0.49	56	750	15	0.08
157	0.49	40	500	30	24.13
158	0.49	40	650	30	7.12
159	0.49	40	750	30	0.25
160	0.49	45	500	30	20.23
161	0.49	45	600	30	9.36
162	0.49	45	650	30	4.12
163	0.49	45	750	30	-0.02
164	0.49	50.8	500	30	19.22
165	0.49	50.8	650	30	4.21
166	0.49	50.8	750	30	0.01
167	0.49	56	500	30	18.15
168	0.49	56	600	30	7.82
169	0.49	56	650	30	3.48
170	0.49	56	750	30	-0.01
171	0.5	45	450	7.5	30.14
172	0.5	45	500	7.5	25.18
173	0.5	45	550	7.5	19.13
174	0.5	45	600	7.5	15.14
175	0.5	45	650	7.5	8.77
176	0.5	45	700	7.5	4.22
177	0.5	45	725	7.5	2.44
178	0.5	45	750	7.5	1.01
179	0.5	45	650	15	5.68
180	0.5	45	650	30	3.76
181	0.5	45	650	60	2.44
182	0.5	45	650	75	2.11
183	0.5	45	650	100	1.76

Figure 75 shows the variation of the time-to-crack initiation (in logarithmic scale) with stress for different grain sizes (e.g., 7.5, 15, and 30 μm. It can be seen that, as expected, the time-to-failure varies inversely with the macroscopic stress. Simultaneously, for any particular stress level, t_f reduces as the grain size increases. However, as the stress increases above 900 MPa, the influence of grain size on t_f decreases.

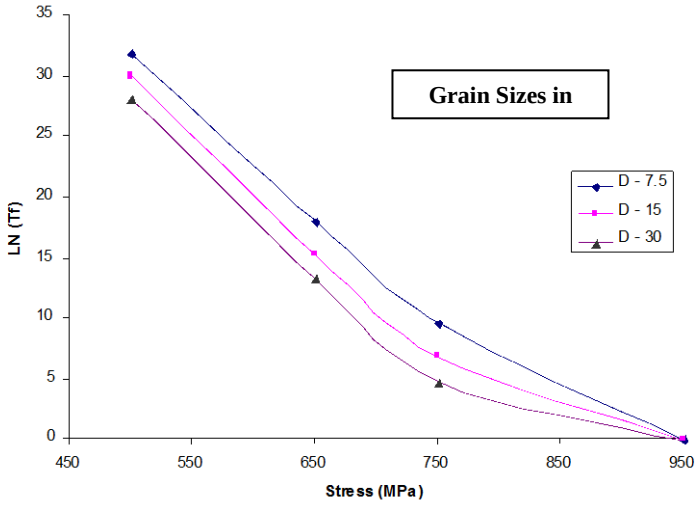

Figure 75. Variation of the time-to-crack initiation with stress for different grain sizes corresponding to SF = 0.45 and θ_{mis} = 32°

Figure 76 plots the variation of time-to-crack initiation with grain size, which is varied from 7.5–100 μm. Here, the SF is maintained at 0.5, with only one misorientation at 45°. It can be seen that the time-to-failure drops with increasing grain size.

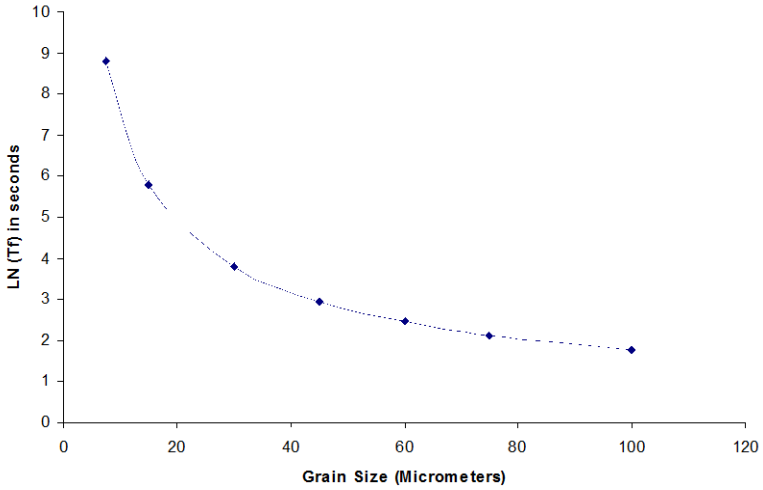

Figure 76. Variation of the time-to-crack initiation with grain size corresponding to SF = 0.5, $\theta_{mis} = 45°$ and P = 650 MPa

Figure 77 plots the variation of time-to-crack initiation with stress for different values of misorientation. It is observed that less macroscopic stress is required for crack nucleation at a particular time as the misorientation increases.

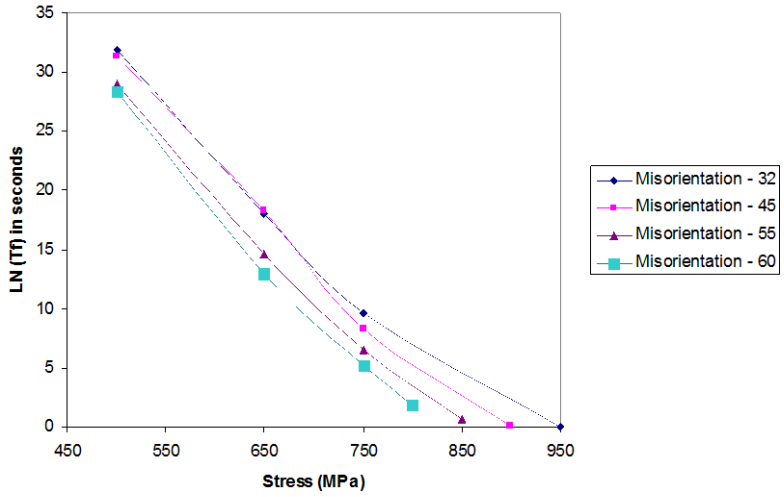

Figure 77. Variation of the time-to-crack initiation with stress for different values of misorientation corresponding to *SF*=0.45 and *D*= 7.5 µm

Figure 78 shows the effect of misorientation on the time-to-failure for different SFs. Time-to-failure decreases with increasing SF as expected. At SF 0.5, the maximum RSS on the soft slip systems is acquired. Correspondingly, the time-to-failure is the minimum.

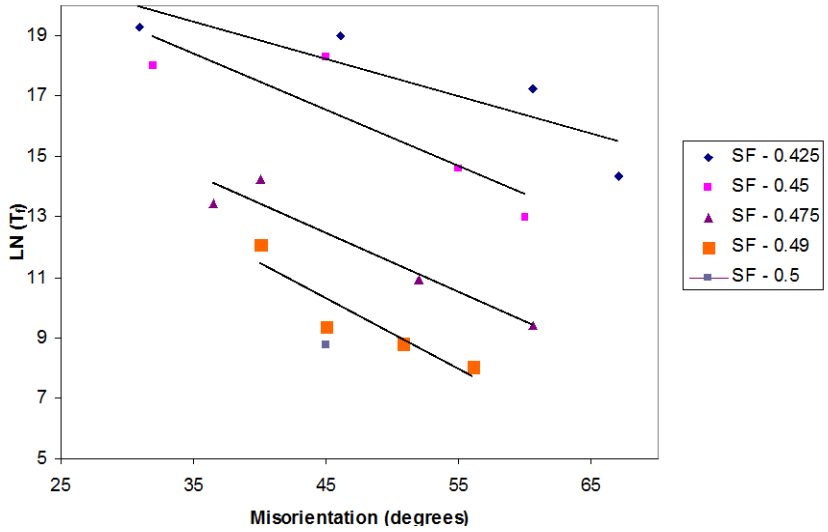

Figure 78. Variation of the time-to-crack initiation with misorientation for different SFs corresponding to *P*= 650MPa and *D*=7.5 µm

3.4.1.1 Functional form of t_f in terms of the microstructural parameters and the stress level

The values of the time-to-crack nucleation (t_f) for different RVEs (see table 17) are used to come up with a functional form of t_f in terms of microstructural parameters (SF, θ_{mis}, and D) and the macroscopic stress level (P). A power law functional form is assumed for this purpose as:

$$Ln(t_f) = (A_1 + B_1\ SF^{\alpha})\ \left(A_2 + B_2\ \theta_{mis}^{\beta}\right)\left(A_3 + B_3\ P^{\gamma}\right)\left(A_4 + B_4\ D^{\eta}\right) \tag{55}$$

Parameters $A_i (i = 1,...,4)$, $B_i (i = 1,...,4)$, α, β, γ, and η are obtained from a least square fit of the data in table 17 with a correlation coefficient of $R^2 = 0.974$ as:

$$Ln(t_f) = (5.66 - 22.295\ SF^{2.579})\ \left(301.476\ - 0.877\ \theta_{mis}^{1.153}\right)\left(-0.0082 + \frac{9.504}{P^{1.046}}\right)\left(2.706\ + \frac{9.511}{D^{0.287}}\right) \tag{56}$$

3.4.2 Probabilistic Macroscopic Crack Nucleation Model for Polycrystalline Ti Microstructures

Once the functional form of t_f versus stress and microstructural parameters is established, the next step would be the development of a probabilistic macroscopic model of crack nucleation for structural Ti components. This model is expected to predict the probability of crack nucleation at any point in the structure at any instant during the loading, knowing the microstructural features and stress level at that point. The model takes into account the distribution functions of orientation (SF), misorientation, and size to characterize the microstructure at a particular point in the structure.

Figure 79(a) shows a cantilever beam along with the distribution of macroscopic stress (σ_{xx}) obtained from a continuum-level FE simulation. Corresponding to any point in this cantilever, there is a microstructure shown in figure 79(b). The contour plot in this figure corresponds to the *c*-axis orientation of the grains. The acting stress state on this microstructure can be obtained from the continuum-level FE results of figure 79(a). If the microstructure associated with the point was simply the two-grain system of figure 73, equation 56 could be used to deterministically calculate the time-to-crack nucleation (or number of cycles-to-crack nucleation) at that point. However, there are many hard-soft grain combinations in the microstructure of figure 79(b). Therefore, instead of one value of *D*, *SF*, and θ_{misa} for the entire microstructure, there are distributions of these parameters. For each grain pair in the microstructure, a constituent grain is designated as hard or soft based on the highest basal/prism SF. Subsequently, the microstructure descriptors *D*, *SF*, and θ_{misa} are determined for each grain pair. Then a joint distribution function is generated for these parameters. The individual distribution functions for *D*, *SF*, and θ_{misa} for one sample microstructure are plotted in figures 79 (c, d and e, respectively). The distribution functions are generated based on the contact area fraction of grain pairs. It means that the grain pairs with larger contact area get more weight.

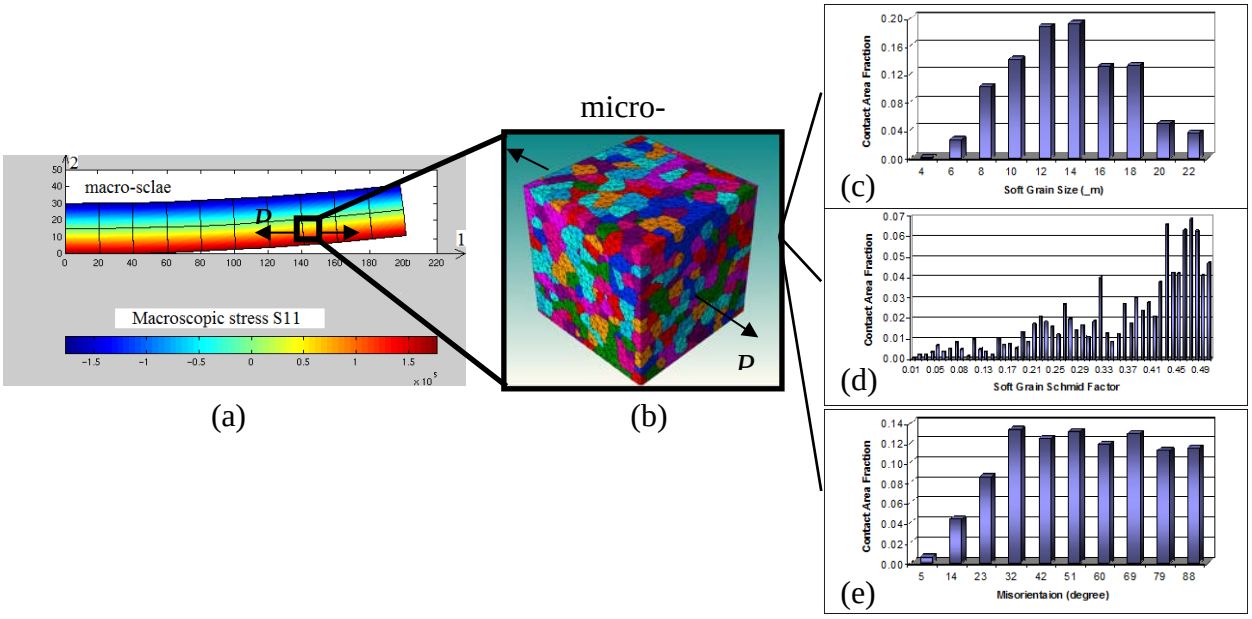

Figure 79. (a) Distribution of macroscopic stress σ_{xx} for a cantilever beam obtained from a continuum-level FE simulation; (b) microstructure corresponding to a material point in the cantilever; and (c–e) individual distribution functions for *D*, *SF* and θ_{mis} for the microstructure

If there are *N* grain pairs in the microstructure and the i^{th} grain pair in the microstructure with descriptors SF^i, θ^i_{mis} and D^i, the time-to-failure would be equal to t^i_f if the microstructure included only this grain pair, where:

$$t^i_f = \exp\left[\left[5.66 - 22.295\,(SF^i)^{2.579}\right]\left[301.476 - 0.877\,(\theta^i_{mis})^{1.153}\right]\left[2.706 + \frac{9.511}{(D^i)^{0.287}}\right]\left(-0.0082 + \frac{9.504}{P^{1.046}}\right)\right] \quad (57)$$

P is the macroscopic stress obtained from continuum-level FE simulations. Here it should be noted that equation 55 is applicable when one of the principal macroscopic stress components is considerably higher than the other components because this equation has been obtained from CPFE simulations of two-grain system RVEs under uniaxial loadings. In this case, SF^i is calculated with respect to the axis of maximum principal stress. This work can be generalized to consider all macroscopic stress components in the macroscopic crack nucleation model by conducting more CPFE simulations under different loading combinations, including shear, biaxial, and triaxial. In this case, instead of one, three SFs with respect to *x*, *y*, and *z* directions need to be considered. The i^{th} grain pair is a small part of the microstructure and does not fill the entire microstructure. Therefore, it is assumed that the probability of crack nucleation at $t = t^i_f$ is:

$$\Pr\Big|_{t=t^i_f} = \frac{C^i}{\sum_{i=1}^{N} C^i} \quad (58)$$

where C^i is the contact area between the constituent grains in the i^{th} grain pair. It should be noted that the definition for crack nucleation in the macroscopic model is different from that for grain-level crack nucleation.

Equation 56 cannot be used to predict grain-level crack nucleation in the microstructure of figure 79(b) for two reasons:

1. Equation 56 was obtained for one hard-soft grain pair where there is no influence of other grain pairs. However, in the microstructure of figure 79(b), every grain pair is affected by other grain pairs.
2. The applied stress on each grain pair of the microstructure is different from the macroscopic stress *P*.

The probability of macroscopic crack nucleation before a particular time t^* is then equal to:

$$\Pr\Big|_{t\le t^*} = \frac{\sum_{I}^{N} C^I}{\sum_{j=1} C^j} \qquad \text{where } I \in \mathbf{g}^* \tag{59}$$

$\mathbf{g}^*$ is the set of all grain pairs *I* for which $t_f^I \le t^*$, where t_f^i is evaluated from equation 57. A *FORTRAN* code has been written to obtain the probability of macroscopic crack nucleation for a given microstructure at different time points. The probability density function of $Ln(t_f)$ for two microstructures, namely M1 and M2, has been obtained using this FORTRAN code and plotted in figure 81(a). These two microstructures have different distributions of SF, θ_{ms} and D, as shown in figure 80 (a–c). M1 and M2 are subject to a creep load of $P = 800MPa$. Figure 81(b) shows the cumulative density function of $Ln(t_f)$ for these microstructures. It can be observed that at any time point the probability of macroscopic crack nucleation is lower for M1.

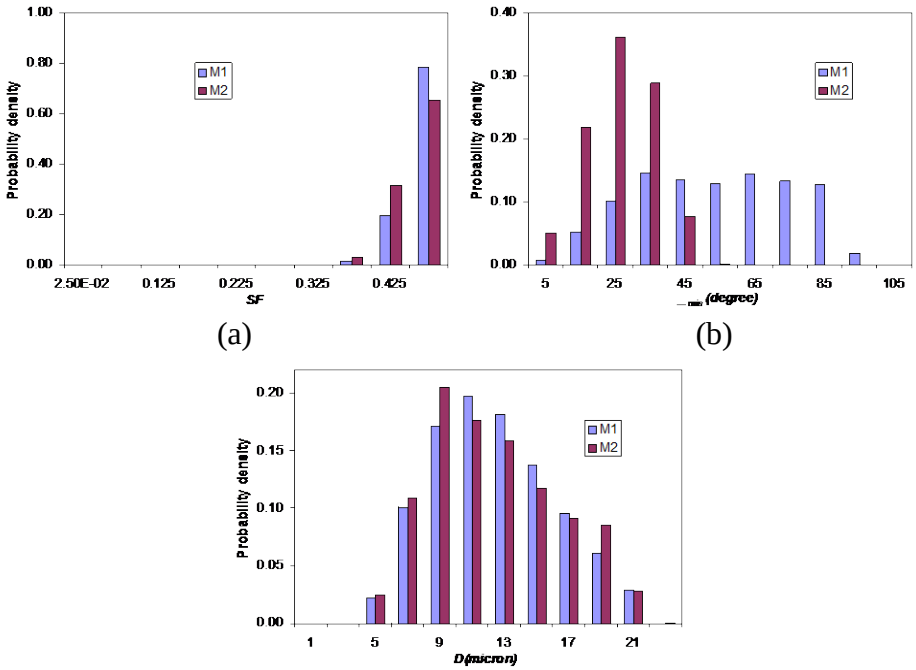

(a) (b) (c)

Figure 80. Distributions of (a) soft-grain SF; (b) misorientation; and (c) soft-grain size for microstructures M1 and M2

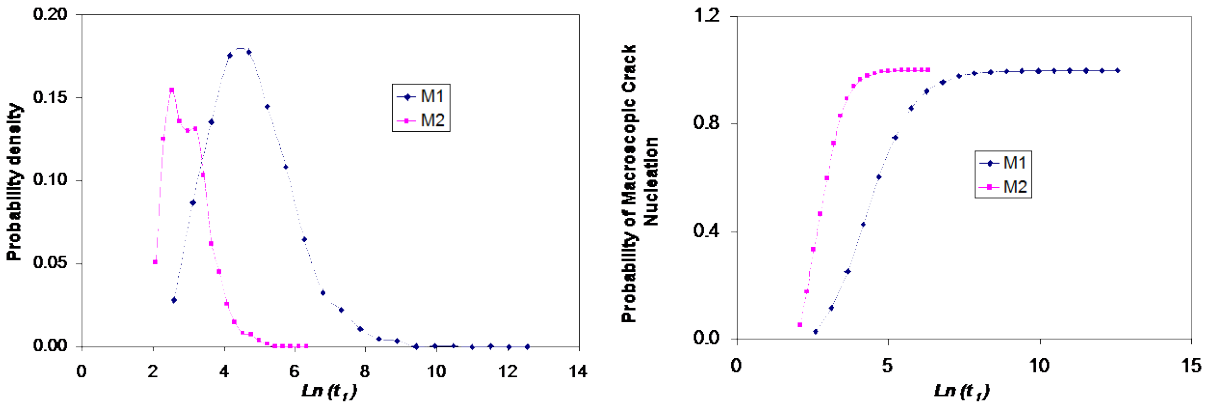

(a) (b)

Figure 81. (a) Probability density function of $Ln(t_f)$ and (b) cumulative density function of $Ln(t_f)$ for microstructures M1 and M2

4. SONIC ASSESSMENTS OF LEGACY HARDWARE

Research performed by the Ohio State University (OSU) team under FAA sponsorship has shown that a major variable in dwell-fatigue susceptibility is the presence, degree, and size of MTR, which are mostly controlled by processing history, including factors such as forging billet diameter and heat treatment practice. Microtexture is physically manifested as regions of the microstructure in which hexagonal α-phase crystallites share a common crystallographic orientation over a long range so that their collective size significantly exceeds the primary α grain size. Discussions with the OEMs have revealed that awareness of the microstructure issue has increased over time. Details of current practices vary between companies, but all are being tailored to manage the presence of microtexture. This creates an important need to assess nondestructively, at least qualitatively, the degree and size of MTRs of older, legacy material. The existence of such nondestructive capabilities for assessing this material characteristic would be very helpful in managing the risk associated with the hardware of varying vintage in the fleet.

Therefore, the main objectives of this part of the project were to demonstrate the existence of correlations between ultrasonic parameters and dwell-sensitive microtextural and microstructural properties, and to develop ultrasonic methods for grading Ti-6242 legacy materials as related to different levels of the microtexture.

The results of the study and development of ultrasonic methods for this purpose are described below.

4.1 APPROACH, RESULTS, AND DISCUSSION

4.1.1 Screening Tests by Ultrasonic Attenuation of Field Legacy Hardware Samples

Twenty samples have been provided by original equipment manufacturer (OEM) #1 as representative of field legacy hardware samples. Screening attenuation and back reflection measurements were performed on all obtained samples (see figure 82). Data representation shown in figure 83 indicates that measured ultrasonic attenuation reasonably correlates with the microtexture factors (the colony factors) that were provided for those samples by the OEM. Both automated and manual measurements by different operators have been explored showing consistency of the results. In addition, some anomalous samples, which did not exhibit correlation similar to most of the samples, were identified.

Analysis of the preliminary results led the team to select several samples (from those 20 OEM samples) for detailed microtextural/microstructural and ultrasonic studies; those samples have included anomalous samples and samples that have the most significantly different ultrasonic attenuations. This selection is sufficiently generic, so the understanding of the ultrasonic wave interaction with microstructure in those samples, and the methodology developed for microtexture grading, are applicable to a wide range of near-alpha titanium alloys.

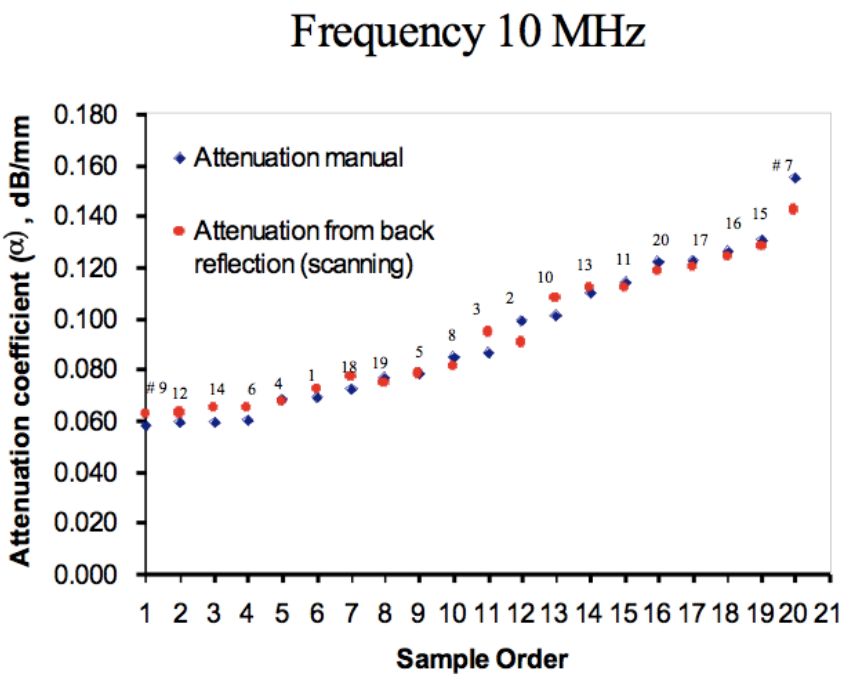

Note: The dark blue points represent the manual attenuation measurements, and the red points are obtained by C-scan using back reflection at 10MHz.

Figure 82. Attenuation coefficients for all samples

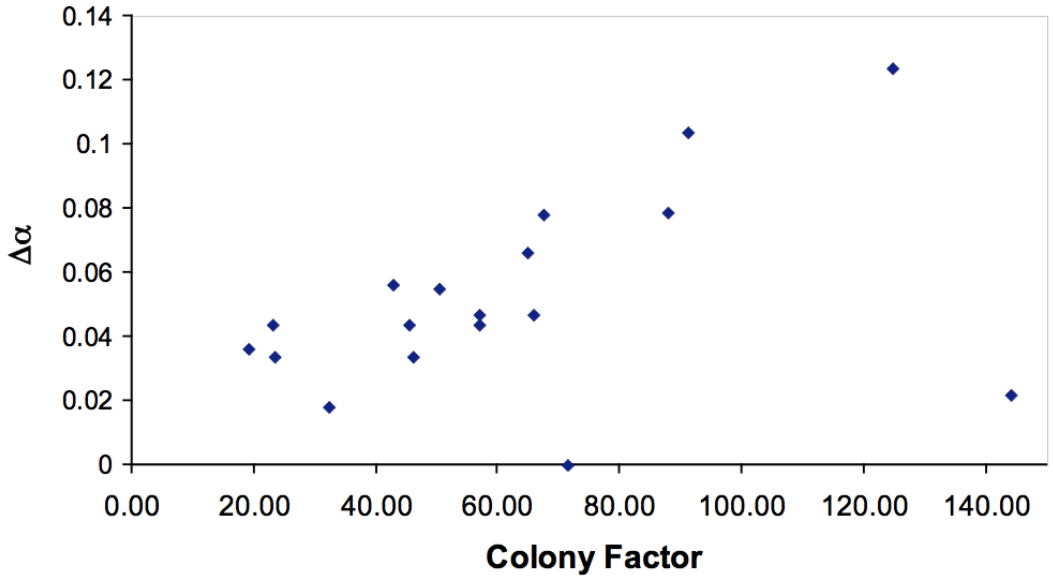

Figure 83. Reduced attenuation coefficient (dB/mm) vs. microtexture (colony) factor at frequency of 15MHz; the colony (microtexture) factor was provided by OEM

4.1.2 Preparation and Material Characterization of Field Hardware Samples

A detailed material characterization study was performed on four different samples selected from those provided by commercial aero-engine companies as representative field legacy hardware. The labels of samples in this group have been changed compared with those listed in figure 82: Sample 1 = Sample 7; Sample 2 = Sample 17; Sample 3 = Sample 9; Sample 4 (perpendicular) = Sample 5 (axial); and Sample 4 (parallel) = Sample 5 (radial). Each of these samples was cut into approximately a 30 x 30 x 60 mm rectangle for ultrasonic measurements. The samples are in the $\alpha + \beta$ forged condition. For metallographic studies, a 3-mm-thick slice was cut from the disc in such a way that the direction of propagation of ultrasonic waves was contained in the plane of polish of the sample (see figure 84(a)). A small rectangular piece was extracted from the slice for metallographic study and EBSD analysis (see boxed region in figure 84(b)). The slices were polished so that that the plane of polish contained the propagation plane of the longitudinal ultrasonic waves.

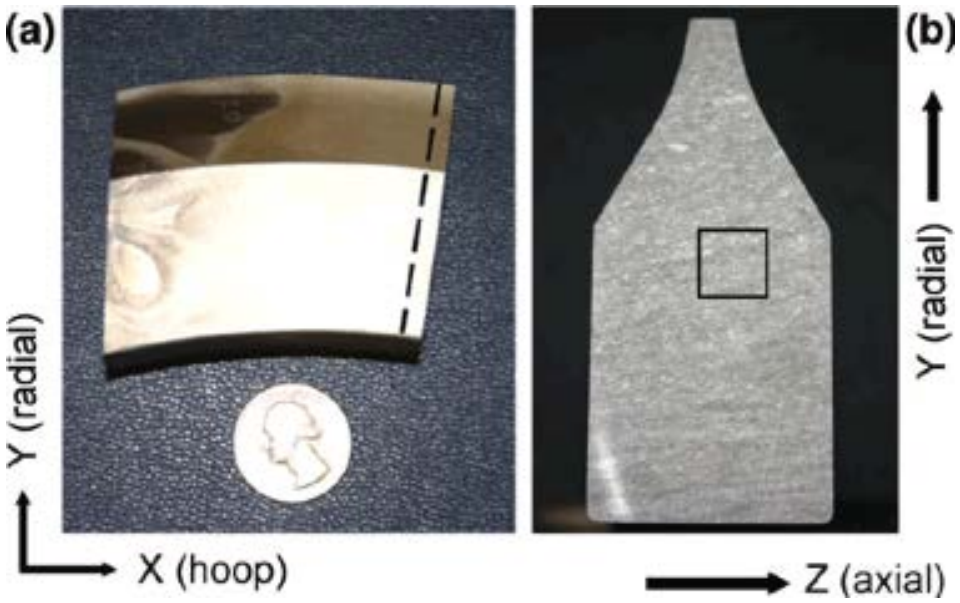

Figure 84. (a) Representative compressor disc section: the direction of longitudinal wave propagation was parallel to the *z*-axis (axial direction, into plane of image); (b)macro-etched metallographic slice from (a) identifying the location of the rectangular piece (boxed) that was excised for metallographic studies

Each sample was mounted on a round, flat stainless-steel platen and polished using MultiPrep™ precision parallel polisher (Allied High Tech Products, Rancho Dominguez, CA) and silicon carbide papers of 600-, 800-, and 1200-fine grit. Final polishing was done on a VibroMet™ 2 (Buehler, Illinois, USA) using 0.05 μm noncrystallizing colloidal silica suspension. Once all polishing had been completed, the samples were examined using SEM.

Backscattered electron images of the microstructures of all four samples are shown in figure 85(a–d). The samples all had bi-modal microstructures consisting of dark regions of globular primary α phase separated by transformed β regions consisting of fine lamellae of α and

β phase. The volume fraction of transformed β was highest in sample 1 and lowest in sample 2, having ~17% and 51%, respectively, whereas samples 3 and 4 contained 26% and 34%, respectively. In the present investigation, the α grain sizes were of the order of 10 μm.

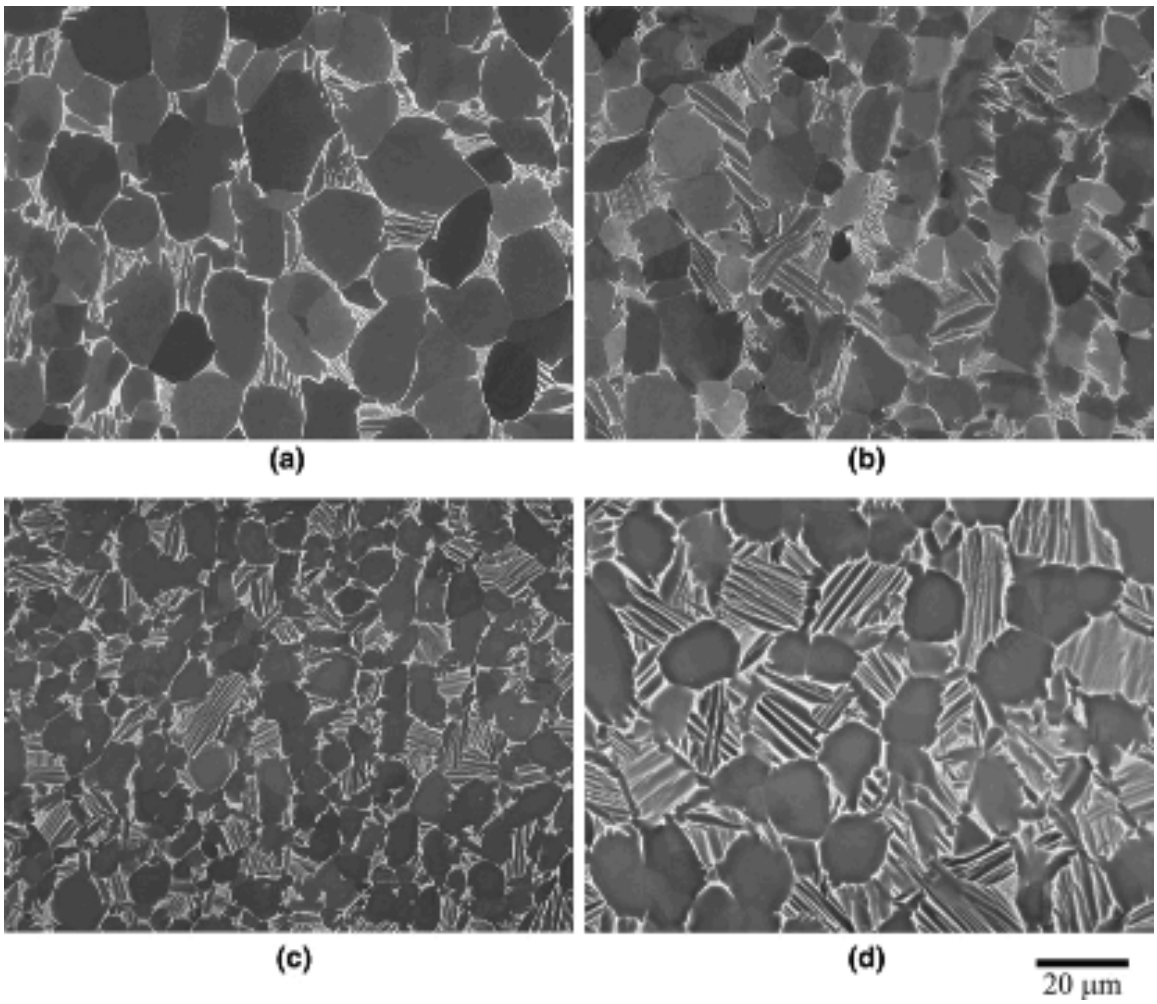

Figure 85. Backscattered electron images showing the microstructure of samples: (a) 1; (b) 2; (c) 3; and (d) 4: the primary (globular) alpha (α) phase appears darker, whereas the transformed beta (β), consisting of fine $\alpha + \beta$ colonies, appear brighter

EBSD data were acquired in the as-polished condition in a scanning electron microscope (Philips XL30 ESEM) to determine the degree of microtexture present in each of the samples. The ESEM was equipped with a field emission source and was operated at an accelerating voltage of 25 kV; a beam current of approximately 3nA EBSD scans was conducted using a combination of beam control (raster scans) and automated stage movements to cover large areas to obtain statistically useful information. Areas ranging from ~2–16 mm^2 were examined on all samples with step sizes between 1 μm and 3 μm to obtain statistically significant data. Larger areas were examined on samples that proved to have higher degrees of microtexture based on preliminary scans. Typical EBSD scans of those samples are shown in figure 86(a–d).

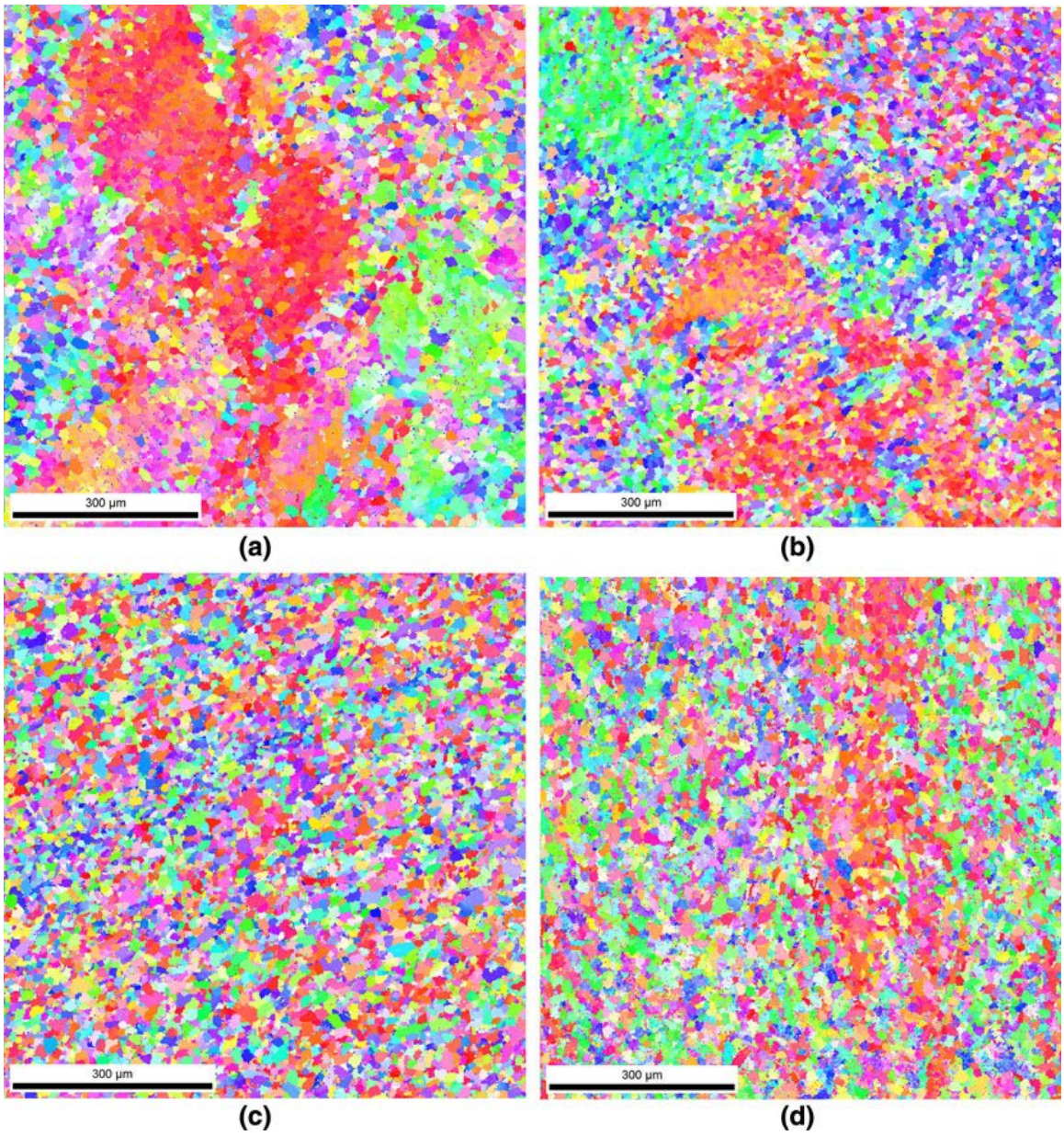

Figure 86. Representative tiles from larger EBSD (OIM) scans of (a) sample 1; (b) sample 2; (c) sample 3; and (d) sample 4: the incident ultrasonic wave traverses from left to right in the images

4.1.3 Ultrasonic Attenuation Measurement

Ultrasonic attenuation measurements were carried out at normal incidence by the immersion method in scanning mode, using a 12.7 mm diameter plane ultrasonic transducer with approximately 10 MHz central frequency of the received signal spectra. The transducer was positioned 25.4 mm from the top surface of the sample (see figure 87(a)). The ultrasonic wave was sent through the thickness of the compressor disc samples shown in figures 84(a) and 86(a) without any surface preparation. Prior to measurement, the sample and transducer were carefully aligned

to ensure normal incidence of the ultrasonic wave. The sample scanning, data acquisition, and data processing were performed using a computer control system developed in-house. Ultrasonic signals were excited and received by a pulser/receiver (Panametrics, USA) operating in pulse-echo mode. The received signals were amplified and digitized with a 12-bit, 125 MHz digitizing board and stored for further processing with in-house software. The digitized waveforms were gated for the fast Fourier transform (FFT), and then the frequency spectra were processed and analyzed. Front surface echo and first and second back wall reflections (figure 87(b and c)) were generally used for analysis. As an example, figures 87(b) and (c) show received-time domain signals (front surface and back reflections) and the corresponding spectra, respectively. Frequency dependencies of the attenuation coefficients, $att(f)$, were obtained for each sample by accounting for the ultrasonic diffraction correction and taking ratios of the frequency responses of the consecutive pulse reflections as:

$$att(f) = \frac{1}{2h} \ln\left[\frac{A_1(f)|D_2(f)|R_{tw}^2}{A_2(f)|D_1(f)|}\right] \tag{60}$$

Here $A_{1,2}(f)$ are the frequency spectrum amplitudes of the first and second reflections from the back surface, h is the sample thickness, and $|D_{1,2}(f)|$ are absolute values of the appropriate diffraction correction coefficients to compensate for beam spreading in the immersion fluid (water) and in the sample. The reflection coefficient $R_{tw} \approx 0.9$ for the Ti-water interface takes into account additional amplitude losses on the front and back surfaces of the sample. The normalized diffraction correction coefficient $D_m(f)$ for the m^{th} reflection in the sample is given in [68, 77]:

$$D_m(f) = 1 - \exp(-iq_m)[J_0(q_m) + iJ_1(q_m)] \tag{61}$$

where $J_{0,1}$ are the cylindrical Bessel functions. Equation 56 accounts for the beam diffraction effect in the immersion fluid and in the sample by use of the parameter $q_m = \pi f a^2/(V_0 Z_0 + m V_l h)$, which depends on the transducer radius a, distance z_0 between the transducer and the sample and its thickness h (the ultrasonic velocity, V_0, is 1.5 mm μs^{-1} in water while the velocity in titanium, V_l, is approximately 6.16 mm μs^{-1}). At the high frequency $(q_m >> 1)$, the normalized diffraction correction coefficient is close to unity but decreases at lower frequencies because of beam spread. Figure 87(d) shows the attenuation coefficient for sample 2 in the frequency range 4 to 17 MHz. The dependence is close to linear, except for the edges of the frequency interval, where the transducer spectrum amplitude is too low (see figure 87(c)), indicating limits of the acceptable frequency range.

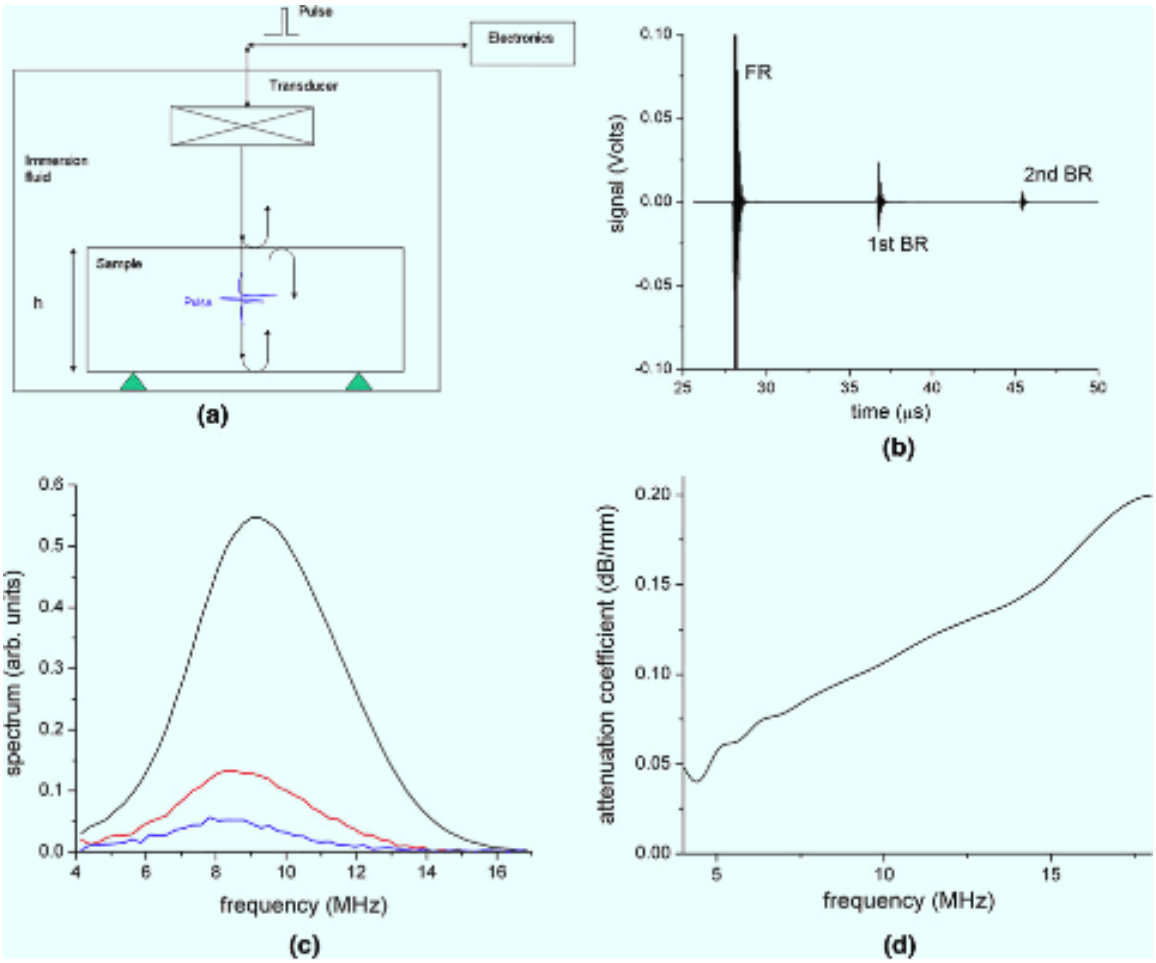

Figure 87. Determination of the attenuation coefficient vs. frequency: (a) measurement setup, (b) trace showing reflected signals vs. time (front surface reflection (FR), first (1st BR) and second (2nd BR) back wall reflections for sample 2), (c) frequency spectra of these signals, and (d) attenuation vs. frequency for sample 2. (Note that the signal and spectra amplitudes of the front surface reflection in (b) and (c) were reduced for the display)Ultrasonic Backscattering Measurement

The team's inversion method for microtexture grading from ultrasonic signature is based on relative directional measurements. The experimental procedure is focused on relative multidirectional measurements of backscattering signals to exclude an absolute transducer correction and other unknown experimental parameters.

The ultrasonic backscattering measurements were performed along several directions in engine-grade near-alpha titanium alloy samples discussed above. Because of forging and heat treatment procedures during processing, the MTRs have different sizes, shapes, and orientations for different samples. The microstructure/microtexture of the samples studied in this work was described in section 3. The MTR sizes vary from 100 microns to a millimeter in diameter, and their shapes may vary from pancake-like to cigar-like, depending on the forging history; in general, they can be modeled as arbitrary ellipsoids. However, the crystallites, in the samples studied, are nearly equiaxial and are 5–12 microns in diameter. Crystallites are mostly primary α grains with a small

fraction of α/β colonies. Detailed OIM and SEM of these samples are reported in section 2.2, where the determination of α crystallites and MTR sizes is described. The elastic properties of hexagonal α crystallites and α/β colonies used in the model have been measured recently [6].

The directional ratio of backscattering coefficients exhibits characteristic behavior in the frequency range 5–20 MHz for the MTRs and crystallite sizes of the samples (see figure 88). Therefore, this frequency range was selected for measurement. In this frequency range, the crystallite size is much smaller than a wavelength, and backscattering depends strongly on their size but is insensitive to their shape.

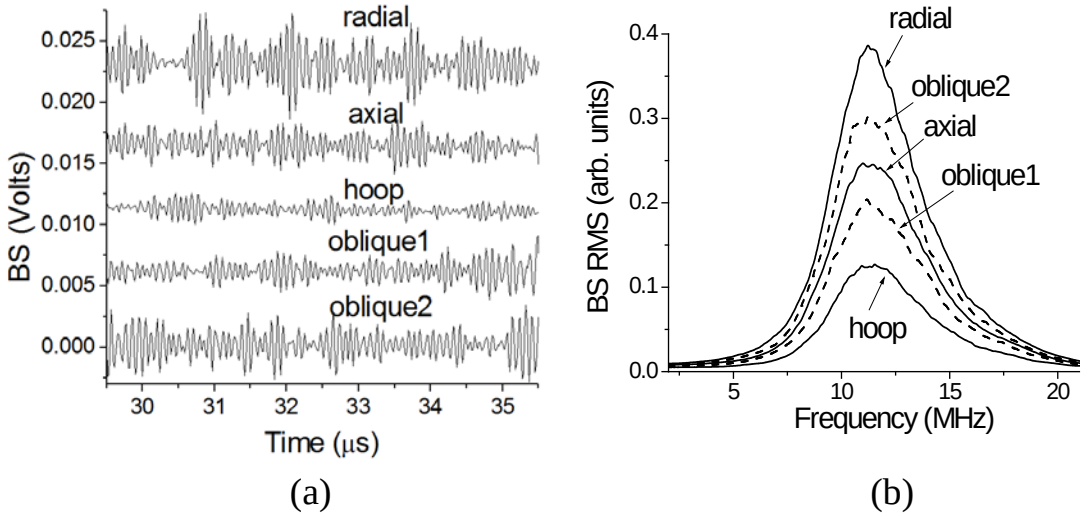

Figure 88. Backscattering measurements in different propagation directions (axial, radial hoop, and two oblique directions) for sample 2: a) backscattering signal vs. time in axial (the time traces in different directions are shown in the same scale and with an offset for comparison), and b) backscattered signal root mean square spectra for propagation in different directions

The root mean square (RMS) of the backscattering signal normalized on the transducer frequency response is proportional to the square root of the backscattering coefficient $\sqrt{\eta(f)}$ [92–94]. The theoretical model expression for this coefficient for near-alpha titanium alloys will be obtained in section 4.15 of this report. Immersion backscattering measurements were performed with a plane transducer 12 mm in diameter in three orthogonal and two oblique directions of the 30 x 30 x 60 mm rectangle samples; the center frequency of the signal spectra is 10 MHz. Oblique measurements were performed at $\pm 5^{o}$ in water, which corresponds to $\pm 21^{o}$ refraction angles in the sample. Samples were prepared from titanium alloy forgings having disk shape; therefore, the three orthogonal directions of the sample are identified as axial, radial, and hoop as they relate to the original part's forging. For normal incidence, samples were scanned over each of the six faces with 1 mm steps, and signals from 600 positions on every face were acquired.

Digitized signals were time averaged and acquired at about 40 μs duration for every spatial position; the first 6 μs of the signal inside the sample were gated for further processing (this

corresponds to the 18 mm propagation length in the sample). The 6 μs gating time of the backscattering signal was dictated by the time spacing between the front and back reflections in the shortest sample direction. Selection of the short gating times is also motivated by minimizing multiple scattering effects. The signal reverberation effect in the transducer was carefully excluded by gating; this reverberation is observed because of the very high amplification gain required for backscattering measurements. Also, the transducer tail and DC offset were removed by subtracting the spatially averaged time domain backscattered signal (BS) from each individual time domain signal [92, 93]. After FFT and spatial averaging, the $\mathrm{RMS} \sim \sqrt{\eta(f)}$ of backscattering signals versus frequency was obtained.

Measurements were performed from all opposite sample faces and two oblique angles (see figure 89). This allowed for an increase in the number of measurements and verification of the symmetry of backscattering in opposite NDs. It was found that in all cases, the RMS of the spatially averaged backscattering signals obtained from the two opposite sample faces were nearly identical for the same depth location inside the sample, while corresponding to different times of flight from the sample surface (i.e., the averaged backscattering attenuation is very small). This is the strongest indication that a single scattering phenomenon is a dominating factor in the measurements, and the effect of multiple scattering is negligible (because the multiscattering effect is expected to increase with the propagation distance as the single-to-multiple scattering transition occurs). The weak multiscattering effect at propagation times used in the experiments results from relatively small elastic anisotropy of the α crystallites [95, 96], which form the MTRs. The absence of multiple scattering effects is important for the interpretation of the measurements and comparison with the model discussed in the section 4.1.6.

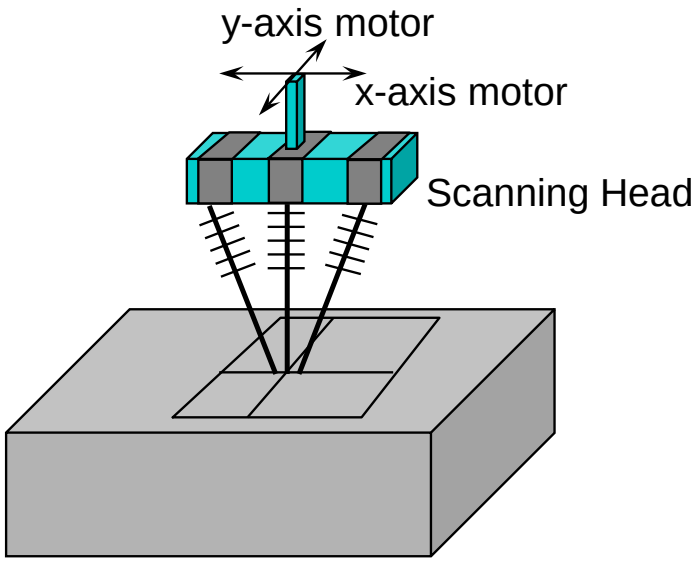

Figure 89. Normal and angle beam scanning with a specially designed scanning head

The ratio of backscattering signals, $\sqrt{\eta(f)} \sim \mathrm{RMS}$, versus frequency has been taken without any additional signal processing. The backscattering attenuation in the sample was not accounted for because it has a negligible effect on the directional ratios. This conclusion was based on the attenuation measurements in those samples. At 10 MHz, the spatially averaged apparent coherent attenuation obtained in pulse-echo mode in the different directions are: radial 0.012 Np/mm, hoop 0.016 Np/mm, and axial 0.013 Np/mm. It should be noted that in the highest backscattering direction (i.e., radial), the attenuation is the smallest, which is consistent with similar observations by others [97]. One should distinguish the apparent coherent attenuation obtained in this way and backscattering signal incoherent attenuations [98, 99]. This is, to a large degree, due to the scattering-induced incoherence of the received ultrasonic signal by a transducer; these attenuations can be different for the duplex titanium alloy by a factor of four [98]. This was also demonstrated by the measurements for the current research; however, further discussion of this topic is beyond the scope of this research because no attenuation correction is required for the data analysis of the directional backscattering ratios described below.

4.1.4 Backscattering/Attenuation Ratio Measurement

Ultrasonic scattering depends on the relative misorientation of crystallites, their elastic properties, and the crystallite size and morphology; however, observing MTRs in figure 86, it is clear that the effective elastic properties of MTRs are a priori unknown and, therefore, quantitative application of the models to analyze ultrasonic measurements is not always possible. Relative directional ultrasonic measurements discussed in section 4.1.4 allow excluding the elastic factor and inverting ultrasonic data for microstructural size determination. However, the backscattering ratio method proposed in this work, and briefly described in [100], requires access from different sides of the sample, which is not always practically possible. Therefore, an alternative relative method was developed for microstructural characterization from a single side of the sample: the backscattering-to-attenuation ratio method. In this method, a new effective parameter of microstructural size is explicitly defined and related to the measured data.

The combined method was then applied to the engine-grade near-alpha titanium samples: approximately 30 x 30 x 60 mm rectangles with the axial, radial, and hoop orthogonal directions. MTRs are generally several hundred microns, whereas crystallites are from 10–30 μm.

Backscattering and attenuation data were collected in a scanning mode from all six faces of the sample. During scan, time averaging of the digitized signal was done at each spatial position to reduce electronic noise for both backscattering and attenuation collection. During data processing, instrumentation noise was removed for backscattering. The first 6 μs of backscattering were gated for backscattering RMS calculation. Then another 6 μs of noise just before front reflection were also gated for the system noise estimation, which was then subtracted from backscattering RMS. Next, the backscattering RMS was divided by the front reflected signal and then normalized to obtain the absolute backscattering coefficient [92] with modification needed for the near field of the transducer. The attenuation coefficient was computed at each spatial position and then spatially averaged to represent attenuation in each sample direction. Using this method [100], the backscattering RMS ratio of every two directions (axial, radial, and hoop directions) of each sample was investigated, and the average interaction lengths of MTRs for each sample were inversely determined (they are consistent with the results determined from OIM).

Experimental results for sample 1 are presented in figure 90. Interaction lengths in axial, radial, and hoop directions determined by the backscattering ratio method are 1.00 mm, 0.80 mm, and 1.04 mm, respectively. Note that backscattering and attenuation have opposite behavior on the ellipsoid radii—in the axial direction, backscattering is smallest and attenuation is largest; in the radial direction, backscattering is largest and attenuation is smallest. These will be discussed in the following sections after a description of the models. Figure 90 shows the backscattering-to-attenuation ratio curves, in which the frequency range for curve fitting is from 10–12 MHz, as marked in the figure by short, dark lines that are used from the models. The principle of selection of the frequency range will be discussed in the simulation sections.

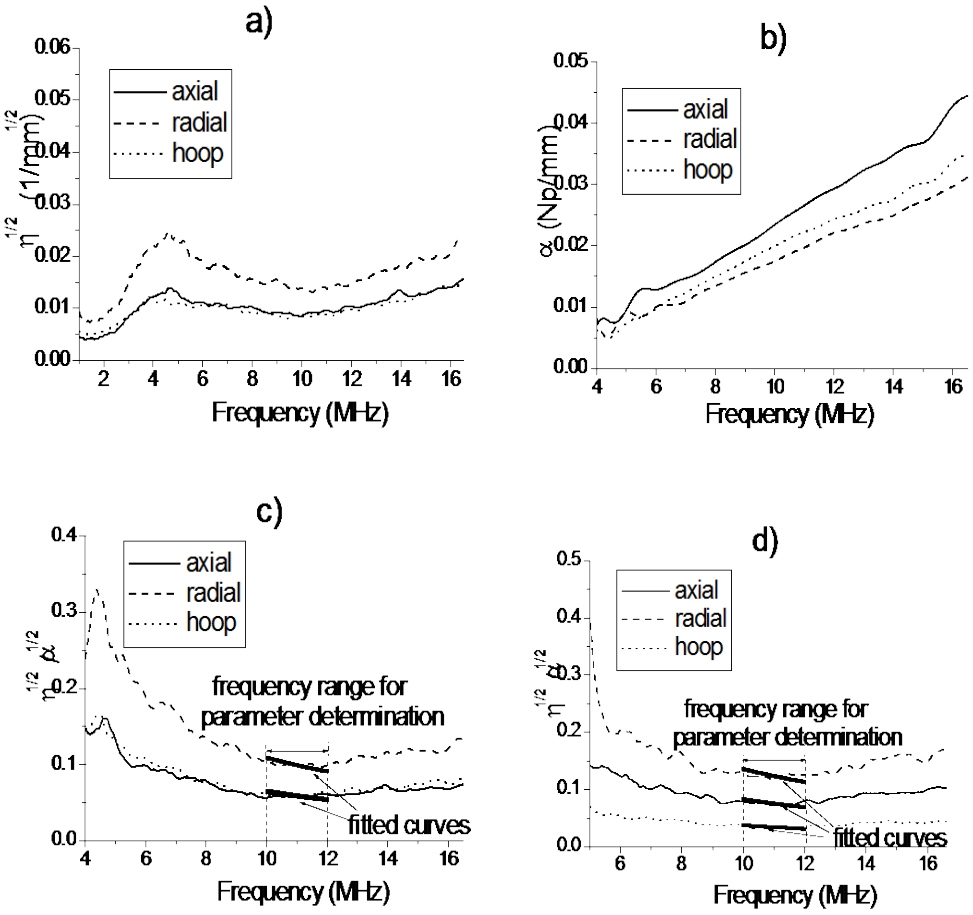

Figure 90. (a), (b), and (c) are experimental backscattering $\sqrt{\eta}$, attenuation α and backscattering-to-attenuation ratios $\sqrt{\eta}/\sqrt{\alpha}$ for the titanium alloy sample 1 in the axial, radial, and hoop directions, respectively; (d) is combined curves for sample 2. In (c) and (d), frequency ranges for the effective size parameter determination are marked by short thick lines

4.1.5 Ultrasonic Backscattering Model

4.1.5.1 Introduction

In this work, based on the backscattering theory [101–104], a new analytical solution was obtained for ultrasonic backscattering in polycrystals with elongated grains. This has allowed a complete analysis of the problem and new physical insights on the dependence of the backscattering signal on different microstructural parameters, and, in particular, demonstrates the dominant effect of ellipsoidal grain size in the direction of wave propagation, compared with that of the ellipsoidal cross-section. The BS dependences on frequency and ellipsoid size are transparent in the formulation. To characterize the degree of backscattering anisotropy, directional ratios of the backscattering coefficient have been introduced, which allow a significant reduction of the number of microstructural parameters needed to characterize the backscattering behavior. The study of materials with elongated grains is motivated by the commonality of such shapes after plastic deformation processing during manufacture. A simplified model was applied to analyze the titanium alloy microstructure shown schematically in figure 91(a) and described below. A detailed discussion of microstructure/microtexture of the titanium alloy samples used in this work is given in section 3.0 and [95]. An example of the model's application for characterization of duplex microstructure of titanium alloy has already been provided in a short communication [100], where the backscattering representation was reported without derivation.

The team's interest is in a different microstructural scale than that evaluated by Han and Thompson [104] and Panetta et al. [97], who have considered the material state in an earlier stage of thermomechanical processing. Whereas Han and Thompson mainly focused on arrangements of a second phase (which they called "colony") in the large macrograins (prime β grains of cubic symmetry), this work considered MTR (colony in their terminology) as the largest size phase formed by a secondary (small-size phase) of prime α crystallites (see figure 91(a)); the effect of those crystallites on backscattering was neglected in the model [104]. This report demonstrates in detail that for small crystallites, the effect of the MTR and crystallite elastic covariances and volumes are reduced to one parameter (i.e., their ratio), which may potentially be obtained from the experiment reported in [100], which showed that the team's backscattering model is applicable to the inversion of microstructural properties from ultrasonic measurements on titanium alloy. However, in [100], the MTR's main ellipsoidal radii were assumed to coincide with the laboratory coordinate system of the sample. This assumption is avoided in this report, and the general case is considered for the data analysis. After a brief theoretical background and the backscattering in single-phase materials with elongated grains, the model for microtextured duplex microstructure on an example of titanium alloys is discussed. It is demonstrated that multidirectional backscattering measurements allow one to reduce the number of parameters on which the backscattering amplitude (BA) depends. Finally, the application of the model to the data analysis in experiments on titanium alloy samples studied is described.

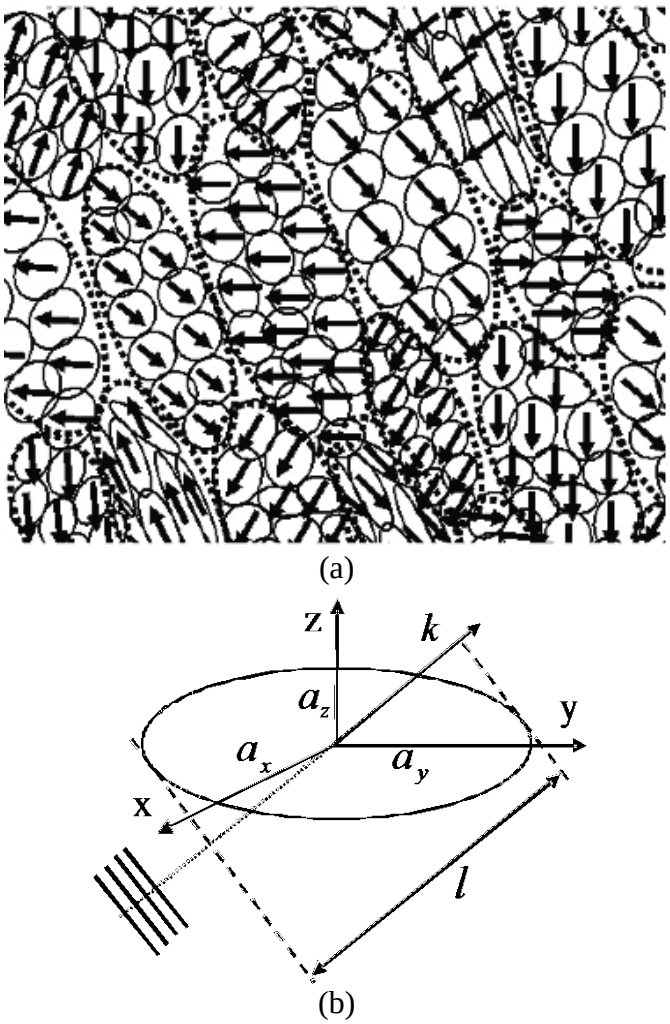

Figure 91. (a) Schematics of the model microstructure showing α crystallites ($10-20\mu m$) size as circles; arrows indicate their crystallographic orientation (the anisotropy axis c). Those crystallites in general may be of ellipsoidal shape. The neighboring crystallites have some degree of common orientation and forming MTRs, which are indicated by dashed ellipses (in the sample volume MTRs are modeled as general ellipsoids). (b) Geometry of ellipsoidal grains with the axes a_x, a_y, a_z. Ultrasonic wave propagates in arbitrary direction with wavevector $\vec{k}$ and l is an interaction length

4.1.5.2 Background: general formulation of backscattering integral for polycrystals

The analysis of this work is based on the general theory of backscattering (BS) developed in the Born approximation for polycrystalline materials [101–104]. In this model, the backscattering coefficient (the differential scattering cross-section per unit volume in the backscattering direction) for any polycrystalline medium is represented in the form of a spatial Fourier transform as:

$$\eta(\mathbf{k}) = \left(\frac{1}{4\pi\rho V_l^2}\right)^2 k^4 \int < \delta C_{3333}(\mathbf{X}) \delta C_{3333}(\mathbf{X}') > \exp\left(2i\mathbf{k}(\mathbf{X}-\mathbf{X}')\right) d^3(\mathbf{X}-\mathbf{X}'), \qquad (62)$$

Here $d^3(\mathbf{X}-\mathbf{X}')$ is the Euclidean volume element $\mathbf{X}$, $\mathbf{X}'$ are radius vectors in the coordinate system *x,y,z* ($|\mathbf{X}| = \sqrt{x^2+y^2+z^2}$); ρ is the density, and V_l is the longitudinal velocity of the homogenized medium; $k = 2\pi f / V_l$ is the wavenumber of the incident field at the frequency f. The function $< \delta C_{3333}(\mathbf{X}) \delta C_{3333}(\mathbf{X}') >$ (covariance) represents the two-point correlation function of the elastic stiffness resulting from elastic modulus fluctuations due to material microstructure. It depends on the local variation of the modulus from the average value C^0_{3333}, that is $\delta C_{3333}(\mathbf{X}) = C_{3333}(\mathbf{X}) - C^0_{3333}$and, assuming statistical homogeneity, it depends only on the radius difference $(\mathbf{X}-\mathbf{X}')$. The notation $< >$denotes ensemble average over the medium and $< \delta C_{3333}(\mathbf{X}) >= 0$.

The elastic and spatial components of covariance can be assumed to be independent for untextured [105, 106] and textured [107] microstructures, and the covariance representation for a single-phase microstructure can be written as:

$$< \delta C_{3333}(\mathbf{X}) \delta C_{3333}(\mathbf{X}') > = < \delta C_{3333}\, \delta C_{3333} > w(\mathbf{X}-\mathbf{X}'); \qquad (63)$$

Here, the covariance of the elastic stiffness $< \delta C_{3333}\, \delta C_{3333} >$ is the average over possible grain orientations, and the function $w(\mathbf{X}-\mathbf{X}')$ is the probability that the two points $\mathbf{X}$ and $\mathbf{X}'$ are located in the same grain; it depends only on the distance $\mathbf{X}-\mathbf{X}'$ between the points $\mathbf{X}$ and $\mathbf{X}'$. Equation 63 assumes that there is only the short-range correlation in one grain or between neighboring grains and that the long-range correlation between distant grains is negligibly small. Although long-range correlation can exist in specific structures, its contribution to backscattering decreases because of the rapidly oscillating exponential term $\exp(2i\mathbf{k}(\mathbf{X}-\mathbf{X}'))$ in equation 62, especially if the distance between these grains is larger than a wavelength ($\mathbf{k}(\mathbf{X}-\mathbf{X}') >> 1$). This means that the exponential term and the decreasing probability function $w(\mathbf{X}-\mathbf{X}')$ destroy any coherence of the distant grain signals, and, therefore, their contribution to backscattering is small.

4.1.5.3 Closed form of the backscattering coefficient for a single phase ellipsoidal grain

If an ultrasonic wave is considered to propagate in the direction $\mathbf{k} = (k_x, k_y, k_z)$ and the average scattering grain is modelled as an arbitrary ellipsoid with three different radii (a_x, a_y, a_z) (see figure 91(b)), in generalizing the exponential spatial correlation function used for equiaxial grains [96, 103]:

$$w(X) = \exp\left(-|\mathbf{X}|/a\right) \qquad (64)$$

where *a* is a correlation distance representing an effective grain radius. Ahmed and Thompson [108] and Han and Thompson [104] have selected the exponential spatial correlation function for an ellipsoidal shape grain as:

$$w(x,y,z) = \exp\left(-\sqrt{\frac{x^2}{a_x^2}+\frac{y^2}{a_y^2}+\frac{z^2}{a_z^2}}\right) \tag{65}$$

where a_x, a_y, a_z are characteristic average ellipsoid radii. The difference from the spherical grain with isotropic probability function is that the probability depends not only on distance but also strongly on direction in (x,y,z) space. Substituting equations 63 and 65 into the backscattering integral of equation 62, the backscattering coefficient becomes:

$$\eta(\mathbf{k}) = Qk^4 \int \exp\left(-\sqrt{\frac{x^2}{a_x^2}+\frac{y^2}{a_y^2}+\frac{z^2}{a_z^2}}\right) \exp(2i\mathbf{kX})\, d^3\mathbf{X}, \tag{66}$$

where the integration is over the whole space $d^3\mathbf{X} = dx\,dy\,dz$ and the integration variable $(\mathbf{X}-\mathbf{X}') \Rightarrow \mathbf{X}$ has been replaced. The normalized elastic covariance Q has been introduced as $Q = <\delta C_{3333}\,\delta C_{3333}> /(4\pi C_{3333}^0)^2$, where $C_{3333}^0 = \rho V_l^2$ is the average macroscopic elastic constant. For single-phase hexagonal polycrystals, the covariance may be expressed as $<\delta C_{3333}\,\delta C_{3333}> = (112A_1^2 + 48A_2^2 + 32A_1A_2)/1575$, where $A_1 = c_{33} - c_{11}$ and $A_2 = -c_{11} + c_{13} + 2c_{44}$, and c_{ij} are elastic constants (for the MTR, they are effective elastic constants).

In defining the probability function in equation 65 and the normalized elastic covariance Q, it can be assumed that ellipsoidal grains are aligned in a preferred direction because of prior material thermomechanical processing history. However, crystallographic orientations of different ellipsoidal grains are random and are not correlated, and the medium is elastically isotropic macroscopically. The integral of equation 66 has been evaluated numerically in spherical coordinates [104], where, for an ellipsoid of rotation $(a_x = a_y)$, it has been reduced to a 2D integral.

In this work, an exact, closed-form solution of the 3D integral of equation 66 was derived in elliptical coordinates for a general ellipsoidal grain shape (the derivation is summarized in section 4.1.6.4). The resulting backscattering coefficient depends on the geometry of the grain, the direction of wave propagation, and its frequency:

$$\eta(\mathbf{k}) = Q\frac{8\pi a_x a_y a_z k^4}{\left(1+4k_x^2a_x^2+4k_y^2a_y^2+4k_z^2a_z^2\right)^2} = \frac{QVk^4}{\left(1+k^2l^2\right)^2}, \tag{67}$$

where $k = \sqrt{k_x^2 + k_y^2 + k_z^2}$ and $V = \int w(x,y,z) d^3\mathbf{X} = 8\pi a_x a_y a_z$ is the effective volume of the grain. The denominator in equation 67 is represented as $\left(1 + k^2 l^2\right)^2$ where $l = 2\sqrt{n_x^2 a_x^2 + n_y^2 a_y^2 + n_z^2 a_z^2}$ is the interaction length, which is the inverse of the reciprocal ellipsoid diameter (size) in the direction of wave propagation and $\mathbf{n}$ is the wavenormal vector. A geometrical interpretation of the interaction length is shown in figure 91(b). The backscattering coefficient for spherical grains ($a_x = a_y = a_z = a$,) reduces to the known form [102, 103]:

$$\eta(k) = \frac{8\pi a^3 Q k^4}{\left(1 + 4k^2 a^2\right)^2}, \tag{68}$$

which does not depend on the wave-propagation direction because of symmetry.

Equation 67 and the introduction and interpretation of the interaction length *l* are the main results of this section.

4.1.5.4 Explicit solution of backscattering integral of equation (61)

The solution of the integral of equation 66 is performed in elliptical coordinates $(R, \theta, \varphi)$with substitution of the variables:

$$x = a_x R \sin\theta \cos\varphi, \;\; y = a_y R \sin\theta \sin\varphi, \;\; z = a_z R \cos\theta, \;\; \sqrt{\frac{x^2}{a_x^2} + \frac{y^2}{a_y^2} + \frac{z^2}{a_z^2}} = R. \tag{69}$$

The Jacobian of this coordinate transformation is $a_x a_y a_z R^2 \sin\theta$, and the scalar product in the complex exponent in the integrand of equation 66 is expressed as $k\mathbf{r} = k_x x + k_y y + k_z z = \; k_x a_x R \sin\theta \cos\varphi + k_y a_y R \sin\theta \sin\varphi + k_z a_z R \cos\theta$. In the new variables, equation 64 becomes:

$$\eta(\mathbf{k}) = Q k^4 a_x a_y a_z \int_0^{\infty} e^{-R} R^2 dR \int_0^{\pi} e^{2ik_z a_z R \cos\theta} \sin\theta \, d\theta \int_0^{2\pi} e^{2iR\sin\theta (k_x a_x \cos\varphi + k_y a_y \sin\varphi)} d\varphi. \tag{70}$$

The inner integral over φ is the integral representation of the zero order cylindrical Bessel function J_0 and equals $2\pi J_0(2\sqrt{k_x^2 a_x^2 + k_y^2 a_y^2}\, R\sin\theta)$, which gives:

$$\eta(\mathbf{k}) = 2\pi Q k^4 a_x a_y a_z \int_0^{\infty} e^{-R} R^2 dR \int_0^{\pi} e^{2ik_z a_z R \cos\theta} J_0(2\sqrt{k_x^2 a_x^2 + k_y^2 a_y^2}\, R\sin\theta) \sin\theta \, d\theta. \tag{71}$$

With the substitution $p = \sin\theta$, the integral on θ is reduced to a table integral [109]:

$$\int_0^{\pi} e^{2ik_z a_z R\cos\theta} J_0(2\sqrt{k_x^2 a_x^2 + k_y^2 a_y^2}\, R\sin\theta)\sin\theta\, d\theta =$$
$$= 2\int_0^1 \frac{\cos(2k_z a_z R\sqrt{1-p^2})}{\sqrt{1-p^2}} J_0(2\sqrt{k_x^2 a_x^2 + k_y^2 a_y^2}\, R\, p)\; p\, dp = \frac{2\sin(klR)}{klR}, \tag{72}$$

where $l = 2\sqrt{n_x^2 a_x^2 + n_y^2 a_y^2 + n_z^2 a_z^2}$ is the interaction length, and n_i is a component of the wavenormal vector. It should be noted that, in spite of the complexity of the integrand, the integral is a real function in accordance with the backscattering coefficient definition. After substitution of equation 71 into 72, the last integral over R is taken by parts:

$$\eta(\mathbf{k}) = \frac{4\pi Q k^4 a_x a_y a_z}{kl}\int_0^{\infty} e^{-R}\sin(klR)\, R\, dR = \frac{8\pi a_x a_y a_z Q k^4}{\left(1 + k^2 l^2\right)^2}, \tag{73}$$

and the final result is:

$$\eta(\mathbf{k}) = \frac{8\pi a_x a_y a_z Q k^4}{\left(1 + 4k_x^2 a_x^2 + 4k_y^2 a_y^2 + 4k_z^2 a_z^2\right)^2} \tag{74}$$

If $a_x = a_y = a_z = a$; $kl = 2ka$, which provides the known result for a sphere:

$$\eta(k) = \frac{8\pi a^3 Q k^4}{\left(1 + 4k^2 a^2\right)^2} \tag{75}$$

4.1.5.5 Backscattering in Microtextured Duplex Titanium Alloys

4.1.5.5.1 Background

To describe multiphase and two-phase duplex alloys, Rose [103] and Han and Thompson [104] proposed a generalization of the factorization given by equation 63. In the current research, the total covariance function can be presented using the two-point correlation functions for both phases as:

$$< \delta C_{3333}(\mathbf{X})\,\delta C_{3333}(\mathbf{X}') > = < \delta C_{3333}\,\delta C_{3333} >_r\, w_r(\mathbf{X}-\mathbf{X}') +$$
$$< \delta C_{3333}\,\delta C_{3333} >_\alpha\, w_r(\mathbf{X}-\mathbf{X}') w_\alpha(\mathbf{X}-\mathbf{X}') \tag{76}$$

The form of the second term emphasizes that the probability of two points falling in the same region of phase *r*, and the same crystallite α inside the phase *r* is the product of the two independent probabilities w_r and w_α. The length scales of the functions w_r and w_α are very different because every MTR (*r*) contains many smaller crystallites (α), and it is assumed that $w_r \approx 1$ in the second term in equation 76. Han and Thompson [104] proposed a model to calculate the covariance function for $< \delta C_{3333}\,\delta C_{3333} >_r$; they considered crystallographic orientations of microtextural

regions for titanium alloys, accounting for the activation of possible slip planes during plastic deformation. The covariance $<\delta C_{3333}\delta C_{3333}>_r$ can depend on metallurgical procedures of the samples and can be different from sample to sample. In their analysis, Han and Thompson [104] neglect the contribution of α crystallites on scattering; however, in the current research model, which is introduced in section 4.1.6.5.2, the α crystallites are the second phase and of major significance.

In section 4.1.6.5.2, a simplified backscattering model for a duplex microstructure, as it is applicable to the forged near-alpha titanium alloy, will be introduced. It is assumed that the larger phase *r* is composed of elongated MTRs, which are formed by smaller size Ti hexagonal primary α crystallites (phase α) with preferred orientation in the region and random small angle misorientations [95, 110]. The preferred orientation of α crystallites is not necessarily along the elongation direction of the MTR. To aid the discussion, the model microstructure is shown schematically in figure 91(a) with the α crystallites shown for simplicity as circles in figure 91(a) and the arrows indicating their crystallographic (c-axis) orientation (those crystallites could be of a general ellipsoidal shape). As shown in figure 91(a) the neighboring crystallites have some degree of common orientation, therefore forming *r*-phase MTR; these regions are indicated in figure 91(a) as dashed ellipses (these regions are modeled as arbitrary ellipsoids). Figure 86 shows examples of actual microtextures of forged Ti samples studied in this research. How the model describes the degree of the misorientation of crystallites in the MTRs will be discussed below.

4.1.5.5.2 M-factored backscattering model for duplex Ti microstructure

The model assumes that MTRs have a general ellipsoidal shape and their axes are preferably oriented because of thermomechanical processes (forging). However, crystallographic orientations of MTRs, determined by preferred orientation of the prime alpha crystallites, are random and not correlated with each other. It means the preferred orientation of the crystallites is arbitrary relative to the ellipsoid axes. It should be noted that because of the hexagonal symmetry of the crystallites, they are elastically isotropic in the plane perpendicular to the anisotropy axis of the crystallite and, therefore, their scatter is independent of rotation around this axis. The representation is further generalized in equation 76 by accounting for misorientation of the α crystallites in the MTR. The covariance function for crystallites includes their ODF to account for this preferred orientation, and after change of the integration variable in the ODF, it can be written as $M*<\delta C_{3333}\delta C_{3333}>_\alpha$. The parameter M $(0 \le M \le 1)$ is an average normalized characteristic, depending on the width of the average ODF, which could be measured from OIM scans by evaluating pole figures of EBSD spectra or other diffraction methods [111]. The homogenized elastic tensor in the covariance function for MTRs (*r*) depends on the ODF, and for the identical orientations of crystallites in the microtextural regions, $M = 0$, the MTR behaves like a single crystal (perfectly identical orientation of crystallites in the ellipsoid regions in figure 91(a)). For random, arbitrary orientation of the crystallites, $M = 1$, and, therefore, MTRs are absent because the covariance function for them is zero (for randomly oriented crystallites the ellipsoids of common orientation in figure 91(a) are absent). To emphasize this behavior, after renormalization, $(1-M)*<\delta C_{3333}\delta C_{3333}>_r$. Directional ratios of the BA will be discussed in section 4.1.8. The model will not require knowledge of *M* and computation of the covariance functions in comparison with the experiment because of mutual normalization of the backscattering directional ratios and because two

covariance functions eventually will be combined into a single parameter *q*, which can be determined from the experiment.

Finally, the backscattering coefficient of the duplex structure in the model is represented as the sum of backscattering coefficients for each phase, and the backscattering integral of equation 66 for the duplex structure is rewritten as:

$$\eta(\mathbf{k}) = (1-M)Q_r k^4 \int w_r(\mathbf{X}) \exp(2i\mathbf{kX})\, d^3\mathbf{X} + MQ_\alpha k^4 \int w_\alpha(\mathbf{X}) \exp(2i\mathbf{kX})\, d^3\mathbf{X} \qquad (77)$$

The normalized covariances of the elastic stiffness for the MTR and for the crystallite $Q_{r,\alpha} = <\delta C_{3333}\, \delta C_{3333}>_{r,\alpha} /(4\pi\rho V_l^2)^2$ were introduced here. The transition from a duplex to a single-phase microstructure can be accomplished in equation 77 by varying a single parameter *M*, representing the degree of the preferred orientation of crystallites in the MTR.

4.1.5.5.3 Backscattering Coefficient. Microstructural q-factor

For ellipsoidal grains with a known form of the probability function $w(\mathbf{X})$ given by equation 65, both integrals in equation 77 are explicitly evaluated as described before. Applying the closed form solution of equation 67 to the backscattering integral in equation 77 for the microtextured region-crystallite duplex microstructure, results in:

$$\eta(\mathbf{k}) = \frac{(1-M)Q_r V_r k^4}{\left(1+4k_x^2 r_x^2+4k_y^2 r_y^2+4k_z^2 r_z^2\right)^2} + \frac{MQ_\alpha V_\alpha k^4}{\left(1+4k_x^2 c_x^2+4k_y^2 c_y^2+4k_z^2 c_z^2\right)^2}, \qquad (78)$$

where r_x, r_y, r_z and c_x, c_y, c_z are characteristic average ellipsoid radii, and V_r and V_α are effective volumes for the two phases. Equation 78 allows one to calculate the total backscattering coefficient of the duplex structure depending on frequency and on the size, shape, and relative orientations of the MTRs and crystallites. Equation 78 was reported in [100] without a derivation and was applied to the average MTR size determination from measurements.

The BA $\sqrt{\eta(\mathbf{k})}$ for duplex structures with elongated MTRs is shown in figure 92 as a function of frequency. In this example, the crystallites are equiaxed grains with average radius $c_x = c_y = c_z = 10\mu\text{m}$ and the MTR is an arbitrary ellipsoid, relatively elongated in the z and y directions, with radii $r_x = 0.2\text{mm}, r_y = 0.4\text{mm}$, and $r_z = 0.3\text{mm}$. The MTR contains approximately $V_r / V_\alpha = 24{,}000$ crystallites. The solid lines in figure 92 show the total BA from the duplex microstructure in three directions. As in the single-phase case, the BS is strongest for wave propagation in the direction of the shortest radius r_x. The dashed lines, emanating from the solid lines, correspond to the backscattering contribution from the MTR only. The dotted line is the backscattering from the spherical crystallites, which is isotropic in all directions. In spite of the large difference in the sizes of MTR and crystallites ($r_x / c_x = 20, r_z / c_z = 30, r_y / c_y = 40$), the backscattering from the crystallites is comparable to MTR backscattering at frequencies above 15 MHz, especially in the larger radii directions y and z, because the MTR-induced backscattering is less in those directions. This example shows the

importance of taking into account the crystallite contribution to the duplex-structure backscattering.

For very high frequencies ($kc_x, kc_y, kc_z >> 1$), the second term in equation 78 will be dominant, and the total curves reach new plateaus, which are not shown in figure 92. Their levels depend on the crystallite shape $\sqrt{\eta_x/\eta_y} = (c_y/c_x)^2$, $\sqrt{\eta_x/\eta_z} = (c_z/c_x)^2$, and $\sqrt{\eta_y/\eta_z} = (c_z/c_y)^2$ in the same way as that of the MTR in the geometrical limit. For spherical crystallites, all total curves come to the same plateau $kc_z >> 1$; $\sqrt{\eta(kc_z)} \approx \sqrt{\pi M Q_\alpha / 2c_z}$.

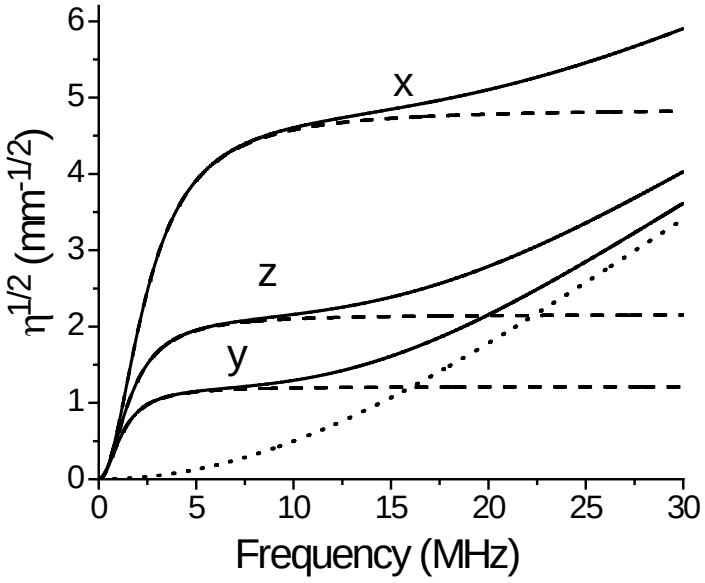

Figure 92. Spectral amplitude $\eta^{1/2}(f)$ of the backscattering signal RMS vs. frequency f for duplex structure (solid lines); dashed lines are the backscattering contribution of MTR without crystallite contributions ($q = 0$); the x, y, z are propagation directions; the dotted line is the backscattering contribution of crystallites solely. The MTR dimensions are $r_x = 0.2$ mm, $r_y = 0.4$ mm, $r_z = 0.3$ mm, and the crystallite dimensions are $c_x = c_y = c_z = 10$ ìm ; $(1-M)Q_r = MQ_c = 1$; $q = 4.17 \times 10^{-5}$

For a typical crystallite with an averaged radius of 0.010 mm, the scattering in the frequency range below 20 MHz is still in the Rayleigh limit (the longitudinal velocity in the titanium alloy is approximately $V_l \approx 6.2$mm/ìs and, therefore $kc_x \le 0.2$). Therefore, even for nonequiaxial crystallites, the backscattering contribution from the crystallites will be independent of their form: spherical, ellipsoidal, or other. It allows replacement of the second term in equation 78 with its Rayleigh limit $M Q_\alpha V_\alpha k^4$, and uses the notation for interaction length l in equation 65 to rewrite equation 78 for the backscattering coefficient as:

$$\eta(\mathbf{k}) = (1-M)Q_r V_r k^4 \left(\frac{1}{\left(1+k^2 l^2\right)^2} + q \right), \tag{79}$$

where a nondimensional microstructural parameter q is introduced:

$$q = MQ_\alpha V_\alpha / (1-M) Q_r V_r. \tag{80}$$

This parameter represents the relative contribution of the second phase (crystallites) to the backscattering signal. The factor V_α / V_r is a volume ratio and can be considered as a cubed size-scaling factor between large MTRs and the primary alpha crystallite. The factor $M/(1-M)$ scales the scattering contribution from MTRs and crystallites depending on crystallite misorientation within the MTRs. The ratio Q_α / Q_r depends on the relative volume fractions of primary α phase and α/β colonies (secondary α phase) in the MTR, which varies for different Ti forgings. If the primary α phase is dominant, the ratio Q_α / Q_r is of the order of one because misorientation of the alpha crystallites in the MTR is mainly accounted for by parameter *M*. Note that whereas $M/(1-M)$ in general is in the $(0-\infty)$ range, in most practical cases q is dominated by the volume ratio (V_α / V_r term). The introduction of a single nondimensional parameter *q* in equation 80 allows one to significantly reduce the number of microstructural parameters that determine ultrasonic backscattering in polycrystals with duplex microstructure, especially when the directional ratios are used.

4.1.5.5.4 Anisotropy of Backscattering Coefficient and Directional Ratios

The structure of equation 79, as a product of two factors, is very convenient for the description of the anisotropy of the backscattering in a duplex structure with elongated grains. The first term in the parenthesis of equation 79 determines the effect of the MTR geometry on backscattering anisotropy, and the second term q is the relative contribution of the second phase (crystallites) to the total backscattering of the duplex structure.

The parameter q is usually small ($q \ll 1$), even for a higher degree of misorientation of the crystallites, when $MQ_\alpha > (1-M)Q_r$; this is because of the small size of the crystallites and domination of the volume ratio factor ($V_\alpha / V_r \sim 10^{-4}$). At low frequencies, the Rayleigh range, ($kr < 1$, *r* is the average radius of the MTR) q can be omitted from the analysis, and the term in the parenthesis approaches 1. In this case, the backscattering coefficient is determined by the factor $(1-M)Q_r V_r k^4$, which is the Rayleigh limit of the backscattering coefficient for the MTR; it is an isotropic function and is independent of the direction of wave propagation.

For higher frequencies ($kr > 1$), the first term in parentheses in equation 79 decreases, and the two terms become comparable (they are equal at $q \approx (2kr)^{-4}$).

To characterize backscattering anisotropy, it is advantageous to introduce the backscattering ratio in different directions. For example, the ratio R_{ij} for i and j directions is:

$$R_{ij}(k) = \sqrt{\frac{\eta_i(k)}{\eta_j(k)}} = \left(\frac{\left(1 + k^2 l_i^2\right)^2 + q}{\left(1 + k^2 l_j^2\right)^2 + q} \right)^{1/2}, \qquad (81)$$

The dimensions l_i, l_j are the interaction lengths in these directions $l_i = 2\sqrt{i_x^2 r_x^2 + i_y^2 r_y^2 + i_z^2 r_z^2}$ and $l_j = 2\sqrt{j_x^2 r_x^2 + j_y^2 r_y^2 + j_z^2 r_z^2}$, where $i_{x,y,z}$ and $j_{x,y,z}$ are components of the unit wavenormal vectors $\mathbf{k}_i / k$ and $\mathbf{k}_j / k$ on the ellipsoid axes. In general, the directions *i*, *j* do not coincide with the ellipsoid axes ($i, j \neq x, y, z$).

The advantage of the directional ratio (see equation 81) is that it represents the relative scattering coefficient for the same sample, and therefore, the ultrasonic system effects are excluded. It depends on the value of the parameter q, which is determined from the experiment. The four directional ratios, R_{ij}, are presented in figure 93 versus frequency f; two for normal incidence on the sample surface, and two for the oblique incident angles in the sample at $\pm 21°$ in the axial-hoop plane. For this example, the main radii of the ellipsoidal MTR are $r_x = 0.16mm$, $r_y = 0.30mm$, $r_z = 0.18mm$ and parameter $q = 6.3 \times 10^{-5}$, *q* corresponds to the crystallite volume $V_\alpha = 8\pi(8\text{im})^3$; $MQ_\alpha/(1-M)Q_r = 1$. The tilt angle of the averaged MTR ellipsoid is θ = 69°, relative to the axial face normal of the sample in the axial-hoop plane. At low frequencies, all these ratios increase from 1, then reach maxima, and start decreasing to 1 beyond 10 MHz; they are larger than 1 because l_{hoop} is the largest interaction length in those directions of the MTR (the smallest BS coefficient). The corresponding ratios for the single-phase medium without the crystallite contribution ($q = 0$) are shown by dashed lines.

The ratio dependences are clear manifestations of the duplex structure, with anisotropic backscattering from the MTR and isotropic backscattering from the crystallites. Their rates of growth at low frequency, positions of maxima, and slopes at higher frequencies are determined by the microstructural parameters, and these factors can be used for their determination.

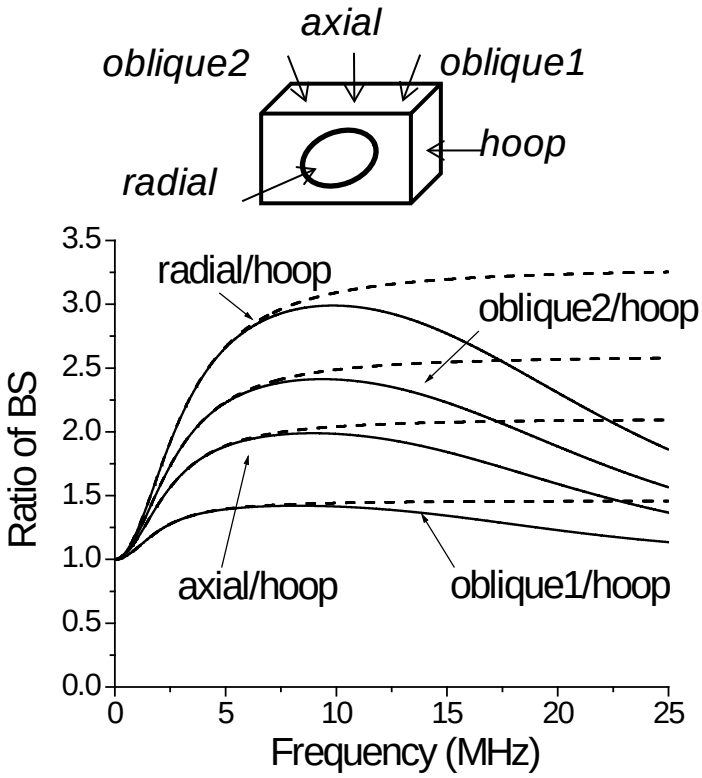

Figure 93. The directional ratios R_{ij} of the backscattering signal RMS vs. frequency f for two normal and two oblique incidence angles on the sample surface (oblique angles in the sample are $\pm 21^{\circ}$ in the axial-hoop plane); solid lines are for duplex structure, and dashed lines are the backscattering contribution of MTR without crystallite contributions ($q = 0$)

4.1.6 Attenuation Model for Titanium Alloys With Elongated Grains

4.1.6.1 Introduction

In this work, the Weaver [106] model is extended to a polycrystalline medium with elongated grains. The material model for titanium alloys was discussed in section 4.1.4 for ultrasonic backscattering. It is assumed that ellipsoidal grains are aligned in a preferred direction due to prior material thermomechanical processing history. However, crystallographic orientations of different ellipsoidal grains are random, and are not correlated, and the medium is elastically isotropic macroscopically. The spatial autocorrelation function applied to describe backscattering is used to characterize the shapes of ellipsoidal grains. A simple analytical equation for the 3D FFT of this autocorrelation function was used to obtain a general solution for attenuation coefficients in a form suitable for effective computation. Explicit expressions were obtained from the general theory for attenuation coefficients in the low frequency (Rayleigh) and stochastic limits. Those solutions were generalizations of the classical Rayleigh and stochastic asymptotes, which allow one to elucidate and obtain new insights on the dependence of the attenuation on different parameters. In particular, in the Rayleigh limit, the attenuation is independent of the ellipsoid shape and

determined by its volume; however, above the Rayleigh regime, the attenuation is dominated by the ellipsoid grain size in the direction of wave propagation and is independent of the ellipsoidal cross-section. This last result is counterintuitive and cannot be discerned from the equiaxed grain model. The shape effect of ellipsoidal grains is further simulated in the entire frequency range below the geometrical limit.

The results obtained are in the Born approximation. This approximation is defined differently from that usually referenced as the Born approximation [105, 106]. Briefly, in this approximation, the term $(k\bar{d})^2-(k_0\bar{d})^2$ is replaced by $2(k_0\bar{d})[(k\bar{d})-(k_0\bar{d})]$, where k is a wavenumber in polycrystalline medium, and k_0 is an unperturbed wavenumber. Some approximations are made to solve the nonlinear dispersion equation regarding k; $\bar{d}$ is an average grain size. As a result, the approximation is applicable when the perturbation in the wavenumber of the propagating wave is small and is not valid in the geometrical acoustics range. The effect of this approximation has been estimated by Stanke and Kino [105], who showed that both solutions are nearly identical for low-anisotropy crystals, such as Al, and have approximately 12% difference in the Rayleigh regime for high-anisotropy crystals, such as iron (this is a relatively small difference when compared with experiment because of variability in grain size and other experimental factors). The results in the Born approximation are valid even in a high-frequency stochastic regime because the anisotropy factor for titanium alloys is relatively low [95, 112].

The detailed derivation of the ultrasonic attenuation model for cubic polycrystalline materials with elongated grains, obtained during this research, is given in [113]. Only the final results of the attenuation model applicable to titanium alloys with elongated grains will be provided in this report because derivation on ultrasonic attenuation in hexagonal polycrystalline materials (near-alpha titanium alloys) is similar. Those results use inner products obtained in this work for hexagonal crystallites as is described in [113].

4.1.6.2 General representation of attenuation coefficients

It has been demonstrated [106, 113] that, in the Born approximation, the general solution for attenuation coefficients may be presented as:

$$\begin{aligned}\alpha_L &= \alpha_{LL}+\alpha_{LT},\\ \alpha_T &= \alpha_{TT}+\alpha_{TL}\end{aligned} \tag{82}$$

where the attenuation components $\alpha_{LL},\alpha_{LT},\alpha_{TL},\alpha_{TT}$ are given as:

$$
\begin{aligned}
\alpha_{LL}(\mathbf{p}) &= \frac{k_L^4}{32\pi^2\rho^2 V_L^4}\int W_{LL}(\mathbf{p},\mathbf{s})IP_{LL}(\mathbf{p},\mathbf{s})d^2\mathbf{s},\\
\alpha_{LT}(\mathbf{p}) &= \frac{k_T^4}{32\pi^2\rho^2 V_L^3 V_T}\int W_{LT}(\mathbf{p},\mathbf{s})IP_{LT}(\mathbf{p},\mathbf{s})d^2\mathbf{s},\\
\alpha_{TL}(\mathbf{p}) &= \frac{1}{2}\frac{V_T^2}{V_L^2}\alpha_{LT}(\mathbf{p})\\
\alpha_{TT}(\mathbf{p}) &= \frac{k_T^4}{64\pi^2\rho^2 V_T^4}\int W_{TT}(\mathbf{p},\mathbf{s})IP_{TT}(\mathbf{p},\mathbf{s})d^2\mathbf{s}
\end{aligned}
\tag{83}
$$

Integration in equation 83 is over a unit sphere; $W_{QM}(\mathbf{p},\mathbf{s})$ is the spatial Fourier transform of the two-point correlation function $w(\mathbf{r})$, which was obtained in this work [113]; $\mathbf{p}$ and $\mathbf{S}$ are the unit propagation and scattering wavevectors. The quantities $IP_{QM}(\mathbf{p},\mathbf{s})$, which will be specified below, are the inner products of the covariance of elastic modulus with the unit propagation p_i and scattering s_i wavevectors, and the respective displacement polarization vectors u_i and v_i. Indices *QM* = *LL*, *LT*, or *TT* describe mode conversion between longitudinal (*L*) and transverse (*T*) waves during scattering. $k_Q = \omega/V_Q = 2\pi f/V_Q$ is the wavenumber, where ω and f are, respectively, the angular and natural frequency, $V_Q = V_L$, V_T is the macroscopic longitudinal (*L*), or transverse (*T*), wave velocity. Equation 83 is of general form and should be evaluated for any specific crystalline symmetry. For the cubic symmetry, the computable form of equation 83 can be found in [77], and that for the hexagonal is given below.

4.1.6.3 Attenuation coefficients for titanium alloys with elongated grains

In a similar manner, the nondimensional attenuation coefficients for hexagonal crystallites are expressed as [113]:

$$
\begin{aligned}
\alpha_{LL}a_x &= \frac{x_L^4 R_0 R_1}{4\pi V_L^4\rho^2}\int_0^{2\pi}\int_0^{\pi}\frac{I_{LL}(\theta,\varphi)}{\left[1+S_{LL}^0+S_{LL}^1+S_{LL}^2\right]}\sin\theta d\theta d\varphi,\\
\alpha_{LT}a_x &= \frac{x_T^4 R_0 R_1}{4\pi V_L^3 V_T\rho^2}\int_0^{2\pi}\int_0^{\pi}\frac{I_{LT}(\theta,\varphi)}{\left[1+S_{LT}^0+S_{LT}^1+S_{LT}^2\right]}\sin\theta d\theta d\varphi,\\
\alpha_{TL}a_x &= \frac{1}{2}\left(\frac{V_T}{V_L}\right)^2\alpha_{LT}a_x,\\
\alpha_{TT}a_x &= \frac{x_T^4 R_0 R_1}{8\pi V_T^4\rho^2}\int_0^{2\pi}\int_0^{\pi}\frac{I_{TT}(\theta,\varphi)}{\left[1+S_{TT}^0+S_{TT}^1+S_{TT}^2\right]}\sin\theta d\theta d\varphi,
\end{aligned}
\tag{84}
$$

where S_{QM}^0, S_{QM}^1 **and** S_{QM}^2 are:

$$\begin{aligned} S_{QM}^0 &= x_Q^2 + x_M^2 - 2x_Q x_M (\mathbf{p}\cdot\mathbf{s}) \\ S_{QM}^1 &= (R_0^2 - 1)(x_Q \cos\tau - x_M \cos\theta)^2 \\ S_{QM}^2 &= (R_1^2 - 1)(x_Q \sin\tau \sin\varphi_\tau - x_M \sin\theta \sin\varphi)^2 \end{aligned} \tag{85}$$

and $x_Q = k_Q a_x$ is the nondimensional frequency index where *Q* designates the wave type *L* or *T*:

$$\begin{aligned} &x_L = \omega a_x / V_L = k_L a_x, \quad x_T = \omega a_x / V_T = k_T a_x \\ &\mathrm{X} = \mathbf{p}\cdot\mathbf{s} = \cos\theta_{ps}, \quad R_0 = a_z / a_x, \quad R_1 = a_y / a_x \end{aligned} \tag{86}$$

θ_{ps} is the angle between propagation and scattering directions.

To calculate the attenuations, the inner products $I_{QM}(\theta,\varphi)$ in equation 84 are necessary for hexagonal crystallite symmetry. As has been discussed in [112, 113], the inner products $I_{QM}(\theta,\varphi)$ characterize the elastic components of the covariance of the moduli fluctuations while waves are propagating in the aggregates. The general form of $I_{QM}(\theta,\varphi)$ can be written in terms of different combinations of inner products of wave propagating, scattering, and polarizing vectors. For simplicity, only final results of the inner products are provided here for calculation of attenuations. Therefore, the inner products may be expressed in the form:

$$\begin{aligned} I_{LL}(X) &= A_{LL} + B_{LL}X^2 + C_{LL}X^4, \\ I_{LT}(X) &= A_{LT} + B_{LT}X^2 + C_{LT}X^4, \\ I_{TT}(X) &= A_{TT} + B_{TT}X^2 + C_{TT}X^4, \end{aligned} \tag{87}$$

where the coefficients $A_{QM}, B_{QM},$ **and** C_{QM} are expressed as:

$$
\begin{aligned}
A_{LL} &= \frac{4}{45}A^2 + \frac{8}{1575}D^2 + \frac{8}{315}AD, \\
B_{LL} &= \frac{4}{15}A^2 + \frac{16}{15}B^2 + \frac{92}{1575}D^2 + \frac{64}{45}AB + \frac{32}{63}BD + \frac{88}{315}AD, \\
C_{LL} &= C_{TT} = -C_{LT} = \frac{16}{45}B^2 + \frac{4}{525}D^2 + \frac{32}{315}BD, \\
A_{LT} &= \frac{2}{15}A^2 + \frac{4}{15}B^2 + \frac{2}{105}D^2 + \frac{4}{15}AB + \frac{4}{35}BD + \frac{8}{105}AD, \\
B_{LT} &= \frac{28}{45}B^2 + \frac{32}{1575}D^2 + \frac{4}{15}AB + \frac{68}{315}BD + \frac{4}{105}AD, \\
A_{TT} &= \frac{13}{45}B^2 + \frac{23}{1575}D^2 + \frac{26}{315}BD, \\
B_{TT} &= -\frac{1}{3}B^2 - \frac{1}{175}D^2 - \frac{2}{21}BD.
\end{aligned}
\tag{88}
$$

Where:

$$
X = \hat{\mathbf{p}} \cdot \hat{\mathbf{s}} = \cos(\phi - \phi_\tau)\sin\theta\sin\tau + \cos\theta\cos\tau, \tag{89}
$$

and:

$$
A = c_{13} - c_{12}, \quad B = c_{44} - c_{66}, \quad D = c_{11} + c_{33} - 2c_{13} - 4c_{44} \tag{90}
$$

and c_{ij} are the effective elastic constants of the MTR.

The inner products $I_{QM}(\theta,\varphi)$ are independent of the shape of the grains. This implies that the final results are only dependent on the separating angle θ_{ps} between wave propagation and scattering directions. The attenuation integrals are defined over the whole spatial region because of directional dependence on elongated grains. As discussed in [113], the obtained solution is not applicable in geometric region; therefore, high-frequency limit should be considered with care. When $a_x = a_y = a_z = a$, the nondimensional attenuations in equation 84 can be reduced to the result of a spherical grain [112]; and the inner products $I_{QM}(\theta)$ are as in equation 86 for equiaxed grains, with $X = \cos\theta_{ps} = \cos\theta$. This results from the assumption of $\tau = 0$, because of symmetry in equation 86, and because the integration in equation 84 is over the angle θ for scattered wave in the spherical coordinate system [112].

4.1.6.4 Rayleigh and stochastic limits

In Rayleigh and stochastic limits, the general attenuations can be simplified to analytical solutions. Those are valuable to illustrate the shape-dependence of ellipsoidal grains. In the Rayleigh limit where $x_L << 1$ and $x_T << 1$, the attenuations are given by:

$$\alpha_L = \frac{2\pi^3 f^4 V}{V_L^3 \rho^2}\left(\frac{\Delta_1}{V_L^5} + \frac{\Delta_2}{V_T^5}\right),$$
$$\alpha_T = \frac{2\pi^3 f^4 V}{V_T^3 \rho^2}\left(\frac{\Delta_3}{V_L^5} + \frac{\Delta_4}{V_T^5}\right), \tag{91}$$

where the coefficients Δ_i (i = 1, 2, 3, 4) are given by:

$$\Delta_1 = \frac{8}{45}A^2 + \frac{32}{75}B^2 + \frac{88}{3375}D^2 + \frac{64}{135}AB + \frac{128}{675}BD + \frac{16}{135}AD,$$
$$\Delta_2 = \frac{2}{15}A^2 + \frac{272}{675}B^2 + \frac{82}{3375}D^2 + \frac{16}{45}AB + \frac{112}{675}BD + \frac{4}{45}AD,$$
$$\Delta_3 = \frac{\Delta_2}{2},$$
$$\Delta_4 = \frac{28}{225}B^2 + \frac{8}{1125}D^2 + \frac{8}{225}BD. \tag{92}$$

The effective grain volume V is defined in a similar manner as $V = 8\pi a_x a_y a_z$. As discussed for cubic symmetry [113], the Rayleigh attenuation coefficients are independent of the shape of ellipsoidal grains, and dependent on the effective grain volume and the fourth power of the frequency. If the value of effective volume of ellipsoidal grains is assumed to be the value of effective volume of equiaxed grains, where $V = 8\pi a_x a_y a_z = 8\pi a^3$, the Rayleigh attenuations are exactly identical to the results discussed in [112]. It is seen that only the effective volume of grains can be inferred once attenuations are measured in this range; the size of grains cannot be determined from Rayleigh attenuations due to independence of the shape. This means that the attenuations are isotropic in the low-frequency range.

In the stochastic limit, the normalized frequencies are $x_L >> 1$ and $x_T >> 1$. As discussed in [113], the attenuations in an arbitrary direction may be written as:

$$\alpha_L^{\text{Stochastic}} = \frac{\pi^2 f^2 \Delta_5}{V_L^6 \rho^2} a_{ell}(a_i, \tau, \varphi_\tau),$$
$$\alpha_T^{\text{Stochastic}} = \frac{\pi^2 f^2 \Delta_6}{2V_T^6 \rho^2} a_{ell}(a_i, \tau, \varphi_\tau), \tag{93}$$

where $a_{ell}(a_i, \tau, \varphi_\tau)$ is the ellipsoid radius in the direction of wave propagation, defined as:

$$a_{ell}(a_i, \tau, \varphi_\tau) = \frac{a_x a_y a_z}{\sqrt{(a_y a_z \sin\tau\cos\varphi_\tau)^2 + (a_x a_z \sin\tau\sin\varphi_\tau)^2 + (a_x a_y \cos\tau)^2}}, \tag{94}$$

The solution in equation 74 can be reduced for propagation along ellipsoid axes. The attenuations are then given in three major axes (i = x, y, z) by:

$$\alpha_L^i = \frac{\pi^2 f^2 a_i}{V_L^6 \rho^2} \Lambda_5,$$
$$\alpha_T^i = \frac{\pi^2 f^2 a_i}{2V_T^6 \rho^2} \Lambda_6, \tag{95}$$

where the coefficients Λ_5 and Λ_6 are written as:

$$\Lambda_5 = \frac{16}{45}A^2 + \frac{64}{45}B^2 + \frac{16}{225}D^2 + \frac{64}{45}AB + \frac{64}{105}BD + \frac{32}{105}AD,$$
$$\Lambda_6 = \frac{14}{45}B^2 + \frac{26}{1575}D^2 + \frac{4}{45}BD. \tag{96}$$

Equations 93 and 94 show that the attenuation coefficients are dependent on the ellipsoidal radius in the propagation direction and are proportional to the frequency squared in high-frequency range. Those ratios of attenuations in this frequency range are linearly dependent on the ratio of the ellipsoidal radii. The ratios are potentially convenient for predicting the size of grains, using experimental measurements. The resulting stochastic attenuation may provide a tool to characterize shape effects of ellipsoidal grains, experimentally, by measuring attenuations.

4.1.6.5 Obtaining backscattering coefficient from attenuation in hexagonal polycrystalline medium with elongated grains

The nondimensional attenuation coefficients in equation 84 physically represent integration over grain scattering in different directions. Therefore, the backscattering coefficient for hexagonal polycrystalline materials with elongated grains can be directly obtained from the integrand in equation 84, given the longitudinal wave propagates in an arbitrary direction $\mathbf{k} = \mathbf{k}_L \mathbf{p}$. The longitudinal backscattering coefficient, $\eta(\mathbf{k})$in polycrystalline materials with elongated grains, directly follows equation 84 for scattering in a backward direction and when the attenuation coefficient is taken for energy flow. Therefore, the longitudinal wave backscattering coefficient for hexagonal polycrystals with elongated grains is:

$$\begin{aligned} \varsigma(\mathbf{k}) &= \frac{1}{\left(4\pi\ \rho V_l^2\right)^2} k_L^4 IP_{LL}(\pi) W_{LL}(\mathbf{q} = 2\mathbf{k}) \\ &= 2\alpha_{LL}(\theta_{ps} = \pi; q = 2k) \\ &= \frac{BS_h\, k^4\, V}{16\pi^2 \rho^2 V_l^4 \left[1 + 4k_{Lx}^2 a_x^2 + 4k_{Ly}^2 a_y^2 + 4k_{Lz}^2 a_z^2\right]}, \end{aligned} \tag{97}$$

where:

$$BS_h = \frac{112}{1575}(c_{33} - c_{11})^2 + \frac{48}{1575}(-c_{11} + c_{13} + 2c_{44})^2 + \frac{32}{1575}(c_{33} - c_{11})(-c_{11} + c_{13} + 2c_{44}), \tag{98}$$

and k_{Lx}, k_{Ly}, k_{Lz} are the longitudinal wavevector projections. Noting that $BS_h / 16\pi^2 \rho^2 V_l^4 = Q$, one observes that equation 97 is identical to that derived previously (equation 67) for the backscattering coefficient. This indicates one consistency of the attenuation and backscattering models.

4.1.7 Backscattering-to-Attenuation Ratio Model

As follows from equation 79, the backscattering coefficient is a sum of backscattering from two phases—MTRs and crystallites. As discussed, l is the interaction length along the wave propagation direction, which is interpreted in figure 94(a) as the distance from the wavefront entrance into the ellipsoid to its exit. The elastic factor Q is a parameter describing the elastic property of the MTRs, which is related to misorientation of the crystallites within the MTR. For samples of the same composition, Q may vary from one sample to another due to the thermomechanical processing history, and, therefore, Q is unknown a priori.

At medium frequencies, when $kl >> 1$ and $1/(k^2 l^2)^2 >> q$, the contribution of crystallites is small and can be neglected, and the backscattering coefficient in equation 79 can be expressed as:

$$\eta = Q \cdot V \cdot \frac{1}{l^4} \tag{99}$$

For attenuation in titanium alloys at MHz frequencies, the scattering from crystallites can also be neglected compared with that from MTRs. At high frequencies, including transition and stochastic regions, the attenuation coefficient is obtained from equation 84 as:

$$\alpha \sim Q \int_0^{\pi} \int_0^{2\pi} \frac{k_l^4 a_x a_y a_z \sin\theta \, d\theta \, d\varphi}{\left(1 + x_l^2 (p_x - \sin\theta\cos\varphi)^2 + y_l^2 (p_y - \sin\theta\sin\varphi)^2 + z_l^2 (p_z - \cos\theta)^2\right)^2} \tag{100}$$

where $x_l = k_l a_x$, $y_l = k_l a_y$, and $z_l = k_l a_z$; (p_x, p_y, p_z) are components of a unit wave vector. The parameter Q is the same as in equation 99. In the stochastic limit, equation 100 can be further simplified as:

$$\alpha = Q \cdot 4\pi^2 k_l^2 r \tag{101}$$

Here, r is the radius of the ellipsoid along the wave propagation direction, which is illustrated in figure 12(a).

By combining equation 99 and 101, the following ratio is given:

$$\sqrt{\frac{\eta}{\alpha}} = \frac{1}{8\pi k_l} \cdot \frac{\sqrt{V}}{(l/2)^2 r^{1/2}} \tag{102}$$

The square root of the ratio is used as it is related to the measured BA. Rewriting equation 102 as:

$$R_{eff} = \frac{(l/2)^2 r^{1/2}}{\sqrt{V/8\pi}} = \left(k_l \sqrt{8\pi} \sqrt{\frac{\eta}{\alpha}} \right)^{-1}, \tag{103}$$

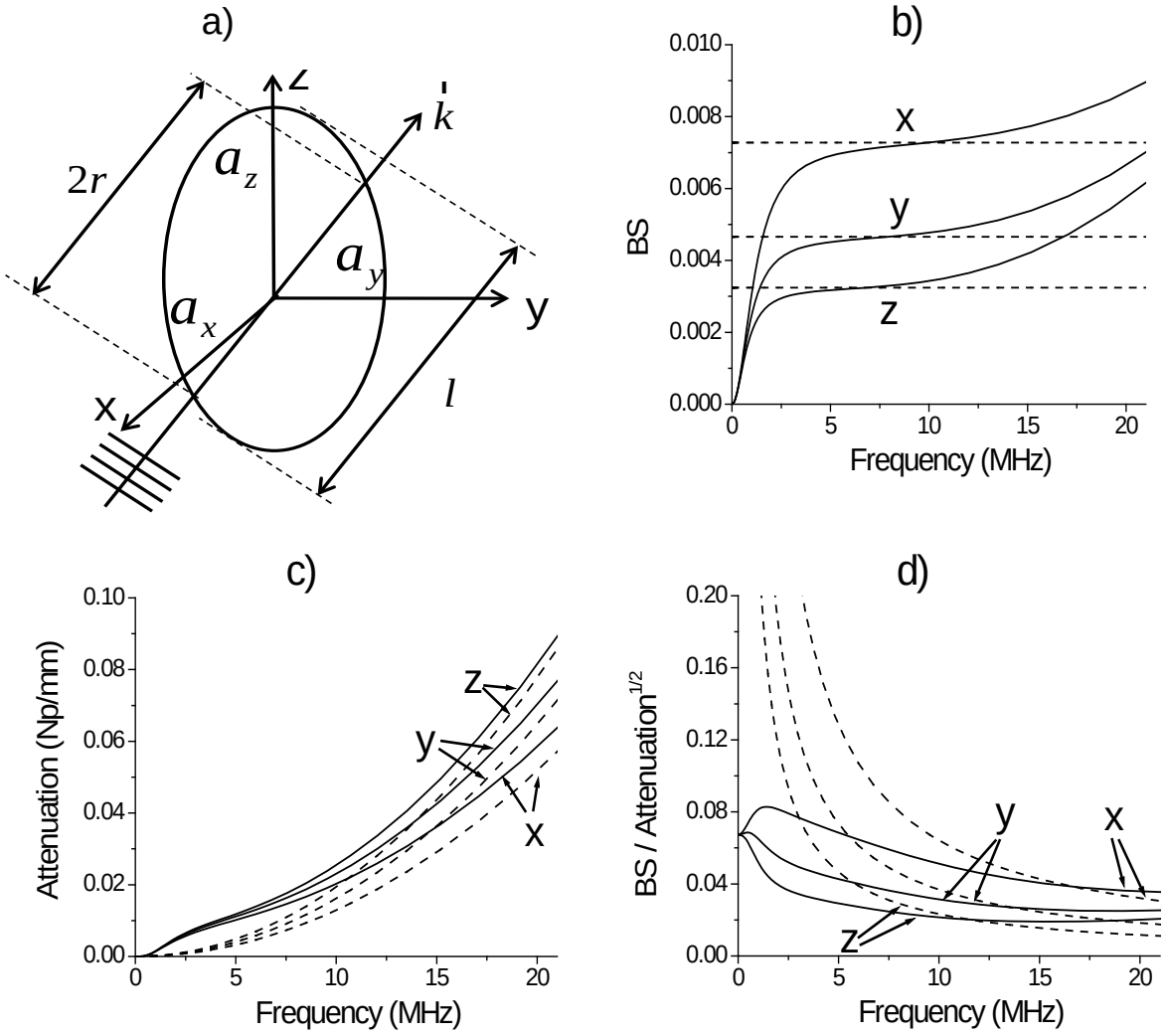

Figure 94. a) Geometry of MTR modeled as a general ellipsoid. Ultrasonic wave propagates in an arbitrary direction with wave vector $\mathbf{k}$; l and r are interaction length and ellipsoidal radius in the propagation direction, respectively. b) Shows BA vs. frequency $\sqrt{\eta}$ along *x*, *y*, and *z* axes. Solid lines are exact amplitude backscattering coefficient, and dashed lines are approximation (see equation 99). c) Shows attenuation coefficient α along *x*, *y*, and *z* axes vs. frequency: solid lines are exact and dashed lines are approximate attenuation coefficients (see equation 101). d) Backscattering-to-attenuation ratios in *x*, *y* and *z* directions vs. frequency. Solid lines are exact, and dashed lines approximate equation 102

One can define an effective size parameter $R_{eff} = (l/2)^2 r^{1/2} / \sqrt{V/8\pi}$, which has dimension of length. The effective size parameter is directly represented through measurable ultrasonic parameters. For equiaxed microstructures, $l = r$ and the effective size parameter R_{eff} equals the radius *r* of the averaged equiaxed grain. Another advantage is that the elastic factor Q is canceled and is not needed in the application of equation 103 and this method.

Because in this method the measurements are performed in a single direction of a sample at normal incidence, the shape of the grain cannot be determined. Therefore, it is advantageous to introduce an equivalent equiaxed grain with radius equal to half the interaction length ($l/2$). This gives:

$$r_{\text{equiaxed}}^{\text{equiv}} = l/2 = \left(k_l \sqrt{8\pi} \sqrt{\frac{\eta}{\alpha}} \right)^{-1} \tag{104}$$

The parameter $r_{\text{equiaxed}}^{\text{equiv}}$ is directly obtained from the measured ultrasonic characteristics substituted in equations 103 or 104.

The method is illustrated by a simulation example for a duplex Ti microstructure of hexagonal symmetry and ellipsoidal MTR with main radii $a_x = 0.4mm$, $a_y = 0.5mm$, and $a_z = 0.6mm$ parameter $q = 5.0 \times 10^{-6}$ used for calculating backscattering. BA coefficient, attenuation, and square root of their ratio along the *x*, *y*, and *z* axes are shown in figure 94 (b, c, and d, respectively), where the solid lines in each figure are exact calculations and the dashed lines are approximate values. As shown in figures 94 (b and c), the backscattering approximation works well between 5 MHz and 12 MHz. The approximation for attenuation cannot be used in the Rayleigh region, and approximation is used starting from the transition region. Figure 94(d) shows the applicability of the approximate ratio (see equation 103) shifts to the intermediate frequency range 10–20 MHz.

4.1.8 Grading of Microtexture in Legacy Hardware Samples; Comparison With OIM Characterization

4.1.8.1 Attenuation size effects

Because the elastic mismatches between adjacent MTRs were determined to be small [95], the sizes of the MTRs must have been the stronger contributor to the experimentally observed ultrasonic attenuation. A simple linear intercept method has been used because no standard exists for measuring the sizes of MTRs from OIM images (see figure 86). The measurements were made on inverse pole figure maps generated without imposing inversion symmetry of the Y-Z plane and colored according to the crystallographic orientations in the wave propagation direction (see the axial direction, z, in figure 84(a)). This orientation criterion was deemed most appropriate because the ultrasonic wave is only significantly scattered when there is an orientation mismatch in its propagation direction (i.e., a large mismatch in c-axis orientation). Therefore, for example, two adjacent regions that shared a common <$2\bar{1}\bar{1}0$> direction in the direction of wave propagation (and, therefore, had the same color in the inverse pole figure maps), but had basal poles misoriented 90° about this direction, were considered as a single region. The measurements were performed in two steps. First, the largest dimension of the MTR in the direction of wave propagation was

measured for all MTRs in the image. Next, the sizes of each region at locations above and below the largest dimension were measured. These locations were chosen to be approximately halfway between the largest dimension and the top and bottom edges of the MTR, and were not necessarily equally spaced. The mean and standard deviations were then calculated from the array of intercept lengths.

Figure 95 shows the ultrasonic attenuation coefficient (i.e., attenuation per unit length obtained by normalizing to the sample thickness) as a function of MTR size at the maximum amplitude of the transducer frequency response. It may be observed from figure 95 that sample 1, which has the largest MTRs in the direction of wave propagation, has the highest attenuation, whereas sample 3, which had the smallest MTRs, had lower attenuation. Sample 4 has lower attenuation and MTRs elongated perpendicular to the axial (z) direction of wave propagation. This occurs because the size of these regions in the ultrasonic wave propagation direction is still small. To test this hypothesis, ultrasonic waves were also sent in a direction perpendicular to the original propagation direction (i.e., parallel to the axis of elongation of the MTRs—denoted as the radial direction in figure 84(a)). In this case, the attenuation coefficient increased by a factor of 2, is shown in figure 95 (sample 4 parallel). Measurements made in the orthogonal directions of the other samples had less pronounced anisotropy than sample 4. The anisotropy in the attenuation coefficient exhibited by sample 4 was also reported by Panetta et al. [97, 114] and Blodgett and Eylon [115]. In the latter investigation, the authors related variations in longitudinal and shear wave velocities to differences in macroscopic texture and to the presence of similarly oriented grains with elongated morphology that behaved as a single scattering unit.

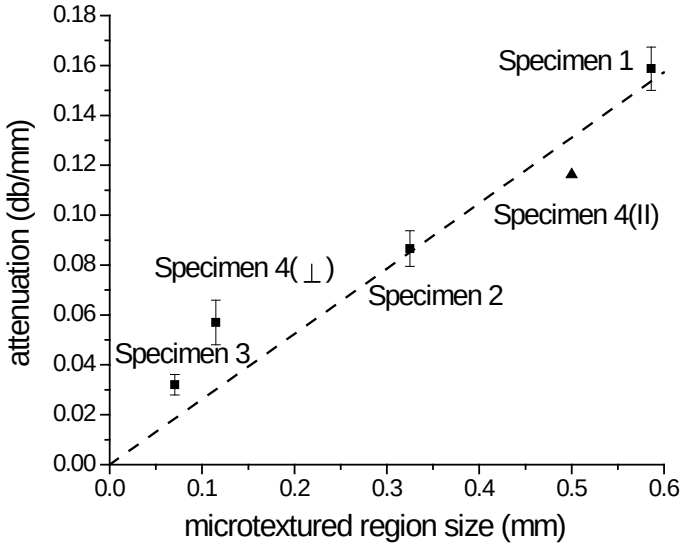

Note: Attenuation is plotted for the frequency of maximum transducer response (8.5 MHz, see figure 87c)

Figure 95. Ultrasonic attenuation coefficient vs. microtexture region size (dashed line is a linear regression)

Figure 96 shows, on a log-log scale, the same experimental data shown in figure 95, along with a theoretical prediction at 8 MHz (the solid line), based on the model developed in this work [112]. The product of the attenuation coefficient and MTR size (in dB, which is nondimensional) is plotted versus the effective MTR size in the direction of wave propagation. Taking the product of

attenuation coefficient and MTR size gives a nondimensional, scaled value of attenuation, which makes it more suitable for comparison with the theoretical model. The model is based on the assumption that the MTRs are equiaxed in shape, where the diameter of the equivalent spherical grains represents the actual MTR region sizes in the propagation direction. The elastic constants used in the model are specified in table 1. It is significant that there were no adjustable parameters used in the model, but the data show very good agreement despite the use of equivalent spherical shapes to represent the actual MTRs. It should also be noted that, of the attenuation data plotted in figures 95, 14 are averages of measurements collected in the vicinity of the slices cut out for EBSD analysis. Significant variation in attenuation was observed throughout each sample (see figure 97), which shows the spatial dependence of the attenuation coefficient.

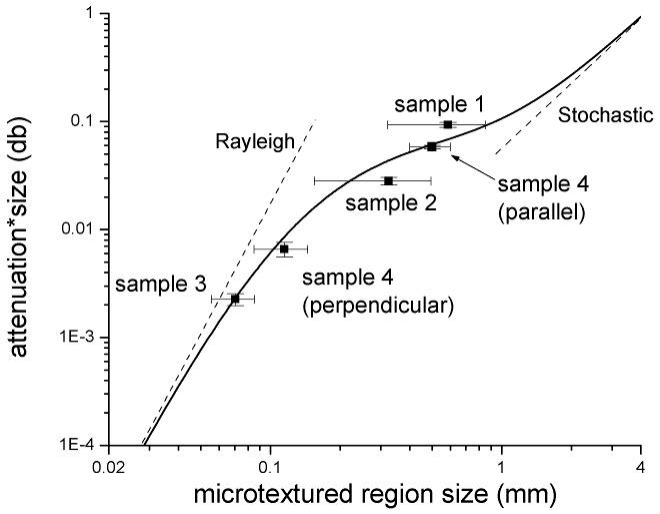

Note: Dashed lines indicate the Rayleigh and stochastic limit asymptotes. MTR sizes were measured in the direction of wave propagation, and the error bars indicate the standard deviation of the measurements

Figure 96. Total attenuation vs. MTR size at the frequency of maximum transducer response, showing comparison of the experimental data (points) and a theoretical model (solid line) in which no adjustable parameters are used

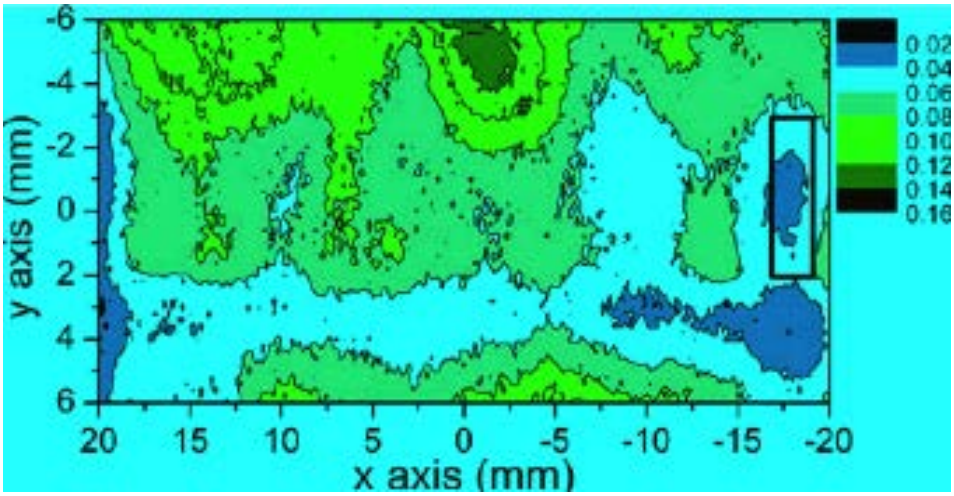

Figure 97. Spatial distribution of attenuation for specimen 4 obtained at a frequency of 8.5 MHz in scanning mode with a step size of 0.2 mm

To the first order, the spatially dependent average MTR sizes can be estimated from the data shown in figure 97.

As follows from the discussion in section 4.1.7, the dependence on the ratio λ/d, the scattering-induced ultrasonic attenuation α, can be divided into three characteristic regimes:

1. The low-frequency Rayleigh regime for $\lambda >> d$, in which attenuation α is proportional to d^3
2. The stochastic regime, in which $\lambda \leq d$ and α is proportional to d
3. The high-frequency, geometric regime, in which $\lambda << d$ and α behaves as $1/d$

These regimes and the transition between them for hexagonal polycrystals was discussed in section 4.1.7 and in [112, 113]. The ultrasonic wavelength, λ, used for the present experiments was approximately 0.77 mm and, therefore, λ/d is in the 0.1–1 range. In addition to the experimental attenuation data, the Rayleigh and stochastic asymptotes are also plotted on figure 96, clearly indicating that λ/d for the present work is in the transition region range.

As shown in figure 96, all experimental measurements are in the Rayleigh-to-stochastic transition range in the attenuation coefficient. The theoretical attenuation makes a smooth transition from fourth, in the Rayleigh regime, to second-power frequency dependence in the stochastic region. In the transition range, the frequency dependence deviates significantly from the Rayleigh or stochastic asymptotes. The transition range for longitudinal wave attenuation is characterized by a hump [105, 112], which is physically explained by a transition of the scattering mechanism—from longitudinal-to-transverse wave scattering in the Rayleigh region to longitudinal-to-longitudinal in the stochastic region. The material response in this region is clearly more complicated than the

simple linear approximation in figure 95, demonstrating the need to use robust models for the prediction of ultrasonic attenuation.

4.1.8.2 Backscattering measurement results and comparison with the model

Typical examples of raw time-domain BS are shown for three orthogonal directions of the sample in figure 88(a) and the spectrum of the spatially averaged BS RMS in figure 88(b). The backscattering in the radial direction is largest, and, therefore, the average MTR size in this direction is the smallest; the smallest backscattering signal is in the hoop direction (the direction of largest MTR size). It should be noted that, although the two oblique measurements are symmetric to the sample surface normal ($\pm 5^{o}$ in water), the BAs are very different. This is an indication of incline elongation orientation of the MTRs and, therefore, a difference in wave interaction length.

The spatial distribution of BS (ultrasonic backscattering maps) is shown in figure 98. This is the result of interaction length variation (MTR size and orientation) within the samples. Equation 81 can be applied to estimate the relative variations (in this case, indices *ij* are interpreted as different *i, j* pixels of the image).

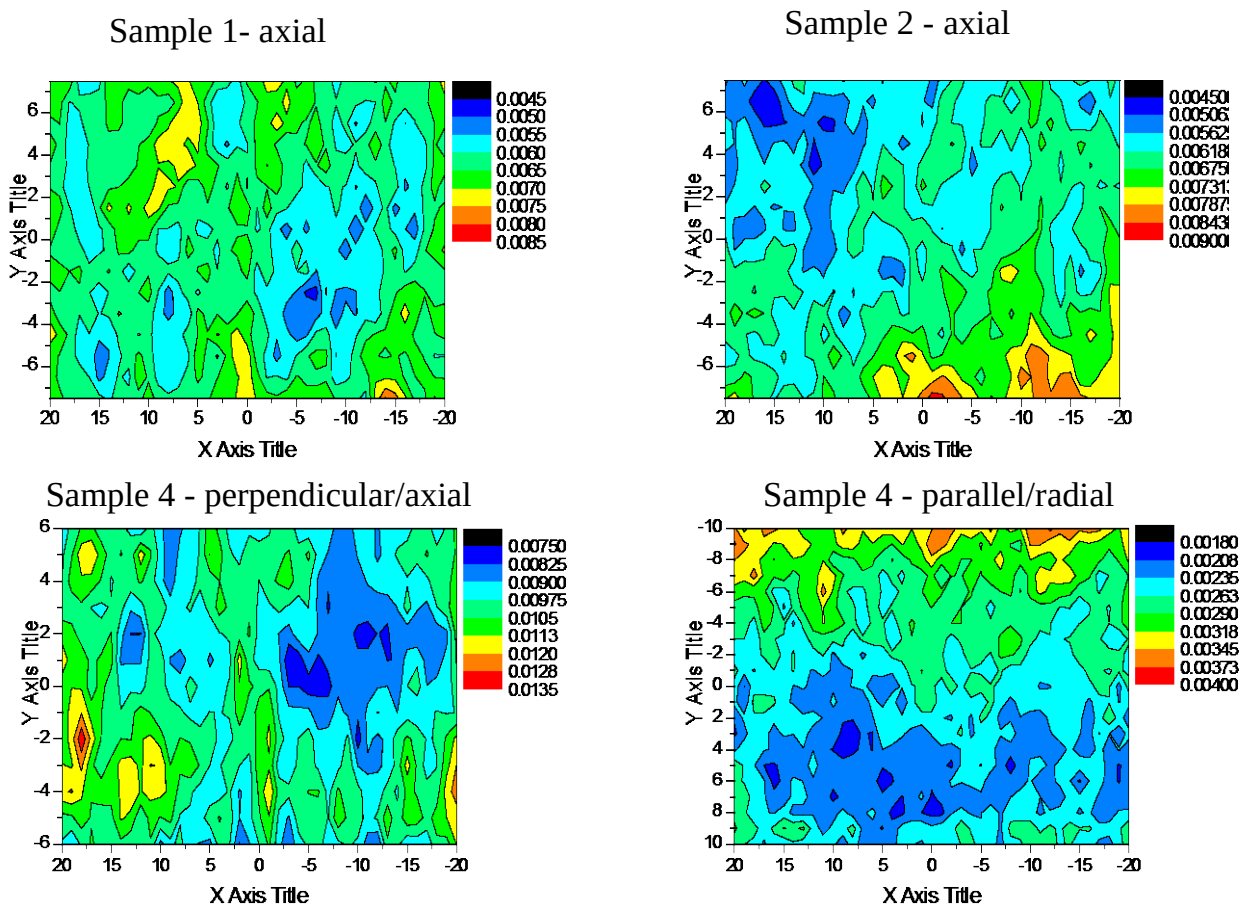

Figure 98. Spatial distribution (maps) of backscattering RMS for several specimens in axial directions (also radial direction for sample 4 is shown) obtained at central frequency 10 MHz in scanning mode with a step size of 0.2 mm

The use of directional backscattering ratios (see equation 81) allows one to decrease the number of microstructural parameters needed to uniquely describe anisotropic behavior of backscattering coefficients. Another advantage of the use of backscattering ratios is improvement and simplification of data analysis for comparison with model predictions. It has been determined in this study that the raw spectrum shown in figure 88(b) has larger bandwidth as compared to the deconvolved front echo-signal spectrum (this is due to a several-order-of-magnitude difference in the backscattering and front wall signals, and the resulting effect of deconvolution-induced noise). This fact prompted the use of the row-spatially-averaged RMS spectra without data deconvolution to obtain the directional backscattering ratios in different propagation directions. The inversion of the experimental data by application of the backscattering ratios to equation 81 removes the effect of noise increase with the deconvolution, and the need to correct for the transducer beam diffraction (for comparison, the beam diffraction and backscattering attenuation were accounted for, and it was determined that their effect on the experimental backscattering ratios was below 1% at 10 MHz).

The experimental BA ratios (normalized on the smallest, hoop, and BS value) are shown in figure 99 by the irregular solid lines; the BS normalization in the form of ratios significantly increases the data quality in the low- and high-frequency ranges. To measure the effect of the system noise, the RMS of the signal gated for $6\mu s$ was processed in the same way before the front reflection (it was assumed that the signal collected for acoustic pass in the immersion fluid-water gives only the RMS value of the noise). This allows obtaining the backscattering signal-to-noise ratio (SNR) RMS ratios at different frequencies: at 10 MHz, the SNR is approximately 50; below 2.5 MHz, the SNR is approximately 1; at 21 MHz, the SNR is 2, and it then quickly drops for higher frequencies. It is estimated that the ratio spectra have acceptable SNRs in the frequency range 2.5–21MHz.

The dashed lines in figure 99 present the theoretical prediction of the ratios; equation 81 calculated for all curves for the MTR face with interaction length $l_{radial} = 0.32\,\text{mm}$, $l_{hoop} = 0.58\,\text{mm}$, $l_{axial} = 0.40\,\text{mm}$, $l_{oblique-1} = 0.48\,\text{mm}$, $l_{oblique-2} = 0.36\,\text{mm}$, and the crystallite nondimensional characteristic parameter $q = 6.3 \times 10^{-5}$. Those values were obtained by nonlinear least squares inversion of the ultrasonic backscattering ratios at normal incidence in radial, axial, and hoop directions.

Microstructure and microtexture for this sample were described in the preceding section and [95] (sample 2). The average MTR size D_i in the propagation direction was determined by OIM [95] $D_{radial} = 0.22\,\text{mm}$, $D_{hoop} = 0.54\,\text{mm}$ $D_{axial} = 0.36\,\text{mm}$, and the average size of α crystallites measured from the scanning electron micrographs is about $10\,\mu\text{m}$ [95]; the MTR sizes are in reasonable agreement with those obtained ultrasonically.

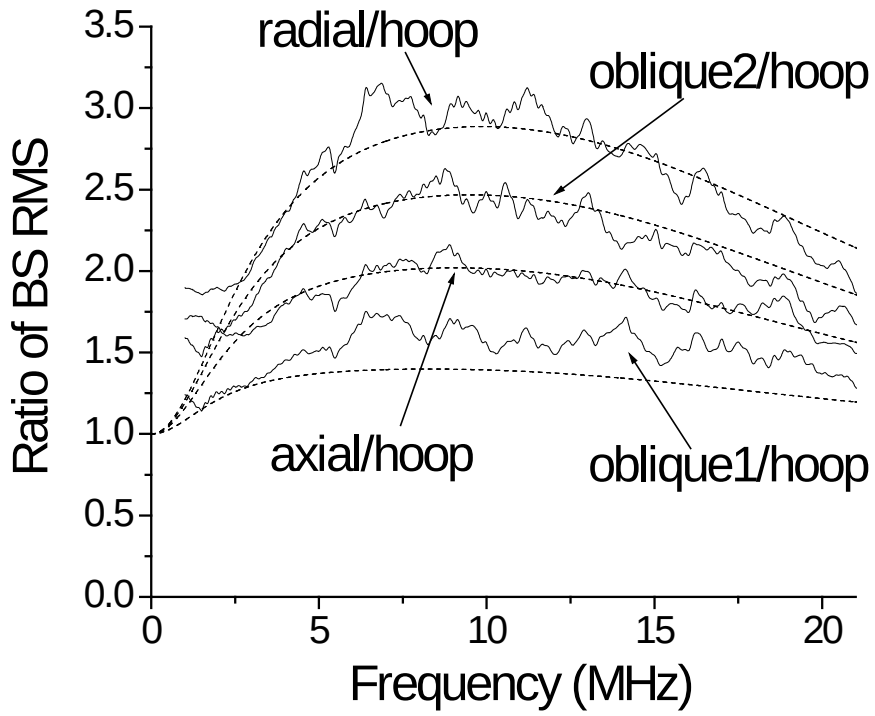

Figure 99. The ratios of backscattering RMS in different propagation directions vs. frequency. The radial-to-hoop ratio, the radial-to-axial ratio, the axial-to-hoop ratio, and two oblique-to-hoop ratios are the solid lines; the dashed lines present theoretical dependence equation (81) for the MTR interaction length $l_{radial} = 0.32\,\text{mm}$, $l_{hoop} = 0.58\,\text{mm}$, $l_{axial} = 0.40\,\text{mm}$, $l_{oblique-1} = 0.48\,\text{mm}$, $l_{oblique-2} = 0.36\,\text{mm}$, and the non-dimensional material parameter $q = 6.3\times10^{-5}$

Knowing the MTR size and *q* allows one to estimate the averaged parameter *M* of misorientation of crystallites in MTRs (see equation 80). Neglecting the contribution of the secondary alpha in MTRs (for this sample, the primary alpha fraction is about 0.74 [95]), and taking the ratio $Q_\alpha / Q_r \approx 1$, the alpha crystallite misorientation parameter in the MTR obtained is $M \approx 0.8$ (see the discussion following equation 80). From equations 78 and 79, the contribution of scattering from MTR (first term) and crystallites can be quantified from the sample. Scattering from MTRs is reduced by the factor (1-M) = 0.2 because of crystallite misorientation and reduction of the MTR effective elastic moduli.

When comparing ultrasonically obtained interaction length for MTR, and those measured from OIM images, the interaction length is generally larger than the ellipsoid size (they are equal in propagation directions along prime ellipsoid radii). For the average MTR shape of the sample, this difference is estimated at between 0% and 17% for an arbitrary propagation direction. One should also note that the ultrasonic data are obtained as an average of the BS over the whole sample volume, whereas the OIM measurements were taken on the sample faces in relatively small areas (about 10 mm^2). Also, the BS model does not account for possible deviation of the actual spatial correlation function (related to the MTR size distribution) from the generalized Poisson

distribution in equation 65. The agreement between two measurements of MTR size is judged to be reasonable because of the variability of MTR sizes.

The frequency dependence of the ratio R_{ij} is sensitive to the parameter q, in spite of its small value. This is evident from the decrease of the experimental spectrum ratios above 10 MHz, although the ratios should remain constant without the crystallite backscattering contribution (see dashed lines in figure 93). The transducer frequency response cannot be the reason for this decrease because this is the frequency range with high transducer efficiency and higher BS level, as is clear from the raw data in figure 88(b). It should be noted that the transducer frequency response is removed in the ratio because of the division of the spectra in different propagation directions. The frequency dependence of attenuation in different directions acts opposite to the backscattering and cannot change the data trend attributed here to crystallites. At the relatively small measuring depth considered, the multiple scattering is also negligible and cannot affect the crystallite backscattering contribution. The example shows that only geometrical parameters of the averaged MTR and parameter q (affected by MTRs and crystallites) need to be considered to describe the frequency dependence of directional backscattering ratios in the duplex structure; inversely, those parameters are determined from the ultrasonic signatures.

4.1.8.3 Effective size determination by backscattering-to-attenuation ratio method

As was discussed in section 4.1.8, the effective MTR size parameter R_{eff} is directly obtained from measurements of the backscattering-to-attenuation ratio in the same direction as the sample (see equation 102).

To illustrate the method, exact ratio curves from 10–22 MHz are assumed as measured, and fitted by equation 103 to determine the effective size parameter in each propagation direction. The results are presented in figure 100 and table 18. In figure 100, solid lines are exact curves, dashed lines are approximate curves, and dotted lines are fitted curves. When fitted curves and approximate curves overlap, the approximate effective size would be the exact value. Table 18 lists the exact and approximate (determined by the curve-fitting) effective size parameters. Acceptable agreement is observed between the determined and the original exact values.

Table 18. Comparison of the original (used for simulation) and inversely determined effective size parameters by fitting the simulated (measured) ratios with equation 104

Simulation of effective size parameter determination

$\frac{\left(\frac{l}{2}\right)^2 \cdot r^{1/2}}{\sqrt{V/(8\pi)}}$ (mm)	x	y	z
Exact value	0.29	0.51	0.80
Approximate value	0.32	0.50	0.68

Note: The propagation directions are in the *x*, *y*, and *z* radii of elongated microstructure

In the example considered, the wave propagation direction is along the main ellipsoid axis of the MTR; therefore, $l/2 = r$, where r is the ellipsoid radius in this direction. In this case, the effective

size parameter $R_{eff} = (l/2)^2 r^{1/2} / \sqrt{V/8\pi}$ becomes $R_{eff} = (l/2)^{5/2} / \sqrt{V/8\pi}$ and, therefore, depends only on the interaction length l and the effective grain volume V. When the wave propagates in an arbitrary direction to the ellipsoid axes, the difference between l and $2r$ increases with the MTR elongation. The dependence of R_{eff} on r is not strong and, in most cases, $R_{eff} = (l/2)^2 r^{1/2} / \sqrt{V/8\pi}$ can be approximated as $R_{eff}^{approx} = (l^{approx}/2)^{5/2} / \sqrt{V/8\pi}$. It was estimated that for a rotationally symmetric ellipsoid, even with its axis length ratio 7, the maximum relative error in l^{approx} is 25% compared to l.

It is important to identify the applicable frequency range for the successful use of equation 102 in this method. For duplex Ti microstructure, the contribution of the crystallite phase becomes significant at high frequency. The ratio curve decreases at high frequency (see figure 94(d)); however, for duplex microstructure, it starts increasing at some frequency because of the crystallite scattering effect (see figure 94(b)). For the purpose of the approximate MTR sizing by this method from a single sample direction, the crystallite effect, can be neglected.

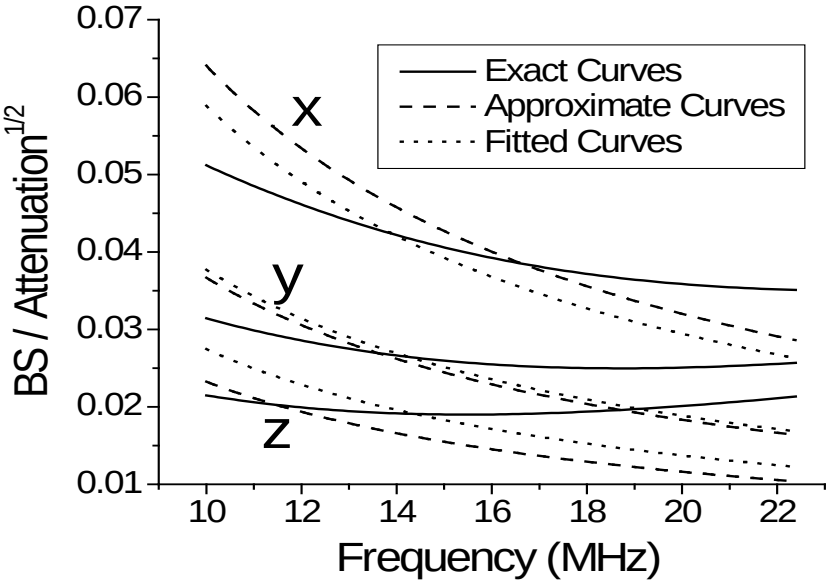

Figure 100. Determination of effective size parameter: Solid lines are exact backscattering-to-attenuation ratios; dashed lines are approximate, equation 104; dotted lines are the ratio after the effective size parameter optimization

Figure 90 (c and d) shows the experimental backscattering-to-attenuation ratio curves, in which the frequency range for curve fitting is from 10–12 MHz, as marked in the figure by short dark lines that are used for the parameter determination from equation 102. The determined effective size parameters are shown in table 19 for sample 1, where the sizes in the first line are from the backscattering ratio method, and those in the second line are from the combined method. As indicated in table 19, the results are consistent.

Table 19. Comparison of effective size parameter in axial, radial, and hoop directions for sample 1 determined by the two methods—backscattering ratio from 3 sides of the sample and backscattering-to-attenuation ratios from each side of sample

Effective size parameter for sample 1

$\frac{\left(\frac{l}{2}\right)^2 \cdot r^{1/2}}{\sqrt{V/(8\pi)}}$ (mm)	axial	radial	hoop
BS ratio from 3 sides	0.55	0.31	0.60
Combined BS and attenuation	0.31	0.18	0.30

The backscattering-to-attenuation ratio method was also applied to sample 2**.** It has interaction lengths in axial, radial, and hoop directions of 0.32 mm, 0.26 mm, and 0.46 mm, respectively (they were determined ultrasonically by the directional backscattering ratio method). Figure 90(d) displays the ratio curves, and table 20 lists the effective size parameters obtained by the backscattering-to-attenuation ratio method and the directional-backscattering ratio method. As shown in table 20, the effective size parameters from the two methods are in reasonable agreement. It should be noted that the error between the results from the two methods is caused not only by the approximation of the combined backscattering and attenuation method, but also by the normalization of backscattering RMS to obtain absolute values.

Table 20. Comparison of effective size parameter in axial, radial, and hoop directions for sample 2 determined by the two methods—backscattering ratio from 3 sides of the sample and backscattering-to-attenuation ratios from each side of sample

Effective size parameter for sample 2

$\frac{\left(\frac{l}{2}\right)^2 \cdot r^{1/2}}{\sqrt{V/(8\pi)}}$ (mm)	axial	radial	hoop
BS ratio from 3 sides	0.18	0.11	0.46
Combined BS and attenuation	0.23	0.14	0.52

5. CONCLUSIONS

5.1 CONSTITUITIVE DATA GENERATION

To accomplish the goal of developing a microstructure-sensitive, crystal-plasticity modeling capability for the dwell-fatigue effect, sound understanding of the constitutive response of the individual components of the microstructure is required. In an effort to provide the broadest possible experimental basis for the parametric studies that are efficiently addressed by the crystal plasticity and derived homogenized models, the fundamental properties of several alloys, including Ti-6242, Ti-811, and single α-phase Ti-7Al alloy, were systematically studied with respect to microstructure variations and loading conditions. Single crystals of α-Ti-7Al and Ti-6242 single-colony crystals were also tested in both compression and tension, in several different crystal orientations, to obtain information about yield strength, hardening rates, and rate sensitivities for individual slip systems. The dramatic effect of microstructure variations on the time-dependent creep response of Ti-6242 was studied to provide additional insight into the critical features influencing the behavior of the two-phase commercial alloys. Through manipulation of heat treatments, the strong effect of lamellar spacing and secondary α was determined.

5.2 EFFECT OF LOADING CONDITIONS ON SINGLE-PHASE α-TI-7 WT % AL

The time-dependent and fracture behaviors of single-phase α-Ti-7 wt % Al were observed under creep, cyclic-fatigue, and dwell-fatigue loading conditions. Experiments show that:

- The dwell effect is observed in single-phase α alloys having textures lacking hard grains. Although dwell loading was found to influence damage accumulation under both tensile and compressive testing, it was found to decrease specimen life under tensile loading.
- Fatigue life and damage accumulation are influenced by slip character. Under tensile loading, homogenous slip was correlated with increases in both cyclic and dwell life and strain accumulation at failure.
- Fatigue life and damage accumulation are influenced by applied waveform. Dwell-loaded specimens were found to strain more at failure than statically loaded specimens, and cyclically loaded specimens displayed the smallest plastic deformation at failure. The applications of non-zero *R*-ratios or load ripples at peak stress was found to affect both part lives and transient responses.
- Failure mechanisms are dependent on both slip character and loading conditions. Under cyclic loading, surface initiated faceting was observed in both ice water quench (IWQ) and air-cooled (AC) specimens. Under creep and dwell loading, internally initiated faceting was observed in AC specimens, and ductile failure at grain boundaries was observed in IWQ specimens.
- Dwell and creep faceting is observed in materials lacking grains orientated with their $\vec{c}$-axes parallel to the loading axis. Facets were observed in alloys with textures where basal planes inclined by more than ~20^{o} to the deformation axis.

5.3 FRACTOGRAPHIC AND DEFORMATION MECHANISMS ASSOCIATED WITH DWELL-FATIGUE FAILURE IN α/β ALLOY TI-811

An extensive investigation of the influence of loading mode on the faceted fracture of the α/β alloy Ti-811 was also conducted, including detailed fractography and fracture facet analysis. In addition, after dwell-fatigue failure, focused ion beam (FIB) extraction of transmission electron microscopy (TEM) foils and complete analysis of deformation processes within initiating and propagating grain facets were also conducted. The following findings were obtained:

5.3.1 Under Continuous Cycling Conditions

- Fatigue crack initiation occurred at the surface of the specimen in a grain whose basal pole was inclined 25° to the loading direction (LD).
- Subsequent propagation also occurred on basal planes that were inclined between ~22° and 41° to the LD, although some facets with unique surface topography were found to be $\{10\bar{1}0\}$ fracture planes.
- Markings on the facet surfaces that resemble fatigue striations indicated that the crack growth rate was on the order of 150 nm per cycle at crack lengths as small as 100 μm.
- Facet surface roughness and crack growth rate increased with increasing crack length, consistent with plasticity controlled crack propagation.

5.3.2 Under Creep Loading Conditions

- Subsurface crack initiation occurred on a facet inclined ~23° to the LD, producing a smooth facet nearly parallel to the basal plane.
- Subsequent crack propagation occurred on irrational $\{hkil\}$ planes inclined between 7° and 20° to (0001). Around the initiation grain, the PFs were more inclined to the LD than at longer crack lengths. Several crystallographic fracture planes were consistent with known hydride habit planes, although no direct evidence of hydrides was found.
- The facet surface topography was consistent with that formed by cracking in small positive pressures of hydrogen gas, consisting of tear ridges extending in the direction of crack propagation.

5.3.3 Under Dwell-Fatigue Conditions

- Cracking occurred at the intersection of an inclined basal slip band with a $\{10\bar{1}7\}$ plane that was nearly perpendicular to the LD. The basal slip band was in a high-RSS orientation (basal pole 42° from LD), whereas the preferred propagation planes were those in which maximum normal stress was resolved onto the $\{10\bar{1}7\}$ plane. Other irrational $\{hkil\}$ planes near $\{10\bar{1}7\}$ were also observed, but less frequently.
- The microscopic surface topography of these facets was consistent with that formed by static loading in air, suggesting that they have all formed by similar mechanisms and that the environment and unload/reload cycles act to modify the rate of crack propagation. Based on the time-to-failure of each specimen, the addition of the unload/reload seemed to slow crack growth, compared with the statically loaded specimens.
- Crack propagation rates within the faceted region were on the order of 2 μm per cycle at

crack lengths between 20 μm and 100 μm, which was considerably higher than those observed during continuous cycling. The cracks grew preferentially through the faceted region because of the higher growth rates, before extending into the adjacent, differently oriented grains. This finding implies that the small crack growth regime may be equally as important to explaining the dwell effect as the crack-initiation stage. These accelerated crack growth rates are particularly detrimental in heavily microtextured material, where there are similarly oriented basal planes affording an easy crack path.

- The dislocation analysis by FIB/TEM associated with the dwell-fatigue-initiated facets include the following features:

  - <a> slip bands on either basal or prism planes in softgrains that impinge on a grain boundary shared by a hardgrain do not facilitate the formation of basal slip bands in the hardgrain if the *c*-axis of the hardgrain is close to the tensile axis.
  - Hard grains, with their *c*-axes close (< ~10 ^{o}) to their tensile axes, deform by <1123> $\{10\bar{1}1\}$ slip.
  - The formation of basal slip bands in a hard grain, due to slip in a neighboring soft grain, may occur if the hardgrain has a *c*-axis inclined more than ~10°–15^{o} to the tensile axis.
  - Hard grains, with their *c*-axes inclined to the tensile axes more than ~10°–15^{o} to the tensile axes, deform by multiple slip on <c+a> $\{10\bar{1}1\}$ and <a> systems.
  - Near-basal cracks do not propagate on basal planes. Evidence of slip band cracking was not observed.
  - Plastic zone size does not increase with crack length for faceted crack growth. Dwell cracks appear to sharpen with increasing crack length.
  - Faceting is not a brittle process. A significant degree of <c+a> slip activity is observed under the crack surface.

5.4 HIGH-ENERGY DIFFRACTION MICROSCOPY FOR IN SITU INVESTIGATION OF POLYCRYSTALLINE DEFORMATION

Initial high-energy diffraction microscopy (HEDM) experiments at the Advanced Photon Source at Argonne National Laboratory beamline 1-ID have been used to quantify grain-scale structure and mechanical response within deforming polycrystalline alloys. The data from HEDM experiments are providing important information regarding deformation and damage evolution at the most important size scales relative to the microstructure effects on dwell fatigue. The principal conclusions of the present work are:

- The microstructural characterization data from near-field HEDM experiments are comparable to the results from the current generation of serial sectioning/EBSD experiments, which provide three-dimensional orientation reconstructions of polycrystalline aggregates. The important distinction is the nondestructive nature of the HEDM experiments.
- Grain boundary topology can be mapped in the near-field geometry, whereas strain and stress states of individual grains are mapped in the far field setting during in situ loading conditions.

- The lattice strain tensors of individual grains within a deforming polycrystal can be measured with resolution of the order of 10^{-4}.
- The relatively small number of grains that are possible to interrogate in a typical HEDM lattice strain experiment has been a limitation in the past—making it difficult to interpret the applicability of the findings. Recent datasets cover statistically representative numbers of grains (hundreds to thousands).
- Evolving dislocation structure has also been investigated by in situ high-resolution reciprocal space mapping and can be augmented by post-mortem TEM.
- This multiple length-scale data open a unique opportunity to validate and develop micromechanical models of damage processes in structural alloys. There exists enormous potential for drastically improving the understanding of grain scale mechanical processes by using these unique experimental results together with modeling formulations.
- These initial experiments were conducted under monotonic loading conditions, but evolution of stress states and microstructure under fatigue loading conditions is a highly promising direction for future work.

5.5 CRYSTAL PLASTICITY FINITE ELEMENT-BASED MODEL DEVELOPMENT AND SIMULATION OF TI-6242

Based upon the constitutive materials data generated and the important physical insights into the dwell-fatigue phenomenon, extensive model development has also been accomplished in this research to two major deliverables to predict the overall stress-strain response and probability of failure initiation in components made of Ti-6242. The models are as follows:

- Homogenized continuum anisotropic plasticity model in terms of microstructural characteristic descriptors (*SFx*, *SFy*, *SFz*, and *D*) and plastic work W_P. Functional forms for rate independent and rate dependent plasticity are given in section 3.3.4.3 and 3.3.4.4. A macroscopic finite element model (FEM) code of the entire engine component can be run with this anisotropic constitutive model to make accurate predictions of evolving stresses and strains at any point of the microstructure. Alternatively, the second development of the probabilistic crack nucleation model (see below) can be used to make the macroscopic crack nucleation predictions.
- Probabilistic macroscopic crack nucleation model for polycrystalline microstructures (developed in section 3.3). This model can predict the probability of crack nucleation at any point in a component at any instant during the loading, knowing the microstructural characteristic descriptors (e.g., Schmid factor, *SF*, misorientation θ_{mis}, and grain size *D*, and the macroscopic stress level). A joint distribution function is generated for these parameters. The probability of macroscopic crack nucleation before a particular time *t'* is given in equation 59.

The research team worked with GE Aviation to test some of the models for suitability with respect to making some of their expected design predictions. The macroscopic models developed from extensive micromechanical modeling of polycrystalline poly-phase Ti-6242 microstructures can be easily incorporated into any commercial FEM codes like ABAQUS®, ANSYS, and MSC-NASTRAN.

5.6 ULTRASONIC BACKSCATTER ATTENUATION EXPERIMENTS AND MODELING

The results of this study show that the ultrasonic backscattering and attenuation coefficients scale with microtexture region sizes. Robust models have been developed for inversion of the mean microtextural region size and morphology from ultrasonic measurements. Estimation of the mean misorientation parameter of crystallites in the microtextured region (MTR) can also be made. This development may potentially lead to model-based correlations between ultrasonically measured microtexture and dwell-fatigue life.

Based on the results of the present investigation, the following conclusions were reached:

- It is possible to use ultrasonic attenuation to differentiate between different degrees of microtexture in $\alpha + \beta$ processed titanium alloys.
- The directional ratios of backscattering signals can be used to size the degrees of microtexture. The ratios depend only on geometrical parameters of the elongated grains and on the newly introduced non-dimensional material parameter, q. All those parameters are determined from ultrasonic signatures, and no adjustable parameters are needed in the model. The ultrasonically measured nondimensional parameter q combines all a priori unknown elastic properties of MTRs and crystallites and their volumes.
- The backscattering-to-attenuation ratio method was developed that allows one to obtain explicitly the effective size parameter of MTR from combined measurement of the ultrasonic backscattering and attenuation from one side of the sample.
- Good agreement was observed between MTR sizes in the direction of wave propagation directly measured by orientation imaging microscopy and the results of inversion by the theoretical models developed that relate the ultrasonic signature to microstructural features (with no adjustable parameters).

6. REFERENCES

1. Air Force Office of Scientific Research. (1976). *Deformation and Solid Solution Strengthening of Ti-Al Single Crystals.* (Report #SC526-7FR). Rockwell International Science Center, Thousand Oaks, CA. Paton N, Williams J, Baggerly R.

2. Suri S. Study of Microstructure and Mechanical Properties of Oriented Single Colony Crystals of a Near-a Titanium Alloy at Room Temperature. vol. Ph.D. Columbus, Ohio: The Ohio State University, Ph.D. Dissertation, p.339 leaves. 2000.

3. Norfleet D. Sample size effects related to nickel, titanium and nickel-titanium at the micron size scale. Columbus, Ohio: The Ohio State University, 2007.

4. Savage M. Microstructural and mechanistic study of low temperature creep and dwell fatigue in single colony alpha/beta Titanium Alloys. vol. Ph.D. Columbus, Ohio: The Ohio State University, Ph.D. Dissertation. p.339 2000

5. Brandes MC. Creep, Fatigue, and Deformation of Alpha and Alpha + Beta Titanium Alloys at Ambient Temperature. Columbus, Ohio: The Ohio State University, Ph.D. Dissertation.2008.

6. Norfleet D, Brandes M, Mills M. Unpublished Research. Columbus, Ohio: The Ohio State University. 2002-2007.

7. FAA Report. (2007). The Evaluation of Cold Dwell Fatigue in Ti-6242. (DOT/FAA/AR-06/24).

8. Suri S., Viswanathan GB, Neeraj T, Hou DH, Mills MJ. (1999). Room temperature deformation and mechanisms of slip transmission in oriented single-colony crystals of an alpha/beta titanium alloy. *Acta Materialia 47*(3), 1019–1034.

9. Savage M, Mills M, Tatalovich J. (2004). Anisotropy in the room-temperature deformation of alpha-beta colonies in titanium alloys: role of the alpha-beta interface. *Philosophical Magazine, 84*(11), 1127–1154.

10. May K. N. Small Scale Tensile Testing of Titanium Alloys. vol. M.S. Columbus, Ohio: The Ohio State University, M.S. Thesis, 2010.

11. Neeraj, T., Hou, D. H., Daehn, G. S., Mills, M.J. (2000). Phenomenological and Microstructural Analysis of Room Temperature Creep in Titanium Alloys, *48*(6), 1225–1238.

12. Thirumalai, N. S. Low Temperature Creep of Titanium Alloys: Microstructure, Deformation Mechanisms and Modeling. Columbus, Ohio: The Ohio State University, Ph.D. Dissertation, 2000.

13. Bridier, F., Villechaise, P., Mendez, J. (2005). Analysis of the different slip systems activated by tension in a alpha/beta titanium alloy in relation with local crystallographic orientation. *Acta Materialia 53*(3), 555–567.

14. Luetjering, G., Gysler, A. (1984). *Fatigue [properties dependence on microstructure for titanium alloys]*. *Titanium '84: Science and Technology*, Proceedings from the World Conference on Titanium, 5th, Munich, Germany.

15. Wojcik, C., Chan, K., Koss, D. (1988). Stage I Fatigue Crack Propagation in a Titanium Alloy. *Acta Metallurgica, 36(5),* 1261–1270.

16. Pilchak, A., Williams, R., Williams, J. (2010). Physical Metallurgy and Materials Science. *Metallurgical and Materials Transactions A, 41*(1), 106–124.

17. Hack, J., Leverant, G.R. (1982). The Influence of Microstructure on the Susceptibility of Titanium Alloys to Internal Hydrogen Embrittlement. *Metallurgical and Materials Transactions A, 13*(10), 1729–1738.

18. Evans, W.J., Bache, M.R. (1994). Dwell-Sensitive Fatigue under Biaxial Loads in the near-Alpha Titanium-Alloy Imi685. *International Journal of Fatigue, 16*(7), 443–452.

19. Sinha, V., Mills, M.J., Williams, J.C. (2007). Determination of crystallographic orientation of dwell-fatigue fracture facets in Ti-6242 alloy. *Journal of Materials Science, 42*(19), 8334–8341.

20. Sinha, V., Mills, M.J., Williams, J.C. (2006). Crystallography of fracture facets in a near-alpha titanium alloy. *Metallurgical and Materials Transactions A, 37*(6), 2015–2026.

21. Gregory, J.K., Brokmeier, H.G. (1995). The relationship between crystallographic texture and salt water cracking susceptibility in Ti-6Al-4V. *Materials Science and Engineering: A, 203*(1–2), 365–372.

22. Evans, W. J. (1987). The Influence of Microstructure on Dwell Sensitive Fatigue in a near Alpha-Titanium Alloy. *Scripta Metallurgica, 21*(4), 469–474.

23. Evans, W. J., Bache, M. R. (1995). Hydrogen and Fatigue Behavior in a near Alpha-Titanium Alloy. *Scripta Metallurgica et Materialia, 32*(7), 1019–1024.

24. Bache, M. R., Davies, H. M., Evans, W. J. (1995). *A model for fatigue crack initiation in titanium alloys. Titanium '95: Science and Technology*. Proceedings of the World Conference on Titanium, 8th, Birmingham, UK.

25. Bache, M. R., Evans, W. J., Davies, H. M. (1997). Electron back scattered diffraction (EBSD) analysis of quasi-cleavage and hydrogen induced fractures under cyclic and dwell loading in titanium alloys. *Journal of Materials Science, 32*(13), 3435–3442.

26. Bache, M. R. (2003). A review of dwell sensitive fatigue in titanium alloys: the role of microstructure, texture and operating conditions. *International Journal of Fatigue, 25*(9–11), 1079–1087.

27. Stroh, A. (1954). The Formation of Cracks as a Result of Plastic Flow. *Proceedings of the Royal Society of London. Series A, Mathematical and Physical Sciences, 223*(1154), 404.

28. Evans, W. J. (1998). Optimising mechanical properties in alpha+beta titanium alloys. *Materials Science and Engineering, A: Structural Materials Properties Microstructure and Processing, 243*(1–2), 89–96.

29. Savage, M., Neeraj, T., Mills, M. (2002). Observations of Room Temperature Creep Recovery in Titanium Alloys. *Metallurgical and Materials Transactions, A: Physical Metallurgy and Materials Science, 33*(13), 891–898.

30. Brandes, M., Mills, M. (2003). *Recovery of Strain Hardening at Low Temperatures in Alpha Ti-6Al and Ti-6242. Titanium '03: Science and Technology*, Proceedings from the World Conference on Titanium, 10th, Hamburg, Germany.

31. Brandes, M., Mills, M. J. Static recovery in titanium alloys at lower temperatures. *Materials Science and Engineering, A: Structural Materials Properties Microstructure and Processing, 387–389*, 570–575.

32. Brandes, M. C., Mills, M.J., Williams, J. C. (2001–2008). Unpublished Research. Columbus, Ohio: The Ohio State University, 2001-08.

33. Gysler, A., Lutjering, G. (1982). Influence of Test Temperature and Microstructure on the Tensile Properties of Titanium-Alloys. *Metallurgical Transactions, A: Physical Metallurgy and Materials Science, 13*(8), 1435–1443.

34. Blackburn, M., Williams, J. (1969). Strength, Deformation Modes and Fracture in Titanium-Aluminum Alloys. *Transactions of the American Society for Metals, 62*, 398.

35. Lim, J. Y., McMahon, C. J. Jr., Pope, D. P., Williams, J. C. (1976). The Effect of Oxygen on the Structure and Mechanical Behaviour of Aged Ti-8 wt% Al. *Metallurgical Transactions A: Physical Metallurgy and Materials Science, 7A*, 139.

36. Williams, J., Lutjering, G. (1980). *The Effect of Slip Length and Slip Character on the Properties of Titanium Alloys. Titanium '80: Science and Technology*. Proceedings from the World Conference on Titanium, 4th, Kyoto, Japan.

37. Pilchak, A., Williams, J.C. (2005–2008). Unpublished Research. The Ohio State University.

38. Le Biavant, K., Pommier, S., Prioul, C. (2002). Local texture and fatigue initiation in a Ti-6Al-4V titanium alloy. *Fatigue & Fracture of Engineering Materials & Structures, 25*(6), 527–545.

39. Hall, J. A. (1997). Fatigue crack initiation in alpha-beta titanium alloys. *International Journal of Fatigue, 19*(93), 23–37.

40. Wells, C. H., Sullivan, C. P. (1969). Low-Cycle Fatigue Crack Initiation in Ti-6Al-4V. *ASM Transactions Quarterly, 62*, 263–270.

41. Benson, D. K., Grosskreutz, J. C., Shaw, G. G. (1972). Mechanisms of Fatigue in Mill-Annealed Ti-6AI-4Vat Room Temperature and 600F. *Metallurgical Transactions, 3*, 1239.

42. University of Dayton Research Institute, Structural Integrity Division. (2004). Life Prediction Methodologies for Aerospace Materials, Annual Report (AFRL-ML-WP-TR-2004-4283).

43. Air Force Research Laboratory Report. (2008). Low Delta K Faceted Crack Growth in titanium alloys. (AFRL-RX-WP-TP-2009-4151).

44. Dunne, F. P. E., Walker, A., Rugg, D. (2007). A systematic study of hcp crystal orientation and morphology effects in polycrystal deformation and fatigue. *Proceedings of the Royal Society a-Mathematical Physical and Engineering Sciences, 463*(2082), 1467.

45. Dunne, F., Rugg, D. (2008). On the mechanisms of fatigue facet nucleation in titanium alloys. *Fatigue and Fracture of Engineering Materials and Structures, 31*(11), 949–958; Under review.

46. Woodfield, A. P., Gorman, M. D., Sutliff, J. A., Corderman, R. R. (1998). *Effect of Microstructure on Dwell Fatige Behavior of TI-6242. Fatigue Behavior of Titanium Alloys.* Proceedings from an International Symposium, TMS Fall Meeting '98, Chicago, Illinois.

47. Woodfield AP. Private Communications. 2003-2008.

48. Wang, W., Brandes, M., Mills, M., Larson, B. C., Ice, G. E. (2003). *X-ray Structural Microscopy Investigation of a Creep Deformed Polycrystalline α−Titanium Alloy*. Proceedings from the TMS Fall Meeting. Chicago, Illinois.

49. Wang, W., Brandes, M., Mills, M., Larson, B. C., Ice, G. E. (2003–2004). Unpublished Research. Argonne, Illinois: Argonne National Laboratory.

50. Meyn, D. A., Sandoz, G. (1969). Fractography and Crystallography of Subcritical Crack Propagation in High Strength Titanium Alloys. *Transactions of the Metallurgical Society of Aime, 245*, 1253.

51. Paton, N., Williams, J., Chesnutt, J., Thompson, A. (1976). *The Effects of Microstructure on the Fatigue and Fracture of Commercial Titanium Alloys*. AGARD Conference Proceedings 1976;185:4.

52. Air Force Materials Laboratory Report. (1978). Chesnutt JC, Thompson AW, Williams JC. The Influence of Metallurgical Factors on the Fatigue Crack Growth Rate in Alpha-Beta Titanium Alloys. (AFML-TR-78-68).

53. McBagonluri, F., Akpan, E., Mercer, C., Shen, W., Soboyejo, W. O. (2005). An investigation of the effects of microstructure on fatigue crack growth in Ti-6242. *Journal of Engineering Materials and Technology-Transactions of the Asme, 127*(1), 46–57.

54. Wanhill, R. J. H., Galatolo, R., Looije, C. E. W. (1989). Fractographic and Microstructural Analysis of Fatigue Crack-Growth in a Ti-6al-4v Fan Disk Forging. *International Journal of Fatigue, 11*(6), 407–416.

55. Air Force Research Laboratory Report. (2009). Low Delta K faceted crack growth in titanium alloys. (AFRL-RX-WP-TP-2009-4151).

56. McBagonluri, F., Akpan, E., Mercer, C., Shen, W., Soboyejo, W. O. (2005). An investigation of the effects of microstructure on dwell fatigue crack growth in Ti-6242. *Materials Science and Engineering a-Structural Materials Properties Microstructure and Processing, 405*(1–2), 111–134.

57. Pilchak, A., Bhattacharjee, A., Williams, R., Williams, J. (2009). Proceedings from the 12th International Conference on Fracture, Ottawa, Ontario, Canada.

58. Pilchak, A. (2009). Materials Science and Engineering, vol. Ph.D. Columbus, Ohio: The Ohio State University, Ph.D. Dissertation.

59. Szczepanski, C. J., Jha, S. K., Larsen, J. M., Jones, J. W. (2008). Microstructural Influences on Very-High-Cycle Fatigue-Crack Initiation in Ti-6246. *Metallurgical and Materials Transactions a-Physical Metallurgy and Materials Science, 39*(12), 2841–2851.

60. Suri, S., Mills, M., Neeraj, T., Viswanathan, G., Hou, D. (1999). Room Temperature Deformation and Mechanisms of Slip Transmission in Oriented Single-Colony Crystals of an α/β Titanium Alloy. *Acta Materialia, 47*(3), 1019–1034.

61. Davidson, D. L., Lankford, J. (1984). Fatigue Crack-Growth Mechanics for Ti-6al-4v (Ra) in Vacuum and Humid Air. *Metallurgical Transactions a-Physical Metallurgy and Materials Science, 15*(10), 1931–1940.

62. Suresh, S. (1998). *Fatigue of Materials*. Cambridge, England: Cambridge University Press.

63. Uta, E., Gey, N., Bocher, P., Humbert, M., Gilgert, J. (2009). Texture heterogeneities in alpha(p)/alpha(s) titanium forging analysed by EBSD-Relation to fatigue crack propagation. *Journal of Microscopy-Oxford, 233*(3), 451–459.

64. ASTM STP 381, 1964, "Fracture Toughness Testing and Its Applications," ASTM International, West Conshohocken, PA, 1964, DOI: 1965:210, www.astm.org.

65. Meyn, D. A. (1972). Cleavage in titanium-8 aluminum-1 molybdenum-1 vanadium caused by hydrogen gas. *Metallurgical Transactions, 3*(8), 2302–2305.

66. ASTM STP 415, 1966, “Fatigue Crack Propagation,” ASTM International, West Conshohocken, PA, 1964, DOI: 1967:131, www.astm.org.

67. Toubal, L., Bocher, P., Moreau, A. (2009). Dwell-fatigue life dispersion of a near alpha titanium alloy. *International Journal of Fatigue, 31*(3), 601–605.

68. Hasija, V., Ghosh, S., Mills, M. J., Joseph, D. S. (2003). Deformation and creep modeling in polycrystalline Ti-6Al alloys. *Acta Materialia, 51*(15), 4533–4549.

69. Bhattacharjee, A., Pilchak, A., Norfleet, D., Williams, J. C. (2005–2009) Unpublished Research. The Ohio State University.

70. Sinha, V., Spowart, J. E., Mills, M. J., Williams, J. C. (2006). Observations on the faceted initiation site in the dwell-fatigue tested Ti-6242 alloy: Crystallographic orientation and size effects. *Metallurgical and Materials Transactions a-Physical Metallurgy and Materials Science, 37*(5), 1507–1518.

71. Woodfield, A. P., Gorman, M. D., Corderman, R. R., Sutliff, J. A., Yamrom, B. (1995). *Effect of microstructure on dwell fatigue behavior of Ti-6242. Titanium '95: Science and Technology*. Proceedings from the World Conference on Titanium, 8th, Birmingham, UK.

72. Venkataramani, G., Deka, D., Ghosh, S. (2006). Crystal plasticity based Fe model for understanding microstructural effects on creep and dwell fatigue in Ti-6242. *Journal of Engineering Materials and Technology-Transactions of the Asme, 128*(3), 356–365.

73. Kirane, K. Columbus, Ohio: The Ohio State University, M.S. Thesis, 2008.

74. Dunne, F. P. E., Rugg, D. (2008). On the mechanisms of fatigue facet nucleation in titanium alloys. *Fatigue & Fracture of Engineering Materials & Structures, 31*(11), 949–958.

75. Acharya, A., Beaudoin, A. (2000). Grain-size effect in viscoplastic polycrystals at moderate strains. *Journal of the Mechanics and Physics of Solids, 48*(10), 2213–2230.

76. Nye, J. (1953). Some geometrical relations in dislocated crystals. *Acta Metallurgica, 1*(2), 153–162.

77. Deka, D., Joseph, D. S., Ghosh, S., Mills, M. J. (2006). Crystal plasticity modeling of deformation and creep in polycrystalline Ti-6242. *Metallurgical and Materials Transactions, A: Physical Metallurgy and Materials Science, 37*(5), 1371–1388.

78. Venkatramani, G., Ghosh, S., Mills, M. (2007). A size-dependent crystal plasticity finite-element model for creep and load shedding in polycrystalline titanium alloys. *Acta Materialia, 55*(11), 3971–3986.

79. Venkataramani, G., Kirane, K., Ghosh, S. (2008). Microstructural parameters affecting creep induced load shedding in Ti-6242 by a size dependent crystal plasticity FE model. *International Journal of Plasticity, 24*(3), 428–454.

80. Ruiz, G., Pandolfi, A., Oritz, M. (2001). Three-dimensional cohesive modeling of dynamic mixed mode fracture. *International Journal for Numerical Methods in Engineering, 52*(1–2), 97–120.

81. Parvatareddy H., Dillard D. A. Effect of mode-mixity on the fracture toughness of Ti-6Al-4V/FM-5 adhesive joints. *International Journal of Fracture, 96*(3), 215–228.

82. Anahid M., Chakraborty P., Joseph D. S., Ghosh S. (2009). Wavelet decomposed dual-time scale crystal plasticity FE model for analyzing cyclic deformation induced crack nucleation in polycrystals. *Modelling and Simulation Science and Engineering, 17*(6).

83. Rokhlin, S., Kim, J. Y., Zoofan, B. (2005). Unpublished Research. Columbus, Ohio: The Ohio State University.

84. Groeber, M., Ghosh, S., Uchic, M. D., Dimiduk, D. M. (2008). A framework for automated analysis and simulation of 3D polycrystalline micro structures. Part 1: Statistical characterization. *Acta Materialia, 56*(6), 1257–1273.

85. Groeber, M., Ghosh, S., Uchic, M. D., Dimiduk, D. M. (2008). A framework for automated analysis and simulation of 3D polycrystalline micro structures. Part 2: Synthetic structure generation. *Acta Materialia, 56*(6), 1274–1287.

86. Ghosh, S., BlIandari, Y., Groeber, M. (2008). CAD-based reconstruction of 3D polycrystalline alloy microstructures from FIB generated serial sections. *Computer-Aided Design, 40*(3), 293–310.

87. Hosford, W. F. (1966). *Texture strengthening*. Metals Park, Ohio : ASM.

88. Cazacu, O., Barlat, F. (2001). Generalization of Drucker's Yield Criterion to Orthotropy. *Mathematics and Mechanics of Solids, 6*(6), 613–630.

89. Cazacu, O., Barlat, F. (2003). Application of representation theory to describe yielding of anisotropic aluminum alloys. *International Journal of Engineering Science, 41*(12), 1367–1385.

90. Perzyna, P. (1966). Fundamental Problems in Viscoplasticity. *Advances in Applied Mechanics, 9*, 243–377.

91. Ghosh, S., Kikuchi, N. (1991). An Arbitrary Lagrangian–Eulerian Finite Element Method for Large Deformation Analysis of Elastic-Viscoplastic Solids. *Computer Methods in Applied Mechanics and Engineering, 86*(2), 127–188.

92. U.S. Air Force Technical Report. (1993). Detectability of Small Flaws in Advanced Engine Alloys, Center for NDE 1993; Iowa State University, Ames, Iowa.

93. Margetan, F. J., Thompson, R. B., Yalda-Mooshabad, I. J. (1994). Backscattered microstructural noise in ultrasonic toneburst inspections. *Journal of Nondestructive Evaluation, 13*(3), 111–136.

94. Thompson, R. B., Margetan, F. J. (2002). Use of Elastodynamic Theories in the Stochastic Description of the Effects of Microstructure on Ultrasonic Flaw and Noise Signals. *Wave Motion, 36*(4), 347–365.

95. Bhattacharjee, A., Pilchak, A., Lobkis, J. W., Foltz, J., Rokhlin, S., Williams, J. Correlating Ultrasonic Attenuation and Microtexture in a Near-Alpha Titanium Alloy. *Metallurgical and Materials Transactions a-Physical Metallurgy and Materials Science, 42*(8), 2358–2372.

96. Kim, J-Y., Rokhlin, S. J. (2009). Determination of elastic constants of generally anisotropic inclined lamellar structure using line-focus acoustic microscopy. *The Journal of the Acoustical Society of America, 126*(6), 2998.

97. Panetta, P. D., Thompson, R. B., Margetan, F. J. (1998). Use of Electron Backscatter Diffraction in Understanding Texture and the Mechanisms of Backscattered Noise Generation in Titanium Alloys. *Review of Progress in Quantitative Nondestructive Evaluation, 17A*(1), 89–96.

98. Thompson, R. B., Margetan, F. J., Haldipur, P., Yu, L., Li, A., Panetta, P. D., Wasan, H. (2008). Scattering of Elastic Waves in Simple and Complex Polycrystals. *Wave Motion, 45*(5), 655–674.

99. Nagy, P., Adler, L. (1988). Scattering Induced Attenuation of Ultrasonic Backscattering. *Review of Progress in Quantitative Nondestructive Evaluation, 7B*(7), 1263–1271.

100. Lobkis, J. W., Rokhlin, S. (2010). Characterization of Polycrystals With Elongated Duplex Microstructure by Inversion of Ultrasonic Backscattering Data. *Applied Physics Letters, 96*(16), 161905.

101. Rose, J. (1991). *Review of Progress in Quantitative Nondestructive Evaluation, 10*, 1677.

102. Rose, J. (1991). *Review of Progress in Quantitative Nondestructive Evaluation, 10*, 1715.

103. Rose, J. (1991). *Review of Progress in Quantitative Nondestructive Evaluation, 10*, 1719.

104. Han, Y. K., Thompson, R. B. (1997). Ultrasonic Backscattering in Duplex Microstructures: Theory and Application to Titanium Alloys. *Metallurgical and Materials Transactions a-Physical Metallurgy and Materials Science, 28*(10), 91–104.

105. Stanke, F. E., Kino, G. S. (1983). A Unified Theory for Elastic Wave Propagation in Polycrystalline Materials. *The Journal of the Acoustical Society of America, 75*(3).

106. Weaver R. L. (1990). Diffusivity of Ultrasound in Polycrystals. *Journal of the Mechanics and Physics of Solids, 38*(1), 55–86.

107. Turner, J. A. (1999). Elastic Wave Propagation and Scattering in Heterogeneous, Anisotropic Media: Textured Polycrystalline Materials. *The Journal of the Acoustical Society of America, 106*(2), 541.

108. Ahmed, S., Thompson, R. B. (1992). Attenuation of Ultrasonic Waves in Cubic Metals Having Elongated, Oriented Grains. *Nondestructive Testing and Evaluation, 8–9*(1–6), 525–531.

109. Prydnikov, A. P., Brychkov, Y. A., Marichev, O. I. (1986). *Integrals and Series* (Vol. 2). New York, NY: Gordon and Breach Science Publishers. pp 201.

110. Luetjering, G., Williams, J. (2003). *Titanium*. New York, NY: Springer-Verlag.

111. Kocks, U. F., Tome, C. N., Wenk, H., Beaudoin, A., Mecking, H. (2000). *Texture and Anisotropy*. Cambridge, UK: Cambridge University Press.

112. Yang, L., Lobkis, J. W., Rokhlin, S. (2011). Explicit Model for Ultrasonic Attenuation in Equiaxial Hexagonal Polycrystalline Materials. *Ultrasonics, 51*(3), 303–309.

113. Yang, L., Lobkis, J. W., Rokhlin, S. (2011). Shape Effect of Elongated Grains on Ultrasonic Attenuation in Polycrystalline Materials. *Ultrasonics, 51*(6), 697–708.

114. Panetta, P. D., Thompson, R. B. (1999). Ultrasonic Attenuation in Duplex Titanium Alloys. *Review of Progress in Quantitative Nondestructive Evaluation, 18B*, 1717.

115. Blodgett, M., Eylon, D. (2001). The Influence of Texture and Phase Distortion on Ultrasonic Attenuation in Ti-6Al-4V. *Journal of Nondestructive Evaluation, 20*(1), 1–16.